



**Regulation of the unfolded protein response, endoplasmic
reticulum stress and autophagy pathways in the host
response to coronavirus infection**

Inaugural Dissertation submitted to the Faculty of Medicine in partial fulfillment of the
requirements for the PhD-Degree of the Faculties of Veterinary Medicine and Medicine of the
Justus Liebig University-Giessen

By
Shikh Shaban, M.Samer
Of
Aleppo-Syria

From the Institute of “Rudolf-Buchheim Institut für Pharmakologie”

Director / Chairman: Prof. Dr. Michael Kracht

of the Faculty of Medicine of the Justus Liebig University Giessen

First Supervisor and Committee Member: Prof. Dr. Michael Kracht

Second Supervisor and Committee Member: Prof. Dr. Friedemann Weber

Committee Members:

Prof. Dr. Michael Kracht

Prof. Dr. Eva Friebertshäuser (Marburg)

Prof. Dr. Norbert Weißmann

Prof. Dr. Friedemann Weber

Date of Doctoral Defense:

Giessen (20.03.2023)

Table of contents

Table of contents	4
Abstract	9
German summary	11
Chapter 1: Introduction	13
1.1 Coronaviruses	13
1.1.1 Coronaviruses genome structure	15
1.1.2 Coronaviruses proteins functions	17
1.1.3 Coronaviruses replication cycle	19
1.2 The endoplasmic reticulum (ER).....	21
1.2.1 ER stress and the unfolded protein response (UPR).....	23
1.2.2 Chemical inducers of ER stress and the UPR.....	26
1.3 Autophagy	28
1.3.1 The formation of autolysosome and autophagy flux measurement.....	29
1.3.2 The role of autophagy in viral infection.....	31
1.4 Aims of the study	33
Chapter 2: Materials	34
2.1 Cell lines.....	34
2.2 Bacterial strains	35
2.3 Expression vectors.....	35
2.4 Oligonucleotides and primers.....	35
2.5 Antibodies	38
2.6 Enzymes	39
2.7 Small molecule inhibitors and inducers	40
2.8 Ready-to-use materials and reagents (including kits).....	40
2.9 Buffers and prepared mediums.....	41
2.10 Chemicals	43
2.11 Plastics and other disposable materials	43
2.12 Devices and apparatuses.....	43
2.12.1 for gel electrophoresis and Western blotting.....	43
2.12.2 for PCR.....	44
2.12.3 for centrifugation and mixing.....	44
2.12.4 for weighting chemicals	44
2.12.5 for cell culture	44
2.12.6 Microscopy.....	44
2.12.7 Others	44
2.13 Software.....	45

Chapter 3: Methods	46
3.1 Mammalian cell culture	46
3.1.1 Thawing and freezing adherent cells	46
3.1.2 Growing and passaging the cells	46
3.1.3 Transfection methods	47
3.1.3.1 Calcium phosphate (CaCl ₂) method	47
3.1.3.2 Lipofectamine 2000 method.....	48
3.1.4 Harvesting the cells	49
3.2 Molecular biology	50
3.2.1 Plasmid extraction	50
3.2.2 RNA extraction.....	50
3.2.3 Reverse transcription.....	51
3.2.4 Quantitative PCR (qPCR).....	51
3.2.5 Agarose gel.....	53
3.2.6 Molecular cloning.....	54
3.2.6.1 Producing CRISPR-CAS-9 vectors	54
3.2.6.2 Producing the BioID vectors	57
3.2.7 Sanger sequencing	60
3.3 Microbiology	60
3.3.1 Bacterial work	60
3.3.2 Virus work.....	61
3.3.2.1 HCoV-229E propagation.....	61
3.3.2.2 Determining virus titer using TCID ₅₀	61
3.3.2.3 Determining virus titer using plaque assay.....	63
3.3.2.4 Working with lenti-virus	64
3.3.2 Testing for mycoplasma	65
3.4 Biochemistry	66
3.4.1 Lysing the cells.....	66
3.4.2 Bradford assay	66
3.4.3 SDS-PAGE.....	67
3.4.4 Semi-dry Western blotting	68
3.4.4 BioID	69
3.4.5 Silver staining.....	71
3.4.6 L-HPG labelling using click chemistry	71
3.4.7 Mass spectrometry.....	73
3.4.7.1 MERS-CoV and SARS-CoV-2 samples processing for mass spectrometry	73
3.4.7.2 BioID-ATF3 samples processing for mass spectrometry.....	74
3.5 Cell biology	74

3.5.1 Assessing cells viability	74
3.5.2 Indirect immunofluorescence (IF).....	75
3.6 Bioinformatics analysis	76
3.6.1 Data analysis of MERS-CoV and SARS-CoV-2 mass spectrometry samples	76
4.6.2 Data analysis of BioID-ATF3 mass spectrometry samples.....	79
Chapter 4: Results	84
4.1 Activation and pharmacological modulation of the ER stress response in CoV-infected cells ..	84
4.1.1 The activation status of the ER stress sensors PERK and IRE1 α in HCoV-229E-infected cells and the consequences of their inhibition for the host response and the viral replication.	84
4.1.2 Effect of inhibiting ER stress sensors, PERK and IRE1 α , on the host de-novo protein synthesis levels in cells infected or uninfected with CoV	88
4.1.3 Effect of the chemical compound thapsigargin on the activation of ER stress in the context of host response and virus replication	90
4.1.4 Effect of prolonged activation of ER stress pathways by thapsigargin on virus-induced translational shutdown.....	96
4.1.5 Reproducibility of thapsigargin anti-viral effect in a different cellular model.....	99
4.1.6 Cytotoxic and effective concentrations of thapsigargin in Huh7 cells for HCoV-229E inhibition	101
4.1.7 Durability of thapsigargin inhibition of HCoV-229E beyond 24 hours.....	105
4.1.8 Inhibitory effect of thapsigargin on the highly pathogenic MERS-CoV and SARS-CoV-2 replication.....	107
4.1.9 PERK role in the thapsigargin-induced anti-viral effect	109
4.1.10 Alterations in the cellular proteomic landscapes induced by thapsigargin treatments and/or CoV infection	111
4.2 Pharmacological modulation of autophagy flux in cells infected with CoV.....	125
4.2.1 Selective and basal autophagy flux are differentially regulated when investigated at the late stage of the 24 hours HCoV-229E infection	125
4.2.2 Bafilomycin A1 inhibition of CoV is pathogen- and time of addition- dependent.....	127
4.2.2 Pharmacological modulations of autophagy flux and PERK pathway in cells infected with CoV	131
4.3 Genetic perturbations of several ER stress factors in Huh7 cells and their effect on CoV replication and host response.....	137
4.3.1 Establishing stable PERK and IRE1 α knockdown cell lines.....	138
4.3.2 Characterizing PERK and IRE1 α knockdown cell lines in the context of HCoV-229E replication.....	143
4.3.3 Establishing stable ATF3 knockdown cell line using lentivirus system	151
4.4 The interactome of major UPR effectors.....	153
4.4.1 Characterization of BirA and miniTurbo constructs	155
4.4.2 The proximity-based interactome of ATF3 in the context of HCoV-229E infection.....	168
Chapter 5: Discussion.....	181
5.1 The roles of the UPR in CoV replication	181

5.1.1 The modulation of major UPR factors by CoV infection.....	181
5.1.2 The effects of attenuating the functions and protein levels of PERK and IRE1 α on CoV replication and host response.....	183
5.1.2.1 The “basal” host response to attenuating the functions and protein levels of PERK ..	183
5.1.2.2 The effects of attenuating the functions and protein levels of PERK and IRE1 α on CoV replication.....	184
5.1.3 Role of thapsigargin activation of UPR in CoV replication.....	187
5.1.3.1 Role of BiP and IRE1 α in thapsigargin-mediated adaptive and anti-viral responses..	187
5.1.3.2 The proteomic changes in response to thapsigargin treatment of CoV-infected cells.	188
5.1.3.3 The translational changes in response to thapsigargin treatment of CoV-infected cells	190
5.1.3.4 CoV might be a direct target of thapsigargin	191
5.1.3.5 The role of the SERCA pump in thapsigargin-mediated anti-viral effect	192
5.2 Role of autophagy in CoV replication and crosstalk with ER stress pathways.....	193
5.2.1 Role of autophagy in HCoV-229E	193
5.2.2 Role of autophagy in MERS-CoV.....	194
5.2.3 Role of autophagy in SARS-CoV-2	194
5.2.4 Is there a role for autophagy in CoV regulation? Integrating data from the study of the three viruses.....	195
5.3 The role of ATF3 in HCoV-229E infection	196
5.3.1 ATF3 knockdown in Huh7 cells in context of CoV replication.....	196
5.3.2 Interactome studies using BioID method	198
5.3.2.1 Attempts to study the interactome of several ER factors using BioID method.....	198
5.3.2.2 Studying the interactome of ATF3 using BioID method.....	199
5.4 Limitations of the study and outlook.....	202
Literature	204
List of abbreviations:.....	226
List of figures:	228
List of tables:.....	231
List of figures involved external contributions:	232
Declaration	234
Acknowledgement:.....	235
Personal data sheet:	236

Abstract

Coronaviruses (CoV) are a group of RNA viruses that have continuously posed risks to humans' health and economy. Since the first recorded major CoV outbreak of SARS-CoV in 2001, using modern scientific methods, tremendous effort and resources have been devoted to better understanding the transmission of these viruses to humans and the associated disease manifestations. Like all known viruses, CoV require and utilize intracellular signaling pathways to replicate in the host cell. In doing so, CoV have apparently evolved diverse strategies to modulate these systems to initiate the formation of novel pathogenic intracellular structures, including so-called double membrane vesicles (DMVs), which collectively have been termed replicative organelles (ROs). DMVs and ROs are essential for successful CoV replication. Their formation, together with massively increased synthesis of viral protein and RNA components, leads to pronounced activation of affected cells. Among the cellular processes modulated early and most strongly during CoV infection are those related to the endoplasmic reticulum (ER) stress response and autophagy.

Activation of ER signaling pathways by CoV results in ER stress and triggering of the unfolded protein response (UPR). The UPR is an adaptive process by which the cell attempts to restore normal ER function through activation of protein kinases, transcription factors, and downstream genetic programs. This involves a number of well-characterized molecular sensor and effector molecules anchored in the ER membrane, which include the protein kinases PERK and IRE1 α and the chaperone BiP (GRP78, HSPA5).

Autophagy refers to a highly dynamic process by which the cell can degrade larger molecular complexes, organelles, or invading pathogens and recycle or destroy the resulting macromolecules. As part of the autophagy process, a double membrane structure (the autophagosome) is formed, which interacts with the proteins LC3B and p62/SQSTM1 (sequestosome1) to coordinate basal, as well as selective, autophagy flux in response to various stressors, including viral infections.

In this work, the central questions were investigated to what extent (i) CoV specifically modulate the ER stress and autophagy system and whether (ii) new starting points for antiviral strategies can be derived from this. To this end, a series of specific molecular but also proteome-wide analyses were performed in pharmacologically and genetically perturbed cellular model systems. Small molecule inhibitors were used to examine the effect of inhibiting PERK, IRE1 α , or both protein kinases on CoV replication as well as on activation of the UPR and host response. One of the major findings of this approach was that inhibition of PERK resulted in a reduction in replication of HCoV-229E and MERS-CoV, but not SARS-CoV-2. HCoV-229E infection of Huh7 cells resulted in induction of the transcription factor ATF3 and suppression of BiP. PERK inhibition abolished both of these effects and led to a reduction in phosphorylation of serine 52 of the translation-inhibitory factor eIF2 α . In contrast, inhibition of IRE1 α resulted in only a small reduction in HCoV-229E replication but completely

prevented virus-induced ATF3 induction. Artificial, "chemical" activation of the UPR by the natural product thapsigargin resulted in strong inhibition of replication of all three CoV tested with a half-maximal effective concentration (EC_{50}) in the low nanomolar range with concomitant low cytotoxicity. Furthermore, thapsigargin treatment of CoV-infected cells was associated with partial abrogation of global HCoV-229E-induced inhibition of protein biosynthesis and resulted in almost complete inhibition of CoV-induced selective and basal autophagy flux. Subsequently, a genetic approach based on the CRISPR-CAS-9 system was used to further investigate the roles of PERK, IRE1 α , and ATF3 in CoV replication. Silencing of PERK resulted in a decrease in HCoV-229E replication, whereas suppression of IRE1 α or ATF3 showed very little or no effect on virus replication. In addition, mass spectrometric techniques were used to comparatively examine changes in the proteome in CoV-infected and thapsigargin-treated cells. Bioinformatic analyses of the differentially expressed proteins resulted in the identification of a number of specific metabolic processes, signaling pathways, and factors that may be responsible for the antiviral effect of thapsigargin, including ER-associated degradation (ERAD) and ER quality control (ERQC) pathways. In the final part of the work, a proximity-based, proteome-wide interaction screen was performed to reveal the intracellular binding partners of ATF3 in the context of HCoV-229E infection. This led to the identification of a number of components of the immune system and mitochondrial homeostasis that are potential ATF3-dependent regulated effector molecules.

In summary, the results obtained in this work provide insight into the CoV-specific activation patterns of the ER stress factors PERK, IRE1 α , BiP, and ATF3 and their role in CoV replication and host response. The extensive evidence for antiviral efficacy of thapsigargin establishes chemical activation of the ER stress system as a novel antiviral therapeutic principle against enveloped RNA viruses such as HCoV-229E, MERS-CoV, and SARS-CoV-2 and identifies thapsigargin as a new prototype of compounds with multimodal host-directed antiviral activity based on molecular mechanisms of action.

German summary

Coronaviren (CoV) umfassen eine Gruppe von RNA-Viren mit einem hohen gesundheitlichen und ökonomischen Gefährdungspotential für die gesamte Menschheit. Seit dem ersten, mit modernen wissenschaftlichen Methoden verfolgbaren CoV-Ausbruch von SARS-CoV im Jahr 2001, wurden enorme Anstrengungen und Ressourcen darauf verwendet, den Übertritt dieser Viren auf den Menschen und die damit verbundenen Krankheitserscheinungen besser zu verstehen. Wie alle bekannten Viren benötigen und nutzen CoV intrazelluläre Signalwege, um in der Wirtszelle zu replizieren. Dabei haben CoV offenbar verschiedene Strategien zur Modulation dieser Systeme entwickelt, um die Bildung neuartiger pathogener intrazellulärer Strukturen zu initiieren, einschließlich sogenannter Doppelmembranvesikel (DMVs), die zusammen als replikative Organellen (ROs) bezeichnet werden. DMVs und ROs sind für die erfolgreiche CoV-Replikation unerlässlich sind. Ihre Bildung führt zusammen mit der massiv erhöhten Synthese von viralen Protein- und RNA Komponenten zu einer ausgeprägten Aktivierung der betroffenen Zellen. Zu den frühzeitig und am stärksten modulierten zellulären Prozessen während einer CoV-Infektion gehören diejenigen, die mit der Stressantwort des endoplasmatischen Retikulums (ER) und der Autophagie zusammenhängen.

Die Aktivierung von ER-Signalwegen durch CoV führt zu ER-Stress und einer Auslösung der unfolded protein response (UPR). Die UPR ist ein adaptiver Prozess, mittels dessen die Zelle versucht, die normale Funktion des ER durch die Aktivierung von Proteinkinasen, Transkriptionsfaktoren und nachfolgenden genetischen Programmen wiederherzustellen. Hierbei sind eine Reihe an gut charakterisierten, in der ER Membran verankerten molekulare Sensor- und Effektormoleküle beteiligt, zu denen die Proteinkinasen PERK und IRE1 α sowie das Chaperon BiP (GRP78, HSPA5) gehören.

Autophagie bezeichnet einen hoch dynamischen Prozess, mit dessen Hilfe die Zelle größere Molekülkomplexe, Organellen oder auch eindringende Krankheitserreger degradieren und die entstehenden Makromoleküle recyceln oder zerstören kann. Im Rahmen des Autophagieprozesses entsteht eine Doppelmembranstruktur (das Autophagosom), welche mit den Proteinen LC3B und p62/SQSTM1 (Sequestosome1) interagiert, um den basalen, aber auch den selektiven Autophagiefluss als Reaktion auf verschiedene Stressoren, einschließlich viraler Infektionen, zu koordinieren.

In dieser Arbeit wurden die zentralen Fragen untersucht, inwieweit (i) CoV die ER Stress- und Autophagie System spezifisch modulieren und ob sich (ii) hieraus neue Ansatzpunkte für antivirale Strategien ableiten lassen. Hierzu wurde eine Reihe an spezifischen molekularen, aber auch proteomweiten Analysen in pharmakologisch und genetisch perturbierten zellulären Modellsystemen durchgeführt. Mittels niedermolekularer Inhibitoren wurde die Wirkung der Hemmung von PERK, IRE1 α , oder beiden Proteinkinasen auf die CoV-Replikation sowie auf die Aktivierung der UPR und der Wirtsantwort untersucht. Eines der wichtigsten Ergebnisse dieses Ansatzes war, dass die Hemmung von PERK zu einer Verringerung der Replikation von HCoV-229E und MERS-CoV, aber nicht von

SARS-CoV-2 führte. Eine HCoV-229E-Infektion von Huh7-Zellen führte zur Induktion des Transkriptionsfaktors ATF3 und zur Suppression von BiP. Die PERK-Hemmung hob diese beiden Effekte auf und führte zu einer Verringerung der Phosphorylierung von Serin 52 des translationshemmenden Faktors eIF2 α . Demgegenüber führte die Hemmung von IRE1 α nur zu einer geringen Verringerung der HCoV-229E-Replikation, verhinderte aber vollständig die Virus-induzierte ATF3-Induktion. Eine artefizielle, „chemische“ Aktivierung der UPR durch den Naturstoff Thapsigargin resultierte in einer starken Hemmung der Replikation aller drei getesteten CoV mit einer halbmaximalen effektiven Konzentration (EC₅₀) im unteren nanomolaren Bereich bei gleichzeitiger geringer Zytotoxizität. Weiterhin war eine Thapsigargin Behandlung von CoV-infizierten Zellen mit einer partiellen Aufhebung der globalen, HCoV-229E- induzierten Hemmung der Proteinbiosynthese assoziiert und führte zu einer fast kompletten Inhibition des CoV-induzierten selektiven und basalen Autophagieflusses. Nachfolgend wurde ein genetischer, auf dem CRISPR-CAS-9 System basierender Ansatz, genutzt, um die Rolle von PERK, IRE1 α und ATF3 bei der CoV-Replikation weiter zu untersuchen. Das Ausschalten von PERK führte zu einem Rückgang der HCoV-229E-Replikation, während die Suppression von IRE1 α oder ATF3 nur eine sehr geringe oder keine Auswirkungen auf die Virusreplikation zeigt. Zusätzlich wurden massenspektrometrische Verfahren verwendet, um Veränderungen des Proteoms in CoV-infizierten und mit Thapsigargin behandelten Zellen vergleichend zu untersuchen. Bioinformatische Analysen der differentiell exprimierten Proteine resultierten in der Identifikation einer Reihe von spezifischen metabolischen Prozessen, Signalwegen und Faktoren, die für die antivirale Wirkung von Thapsigargin verantwortlich sein könnten, einschließlich ER-assoziiertes Abbau- (ERAD) und ER-Qualitätskontrollwege (ERQC). Im letzten Teil der Arbeit wurde ein proximitäts-basierter, proteomweiter Interaktions *Screen* durchgeführt, um die intrazelluläre Bindungspartner von ATF3 im Zusammenhang mit einer HCoV-229E-Infektion aufzudecken. Dieses führte zur Identifikation einer Reihe von Komponenten des Immunsystems und der mitochondrialen Homöostase, die als potentielle ATF3-abhängig regulierte Effektormoleküle in Frage kommen.

Zusammenfassend geben die in dieser Arbeit erzielten Ergebnisse einen Einblick in die CoV-spezifischen Aktivierungsmuster der ER-Stress Faktoren PERK, IRE1 α , BiP und ATF3 und ihrer Rolle bei der CoV Replikation und der Wirtsantwort. Die umfangreiche Evidenz für eine antivirale Wirksamkeit von Thapsigargin etabliert die chemische Aktivierung des ER Stress Systems als ein neues antivirales Therapieprinzip gegen umhüllte RNA-Viren wie HCoV-229E, MERS-CoV und SARS-CoV-2 und identifiziert Thapsigargin anhand der molekularen Wirkmechanismen als einen neuen Prototyp von Verbindungen mit multimodaler, auf den Wirt gerichteter antiviraler Aktivität.

Chapter 1: Introduction

1.1 Coronaviruses

Coronaviruses (CoV) are plus single-stranded RNA viruses with a wide range of hosts including human beings. At the organismic level, the pathology associated with CoV can manifest itself in different systems including the upper and lower respiratory tracts, the enteric system, and the nervous system (Jacob Machado et al. 2021).

Coronaviruses got their name first when a group of virologists observed an avian infectious bronchitis virus under electron microscopy. The virus had corona-like projections surrounding the round body of the particle and hence it was named for this appearance (J. D. Almeida et al, 1968). The characterized virus by J. D. Almeida et al resembled other previously isolated viruses including a murine hepatitis virus (MHV) and a human virus named 229E (later to be renamed HCoV-229E)(D. X. Liu, Liang, and Fung 2021). HCoV-229E was first isolated in 1966 from a human respiratory tract sample (Hamre and Procknow 1966). The discovery of many other viruses sharing the same distinct corona-like appearance led to the establishment of the Coronaviridae family in 1975 (Weiss and Navas-Martin 2005). The family Coronaviridae belongs to the order of Nidovirales which is in the realm of Riboviria (Gorbalenya et al. 2020). Coronaviridae is further divided into two major subfamilies namely Letovirinae, and Orthocoronavirinae. This latter subfamily is subdivided into four genera: Alphacoronavirus, Betacoronavirus, Gammacoronavirus, and Deltacoronavirus (data updated regularly by the International Committee of Taxonomy of Viruses, ICTV) (Fig. 1).

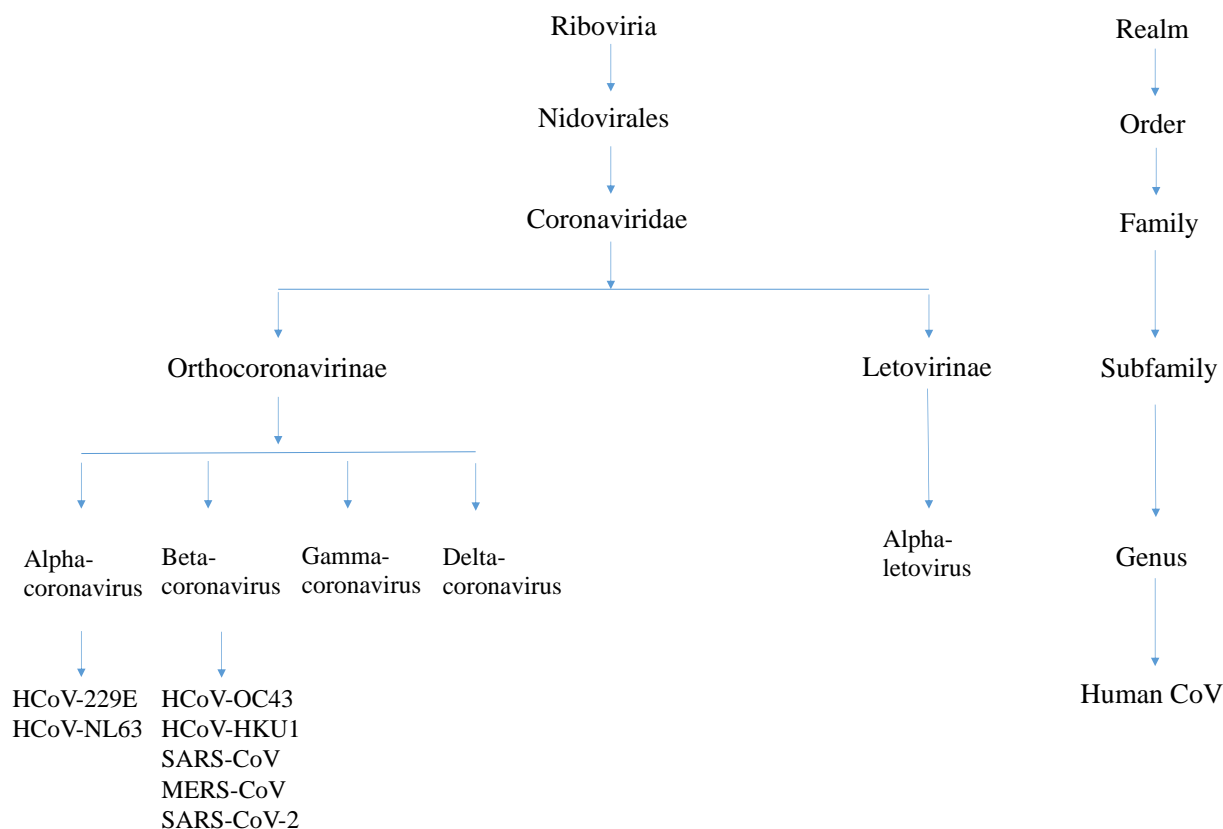


Figure 1: Taxonomy of Coronaviridae with the seven coronaviruses that infect human beings.

A schematic representation of Coronaviridae family higher and lower classifications with emphasis on Alpha- and Beta-coronaviruses that infect human beings.

Of the animal CoV, porcine epidemic diarrhea virus (PEDV), transmissible gastroenteritis virus (TGEV), both infecting pigs, and bovine coronavirus (BCoV) are of particular economic importance given their respective hosts and the pathology associated with the infection.

MHV is a Betacoronavirus belonging to murine coronaviruses, first isolated in 1949, is one of the most studied CoV and is considered a model virus for human CoV infection and disease (Bailey et al. 1949) (Weiss 2020).

Of the human CoV, four are endemic and usually associated with a mild, upper respiratory tract disease (HCoV-229E, -OC43, -NL63, -HKU1). The three highly pathogenic ones (the Middle East respiratory syndrome (MERS)-CoV, severe acute respiratory syndrome (SARS)-CoV and SARS-CoV-2) are a result of a recent introduction from animals to humans (zoonosis). These viruses are known to infect the lower respiratory tract, potentially causing severe diseases, including acute respiratory distress syndrome (ARDS) (Lamers and Haagmans 2022) (Fig. 1).

First observed in 2003, SARS-CoV caused a relatively small but worldwide outbreak that resulted in 8098 known cases of infection and 774 registered fatalities (Lui et al. 2020). The overall case fatality rate (CFR) of SARS-CoV was hovering around 10% while the CFR for patients aged 60 and above was

more than 50% (“Consensus Document on the Epidemiology of Severe Acute Respiratory Syndrome (SARS)” 2003.). The relatively high CFR of this outbreak alerted the world to the impending danger posed by CoV. Intriguingly, no known cases of SARS-CoV were ever registered after 2004 (Z. Zhu et al. 2020).

Nine years later, the world was on a rendezvous with a new, relatively small, outbreak of CoV caused by a zoonotic spillover from camels to humans. The virus was named MERS-CoV. It resulted in 2,506 infections (so far) with a relatively very high overall CFR, nearing 35% (Y. Liang et al. 2020). Unlike SARS-CoV, MERS-CoV cases are still being sporadically reported, mainly in the Arabian Peninsula (Z. Zhu et al. 2020).

With these two outbreaks in mind, many scientists saw a sweeping pandemic of coronavirus as a pending, inevitable event (Cheng et al. 2007) (Menachery et al. 2015). Not to their surprise, at the end of 2019, news from China of a cluster of patients with pneumonia of unknown etiology heralded the emergence of a novel coronavirus that was later named SARS-CoV-2 and is the causative agent of COVID-19 (Huang et al. 2020) (Gorbalenya et al. 2020). Although the overall CFR of the new CoV is relatively low (estimations might differ between sources) the outbreak resulted so far in massive losses of lives and a major setback to global economies given the magnitude of the spread of this virus (Lui et al. 2020). Patients aged 60 or more, and those with co-morbidities experienced a significantly higher CFR and more severe symptoms than younger, otherwise healthy, patients did (Z. Zhu et al. 2020).

The undeniable current and predicted risks posed by coronaviruses necessitate thorough research and understanding of these viruses’ replicative cycle and the respective host response. Such research would allow identifying points of interventions in the CoV replicative cycle or the host response that eventually lead to the development of efficient anti-viral strategies.

1.1.1 Coronaviruses genome structure

The genome of CoV is organized into two major regions. The first region comprises the replicase gene region occupying about 22Kb (two-thirds) while the second one comprises the structural and accessory genes region (varying in numbers from one CoV to another) making up the rest one-third of the genome (Brant et al. 2021). At its five prime end, the genome is capped with an m7G-cap structure (m7GpppA1), protecting it from degradation by host enzymes and facilitating ribosomal translation by the host (Wilamowski et al. 2021, 2). The five prime end also contains an untranslated region (UTR) that is most likely involved in regulating viral RNA synthesis (Madhugiri et al. 2014). The 3 prime end of the genome is endowed with a poly(A) tail ranging from 30 to 60-nt in length and a UTR with still elusive, possibly regulatory, functions (D. Zhang et al. 2022) (Miao et al. 2008) (Fig. 2).

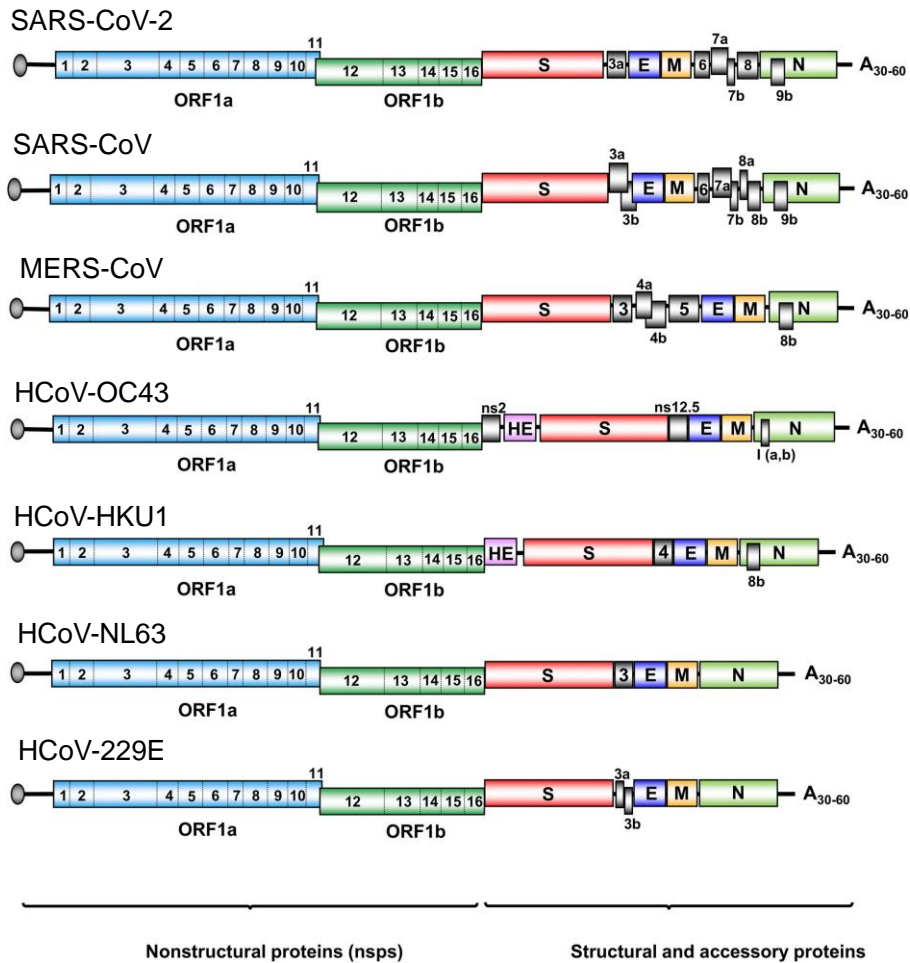


Figure 2: Genomic structure of the seven coronaviruses that infect human beings.

A schematic representation of the two major regions of the CoV genome coding for nonstructural proteins (NSPs) and structural and accessory proteins. The grey circle at the five prime end represents the cap and “A₃₀₋₆₀” indicates the poly-A tail at the three prime end. Abbreviations for viral structural proteins are as follows: Spike (S), the envelope (E), the membrane (M), the nucleocapsid (N), and hemagglutinin esterase (HE). NSPs are indicated by blue and green, numbered boxes in the replicase gene region. Accessory proteins are indicated by gray, numbered boxes in the second region of the genome. ORF, open reading frame.

The figure was adapted from figure 1, Brant et al. 2021. under a Creative Commons Attribution 4.0 International License (Brant et al. 2021).

The replicase gene has two overlapping open reading frames, ORF1a and ORF1b. At the junction between the two ORFs, a pseudoknot RNA structure is formed that leads to a -1 ribosomal frameshift (Kelly et al. 2020). This frameshift produces two major polypeptides (Giedroc and Cornish 2009). The two major polypeptides (pp), pp1a and pp1ab, are further processed and cleaved into 16 non-structural proteins (NSPs) using the two viral proteases chymotrypsin-like protease, 3CLpro, also called viral main protease Mpro, and Papain-like protease, PLpro (Ziebuhr, Snijder, and Gorbalenya, 2000). These NSPs are involved in the replication and transcription of the viral genomic RNA, among other functions that will be discussed in the subsequent sections.

Downstream from the replicase gene region reside sequences encoding for structural and accessory proteins. The production of these proteins requires a different approach than the one used for the NSPs.

These proteins are translated from a group of sub-genomic messenger RNAs (sgmRNAs) that are produced through a process of discontinuous transcription during the negative RNA strand synthesis (H.-Y. Wu and Brian 2010). This process generates nested sgmRNAs with a shared 5 prime leader sequence, 5 prime cap structure, and a 3 prime poly(A) tail (Finkel et al. 2021). The shared leader sequence is a transcription regulatory sequence (**TRS-Leader**) that is found at the 5 prime end of the genomic viral RNA (Yang et al. 2021). During the process of discontinuous transcription, the viral RNA-dependent RNA polymerase (RdRp) pauses upon encountering a transcription regulatory sequence in the body of the genome (**TRS-Body**) (Brant et al. 2021). TRS-B sequences are located throughout the length of the second region of the viral genome at different locations (Brant et al. 2021). This pause upon encountering TRS-B triggers the polymerase to fall off and “jump” back to TRS-L, incorporate it, and then start a new round of mRNA transcription and continue the synthesis until encountering the next TRS-B (D. Kim et al. 2020). The process will repeat until the last TRS-B is encountered, generating the nested sgmRNAs (D. Kim et al. 2020) (Fig. 3).

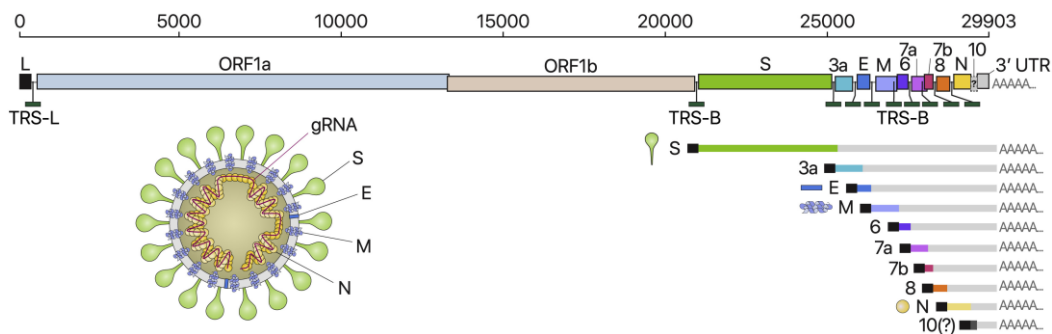


Figure 3: CoV structural and accessory proteins are produced from sub-genomic messenger RNAs.

A schematic representation of SARS-CoV-2 genomic structure (as an example) illustrating the nine sub-genomic messenger RNAs produced through the process of discontinuous transcription (during the negative RNA strand synthesis). Abbreviations are as follows: Transcription regulatory sequence-leader (TRS-L), Transcription regulatory sequence-body (TRS-B), Spike (S), the envelope (E), the membrane (M), and the nucleocapsid (N). The question mark at ORF10 indicates an unconfirmed expression. gRNA, genomic RNA.

The figure was adapted from figure 1, Kim et al. 2020. Open access under the COVID-19 resource centre (D. Kim et al. 2020).

The positive strands of each of these sgmRNAs will be then translated into structural proteins, including the spike (S), the envelope (E), the membrane (M) and the nucleocapsid (N), and multiple accessory proteins.

1.1.2 Coronaviruses proteins functions

The poly-cistronic (multiple polypeptides encoded from one messenger RNA) genomic RNA of CoV is capable of producing 16 NSPs (Brant et al. 2021). These NSPs have diverse and crucial functions that ensure a successful replicative cycle and contribute to the evolutionary adaptation of the virus to its host.

The first major polypeptide to be translated is pp1a followed by the frameshift product pp1ab, consisting of about 4000 and 7000 amino acids respectively (Ziebuhr and Siddell 1999). Included in these polypeptides are regions with proteolytic activities, namely 3CLpro (NSP5), and PLpro (NSP3), that would auto-process both polypeptides at specific conserved sites to liberate themselves first (Thiel et al. 2003). The now liberated proteinases will further cleave the two polypeptides to liberate the remaining NSPs. 3CLpro (NSP5) cleavages of pp1a at seven conserved sites release NSP4 to NSP11. The same proteinase cleaves pp1ab at 11 conserved sites to excise NSP4 to NSP16 (Moustaqil et al. 2021). NSP1 to NSP4 are cleaved by PLpro (NSP3) (Thiel et al. 2003). The now-released NSPs will be able to carry out their corresponding functions.

NSP1 is involved in damping down the immune system of the host by inducing host mRNAs degradation (Kamitani et al. 2006). The cleaved form of NSP2 is reported to have still unknown, unessential function in the production of infectious particles (Graham et al. 2006). Besides its role as a proteinase, the multi-domain NSP3 has an important deubiquitinating and reversal of protein ADP-ribosylation functions making it a major antagonist of host immune signaling (J. Lei, Kusov, and Hilgenfeld 2018; Russo et al. 2021). An additional role of NSP5 has been reported in modulating the host immune response through interacting with histone deacetylase 2 (HDAC2), an epigenetic regulator known to play a role in the expression of inflammatory genes (Gordon et al. 2020).

Together with NSP3 and NSP4, NSP6 contributes to the formation of the double-membrane vesicles (DMVs) through an incompletely understood mechanism that partly involves components of the autophagosome biogenesis (Cottam et al. 2011).

To replicate the viral genome several NSPs close cooperate to achieve this mission. Central for this collaboration is a canonical, primer-dependent, viral RNA-dependent RNA polymerase (RdRp) domain residing in the c-terminal of NSP12 and a complex of NSP7 and NSP8 acting as cofactors (te Velthuis, van den Worm, and Snijder 2012). Wherein this complex, NSP8 acts as a 3'-Terminal Adenylyltransferase (Tvarogová et al. 2019.).

Although reports of its importance for viral replication are numerous, NSP9 has been identified as an RNA-binding protein with yet an unconfirmed function. The protein has also been recently reported to be a target of the nidovirus RdRp associated nucleotidyl transferase (NiRAN) domain of NSP12 for nucleoside monophosphate (NMP) transfer (NMPylation) (Slanina et al. 2021). In the category of NSPs with still unknown functions falls also the small NSP11 (Gadhavé et al. 2021).

The formation of a cap on the five prime end of the viral mRNA is an essential step for immune evasion (Park et al. 2022). This still-under-investigation step is performed through the action of multiple NSPs. To form the cap, NSP14 and NSP16 act as guanine-N7-methyltransferase and 2'-O-methyltransferase, respectively while NSP13 function as an RNA 5'-triphosphatase (V'kovski et al. 2021). In this process NSP10 acts as a cofactor (V'kovski et al. 2021).

In addition to the above-mentioned function in cap formation, NSP14 acts as an exonuclease with RNA proofreading capabilities (Ogando et al. 2020). NSP13 belongs to 1B helicase superfamily that catalyzes the unwinding of double-stranded DNA or RNA (Newman et al. 2021).

CoV structural proteins, on the other hand, are translated from nested sub-genomic mRNAs. The spike (S) protein which contains the receptor binding domain (RBD) is responsible for initiating contact with the host receptor and the eventual fusion with the host plasma membrane (Z. Li et al. 2019). Additionally, for some CoV, the S protein is displayed on the surface of the host cell and induces the fusion of infected cells with nearby uninfected cells, facilitating the spread of infectious particles (Qian, Dominguez, and Holmes 2013a).

The envelope (E) protein is the smallest of the structural proteins (Yadav et al. 2021, 19). It consists of about 100 amino acids and function as an ion channel and integral part of the viral envelope, contributing to the assembly and release of the virions (Schoeman and Fielding 2019).

The membrane (M) protein is composed of about 220–260 amino acids (Satarker and Nampoothiri 2020). Aside from its integral role in the assembly of the virion, the M protein is reported to modulate host immune response through interacting with IKK β , one of the two protein kinases that phosphorylate the I κ B α protein, which is the most powerful inhibitor of the innate immunity regulator NF- κ B (Fang et al. 2007).

The nucleocapsid (N) protein is an RNA-binding protein that forms the core of the virus. The N protein is expressed abundantly in the infected cells, including the nucleus (McBride, Van Zyl, and Fielding 2014). It plays major roles in viral replication and viral RNA synthesis, host immune response modulation through antagonizing type I interferon pathways and contributes to the virus-induced cellular stress response through interacting with other viral and host proteins (McBride, Van Zyl, and Fielding 2014; Mu et al. 2020, 2).

1.1.3 Coronaviruses replication cycle

The completion of a successful CoV replicative cycle requires an intricate interplay between multiple host factors and signaling pathways, and viral proteins. The replication cycle of CoV starts with the attachment of the S protein to the host receptor. Different CoV utilize different host receptors. For instance, HCoV-229E uses aminopeptidase N (*ANPEP*) while SARS-CoV-2 uses angiotensin-converting enzyme 2 (ACE2) (Vijgen et al. 2004; Masre et al. 2021). Once this attachment is established, a series of conformational changes and cleavages by host proteases (e.g. type II transmembrane protease serine 2, TMPRSS2) takes place to expose the receptor binding domain (RBD) (Hoffmann et al. 2020). This eventually lead to the fusion of the viral and host membranes and hence viral entry (Hoffmann et al. 2020). Alternatively, CoV can enter via the endosomal route (Kawase et al. 2009). Subsequently, the viral core consisting of genomic RNA coated with the N protein will be released into the cytoplasm (V'kovski et al. 2021, 2). Once uncoated, the positive strand, capped and polyadenylated viral gRNA is

ready for direct translation by host ribosomes. The two modes of translation, continuous and discontinuous, will proceed to produce the above-mentioned NSPs, structural proteins and accessory proteins, collectively referred to as the replication-transcription complex (RTC).

To replicate the viral gRNA, CoV induce the formation of replicative organelles to which RTC attaches and synthesis the viral genome (van Hemert et al. 2008). The replicative organelles are composed of convoluted membranes (CMs) and double membrane vesicles (DMVs), most likely derived, at least in part, from the endoplasmic reticulum membrane (Netherton and Wileman 2011; Knoops et al. 2008; Klein et al. 2020). These structures might function as a spatial place where the gathering and organization of different viral factors important to produce mature infectious particles occur and, additionally, shield them from recognition by host defense mechanisms (Malone et al. 2022; Romero-Brey and Bartenschlager 2016; Klein et al. 2020). Specifically, the synthesis of the viral genome produces double stranded RNA and negative strand RNA; these intermediate products are recognized by host immune surveillance components as foreign entities require clearing. Hence, another possible benefit of such subcellular structures might be to shelter these intermediate products (Wong et al. 2021).

With all the important components of a mature infectious particle are produced, the assembly of the new virions take place at the ER/Golgi intermediate compartment (ERGIC) (Sicari et al. 2020). As previously mentioned, the M protein plays a pivotal role in this process by acting as a general scaffold and recruiter of other structural proteins leading to their incorporation in the newly-formed virion. The assembly process is finalized by the incorporation of the plus, single-stranded viral genomic RNA (+ssgRNA) tightly bound to it the nucleocapsid protein (de Haan et al. 1998; D. X. Liu, Liang, and Fung 2021).

The budding process is shown to be effectuated through different routes depending on the CoV in question. Some CoV exit the infected cell through exocytosis while others (including MHV and SARS-CoV-2) utilize lysosomal trafficking pathways (V'kovski et al. 2021). Figure 4 offers a schematic summary of the CoV replication cycle.

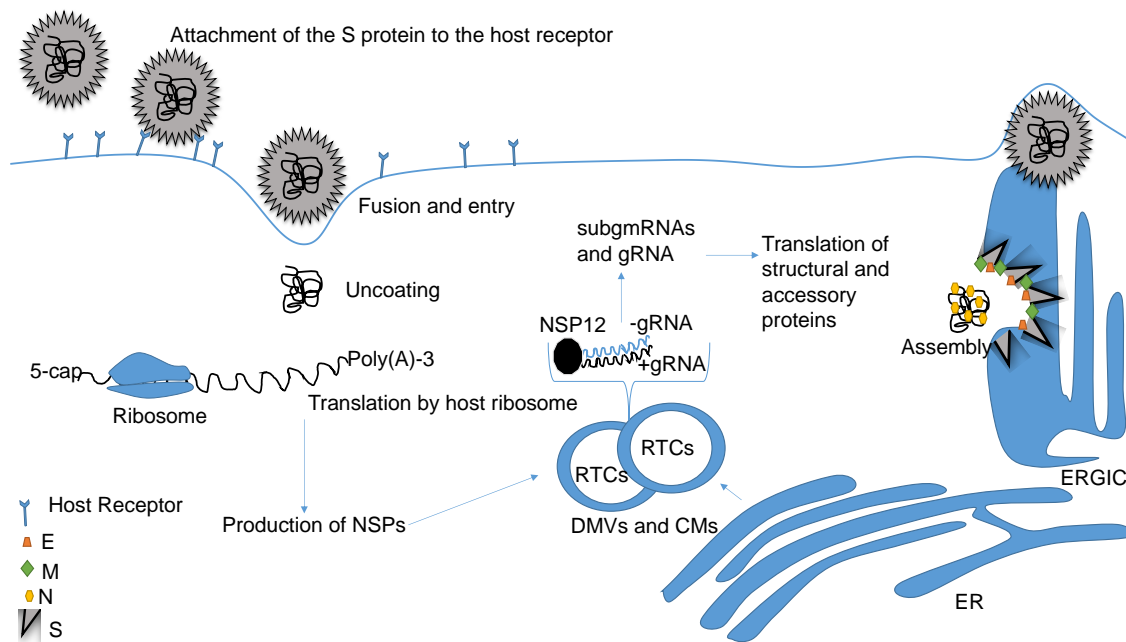


Figure 4: CoV replication cycle.

A schematic representation of a general CoV replication cycle. See text above for details. ERGIC: endoplasmic reticulum–Golgi intermediate compartment.

The reliance of CoV on the ER membrane to form the DMVs and CMs leads to perturbation of physiological ER structure, its depletion and invocation of ER stress and the unfolded protein response (UPR). CoV replication can also lead to the modulation of NF- κ B pathways and activation of JNK and p38 MAPK pathways (Poppe et al. 2017). Interestingly, multiple studies have indicated a convergence and cross-talk between the UPR and NF- κ B pathways through the action of multiple transcription factors including ATF4, ATF3, CCAAT/enhancer-binding and NF- κ B subunits (Schmitz et al. 2018; Poppe et al. 2017).

On the other hand, utilizing the lysosomal trafficking route to exit the infected cell necessitates the tampering of the virus with lysosomal acidification, which in turn alter the process of autophagy flux (S. Ghosh et al. 2020).

Both of these major cellular pathways (UPR and autophagy) and their modulations by CoV infection will be the topic of the upcoming sections.

1.2 The endoplasmic reticulum (ER)

The ER is a large cellular organelle where the biosynthesis (of about 30 % of all proteins) and folding of newly synthesized or misfolded polypeptides takes place (Braakman and Hebert 2013). It also functions as a major site for calcium storage and lipid synthesis (Malek et al. 2021). It consists of a dynamic, elaborate network of membranes, referred to as cisternae, extensively interconnected by

tubules through which proteins (and other substances) translocate (Schwarz and Blower 2016). The ER can be subdivided into two distinct regions based on their appearance, a rough ER dotted with ribosomes and smooth ER lacking their presence (Sanvictores and Davis 2022).

Membranous and secreted proteins are mainly synthesized and folded in the ER (Teske, Baird, and Wek 2011). The translation of these proteins starts at a free ribosome in the cytosol until a signal sequence is encountered and translated (Schaletzky and Rapoport 2006). This signal sequence induces the translocation and the docking of the ribosome-mRNA-(partial) nascent-polypeptide complex to the surface of the ER membrane (Walter and Johnson 1994).

After being released from the translating ribosome, the life cycle of these proteins starts in the ER lumen as a chain of unfolded polypeptide. To function properly, the polypeptide needs to be folded correctly. Multiple ER chaperones assume this function (Braakman and Hebert 2013). The quality of the outcome of the folding process is closely monitored by an ER surveillance system termed ER quality control (ERQC) (Araki and Nagata 2011). If the folding process fails at producing the intended functional three-dimensional confirmation, another process named ER-associated degradation (ERAD) assume the function of degrading these aberrant proteins through proteasomal pathways (Vembar and Brodsky 2008).

Calcium acts as a signaling molecule and is involved in multiple vital biological processes including the proper folding, functioning and localization of proteins (Torres et al. 2011). The ER acts as a major storage site for intracellular calcium. The ER regulates the levels of intracellular calcium concentrations (including its cytosolic concentration) using multiple calcium channels and calcium-releasing receptors (Santulli et al. 2017). Of relevance to this study, are the sarcoendoplasmic reticular calcium ATPases (SERCAs), which function as ion pumps or major transporters of leaked calcium from the cytoplasm back to the ER (Tong, Evangelista, and Cohen 2010). More on this pump will be discussed in the section related to thapsigargin.

Another important function of the ER is the manufacturing and modification of membrane lipid. This process occurs at the ER-Golgi intermediate compartment (ERGIC), from which they will be distributed to their destined locations (Ge et al. 2013).

As delineated above, the extensive involvement of the ER in the synthesis, folding, routing and degradation of large portion of the cell proteome is very well documented (Oikonomou and Hendershot 2020). Any large, unexpected, influx of misfolded or unfolded proteins can result in an imbalance between the capacity of the ER folding machinery and the incoming proteins. This imbalance will trigger ER stress and will require the activation of a set of pathways to counter it and restore a homeostatic ER. These pathways are termed the unfolded protein response (UPR). ER stress and UPR will be the topic of the next section.

1.2.1 ER stress and the unfolded protein response (UPR)

Many external or internal events can trigger ER stress and the accumulation of unfolded/misfolded proteins. Examples of such events can be deficiencies in degradation pathways (proteasomal and/or lysosomal, autophagic), nutritional deprivation, energy and oxygen level reductions, calcium level fluctuations or inflammation (M. Wang and Kaufman 2016). Faced with influx of unfolded or misfolded proteins due to these (patho-) physiological events, the stressed ER will activate set of genetic programs and pathways (the UPR) to slow down this influx, try to correctly fold the already-produced proteins, or degrade those whose folding attempts terminally failed (Shapiro et al. 2016). If these measures fall short of restoring proteostasis, a prolonged UPR activation will switch the response from being adaptive to apoptotic (M. Wang and Kaufman 2014).

UPR pathways are heavily involved in multiple pathological conditions including diabetes, cancer and viral replication (Schmitz et al. 2018). For instance, tumor cells are metabolically very active and divide far more often than a normal cell does. This increase the demand to produce and fold more proteins than usual, leading to the overwhelming of the ER folding capacity and hence a sustained activation of the UPR (Benedetti et al. 2022). Nevertheless, cancer cells evolved mechanisms to exploit this prolonged activation of UPR to promote tumor development at all of its known stages rather than the usual switching to the apoptotic mode (Madden et al. 2019).

Viral infection is another example of an external event that triggers ER stress and UPR activation. By their nature, viruses are obligate intracellular parasites. To complete their replicative cycle, viruses either exploit, counter or modulate host factors and pathways including the UPR (Chan 2014). UPR activation can either serve an anti-viral purpose through the modulation of immunity and inflammation pathways or can be exploited to promote viral infection (Grootjans et al. 2016). Initial transcriptomic studies in our group indicated that HCoV-229E infection triggers cellular changes associated with a form of UPR activation (Poppe et al. 2017). These changes were seen as deregulation of multiple genes products involved in ER stress signaling (Poppe et al. 2017). To understand how CoV modulate UPR to their advantage, a closer look at the components through which the ER monitor and respond to any abnormal functioning or influx of unfolded proteins is necessary.

The UPR operates through the activity of three ER transmembrane sensors. These are protein kinase RNA-like endoplasmic reticulum kinase (PERK; also called EIF2AK4), inositol requiring enzyme-1A (IRE1 α ; also called ERN1), and activating transcription factor 6 (ATF6) (C. Li et al. 2018). Under normal conditions, a chaperone called binding immunoglobulin protein (BiP, also called GPR78 or HSPA5) binds to the luminal domains of PERK or IRE1 α in their monomeric forms and to ATF6 resulting in their deactivation. An abnormal influx of unfolded or misfolded proteins to the lumen of the ER will result in an increased demand for BiP to attend to these proteins, which results in its dissociation from the three sensors. This dissociation results in an indirect activation of the three sensors, and subsequently the activation of their downstream pathways and genetic programs (A. S. Lee 2005). PERK

and IRE1 α activation is effectuated through oligomerization, trans(auto)-phosphorylation and conformational changes while ATF6 is activated by sequential proteolysis (Gardner et al. 2013). Intriguingly, IRE1 α activation can also occur because of direct interaction between unfolded proteins and the ER-luminal amino-terminal side of the sensor (Gardner and Walter 2011).

The now activated serine/threonine kinase domain of PERK can phosphorylate the alpha subunit of the eukaryotic initiation factor 2 (eIF2) at serine 51 (Cui et al. 2011). Under normal conditions, the dephosphorylated eIF2 α binds GTP and tRNA-methionine forming a ternary complex required for the initiation step of translation and the transfer of tRNA^{Met} to the 40S subunit of the translating ribosome (Y. Liu et al. 2020). Completion of this initiation step is finalized by the hydrolysis of the GTP bound to eIF2 to GDP and the release of the eIF2-GDP complex from the ribosome for another round of pairing with tRNA^{Met} (Y. Liu et al. 2020). However, the re-pairing of eIF2-GDP to tRNA^{Met} requires exchange of GDP to GTP, a step that is accomplished by the binding of eIF2-GDP to eIF2B (Kershaw et al. 2021). The phosphorylation of eIF2 on its alpha subunit by one of the four known eIF2 kinases (HRI, PKR, PERK, and GCN2) results in a sequestration of its binding to eIF2B (Donnelly et al. 2013). This will halt the recycling process of eIF2 and as a result, impairing the translation initiation step and imposing a general translation shutdown (Donnelly et al. 2013).

Under stress conditions, a set of mRNAs escape this translational shutdown as a virtue of a 5 prime upstream ORF. This ORF induces a switch of usage from canonical translation initiation factors to non-canonical ones, namely eIF2D and DENR (Vasudevan et al. 2020). A prominent example of such mRNA is that of ATF4 (also called CREB2). ATF4 is a major regulator of ER stress-related genes and processes, including anti-oxidant response, amino acid metabolism, autophagy and the pro-apoptotic DNA damage-inducible transcript 3 (DDIT3, also called GADD153 or CHOP) (Grootjans et al. 2016). Together with ATF4, DDIT3 induces the expression of growth arrest and DNA damage inducible protein 34 (GADD34), a negative regulator of eIF2 α phosphorylation (Novoa et al. 2001).

The cytosolic side of IRE1 α possesses a serine/threonine kinase domain and a carboxyl-terminal ribonuclease (RNase) domain (Adams et al. 2019, 1). Once activated, the RNase domain of IRE1 α splices a 26-nucleotide fragment from its substrate, the unspliced X-box binding protein 1 (XBP1) mRNA, producing a transcript encoding a functional transcription factor (Cox and Walter 1996). The spliced XBP1 protein upregulates a set of genes aimed at increasing ER folding capacity (molecular chaperones, including BiP, and protein-folding enzymes) and genes related to ER quality control, making this transcription factor a promotor of cell survival (Travers et al. 2000; A.-H. Lee, Iwakoshi, and Glimcher 2003).

Furthermore, IRE1 α is involved in a process termed regulated IRE1-dependent decay of mRNA (RIDD). This process disposes of certain mRNAs located in the ER through cleaving them at specific sequences that resemble XBP1 splicing sites, followed by their degradation by exoribonucleases (Hollien and Weissman 2006). At earlier stages of the UPR, RIDD can be part of the adaptive response of the UPR

by reducing the burden of newly synthesized proteins. Nevertheless, extended activation of IRE1 α RNase domain induces RIDD to target microRNAs that inhibit apoptosis and the mRNA of BiP, switching this process from pro-survival to pro-apoptotic one (Han et al. 2009).

Unlike PERK and IRE1 α , The dissociation of BiP from ATF6 luminal domain leads to its translocation to Golgi apparatus where its activation proceeds through a series of proteolytic cleavages effectuated by site-1 and site-2 proteases (S1P and S2P) (Shen and Prywes 2004, 6). The outcome of this process is the liberation of the bZip transcription factor domain residing in the cytosolic, amino-terminal side of ATF6 (Hillary and FitzGerald 2018). The released active transcription factor transfers to the nucleus and binds to the ER stress response element (ERSE), leading to the activation of multiple UPR related genes (Gardner et al. 2013; Yoshida et al. 1998). Given that ATF6 was not part of this work, henceforward, it will only be mentioned succinctly and when the context demands.

Downstream from PERK (and possibly IRE1 α) pathways, an ER stress-induced transcription factor named ATF3 with yet poorly understood relevance and functions especially in CoV replication. ATF3 is a transcription regulator, that is part of the ATF/ cAMP response element-binding (CREB) protein family of transcription factors with reported induction as a result of various (patho-) physiological signals including inflammation and CoV infection (Poppe et al. 2017; G. Liang et al. 1996). The consensus sequence on the target genes promoters to which ATF3 binds is TGACGTCA (Thompson, Xu, and Williams 2009). Nevertheless, ATF3 can bind other sequences including TTGCATCA on the promoter of GADD153 leading to its repression (Wolfgang et al. 1997). Similar to other member of ATF/CREB family, ATF3 has a leucine zipper region through which it binds DNA and form homo- or hetero-dimers with other members of this family including ATF2 and JUND (Thompson, Xu, and Williams 2009). The functions carried out by the new complex can be either activation, repression or are independent from ATF3 role as a transcription regulator. Example of such hetero-complex is the heterodimerization of ATF3 and JUN, which results in activating the transcription of the target genes including Interferon gamma (*IFNG*)(Danzi et al. 2018; Filén et al. 2010).

Another way ATF3 can alter its transcriptional activity is through posttranslational modification. For instance, the SUMOylation of ATF3 on lysine 42 is essential for effective repression of TP53 gene (also known as P53, a well-known regulator of cell division and tumor proliferation) (C.-M. Wang et al. 2013). On the other hand, ATF3 is known to establish protein-protein interactions with TP53 to prevent its ubiquitination and subsequent degradation by the proteasome (Yan et al. 2005).

ATF3 has also been reported to be involved in the modulation of the immune system including the regulation of multiple inflammatory genes transcription and gene products functions (Thompson, Xu, and Williams 2009). For instance, ATF3 inhibits the expression of IL-6 up-regulator CEBP δ leading to IL-6 down regulation (Thompson, Xu, and Williams 2009; Litvak et al. 2009). Figure 5 summarizes the functioning of these sensors graphically.

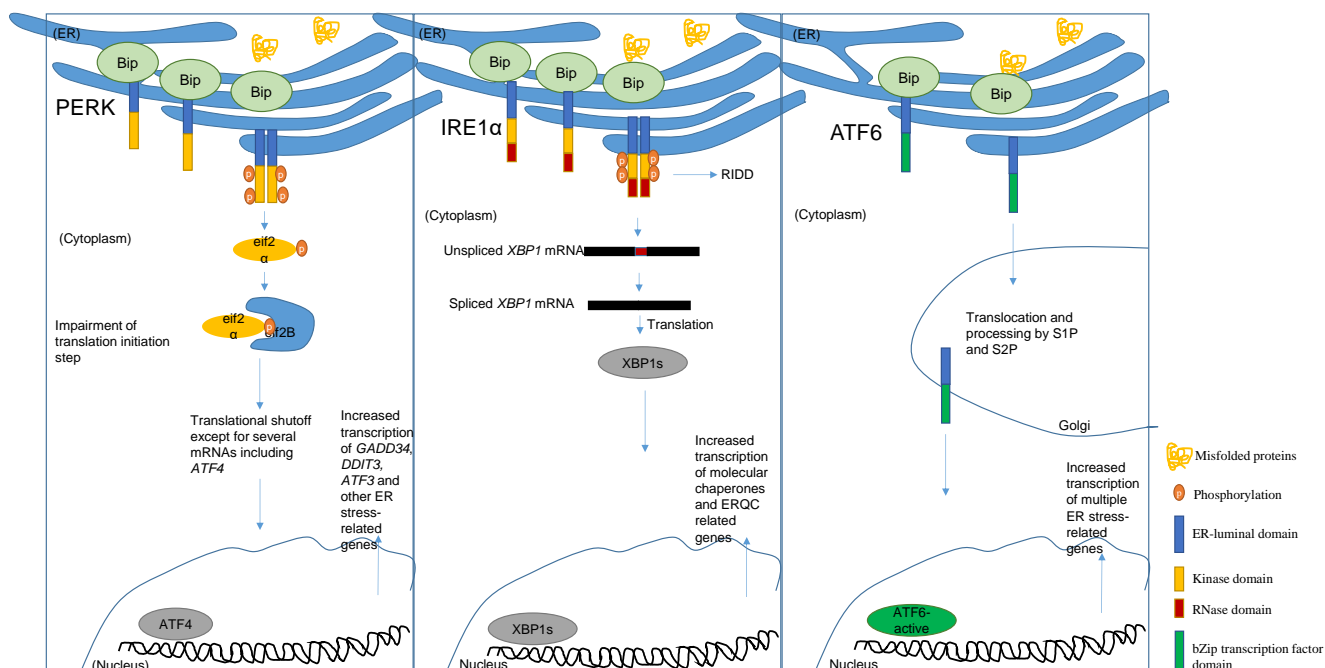


Figure 5: The three branches of UPR.

A schematic representation of the three sensors of UPR, their activation and some of their downstream pathways. See text above for details. Worth to note here that these sensors crosstalk intimately with each other (Chang et al. 2018). For sake of simplicity, these cross-talking pathways were omitted.

Inducing ER stress and the subsequent activation of the UPR pathways can be achieved chemically through the treatment of investigated cellular models with compounds such as tunicamycin, dithiothreitol (DDT), thapsigargin and others. These pharmacological inducers of ER stress can be used as a reference to study and compare the activation of UPR as a result of different biological conditions (including viral infection), and amongst different cellular models (Osowski and Urano 2011; Bergmann et al. 2018). In the case of viral infection, the usage of UPR inducers and inhibitors can give the chance to assess whether the induction of UPR is protecting the host or promoting viral replication. Chemical inducers of ER stress, with focus on thapsigargin, were discussed in the next section.

1.2.2 Chemical inducers of ER stress and the UPR

The induction of ER stress through pharmacological compounds proceed through interfering with an essential step required either for the correct folding or for the elimination of misfolded proteins, leading to their accumulation and activation of UPR. For instance, Tunicamycin inhibits glycosylation, an important process involved in correct folding of proteins and quality control (C. Xu and Ng 2015), while DDT blocks the formation of disulfide-bond leading to the missfolding of newly synthesized proteins in the ER but also in the cytosol (Y. Wang et al. 2020; Cleland 1964).

Thapsigargin, a compound that is extracted from a plant called *Thapsia garganica*, depletes the endoplasmic calcium through a specific, non-competitive, covalent and irreversible binding to the SERCA pump leading to a malfunctioning in several ER chaperones that depend on calcium for their activities (Shaban, Mayr-Buro, et al. 2022).

Under normal conditions, a massive difference in calcium concentration between the lumen of the ER (>100 μM) and the cytosol (around 100 nM) can be observed (Samtleben et al. 2013). The calcium in the ER lumen can temporary leak to the cytosol through several ER calcium channels. The brief increase in the cytosolic calcium leads to the activation of several calcium-dependent enzymes, and to an increase in ATP production in the mitochondria (Mekahli et al. 2011). The SERCA pumps assume the responsibility of transferring back the leaked calcium into the lumen of the ER, further sustaining this massive difference in calcium concentration (Isaacs et al. 2021; Schwarz and Blower 2016).

Within short time of its entry into the cell, thapsigargin binds a region in SERCA formed by multiple transmembrane helices, namely TM3, TM4, TM5 and TM7 (Shaban, Mayr-Buro, et al. 2022). This interaction is further stabilized by hydrophobic interactions with residues F256, L260, V263, Ile761, V769, I829, F834, and M838 (Shaban, Mayr-Buro, et al. 2022). The result of thapsigargin binding is a potent inhibition of the pump, a subsequent disruption of the calcium gradient, and diminishing the ER capacity to fold protein properly (through impairing calcium-dependent ER chaperones) leading to a prolonged activation of pro-apoptotic UPR (Shaban, Mayr-Buro, et al. 2022).

Worth noting here that the UPR induced by these chemical compounds has been proven to have distinct characteristics from that induced by loading the ER with unfolded proteins (Bergmann et al. 2018). Additionally, multiple lines of research have indicated that the induction of ER stress can lead to the activation of autophagy (Yorimitsu et al. 2006; Ciechomska et al. 2013). Nevertheless, thapsigargin has been shown to block the fusion of autophagosomes with lysosomes, an essential step for the completion of autophagy flux cycle, without affecting the endocytic system, leading to an arrest in autophagy flux (Ganley et al. 2011).

In the next chapter, the concept of autophagy flux and its implication and connection to viral replicative cycle and ER stress will be discussed in more details.

1.3 Autophagy

First coined by “Christian de Duve”, the term Autophagy means “self-eating” and it refers to a process by which the cell degrades and recycles its own components or materials from foreign invaders (de Duve et al. 1955).

The field of autophagy received a major advancement after the discovery and characterization of multiple essential autophagy-related genes (ATGs) in yeast by Yoshinori Ohsumi’s laboratory. To uncover these genes, Ohsumi followed a genetic screening approach (Tsukada and Ohsumi 1993). This advancement uncovered an extensive involvement of autophagy in multiple important (patho)-physiological processes including the UPR, immune response, certain neurodegenerative diseases, and the replicative cycle of many viruses (e.g. the human immunodeficiency virus, HIV), amongst others (Dikic and Elazar 2018; Nardacci et al. 2017).

The process of autophagy depends on the shipment of cargo destined for degradation to the lysosome through three known sub-processes; namely, chaperone-mediated autophagy, microautophagy, and macroautophagy (Parzych and Klionsky 2014). Chaperone-mediated autophagy (CMA) depends on the selective delivery of certain targeted proteins, that functions might not be needed anymore, to the lysosome through binding to a chaperon protein (Kaushik and Cuervo 2018). Microautophagy proceeds through a direct, random, capturing of material in the cytoplasm by the lysosome (Schuck 2020). Microautophagy is mediated by invaginations in the lysosomal membrane (Schuck 2020). Macroautophagy, hereafter referred to as autophagy, is the most investigated type of autophagy and the subject of characterization in this study. Autophagy is effectuated through the biogenesis of double-membrane vesicles (called autophagosomes) that sequester cargo destined for degradation (Mijaljica, Prescott, and Devenish 2012). Mature autophagosomes fuse with the lysosomes, forming autolysosomes in which their contents are degraded (Klionsky, Eskelinen, and Deretic 2014). The engulfed cargo in the autophagosomes can be endogenous (e.g. dysfunctional organelle) or exogenous (e.g. invading pathogens). Unlike CMA, the selectivity of autophagy is context-dependent. For instance, autophagy can proceed in a non-selective manner when the cell is under starvation where the target cargo is the bulk of the cytoplasm. Alternatively, selective autophagy can be induced to recycle unwanted organelles, including the ER (ER-phagy) or the mitochondria (mitophagy) or invading pathogens (xenophagy) (Feng et al. 2014).

Although each of the sub-types of autophagy (ER-phagy, mitophagy, xenophagy...etc) operates through unique components, they still all share a common core machinery that leads to the formation of the autolysosome (Xie and Klionsky 2007). In the next section, this core machinery and the concept of autophagy flux will be discussed.

1.3.1 The formation of autolysosome and autophagy flux measurement

The formation of the autolysosome starts with the biogenesis of autophagosomes. In mammalian cells, upon inhibition by a relevant signal (e.g. stress or starvation), the mechanistic target of rapamycin complex 1 (mTORC1) is no longer able to phosphorylate and inhibit the autophagy initiators ULK1 complex and ATG13 (Rabanal-Ruiz, Otten, and Korolchuk 2017). Once activated, the ULK1 complex (including ATG13,) acts as a scaffold to recruit and modulate the activities of further autophagy factors including AMBRA1 (Nazio et al. 2013). AMBRA1 phosphorylation leads to the activation of the PI3KC3 complex (composed of Beclin1, VPS34, VPS15 and ATG14L) through interacting with Beclin1 (Nazio et al. 2013). The membrane of the autophagosomes can be derived from different membranous organelles including the ER and the ERGIC (Ge et al. 2013). Activated VPS34 infix a phospholipid, called phosphatidylinositol-3-phosphate (PtdIns3P) onto certain regions of these membranes creating what is referred to as isolation membranes or phagophores. The phospholipid on the phagophores acts as beacon for the recruitment of further factors including the WD repeat domain phosphoinositide-interacting proteins WIPs (Nascimbeni, Codogno, and Morel 2017). This recruitment leads to further elongation of the phagophores until they morph into cup-like curved structures.

The next steps depend on two ubiquitin-like (UBL) systems. Once attached to the phospholipid on the phagophore, the WIPs recruit ATG16L1 complex (Strong et al. 2021). To form this complex, the cell relies on an UBL conjugation system that involves the conjugation of UBL molecule, ATG12, to ATG5 (Kaiser et al. 2012). This process is carried out through the action of ATG7 and ATG10 mimicking the actions of E1 (ubiquitin-activating) and E2 (ubiquitin-conjugating) enzymes respectively (Kaiser et al. 2012). The resulting conjugated molecule of ATG5-ATG12 binds to the ATG16L1 molecule. LC3 is the second crucial UBL molecule that is C-terminally cleaved by ATG4B protease, exposing a glycine 120 residue that is important for the next conjugation step (Satoo et al. 2009). The cleaved LC3-I is then subjected to an UBL conjugation reaction through the action of ATG7 (E1) and ATG3 (E2). The ATG16L1 complex subsequently acts as an E3 ubiquitin-protein ligase and transfers phosphatidylethanolamine (PE) to LC3-I on the exposed glycine. The now lipidated LC3-I molecule (called LC3-II) can cover large areas of the inner part of the forming phagophore and plays multiple roles in the autophagy process including the further extension of the phagophore, bulk engulfment of cytoplasmic materials and the overall formation of the mature autophagosome (Choi, Bowman, and Jung 2018; Runwal et al. 2019; Kabeya et al. 2000). LC3-II is also involved in selective autophagy through interacting with the LC3-interacting region (LIR) of cargo receptor proteins such as p62 (also called sequestosome1, SQSTM1) (Putyrski et al. 2020). Through its ubiquitin acceptor (UBA) domain, p62 selectively bind materials destined for degradation by an ubiquitin tag and sequester them to the growing phagophore. Hence, p62 carries out this mission through acting as an intermediate (adaptor) molecule between the cargo and LC3-II molecules present on the inner membrane of the phagophore (Johansen and Lamark 2011). Additionally, p62 contains a TRAF6 binding (TB) domain that regulates the

activities of TRAF6 (E3 ligase) resulting in an enhanced oligomerization and polyubiquitination activities of this E3 enzyme (Chen et al. 2020).

Once the extension of the phagophore and the engulfment of the to-be-degraded materials has been finalized, the mature autophagosome fuses with the lysosome forming an autolysosome. The fusion machinery is composed of multiple complexes and factors including the SNARE complex (Y. Wang et al. 2016). This complex is composed of a group of proteins that assume the generic function of intercellular membrane fusions through a mutual interaction between SNARE proteins present on both merging membranes, bringing them together and eventually causing their merger (Nakatogawa 2020).

After the formation of the autolysosome, the captured materials inside of this structure will be now accessible to the swarm of lysosomal enzymes. The optimal functioning of these hydrolytic enzymes intimately relies on the acidification of the autolysosome and hence any impairment of this process results in arrested autophagy and accumulation of dysfunctional autolysosomes (J.-H. Lee et al. 2022). The acidification of the autolysosome proceeds through the action of V-ATPase pumps that transfer protons into the lumen of the autolysosomes (and other membranous compartments) resulting in the low pH environment required for their functioning (Song et al. 2020). If completed successfully, the products of the degradation process are then released and recycled, completing the process of “self-eating” (Yim and Mizushima 2020; Mauvezin et al. 2015; Khandia et al. 2019). Figure 6 summarizes the process of autolysosome formation graphically.

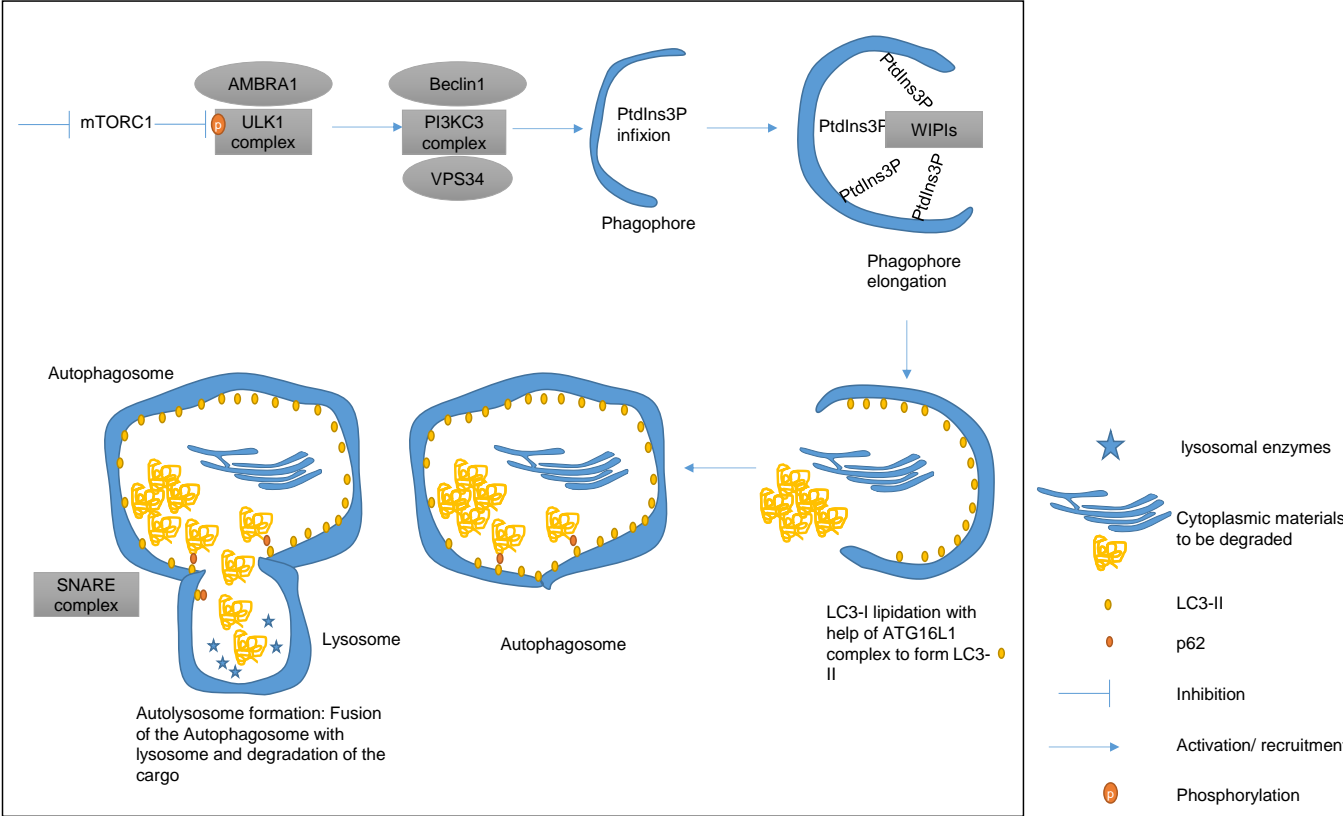


Figure 6: Autolysosome formation.

A schematic representation of the different stages of autolysosome formation. See text above for details.

The process described above, from the formation of the autophagosome, the fusion with lysosome and the final degradation of engulfed cargo, results in highly dynamic cycles of synthesis and degradation, that are summarized by the term autophagy flux. Given their early involvement and subsequent degradation within the autolysosome, the turnover of both LC3-II and p62 is used to calculate the rate of autophagy flux (Yoshii and Mizushima 2017).

Assessing autophagy flux using these factors can be done through comparing their levels on Western blotting in the presence or absence of an autophagy flux blocker. One such blocker is bafilomycin A1, which acts as an inhibitor of the V-ATPases pumps and hence the acidification of the autophagosome. The accumulation (or lack thereof) of these factors is used to calculate the rate of degradation that would have occurred if the autophagy flux was not blocked. Hence, this method provides an indirect estimate of the flux under normal conditions (steady-state) or in the presence of autophagy-inducing or -suppressing signal (Yoshii and Mizushima 2017). One of the best-understood inducers of autophagy flux is starvation, which uses this process to recycle intracellular materials in the absence of sufficient nutrients (Kankuan et al. 2017).

Another way to measure autophagy flux is through using fluorescently labeled antibodies. Thereafter Fluorescence microscopy can be used to count and compare the numbers of LC3-II and p62 puncta (resembling autophagosomes) in the presence or absence of an autophagy flux blocker. The increase in the puncta usually reflects the number of autophagosomes that would have been degraded if the flux was not blocked (Loos, du Toit, and Hofmeyr 2014; Yoshii and Mizushima 2017).

Alternatively, the expression of a chimeric protein consisting of monomeric red fluorescent protein (mRFP), green fluorescent protein (GFP) and LC3 in tandem can be used to visualize autophagy flux. The method relies on quenching the green signal of the GFP fluorescence and the stability of the red signal of the mRFP under acidic conditions presents in the autolysosome. The change of acidity accompanying the different stages of autophagy flux from autophagosomes to autolysosomes formations can be then visualized as change in the color of this construct (Kimura, Noda, and Yoshimori 2007).

1.3.2 The role of autophagy in viral infection

The involvement of autophagy in viral replication and host defense is multifaceted and can be both anti- or pro-viral. Moreover, the mechanisms by which CoV induce autophagy is still largely poorly understood (Zhenyu Zhao et al. 2021).

For instance, several studies indicated an extensive involvement of the selective autophagy cargo-receptor p62 in targeting essential viral components for degradation. A prominent examples of such

targeting are that of Tat protein (an essential factor for activating the transcription of the integrated viral DNA) of HIV in HEK293T cells and the capsid protein of Sindbis virus (SV) to the autophagosome (Sagnier et al. 2014; Orvedahl et al. 2010; Ahmad, Mostowy, and Sancho-Shimizu 2018).

Another way by which autophagy can play an anti-viral role is through modulating innate and adaptive immunity. The first cellular line of defense against invading pathogens includes receptors (called pattern recognition receptors, PRRs) that recognize specific viral elements (called pathogen-associated molecular patterns, PAMPs) and subsequently activates anti-viral interferon response (Amarante-Mendes et al. 2018). Autophagy can regulate this response through either inducing and amplifying it (by delivering PAMPs to PRRs) or terminating aspects of this response (through actively degrading some of its components)(Choi, Bowman, and Jung 2018).

As for adaptive immunity, autophagy has been reported to be involved in the process of delivering viral antigens to major histocompatibility complex (MHC) class II where they are presented by dendritic cells for the T-cell to recognize (Crotzer and Blum 2010).

On the other hand, multiple studies indicated a beneficial role of autophagy in the replication of several RNA viruses. The replication of the genome of these viruses leads to the formation of double-stranded and other intermediate RNA molecules that are recognized and degraded by host defense machineries. To prevent such recognition, many RNA viruses evolved to induce the formation of double-membrane compartments, most likely through exploiting autophagy pathways, in which the replication of the viral genome can occur “safely” (Roingard et al. 2022). Example of such viruses are Enteroviruses (positive-sense single-stranded RNA viruses, example of which is poliovirus) which have been shown to induce a pro-viral autophagy response and coronaviruses (Lennemann and Coyne 2015; Maity and Saha 2021). Worth noting here is that these double membrane structures also serve (as discussed above) an important role in assembling viral proteins required for the replication of the genome.

Finally, a successful completion of a viral replicative cycle requires the budding of the virions from the infected cell. Viruses evolved to exploit the exocytotic machinery, which is intimately connected to autophagy pathways especially in aspects related to membrane formations and fusions. Examples of such exploitation can be seen in picornaviruses and orthomyxoviruses infected cells (Münz 2017). Indeed, it has been shown that poliovirus can exit the cells in an autophagosome-mediated manner without leading to cell lysis (Sun et al. 2019). In such a process, the virus infection will trigger the autophagosomes to fuse with the plasma membrane rather than the canonical fusion with the lysosomes. This in turn will cause the release of these virions-loaded vesicular structures into the extracellular milieu (Sun et al. 2019).

Overall, the interplay between autophagy and viral infection is intricate and often proceed in a pathogen specific manner, reflecting the evolutionary adaption of each virus (or family of viruses) to its host. Hence, investigating this interplay for coronaviruses can yield a plethora of information and novel

mechanisms to counter virus infection, a topic that is still largely under-investigated and hence it was part of this study.

The next section summarized the aims of this work.

1.4 Aims of the study

From the first major CoV outbreak of SARS-CoV in 2001 to the recent SARS-CoV-2 pandemic beginning in early 2020, a considerable amount of research has been conducted with the goal of achieving a better understanding of viral replication and its interaction with the host.

However, the specific roles of ER stress and autophagy in CoV replication remain incompletely understood, leaving many aspects and the (therapeutic) potential of these processes to be further explored.

At the outset of this work, previous research in our group and by others had shown that upon CoV infection of cell models, the PERK kinase-eIF2 α signaling pathway and a subsequent UPR response are activated.

Based on these initial findings, the main objectives of this thesis were to (i) gain deeper mechanistic insight into the differential roles of ER stress and autophagy signaling pathways in the replication of various human CoV and (ii) pursue the hypothesis that targeting these signaling pathways may provide a means to efficiently inhibit CoV replication.

To this end, pharmacological (using small molecule inhibitors) and genetic (employing CRISPR-CAS-9-mediated loss-of-function strategies) were used to investigate the roles of the UPR components PERK, IRE1 α , and ATF3 in CoV replication and the host response. An additional pharmacological intervention approach was implemented to chemically activate ER stress (with thapsigargin) or inhibit autophagic flux (with bafilomycin A1) and investigate the consequences on CoV replication and host response. To gain further mechanistic and molecular insights at the proteomic level, proteome-wide studies using quantitative mass spectrometry and bioinformatics analyses were performed to investigate the impact of chemical ER stress on protein levels of infected cells and the interactome of the ER stress effector ATF3.

Chapter 2: Materials

2.1 Cell lines

Cell Line	Origin/Engineered by	Parental or Engineered
Huh7	Human hepatoma cells (Japanese Collection of Research Bioresources (JCRB) cell bank (Nakabayashi et al. 1982)	Parental, a gift from Prof. John Ziebuhr
MRC-5	Human embryonic lung fibroblasts (ATCC, CCL-171)	Parental
VERO-E6	African green monkey kidney epithelial cells (ATCC CRL-1586)	Parental, laboratory of Prof. John Ziebuhr
HEK293FT	Human kidney cells (Thermo Fisher Scientific, R70007)	Parental
Huh7-pX459-sg1-PERK	Engineered by: M.Samer Shaban (M.S.S)	CRISPR-CAS9 Engineered, this study
Huh7-pX459-sg2-PERK	Engineered by: M.S.S	CRISPR-CAS9 Engineered, this study
Huh7-pX459-sg1+2-PERK	Engineered by: M.S.S	CRISPR-CAS9 Engineered, this study
Huh7-pX459-sg3+4-PERK	Engineered by: M.S.S	CRISPR-CAS9 Engineered, this study
Huh7-pX459-sg1+2+3+4-PERK	Engineered by: M.S.S	CRISPR-CAS9 Engineered, this study
Huh7-pX459-sg1+2-IRE1 α	Engineered by: M.S.S	CRISPR-CAS9 Engineered, this study
Huh7-pX459-sg3+4-IRE1 α	Engineered by: M.S.S	CRISPR-CAS9 Engineered, this study
Huh7-pX459-sg1+2+3+4-IRE1 α	Engineered by: M.S.S	CRISPR-CAS9 Engineered, this study
Huh7-pX459-sg1-ATF3	Engineered by: M.S.S	CRISPR-CAS9 Engineered, this study
Huh7-pX459-sg2-ATF3	Engineered by: M.S.S	CRISPR-CAS9 Engineered, this study
Huh7-pX459-EV	Engineered by: M.S.S	CRISPR-CAS9 Engineered, this study
Huh7-LentiVirus-sg1-ATF3	Engineered by: M.S.S	CRISPR-CAS9 Engineered, this study
Huh7-LentiVirus-sg2-ATF3	Engineered by: M.S.S	CRISPR-CAS9 Engineered, this study
Huh7-LentiVirus-sg3-ATF3	Engineered by: M.S.S	CRISPR-CAS9 Engineered, this study
Huh7-LentiVirus-sg4-ATF3	Engineered by: M.S.S	CRISPR-CAS9 Engineered, this study
Huh7-LentiVirus-sg5-ATF3	Engineered by: M.S.S	CRISPR-CAS9 Engineered, this study
Huh7-LentiVirus-sg6-ATF3	Engineered by: M.S.S	CRISPR-CAS9 Engineered, this study
Huh7-LentiVirus-EV	Engineered by: B.Vincent Albert (B.V.A)	CRISPR-CAS9 Engineered, this study

2.2 Bacterial strains

Strain Name	Source	Genotype
XL1-Blue E.coli	Thermo Fisher Scientific	F' Tn10(Tetr) proA +B + lacIqΔ(lacZ)M15I recA1 gyrA96 (Nalr) tbi-1bsdR17 (r-k m-k) glnV44 relA1 lac
TOP10 E.Coli	Thermo Fisher Scientific	F-mcrAA(mrr-hsdRMS-mcrBC) Φ80lacZΔM15 ΔlacX74 recA1 deoR araD139 Δ(ara-leu)7697galU galK rpsL (StrR) endA1 nupG

2.3 Expression vectors

Name	Source
pSpCas9(BB)-2A-Puro (pX459)	Addgene (#48139)
pX459-sg1-PERK	Cloned by M.S.S, this study
pX459-sg2-PERK	Cloned by M.S.S, this study
pX459-sg1+2-PERK	Cloned by M.S.S, this study
pX459-sg3+4-PERK	Cloned by M.S.S, this study
pX459-sg1+2+3+4-PERK	Cloned by M.S.S, this study
pX459-sg1+2-IRE1α	Cloned by M.S.S, this study
pX459-sg3+4-IRE1α	Cloned by M.S.S, this study
pX459-sg1+2+3+4-IRE1α	Cloned by M.S.S, this study
pX459-sg1-ATF3	Cloned by M.S.S, this study
pX459-sg2-ATF3	Cloned by M.S.S, this study
psPAX2	Addgene (# 12260)
pMD2.G	Addgene (#12259)
LentiCRISPR V2	Addgene (#52961)
LentiVirus-sg1-ATF3	Cloned by M.S.S, this study
LentiVirus-sg2-ATF3	Cloned by M.S.S, this study
LentiVirus-sg3-ATF3	Cloned by M.S.S, this study
LentiVirus-sg4-ATF3	Cloned by M.S.S, this study
LentiVirus-sg5-ATF3	Cloned by M.S.S, this study
LentiVirus-sg6-ATF3	Cloned by M.S.S, this study
PERK.WT.9E10.pCDNA	Addgene (#21814)
IRE1 alpha-pcDNA3.EGFP	Addgene #13009)
pRK-ATF3	Addgene (#26115)
pCMV BiP-Myc-KDEL-WT	Addgene (#27164)
pTet-on_Puro_Myc-BirA (MYC-BirA)	A gift of Prof. L. Schmitz
pTet-on_Puro_HA-miniTurbo (HA-miniTurbo)	A gift of Prof. L. Schmitz
MYC-BirA-PERK	Cloned by M.S.S, this study
MYC-BirA-IRE1A	Cloned by M.S.S, this study
MYC-BirA-BiP	Cloned by M.S.S, this study
MYC-BirA-ATF3	Cloned by M.S.S, this study
HA-miniTurbo-PERK	Cloned by M.S.S, this study
HA-miniTurbo-ATF3	Cloned by M.S.S, this study

2.4 Oligonucleotides and primers

All sequences are written in the direction of the 5-prime end to the 3-prime end.

Red color donates restrictions enzymes sites.

se: sense, as: anti-sense.

Oligonucleotides for cloning *EIF2AK3* (PERK) directed sgRNAs into the pX459 vector:

Name	Sequence
sg1_ EIF2AK3_se:	CACCGTGGAGCGCGCCATCAGCCCG
sg1_ EIF2AK3_as:	AAACCGGGCTGATGGCGCGCTCCAC
sg2_ EIF2AK3_se:	CACCGCGGTACTCGCGTTCGCTGAGG
sg2_ EIF2AK3_as:	AAACCTCAGCGACGCGAGTACCGC
sg3_ EIF2AK3_se:	CACCGTTTCACGGTCTTGGTCCCAC
sg3_ EIF2AK3_as:	AAACGTGGGACCAAGACCGTGAAAC
sg4_ EIF2AK3_se:	CACCGAGAAGTGATTCAACTGTGAA
sg4_ EIF2AK3_as:	AAACTTCACAGTTGAATCACTTCTC

Oligonucleotides for cloning *ERN1* (IRE1 α) directed sgRNAs into the pX459 vector:

Name	Sequence
sg1_ ERN 1_se:	CACCGTCACCGCCTCGCTGTCGTCG
sg1_ ERN 1_as:	AAACCGACGACAGCGAGGCGGTGAC
sg2_ ERN 1_se:	CACCGCCGGTCACTCACCCCGAGGC
sg2_ ERN 1_as:	AAACGCCTCGGGGTGAGTGACCGGC
sg3_ ERN 1_se:	CACCGGTGAATCTGGGGACGTCCTG
sg3_ ERN 1_as:	AAACCAGGACGTCCCCAGATTCACC
sg4_ ERN 1_se:	CACCGCATGAAGGTCAGATAGCGCA
sg4_ ERN 1_as:	AAACTGCGCTATCTGACCTTCATGC

Oligonucleotides for cloning *ATF3* directed sgRNAs into the pX459 vector:

Name	Sequence
sg1_ ATF3_se:	CACCGTAACCTGACGCCCTTTGTCA
sg1_ ATF3_as:	AAACTGACAAAGGGCGTCAGGTTAC
sg2_ ATF3_se:	CACCGGGTGTCCATCACAAAAGCCG
sg2_ ATF3_as:	AAACCGGCTTTTGTGATGGACACCC

Oligonucleotides for cloning *ATF3* directed sgRNAs into the LentiCRISPR V2 vector:

Name	Sequence
HGLibA_03436_se:	CACCGCTGAGCCCGGACAATACACG
HGLibA_03436_as:	AAACCGTGTATTGTCCGGGCTCAGC
HGLibA_03437_se:	CACCGCCACCGGATGTCCTCTGCGC
HGLibA_03437_as:	AAACGCGCAGAGGACATCCGGTGGC
HGLibA_03438_se:	CACCGGGTGTCCATCACAAAAGCCG
HGLibA_03438_as:	AAACCGGCTTTTGTGATGGACACCC
HGLibB_03434_se:	CACCGTATACATGCTCAACCTTCAT
HGLibB_03434_as:	AAACATGAAGGTTGAGCATGTATAC
HGLibB_03435_se:	CACCGTGAGTCAACAGCCCATATGC

HGLibB_03435_as:	AAACGCATATGGGCTGTTGACTCAC
HGLibB_03436_se:	CACCGTTCTGGACCCAAAAGGGCCT
HGLibB_03436_as:	AAACAGGCCCTTTTGGGTCCAGAAC

Primers for PERK (from PERK.WT.9E10.pCDNA vector) sub-cloning into MYC-BirA vector:

Direction	Sequence
Forward Primer:	TAAGCAGAATTCATGGAGCGCGCCACCCGG
Reverse Primer:	TGCTTACTCGAGCTAGCCAGGCAGTGGCGTG

Primers for IRE1 α (from IRE1 alpha-pcDNA3.EGFP vector) sub-cloning into MYC-BirA vector:

Direction	Sequence
Forward Primer:	TAAGCAGAATTCATGCCGGCCCGGCGGCT
Reverse Primer:	TGCTTACTCGAGTCAGAGGGCGTCTGGAGTC

Primers for ATF3 (from pRK-ATF3 vector) sub-cloning into MYC-BirA vector:

Direction	Sequence
Forward Primer:	TAAGCAGAATTCATGATGCTTCAACACCC
Reverse Primer:	TGCTTACTCGAGTTAGCTCTGCAATGTTCC

Primers for BiP (from pCMV BiP-Myc-KDEL-wt vector) sub-cloning into MYC-BirA vector:

Direction	Sequence
Forward Primer:	TAAGCAGCTAGCATGAAGCTCTCCCTGGT
Reverse Primer:	TGCTTACTCGAGTCACAACCTCATCTTTTTCTGCTG

Primers for ATF3 (from pRK-ATF3 vector) sub-cloning into HA-miniTurbo vector:

Direction	Sequence
Forward Primer:	TAAGCAGAATTCATGATGCTTCAACACCC
Reverse Primer:	TGCTTAGCGGCCGCGCTCTGCAATGTTCTT

Primers for PERK (from PERK.WT.9E10.pCDNA vector) sub-cloning into HA-miniTurbo vector:

Direction	Sequence
Forward Primer:	TAAGCAGAATTCATGGAGCGCGCCACCCGG
Reverse Primer:	TGCTTACTCGAGCGCCAGGCAGTGGCGTG

Primers designed for RT-qPCR detection:

Direction/Target	Sequence
Forward Primer/ <i>EIF2AK3</i>	AGAGATTGAGACTGCGTGCC

Reverse Primer/ <i>EIF2AK3</i>	TCCCAAATACCTCTGGTTTGCT
Forward Primer/HCoV-229E S RNA	TTTCAGGTGATGCTCACATACC
Reverse Primer/HCoV-229E S RNA	ACAAACTCACGAACTGTCTTAG
Forward Primer/HCoV-229E nsp8 RNA	GCTGTTGCAAATGGTTCCTCAC
Reverse Primer/HCoV-229E nsp8 RNA	GATGCACATTCTTACCATCATTATCC

2.5 Antibodies

The following primary antibodies were used:

Antibody	Species	Source	Applications and Dilutions
Anti- β -actin (C4)	mouse	Santa Cruz (Sc-47778)	WB: 1:1000 in TBS-T with 5% milk
Anti-PERK (B-5)	mouse	Santa Cruz (Sc-377400)	WB: 1:1000 in TBS-T with 5% milk
Anti-IRE1 α (B-12)	mouse	Santa Cruz (Sc-390960)	WB: 1:1000 in TBS-T with 5% milk
Anti-CREB-2/ATF4 (B-3)	mouse	Santa Cruz (Sc-390063)	WB: 1:1000 in TBS-T with 5% milk
Anti-ATF3 (C-19)	rabbit	Santa Cruz (Sc-188) - discontinued	WB: 1:500 in TBS-T with 5% milk
Anti-SQSTM1/p62 (D-3)	mouse	Santa Cruz (Sc-28359)	WB: 1:500 in TBS-T with 5% milk IF: 1:100
Anti-PERK	rabbit	Abcam (Ab65142)	WB: 1:1000 in TBS-T with 5% milk
Anti-BiP (C50B12)	rabbit	Cell Signaling (3177)	WB: 1:1000 in TBS-T with 5% milk
Anti-eIF2 α	rabbit	Cell signaling (9722)	WB: 1:1000 in tBS-T w/ 5% BSA
Anti-P (Ser51)-eIF2 α	rabbit	Cell signaling (9721)	WB: 1:1000 in TBS-T w/ 5% BSA + 10% NaF
Anti-LC3B (D11) XP®	rabbit	Cell signaling (3868)	WB: 1:1000 in TBS-T with 5% milk
Anti-P (Ser724)IRE1 α	rabbit	Novus Biologicals (NB100-2323)	WB: 1:1000 in TBS-T w/5% dry milk + 10% NaF
Anti-HCoV-229E N protein (1E7)	mouse	Eurofins/Ingenasa M.30.HCo.B1E7; Batch 250609	WB: 1:500 in TBS-T with 5% milk
Anti-MERS-CoV N Protein	rabbit	SinoBiological (100213-RP02)	WB: 1:1000 in TBS-T with 5% milk
Anti-SARS-CoV N Protein (cross-reacting with related CoV's)	rabbit	Rockland Inc. (200-401-A50)	WB: 1:2000 in TBS-T with 5% milk
Anti-Puromycin [3RH11]	mouse	Kerafast Inc. (EQ0001)	WB: 1:1000 in TBS-T with 5% milk
Anti-double stranded RNA (J2)	mouse	SCICONS/Nordic-MUbio (10010200)	IF: 1:100
Anti-HCoV-229E nsp8	rabbit	Prof. John Ziebuhr	WB: 1:500 in TBS-T with 5% milk, IF: 1:100

Anti-HCoV-229E nsp12	mouse	Carsten Grötzinger	WB: 1:500 in TBS-T with 5% milk, IF: 1:100
Anti-MYC	mouse	Cell signaling (2276)	WB: 1:1000 in TBS-T with 5% milk
Anti-HA	mouse	Roche (115 838 16007)	WB: 1:500 in TBS-T with 5% milk
Anti-I κ B α	rabbit	Cell Signaling 9242	WB: 1:1000 in TBS-T with 5% milk
Anti-Ubiquitin	mouse	Santa Cruz (#sc-8017)	WB: 1:200 in 5% MP/TBST

The following secondary antibodies were used:

Antibody	Species	Source	Applications and Dilutions
Anti-mouse Immunglobilins/HRP	goat	Dako	WB:1:2500 in TBS-T w/ 5% dry milk
Anti-rabbit Immunglobilins/HRP	goat	Dako	WB:1:2500 in TBS-T w/ 5% dry milk
Cy3-coupled anti rabbit IgG	donkey	Merck Millipore	IF final: 1:200 (pre dilution 1:2 \rightarrow 1:100)
Dylight488-coupled anti mouse IgG	donkey	ImmunoReagent	IF final: 1:200 (pre dilution 1:2 \rightarrow 1:100)
Goat Anti-Mouse IgG (H+L), Alexa Flour594	goat	Invitrogen	IF final: 1:100
F(ab') ₂ -Goat anti-Rabbit IgG (H+L), Alexa Fluor 488	goat	Invitrogen	IF final: 1:100

The following reagent was used to detect the Biotin-Streptavidin signal:

Streptavidin-Horseradish Peroxidase (HRP) from PerkinElmer (NEL750001EA).

2.6 Enzymes

The following enzymes were used:

Name	Source
GoTaq G2 Flexi DNA Polymerase	Promega (#M7805)
M-MuLV Reverse Transcriptase	Thermo Fisher Scientific EP0352
Pfu DNA Polymerase	Thermo Fisher Scientific EP0571
Phusion™ High-Fidelity DNA Polymerase	Thermo Fisher Scientific F-530XL
T4 DNA Ligase	Thermo Fisher Scientific EL0014
T4 Polynucleotide Kinase	Thermo Fisher Scientific EK0031
Plasmid-Safe ATP-Dependent DNase	Biozym 161010
DNaseI	Thermo Fisher Scientific EN0521
FastDigest BbsI	Thermo Fisher Scientific FD1014
EcoRI	Thermo Fisher Scientific ER0271
FastDigest XhoI	Thermo Fisher Scientific FD0694
BspOI (BmtI)	Thermo Fisher Scientific ER2041
NotI	Thermo Fisher Scientific ER0591

Calf Intestinal Alkaline Phosphatase (CIAP)	Thermo Fisher Scientific EF0654
---	---------------------------------

2.7 Small molecule inhibitors and inducers

Name	Source	Solvent	Stock-final concentrations
Bafilomycin A1	Cayman Chemicals Cay11038	DMSO	1 mM-See figure legends
Thapsigargin	Cayman Chemicals Cay10522-1	DMSO	10 mM-See figure legends
GSK2656157	Cayman Chemicals Cay17372	DMSO	10 mM-See figure legends
GSK2606414	Cayman Chemicals Cay17376	DMSO	10 mM-See figure legends
Remdesivir	Cayman Chemicals Cay30354	DMSO	10 mM-See figure legends
Leupeptin hemisulfate	Carl Roth CN33.2	Water	5 mg/ml-10 µg/ml
Microcystin	Enzo Life Sciences ALX-350-012-M001	Ethanol	1 mM-1 µM
Pepstatin A	Applichem A2205	Ethanol	1 mg/ml-1 µg/ml
PMSF	SigmaAldrich P-7626	Ethanol	200 mM-1 mM
Protease inhibitor cocktail tablets	Roche 11873580001	Water	One tablet in 2 ml 25x-1x

2.8 Ready-to-use materials and reagents (including kits)

Name	Source
6x DNA Loading Dye	Thermo Fisher Scientific R0611
GeneRuler DNA Ladder Mix	Thermo Fisher Scientific SM0331
Ethidium bromide 1%	Carl Roth 2218.2
Fast SYBR Green PCR Master Mix	Applied Biosystems 4385612
TaqMan Fast Universal PCR Master Mix	Applied Biosystems 4352042
Random Hexamer Primer	Thermo Fisher Scientific S0142
dNTP Mix	Thermo Fisher Scientific R0192
MgCl ₂ (25mM)	Thermo Fisher Scientific R0971
ATP	Thermo Fisher Scientific R0441
10x FastDigest Buffer	Thermo Fisher Scientific B64
10x Tango-Puffer	Thermo Fisher Scientific BY5
10x Buffer O	Thermo Fisher Scientific BO5
4% Paraformaldehyde (in PBS)	Santa Cruz sc-281692
Saponin	Sigma-Aldrich S4521-10G
Normal Donkey Serum	Jackson ImmunoResearch 017-000-121
Hank's BSS (HBSS)	PAN P04-32505
Hoechst 33342	Thermo Fisher Scientific H3570
ibiTreat µ-Slide VI 0.4	Ibidi 80606
Lithium Chloride Precipitation Solution	Thermo Fisher Scientific AM9480
NucleoBond PC500	Macherey&Nagel 740574.50
NucleoSpin Gel and PCR Clean-Up	Macherey&Nagel 740609.250
NucleoSpin Plasmid	Macherey&Nagel 740588.250
NucleoSpin RNA II	Macherey&Nagel 740955.250
Roti-Load 1	Carl Roth K929.3
Rotiphorese Gel 30	Carl Roth 3029.1
PageRuler Prestained Protein Ladder	Thermo Fisher Scientific 26616
Ponceau S	Serva 33429
Roti-PVDF	Carl Roth T830.1
Filterpapier	Whatman

Roti-Quant	Carl Roth K015.1
Gel Blotting Paper GB005	GE Healthcare 10426994
Immobilion Western Chemiluminescent HRP-Substrate	Merck Millipore WBKLS0500
Amersham ECL Western Blotting Detection Reagent	GE Healthcare RPN2106
Soc-Medium	Invitrogen 15544-034
Trypsin/EDTA Solution	PAN Biotech P10-023100
DPBS	PAN Biotech P04-36500
L-Homopropargylglycine (L-HPG)	Jena Bioscience CLK-1067-25
Biotin-Azide	Cayman Chemicals Cay13040
TCEP	Sigma-Aldrich S C4706
CuSO ₄ *5H ₂ O	Merck 102790
Zebra spin 0.5 ml 7K desalting columns	Thermo Fisher Scientific 89882
High Capacity Streptavidin Agarose Resin	Thermo Fisher Scientific 20361
Streptavidin Agarose Resin	Thermo Fisher Scientific 20353
Pierce™ Coomassie (Bradford) Protein-Assay	Thermo Fisher Scientific 23200
TrypLE™ Express Enzyme (1x)	Thermo Fisher Scientific 12604013
Polybrene (Hexadimethrine bromide)	Sigma-Aldrich S107689-10G
Lipofectamine™ 2000	Thermo Fisher Scientific 11668019
PLUS™ Reagent	Thermo Fisher Scientific 11514015
Trypsin/EDTA	PAN Biotech P10-023100
Opti-MEM®	Thermo Fisher Scientific 51985-034
10x T4 DNA-Ligase-Buffer	Thermo Fisher Scientific B69
CellTiter-Glo Luminescent Cell Viability Assay	Promega G7571
CellTiter 96® AQueous One Solution Cell Proliferation Assay kit	Promega G3582
ATPlite assay	Perkin Elmer
DMEM	PAN Biotech P04-03550
FBS Good Forte	PAN Biotech P40-47500
Doxycyclin	Sigma-Aldrich D9891
L-Glutamin	PAN Biotech P04-80100
Penicillin/Streptomycin	PAN Biotech P06-07100
Ampicillin sodium salt	BioChemica A0839,0025
Puromycin	Merck Millipore 540411-100MG
Kanamycin Sulfate	Carl Roth T832.3
Biotin	Sigma-Aldrich B4501-100MG
Standard nutrient agar 1	Merck 1.07881.0500
FBS Premium, South America origin, fetal bovine serum, tetracycline free, 0.2 µm sterile filtered	PAN Biotech P30-3602
BD Difco™ Dehydrated Culture Media: LB Broth, Miller (Luria-Bertani)	BD 244610
Avicel®	FMC Biopolymer RC591

2.9 Buffers and prepared mediums

Buffer/Medium name	Recipe
Whole cell extract (“Special lysis”) buffer	30 mM Tetrasodium pyrophosphate 50 mM NaCl 1% (v/v) Triton X-100 2 mM Na ₃ VO ₄ 50 mM NaF 20 mM β-Glycerophosphate 10 mM Tris (pH 7.05 / HCl)

	Add fresh: 1 µg/ml Pepstatin (=1,5 mM) 10 µg/ml Leupeptin (=23,4 mM) 1 mM PMSF 1 µM Microcystin
Click lysis buffer	100 mM pH 7.5 Hepes 150 mM NaCl 1% Nonidet P-40 Freshly added 2 mM PMSF Freshly added 1x Roche
BioID lysis buffer	50 mM Tris (pH 7.5/HCl) 500 mM NaCl 2% SDS (w/v) Freshly added 1mM DTT Freshly added 1x Roche Inhibitor Cocktail
TAE buffer for agarose gel	40mM Tris 1mM EDTA 0.11% (v/v) acetic acid
stacking gel buffer	1 M Tris (pH 6.8/HCl)
Separating Gel Buffer	1 M Tris (pH 8.8/HCl)
TBS buffer	10 mM Tris 150 mM NaCl (pH 7.4/HCl) + 0,05% (v/v) Tween 20 for TBS-T
Ponceau S	0.1% (w/v) Ponceau S in 5% (v/v) acetic acid
1x Laemmli running buffer	25 mM Tris 192 mM glycine 0.1% (w/v) SDS
Blotting buffer	25 mM Tris 192 mM glycine 20% (v/v) Methanol
CaCl ₂ solution	2 M CaCl ₂
2x HEBS	280 mM NaCl 50 mM HEPES 1.5 mM Na ₂ HPO ₄ (pH 7.12/NaOH)
BioID washing buffer I	2% SDS (w/v)
BioID washing buffer II	50 mM HEPES (pH 7.5/HCl) 1mM EDTA 500 mM NaCl 0.1% Sodium Deoxycholate (w/v) 1% Triton X-100 (v/v)
BioID washing buffer III	10 mM Tris (pH 7.5/HCl) 1 mM EDTA 250 mM LiCl 0.5% Sodium Deoxycholate (w/v) 0.5% NP-40 (w/v)
BioID washing buffer IV	50 mM Tris (pH 7.5/HCl) 50 mM NaCl 0.1% NP-40 (w/v)
BioID washing buffer V	50 mM Tris (pH 7.5/HCl)
Biotin Stock Solution (20x)	1 mM Biotin in DMEM (without Pen/Step, without L-Glutamine) followed by sterile filtration
Silver staining- fixing solution	12.5% w/v TCA

Silver staining- incubation solution	500 mmol/L anhydrous sodium acetate 20mmol/L Sodium Thiosulfate 2% v/v 25% glutaraldehyde
Silver staining- staining solution	6mmol/L silver nitrate 0.05% v/v formaldehyde 37%
Silver staining- developer solution	235mmol/L sodium carbonate 0.01% v/v formaldehyde 37%
Silver staining- stop solution	5% acetic acid
Full DMEM (cell-culture) medium	10% (v/v) FBS 100 µg/ml Streptomycin 100 U/ml Penicillin 2 mmol/l L-Glutamine
LB-Medium	10 g Bacto™ Tryptone 10 g NaCl 5 g Yeast extract H ₂ O to a volume of 1L Autoclaving
LB-medium for plates	18.5 g Standard I nutrient agar H ₂ O to a volume of 0.5L Autoclaving

2.10 Chemicals

Chemicals used in this study were purchased from the following companies, unless otherwise stated: Baker, Roche, Merck, Promega, Biomol, Invitrogen/Thermo Fisher Scientific, Sigma, Pharmacia, Roth, Serva, and Fluka.

2.11 Plastics and other disposable materials

The following companies were the source of all plastic and disposable materials used in this study: Eppendorf, Ibidi, Greiner, Ansell, Sarstedt, Neolab, Roth, Nerbe-Plus, Nunc, Omnilab, and Brand.

2.12 Devices and apparatuses

2.12.1 for gel electrophoresis and Western blotting

Name	Source
Elektrophorese Power Supply EPS 600, 601, 3500	Pharmacia Biotech
Owl P9DS	Owl Separation Systems
Mighty Small II	Hoefer
PerfectBlue 'Semi-Dry'-Blotter, Sedec	VWR Peqlab
Mupid-exU	Takara
Chemi Doc Touch Imaging System	Bio-Rad
Gel iX Imager UV-Transilluminator	INTAS

2.12.2 for PCR

Name	Source
7500 Fast Real Time PCR System	Applied Biosystem
Thermocycler T Professional	Biometra

2.12.3 for centrifugation and mixing

Name	Source
Sorvall RC5S Plus	Thermo Fisher Scientific
Table-centrifuge 5415 R	Eppendorf
Table-centrifuge 5424	Eppendorf
Table-centrifuge 5424 R	Eppendorf
TJ-25 centrifuge	Beckman Coulter
Thermomixer comfort	Eppendorf
Thermomixer compact	Eppendorf
Vortex Top Mix Stirrers	Heidolph
Vortex mixer	neoLab

2.12.4 for weighting chemicals

Name	Source
AT 250	Mettler
FI 310	Fischer
XP205 DelaRange	Mettler Toledo
MP-3000	Chyo

2.12.5 for cell culture

Name	Source
BBD 6220 CO2 Incubator	Thermo Scientific
CO2 Incubator Autozero	Heraeus
Safe 2020 (Sterile work bench)	Thermo Scientific

2.12.6 Microscopy

Name	Source
CKX41	Olympus
DMi1	Leica
DMi8	Leica

2.12.7 Others

Name	Source
Nano Drop ND-1000 Spectrophotometer	Peqlab
Sonifier 250	Branson
Spectramax Plus Microplate Spectrophotometer	Molecular Devices

Concentrator Plus SpeedVac	Eppendorf
Bioruptor TO NextGen	Diagenode
Multitron Standard	Infors HT
CH-4103 Shaker	Infors HT

2.13 Software

Name	Version/link
GraphPad Prism	5.0 or 8.4.3
ImageLab	5.2.1 or 6.0.1
Microsoft Excel	2016
Perseus	(see methods)
MaxQuant	(see methods)
ImageJ	1.51j8
DNASTAR navigator	11.1.0.54
Leica LASX	3.4.2.18368
Metascape	Express settings (Zhou et al. 2019) https://metascape.org/
Cytoscape	3.8.0 or 3.9.1
STRING	version 10 or 11.5, https://string-db.org/
Venn diagram tool	https://bioinformatics.psb.ugent.be/webtools/Venn/
Chromos	2.6.6
Zotero	6.0.14

Chapter 3: Methods

3.1 Mammalian cell culture

For the following methods related to the culturing of mammalian cells, strictly sterile tubes, dishes, vials, pipette tips and any other related tools were utilized.

3.1.1 Thawing and freezing adherent cells

Freezing cell lines was done according to the following procedure: confluent cells (90% of T145 dish) were first observed under light microscopy for any visible signs of contamination. Particular care was given to Mycoplasma contamination (see section 3.3.2). Afterward, cells were trypsinized, re-suspended in 10 ml of pre-warmed cell-culture medium, and transferred to 15 ml tubes. Cells were then centrifuged for 5 minutes, at 1000 RPM (TJ-25 centrifuge) at 4 C. Supernatant was removed and cell pellets were re-suspended in 2 ml freezing medium (full DMEM medium + 10% DMSO). The cell re-suspension was then transferred to cryo-tubes (from Nalgene) and stored overnight at -80 C and then transferred to a permeant location in the liquid nitrogen tank.

Thawing the cells from their storage place in the liquid nitrogen tank was carried out as follows: Vials of frozen cells were initially thawed in a 37°C water bath until only the core of the vial remained frozen. The semi-frozen content of the vial was then transferred to a 15 ml tube containing a 9 ml pre-warmed cell-culture medium. The tubes were then centrifuged for 5 minutes, at 1000 RPM at room temperature and the supernatant (freezing medium) was removed by suction (to remove any remaining DMSO). The cell pellet was re-suspended in fresh 10 ml pre-warmed medium and added to a T145 dish containing 10 ml fresh medium. When other dish sizes were used, appropriate adjustments for medium volume were made accordingly. Cells were then allowed to attach to the dish and grow in the incubator at 37°C and monitored frequently for morphology and growth rate.

3.1.2 Growing and passaging the cells

Huh7 human hepatoma cells (Japanese Collection of Research Bioresources (JCRB) cell bank) and VERO-E6 African green monkey kidney epithelial cells (ATCC CRL-1586) were grown in Dulbecco's modified Eagle's medium (DMEM, including 3.7 g/l NaHCO₃; PAN Biotech Cat No P04-03550). The medium was supplemented with 10% of filtrated bovine serum (FBS Good Forte; PAN Biotech, Cat No. P40-47500) or fetal calf serum for VERO-E6 cells (FCS; PAN Biotech Cat No. 1502-P110704), 2 mM L-glutamine (Gibco, 21935-028), 100 U/ml penicillin, and 100 µg /ml streptomycin.

MRC-5 human embryonic lung fibroblasts (ATCC, CCL-171) were grown in DMEM. The medium contained 1.5 g/l (w/v) NaHCO₃ and was supplemented with 10% fetal calf serum (FCS; PAN Biotech Cat No. 1502- P110704), 2 mM L-glutamine, 100 U/ml penicillin, and 100 µg/ml streptomycin, 1% minimum essential medium non-essential amino acids (100x MEM NEAA; Gibco Cat No 11140-035) and 1 mM sodium pyruvate (100 mM; Gibco 11360- 039).

HEK 293FT primary embryonal human kidney cells (Gibco-Thermo fisher scientific, R 70007) were grown in DMEM medium containing 10% FBS supplemented with 0.1 mM MEM Non-Essential Amino Acids, 1 mM sodium pyruvate, and 2 mM L-glutamine.

Cells were allowed to grow up to a maximum of 90% of any given dish capacity to avoid overcrowding. Once the cells in the dish reached this level of confluency, the cells were trypsinized using Trypsin/EDTA (PAN Biotech #P10-023100). Around 2 ml of trypsin was added to cover the entirety of the dish and then removed immediately by suction. Cells were then incubated for 5 minutes at 37°C. Afterward, the cells are immobilized and easily re-suspendable in a fresh corresponding full cell-culture medium. The cell re-suspension is then used to seed new dishes.

Given their tendency to dislodge from the dish very easily, HEK 293FT cells were particularly handled with care and never allowed to reach a confluency of over 70%.

3.1.3 Transfection methods

3.1.3.1 Calcium phosphate (CaCl₂) method

Transient or stable transfection of expression plasmids in this study was carried out using mainly the calcium phosphate (CaCl₂) method. This method of transfection relies on the formation of calcium phosphate-DNA precipitate that allows an easy binding of the DNA to the cell surface. Aided by a glycerol shock and endocytosis, the DNA anchored to the cell surface is delivered to the inside of the mammalian cell to be expressed. If the plasmid carries a selection marker (e.g. against a toxic antibiotic such as puromycin), cells that internalized it can be selected for, and hence a stable transfection can be established.

The following mixture was prepared to transfect one plasmid into Huh7 cells in the indicated dish size as an example:

Huh7 cells in (100 mm dish)
1500 µl H ₂ O
1350 µl 2x HEBS
30 µg plasmid
189 µl 2M CaCl ₂

After vortexing, the transfection mixture was added slowly to the cells and then followed by a glycerol shock after 5 hours. The glycerol shock was carried as follows: the medium was removed from the cells and 3 ml of shock-medium (full DMEM medium + 10% glycerol) was added for 3 minutes at room temperature. Thereafter, the shock medium was removed and the cells were washed with warm PBS two times. 10 ml of full fresh medium was then added overnight.

For the stable transfection of CRISPR-CAS-9 plasmids, the selection process started the next day by adding 1 µl of puromycin (10 ug/ml) directly to 10 ml of medium.

Scaling this procedure (or any other cell culture related procedures in this study) up or down is done by adapting the volumes of the reagents as a function of the dish size as shown in the table below:

Factors for conversion between cell culture vessels		T175 flask	T145 dish	T75 flask	100mm dish	T25 flask	60mm dish	6 Well	35mm dish	12 well plate	24 Well Platte	48 well plate	6 canal Ibbidi	96 well plate	18er Ibbidi
	surface area (cm ²)	175	143	75	58	25	21	9.6	8.7	3.9	1.9	1	0.6	0.34	0.2
T175 flask	175		0.82	0.43	0.33	0.14	0.12	0.05	0.05	0.02	0.01	0.006	0.003	0.002	0.0011
T145 dish	143	1.22		0.52	0.41	0.17	0.15	0.07	0.06	0.03	0.01	0.007	0.004	0.002	0.0014
T75 flask	75	2.33	1.91		0.77	0.33	0.28	0.13	0.12	0.05	0.03	0.013	0.008	0.005	0.0027
100mm dish	58	3.02	2.47	1.29		0.43	0.36	0.17	0.15	0.07	0.03	0.017	0.010	0.006	0.0034
T25 flask	25	7.00	5.72	3.00	2.32		0.84	0.38	0.35	0.16	0.08	0.040	0.024	0.014	0.0080
60mm dish	21	8.33	6.81	3.57	2.76	1.19		0.46	0.41	0.19	0.09	0.048	0.029	0.016	0.0095
6 well plate	9.6	18.23	14.90	7.81	6.04	2.60	2.19		0.91	0.41	0.20	0.104	0.063	0.035	0.0208
35mm dish	8.7	20.11	16.44	8.62	6.67	2.87	2.41	1.10		0.45	0.22	0.115	0.069	0.039	0.0230
12 well plate	3.9	44.87	36.67	19.23	14.87	6.41	5.38	2.46	2.23		0.49	0.256	0.154	0.087	0.0513
24 well plate	1.9	92.11	75.26	39.47	30.53	13.16	11.05	5.05	4.58	2.05		0.526	0.316	0.179	0.1053
48 well plate	1	175.00	143.00	75.00	58.00	25.00	21.00	9.60	8.70	3.90	1.90		0.600	0.340	0.2000
6 canal Ibbidi	0.6	291.67	238.33	125.00	96.67	41.67	35.00	16.00	14.50	6.50	3.17	1.67		0.567	3.0000
96 well plate	0.34	514.71	420.59	220.59	170.59	73.53	61.76	28.24	25.59	11.47	5.59	2.94	1.76		0.5882
18er Ibbidi	0.2	875.00	715.00	375.00	290.00	125.00	105.00	48.00	43.50	19.50	9.50	5.00	3.00	1.70	

Table 1: Factors for conversion between cell culture vessels.

The table was created and updated by Helmut Mueller and Hendrik Weisser respectively. Blue cells indicate frequently used vessels in this study. Yellow cells indicate invalde conversion.

3.1.3.2 Lipofectamine 2000 method

Another transfection method used in this study (mainly for Lentivirus plasmids transfection in HEK 293FT cells) was Lipofectamine 2000. The Lipofectamine 2000 achieves transfection of plasmids (and other nucleic acids) using Lipofection. This process relays on the formation of vesicles (called liposomes) carrying the plasmid of interest. Since liposomes and cellular membranes are made of a phospholipid bilayer, they can merge easily together, delivering the content of the vesicles to the inner of the cell.

Maintaining the HEK 293FT cells at a density below 70% of the dish capacity was a crucial step for a successful transfection and to avoid any toxicity induced by Lipofectamine 2000 reagent.

To transfect the three lentivirus plasmids, the following lentiviral target mixture was prepared in a 50 ml tube for the indicated flask size:

Component	Amount per T175 flask
Opti-MEM	2250 μ l
pMD2.G (lentiviral helper plasmid)	15.3 μ g
psPAX (lentiviral helper plasmid)	23.4 μ g
Lentiviral target plasmid	30.6 μ g

To increase cationic lipid-mediated transfection efficiencies and cellular viabilities a PLUS reagent mixture was included in the lentiviral target mixture. The PLUS reagent mixture consisted of 2250 μ l of Opti-MEM and 297 μ l of PLUS reagent (Cat. no. 11514-015). The PLUS reagent mixture was then added to the lentiviral target mixture, mixed by inversion, and incubated at room temperature for 5 minutes. Thereafter, the Lipofectamine 2000 reagent mixture was prepared by combining 4500 μ l of Opti-MEM with 270 μ l of Lipofectamine 2000. This mixture was then added to the previous one (lentiviral target mix+ PLUS mix) and incubated at room temperature for 5 minutes. Finally, 9 ml of the resultant mixture was added to the T175 flask. A gentle shake was applied and the T175 flask was returned to the 37°C incubator.

3.1.4 Harvesting the cells

The process of harvesting the cells was carried out at 4°C on an ice bucket. The cell dishes were taken from the incubator at the end of the experiment and placed on ice. The medium was either discarded or collected in special tubes for downstream applications. Cells were then washed two times with ice-cold PBS. 2 ml of ice-cold PBS was added to the cells afterwards and the cells were scraped using a scarper. PBS containing the cells were then collected in tubes. The cells were then centrifuged at 500 RPM (Table-centrifuge 5424) for 5 minutes at 4°C. The cell pellet was either lysed directly or stored at -80 C for later usage.

3.2 Molecular biology

3.2.1 Plasmid extraction

Extracting DNA plasmid constructs from bacteria was done in two scales: mini-prep and maxi-prep scales depending on the needed amount of the plasmids for downstream usage.

Preparation of plasmids on the mini-prep scale was carried out as follows: bacterial strain transformed with the plasmid of interest was inoculated into 5 ml of LB medium containing the appropriate antibiotic marker. The bacteria were then allowed to grow overnight at 37°C with continuous shaking (for oxygenation) at 250 RPM. If after the passage of 16 hours, the LB medium containing the transformed bacteria became turbulent, indicating healthy growth of the bacteria, 4 ml of the suspension was taken for the extraction of the DNA plasmid. The extraction process was done using the NucleoSpin® plasmid kit (Machery & Nagel) and in accordance with the provided protocol. The final elution step of the DNA was done using ddH₂O pre-warmed to 60°C to increase the efficacy of the elution. The amount of water used for elution was 30 µl. The eluted plasmid concentration was then measured using ND-1000 Nanodrop® and stored at -20°C.

Preparation of plasmids on the maxi-prep scale was carried out as follows: bacterial strain transformed with the plasmid of interest was inoculated into 150 ml of LB medium containing the appropriate antibiotic marker. The bacteria were then allowed to grow overnight at 37°C with continuous shaking at 160 RPM. If after the passage of a maximum of 18 hours, the LB medium containing the transformed bacteria became turbulent, indicating healthy growth of the bacteria, all of the 150 ml was used for the extraction of the DNA plasmid. The extraction process was done using the NucleoBond® Maxi Kit (Machery & Nagel) and in accordance with the provided protocol. The final elution step of the DNA was done using ddH₂O pre-warmed to 60°C to increase the efficacy of the elution. The amount of water used for elution ranged from 200 to 300 µl. The eluted plasmid concentration was then measured using ND-1000 Nanodrop® and stored at -20°C for short-term usage or at -80°C for longer storage.

3.2.2 RNA extraction

Extracting total RNA from the cell pellet was carried out using the NucleoSpin® RNA kit and in accordance with the manufacturer protocol. The RNA was then eluted with 60 µl of RNase-free H₂O and the concentration was measured using ND-1000 Nanodrop®. The quality of the extracted RNA was controlled using the ratio of 260 nm absorbance to that of 280 nm. The RNA was then stored at -20°C for short-term usage or at -80°C for longer storage.

3.2.3 Reverse transcription

Obtaining cDNA from the total RNA extracted from cells for further studies (using quantitative PCR for example) was done using the reverse transcriptase enzyme (RNA-dependent DNA polymerase) of Moloney Murine Leukemia Virus (M-MuLV). One reaction consisted of a volume of 20 μ l with the following components:

Component	Amount
Reverse transcription (RT) Buffer (5x)	4 μ l
Random hexamer primers	0.5 μ l
dNTP mix (each 10 mM)	0.5 μ l
M-MuLV transcriptase (20 U/ μ l)	0.5 μ l
total RNA	1 μ g
H2O	adjusted to 20 μ l

The reaction mix was then very gently vortexed and span for a few seconds. Thereafter, thermocycler T-Professional was used to carry out the reverse transcription reaction using the following temperatures and times:

Temperature	Time
25°C	10 minutes
42°C	60 minutes
70°C	10 minutes
10°C	Pause Temperature
97°C	Lid Temperature

The now cDNA was either used directly (for qPCR) or stored at -20°C for later usage.

3.2.4 Quantitative PCR (qPCR)

The cDNA converted from total RNA represents a wealth of information that can be used to obtain knowledge on expressed genes under certain experimental or physiological conditions. One molecular biology technique that can be used to this end is quantitative PCR. The method allows the monitoring of the levels (or quantity) of a specific DNA segment in a sample by amplifying it. Using a fluorescent reporter, the amount of the amplification product (amplicon) can be monitored in real-time after each cycle of amplification. If the fluorescence of the amplicons exceeds that of the background levels after a certain number of amplification cycles, the product is said to be detected in the sample. The amplification cycle after which this detection happens is called the ct (cycle threshold) value. The lower this value is, the more abundant the gene (or specific DNA of interest) is in the sample.

To achieve this, two principles of monitoring can be utilized: SYBR Green and TaqMan assay.

SYBR green method depends on an intercalating fluorescent dye that binds only to double stranded DNA (dsDNA). At the beginning of the amplification process, the two strands of the DNA will separate,

and the synthesis of new complementary strands takes place. At the end of the cycle, the newly formed dsDNA will be available to the SYBR green reporter to bind to and produce an observable signal that is registered by the machine. The process will repeat with each amplification cycle until enough fluorescent signal has accumulated above the background (reaching a ct) or, if the target is not present, until the reaction is stopped.

The TaqMan assay system depends on probes designed to target specific DNA sequences (of a specific gene). These short probes carry a fluorescent reporter at their 5 prime end and a quencher of the FRET (Förster Resonance Energy Transfer) signal emitted by the reporter on their 3 prime end. As long as the two components (the reporter and the quencher) are next to each other (i.e. the probe is intact) the fluorescence will be undetectable. At the beginning of the amplification process, the two strands of the DNA will separate, and the probe will bind to its target sequence on the single-stranded DNA. The synthesis of new complementary strands takes place through the action of the Taq polymerase. During this process, the probe is degraded by the 5'-exonuclease activity of the Taq polymerase. This will result in the separation of the reporter from the quencher and hence the release of an observable signal that is registered by the machine. The process will repeat with each amplification cycle until enough fluorescent signal has accumulated above the background (reaching a ct) or until the reaction is stopped if the target is not present.

To calculate the relative abundance of a detected DNA segment (e.g. relative fold expression of a gene), the $\Delta\Delta C_t$ method is applied. This method involves two normalization steps and depends on measuring the levels of a housekeeping gene. The first normalization step involves using the housekeeping gene as a reference to calculate the ΔC_t value:

$$\Delta C_t = C_t (\text{target gene}) - C_t (\text{housekeeping gene}).$$

The next step is to normalize the ΔC_t value to the control sample of the experiment. This will result in the $\Delta\Delta C_t$ value:

$$\Delta\Delta C_t = \Delta C_t (\text{treatment}) - \Delta C_t (\text{control}).$$

Finally, the resulting $\Delta\Delta C_t$ value can be fed into the following formula to calculate the fold change of a gene expression = $2^{(-\Delta\Delta C_t)}$

Another way of determining the expression of a specific gene can be done through absolute quantification against a standard curve derived from gel-purified RT-PCR products of the same genes RNA.

To set up a 10 μ l TaqMan qPCR reaction for one probe, the following components were added:

Component	Amount
TaqMan FAST 2x PCR Master Mix	5 μ l
TaqMan Assays on Demand	0.25 μ l

H ₂ O	3.75 µl
cDNA	1 µl

To set up a 10 µl SYBR green qPCR reaction for one gene, the following components were added:

Component	Amount
SYBR green 2x PCR Master Mix	5 µl
Forward primer (1:10 diluted)	0.5 µl
Reverse primer (1:10 diluted)	0.5 µl
H ₂ O	3 µl
cDNA	1 µl

The qPCR reaction was carried out on Applied Biosystems™ 7500 Fast Real-Time PCR Instrument as two technical duplicates for each sample on a 96-well plate with the following temperature settings:

Temperature	Time	
95°C	20 seconds	
95°C	3 seconds	} 40 cycles
60°C	30 seconds	

The last two steps were repeated for **40 cycles**.

3.2.5 Agarose gel

Resolving DNA molecules according to their size is made possible by using agarose gel. The principle behind this separation relies on an electric field that pushes the negatively charged DNA molecules through the matrix of the agarose gel towards the positively charged anode. Bigger DNA fragments will travel slower and hence stay in the upper part of the gel, while smaller fragments will travel faster, ending up in the lower part of the gel. Additionally, the confirmation of the DNA and the percentage of the agarose used in the gel play important roles in the separation process. An intercalating dye (such as ethidium bromide) can be added to the gel to visualize the DNA fragments migrating through the matrix using UV radiation excitation.

Throughout this study, agarose gel was used extensively to visualize or excise DNA fragments for further processing according to the following protocol: depending on the application (visualization vs excision and purification) a percentage of 1.5 or 2% (w/v) agarose gels were prepared by dissolving the appropriate amount of agarose in 1x TAE buffer. The mixture was then boiled for a very short time repeatedly until all the agarose particles were completely dissolved. The mixture was then allowed to cool down to a touch-possible temperature and 0.1 µg/ml ethidium bromide was added. This final mixture was then casted into an appropriate stand with a comb and left until it solidified. DNA samples mixed with 6x DNA Loading Dye were applied to the wells. The MUPID-exU submarine electrophoresis system was used to apply the current using 100 V for 30-45 minutes in 1x TAE running

buffer. Finally, the UV transilluminator Gel iX Imager was used to visualize the DNA fragments at 260 nm.

3.2.6 Molecular cloning

Molecular cloning is a process through which a DNA fragment (representing a gene of interest for example) is isolated or produced and then inserted (i.e. cloned) into an appropriate vector for a downstream application. In this work, molecular cloning has been extensively utilized to generate expression vectors to mediate CRISPR-CAS-9 knockdowns or to produce BioID vectors expressing chimeric constructs composed of a biotin ligase and a bait protein.

3.2.6.1 Producing CRISPR-CAS-9 vectors

The idea of the CRISPR-CAS system has been eloquently described in the following publication (Ran et al. 2013). Currently, there are multiple types of CRISPR-CAS systems. For the sake of space and relevance, only the CRISPR-CAS-9 system, which is a type II system, will be described based on Ran et al publication.

Faced with relentless invasions of bacteriophages, bacteria have evolved a mechanism to snatch parts of the genomic sequence of the invading pathogens. The snatched foreign DNA sequences are stored in a specific location in the bacterial chromosome called the CRISPR locus and used to recognize and fight re-infection.

The CRISPR locus consists of the foreign DNA sequences (called spacers) flanked by palindromic repeats, forming together a CRISPR array. Each of these spacers is always associated with a protospacer adjacent motif (PAM) that is found only in the genome of the pathogen (i.e. the bacterial CRISPR locus does not contain PAM). The spacer associated with PAM in the invading pathogen is called protospacer. The PAM sequences are recognized by the CRISPR-associated nuclease protein (CAS) enzymes. PAM sequences vary in requirements according to the specific CRISPR system. The CAS-9 enzyme from *Streptococcus Pyogenes* (used in this study) recognizes 5'-NGG PAM (N: any nucleotide) that has to be immediately next to the protospacer in the genome of the pathogen.

The CRISPR array is transcribed to form a pre-CRISPR RNA (crRNA) that pairs with the palindromic repeats and a tracrRNA (trans-activating CRISPR RNA, allows the association of the CAS enzyme) to form an effector complex. Upon a re-infection event with a pathogen whose part of its genome is already stored in the CRISPR array, the effector complex will scan the invader genome looking for the PAM sequence and the associated protospacer. When found, the crRNA will pair with the complementary section of the pathogen genome (i.e. complimentary to the spacer) and the CAS-9 enzyme will cleave the genome of the foreign invader 3 nucleotides upstream of the PAM sequence. Hence, the CRISPR-

CAS can be thought of, as an adaptive immunity mechanism that is used to protect against re-infection with foreign pathogens.

Given its potential, the CRISPR-CAS-9 system has been adapted/modified to be used as a guided/precise method for genome editing in eukaryotic cells. In this modified version, the crRNA and the tracrRNA were combined together into one chimeric RNA molecule termed single guide RNA (sgRNA). Within this sgRNA, a 20-nucleotide variable guide sequence that can be designed to target specific region of the genome in the immediate vicinity of a PAM sequence. This 20-nucleotide variable guide sequence is henceforward referred to as sgRNA for simplicity. In this study, sgRNAs were designed using either crispr.mit.edu (tool is deprecated), https://eu.idtdna.com/site/order/designtool/index/CRISPR_SEQUENCE or directly obtained from the published Genome-wide CRISPR screens library of sgRNAs from the Broad institute (Sanjana, Shalem, and Zhang 2014; Shalem et al. 2014). This sgRNA will guide CAS-9 protein to the intended area of interest in the genome. Once encountering the PAM sequence adjacent to the region complementary to the designed sgRNA sequence, the CAS-9 will induce a dsDNA break. In the absence of a repair template, this dsDNA break will induce a non-homologues end joining (NHEJ) DNA repair mechanism leading to insertion or deletion (indel) mutations disrupting the expression of the targeted gene. Hence, the corresponding protein product will either no longer be expressed or expressed in a mutated, non-functional form.

The sgRNAs targeting genes of interest (*EIF2AK3*, *ERN1* and *ATF3*, sequences in the Materials section) were cloned into the compatible pSpCas9(BB)-2A-Puro (pX459) vector. This vector contains the chimeric RNA sequence and CAS-9 gene. After designing the sgRNAs as mentioned above with recognition site for the restriction enzyme BbsI (CACCG) added to them (for insertion in the pX459 vector), they were ordered from Eurofins Genomics as both, sense and antisense strands. The received oligonucleotides were re-suspended in water to a final concentration of 100 μ M and then annealed together to produce double-stranded oligonucleotides as follows:

Component	Amount
sgRNA sense (100 μ M)	1 μ l
sgRNA antisense (100 μ M)	1 μ l
T4 PNK Buffer A (10x)	5 μ l
ddH ₂ O	43 μ l

The following temperature settings were used to carry out the reaction on the Thermocycler T-Professional:

Temperature	Time
95°C	4 minutes
70°C	10 minutes
37°C	15 minutes
4°C	PAUSE

The annealed oligonucleotides were then phosphorylated as follows:

Component	Amount
Annealed oligonucleotides	2 μ l
T4 PNK (polynucleotide kinase) Buffer A (10x)	1 μ l
1 mM ATP (10 mM)	1 μ l
T4 PNK	1 μ l
ddH ₂ O	5 μ l

The following temperature settings were used to carry out the reaction on the Thermocycler T-Professional:

Temperature	Time
37°C	30 minutes
70°C	10 minutes (heat inactivation of T4 PNK enzyme)
4°C	PAUSE

The annealed and phosphorylated oligonucleotides are now ready for the simultaneous restriction enzyme digestion and ligation into the vector as follows:

First, the oligonucleotides from the previous step were 1:8 diluted

Component	Amount
Diluted oligonucleotides	2 μ l
Vector	100 ng
Fast digest buffer 10x	2 μ l
Fast digest Bbs1	1 μ l
ATP (10 mM)	1 μ l
T4 ligase	1 μ l
ddH ₂ O	Adjusted to 20 μ l

The following temperature settings were used to carry out the reaction on the Thermocycler T-Professional:

Temperature	Time	
37°C	5 minutes	} 6 cycles
21°C	10 minutes	

Repeated for **6 cycles**.

Finally, any residual, linearized DNA was digested using PlasmidSafe exonuclease as follows:

Component	Amount
The ligation reaction from the previous step	10 μ l
PlasmidSafe buffer (10X)	1.5 μ l
ATP (10 mM)	1.5 μ l
PlasmidSafe exonuclease (10 U/ μ l)	1 μ l

The following temperature settings were used to carry out the reaction on the Thermocycler T-Professional:

Temperature	Time
37°C	30 minutes
70°C	30 minutes

The reaction was then used for bacterial transformation immediately or stored at -20 °C for later usage.

Alternatively the sgRNAs targeting ATF3 were cloned into the compatible Lenti-CRISPR V2 empty vector using the same procedure described above with the following exceptions:

- 1) The restriction enzyme used was Esp3I (10 U/ μ l).
- 2) The PlasmidSafe step was not included as including this treatment resulted in no colonies.

3.2.6.2 Producing the BioID vectors

The BioID method depends on producing vectors expressing chimeric constructs composed of a biotin ligase and a bait protein. Hence, the first step included obtaining DNA fragment of gene of interest flanked with appropriate restriction enzyme sites to be inserted into the BioID vector of choice, pTet-on_Puro_Myc-BirA or pTet-on_Puro_HA-miniTurbo.

To obtain DNA of gene of interest from a donor plasmid, PCR-cloning approach was implemented using set of primers (forward and reverse) that amplifies the whole cDNA of the gene. The primers contained the following components based on protocol provided on <https://www.addgene.org/protocols/pcr-cloning/>:

1. Leader Sequence: 3 to 6 extra base pair (bp). This additional bps were proven to improve restriction enzymes digestion.
2. Restriction enzyme sequence: sequence representing the selected appropriate restriction enzymes. Usually (6-8 bp)
3. The Hybridization Sequence: sequence that binds to the DNA of interest. Usually 18-21 bp.

The selection of appropriate restriction enzymes rests on multiple criteria including:

1. Enzymes that do not cut within the fragment of interest.
2. Enzymes that do cut in the Multiple Cloning Site (MCS) of the recipient plasmid, but do not outside this region.
3. Have appropriate and compatible temperatures and buffers.

The primers were then order from Eurofins Genomics and were re-suspended in water to a final concentration of 100 μ M. The following PCR reaction was set up to obtain the DNA fragments from the donor plasmids:

Component	Amount
Phusion Buffer (5x)	10 μ l
Forward primer (1:25 diluted)	1 μ l
Reverse primer (1:25 diluted)	1 μ l
dNTPs (10 mM each)	1 μ l
Donor plasmid	40 ng
Phusion Polymerase	0.5 μ l
DMSO	2.5 μ l (5%)
ddH ₂ O	Adjusted to 50 μ l

The following temperature settings were used to carry out the reaction on the Thermocycler T-Professional:

Temperature	Time	
95°C	Lid temperature	
98°C	30 seconds	
98°C	10 seconds	} 30 cycles
60°C	30 seconds	
72°C	30 seconds/ kilo-base the of total plasmid length	
72°C	5 minutes	
4°C	PAUSE	

The PCR product is now the DNA fragment of interest flanked by selected restriction enzyme sites. This product is then purified using NucleoSpin® Gel and PCR Clean-up Kit according to the manufacturer's protocol.

Next the PCR fragment and the recipient plasmid were digested by the selected restriction enzymes as follows:

Construct	Restriction Enzyme 1	Restriction Enzyme 2	Buffer	Temperatures	PCR product amount	Recipient plasmid amount
BirA- <i>EIF2AK3</i>	3 μ l EcoRI	3 μ l XhoI	12 μ l 10x Tango Buffer	1h 37°C 20 min 80 °C	15 μ l PCR reaction	4 μ g Plasmid DNA
BirA- <i>ERN1</i>	3 μ l EcoRI	3 μ l XhoI	12 μ l 10x Tango Buffer	1h 37°C 20 min 80 °C	15 μ l PCR reaction	4 μ g Plasmid DNA
BirA- <i>Bip</i>	3 μ l BspOI (BmtI)	3 μ l XhoI	6 μ l R Buffer	1h 37°C 20 min 80 °C	25 μ l PCR reaction	4 μ g Plasmid DNA
BirA- <i>ATF3</i>	3 μ l EcoRI	3 μ l XhoI	12 μ l 10x Tango Buffer	1h 37°C 20 min 80 °C	15 μ l PCR reaction	4 μ g Plasmid DNA
miniTurbo- <i>EIF2AK3</i>	3 μ l EcoRI	3 μ l XhoI	12 μ l 10x Tango Buffer	1h 37°C 20 min 80 °C	15 μ l PCR reaction	4 μ g Plasmid DNA
miniTurbo- <i>ATF3</i>	3 μ l EcoRI	3 μ l NotI	6 μ l 10x O Buffer	1h 37°C 20 min 80 °C	25 μ l PCR reaction	4 μ g Plasmid DNA

All enzymes had 10 U/ μ l except XhoI FastDigest ThermoFisher (see manufacturer instructions).

After the digestion of the recipient plasmid, it was gel-purified using NucleoSpin® Gel and PCR Clean-up Kit according to the manufacturer's protocol.

The gel-purified, digested plasmid was then subjected to a dephosphorylation reaction (to prevent re-ligation) as follows:

Component	Amount
10x Buffer O	4 µl
CIAP (20 U/µl)	1 µl
DNA Digested Plasmid	10 µl
ddH ₂ O	Adjusted to 25 µl

The following temperature settings were used to carry out the reaction on the Thermocycler T-Professional:

Temperature	Time
37°C	30 minutes
85°C	15 minutes

The dephosphorylated-digested recipient plasmid was then purified using NucleoSpin® Gel and PCR Clean-up Kit according to the manufacturer's protocol.

The final step was the ligation of the PCR fragment into the plasmid as follows:

Ligation:

Ratio of insert to vector: 1:5 or 1:3

$$\text{ng (Insert)} = \text{Factor} \times \text{ng(Vector)} \times [\text{bp(Insert)} / \text{bp(vector)}]$$

$$= \text{Factor} \times 50 \times (560/9500) \dots \dots (\text{example for } ATF3 \text{ insert into the miniTurbo plasmid})$$

Ratio	Components
1:5	50 ng Vector 15 ng Insert 2µl 10x Ligase Buffer 1µl 10mM ATP 1µl T4 DNA Ligase ddH ₂ O adjusted to 20µl
1:3	50 ng Vector 9 ng Insert 2µl 10x Ligase Buffer 1µl 10mM ATP 1µl T4 DNA Ligase ddH ₂ O adjusted to 20µl

The reaction was left for 2 hours at room temperature followed by 20 minutes at 70°C for inactivation of the ligase.

3.2.7 Sanger sequencing

To control for the correct insertion of oligonucleotides or PCR fragments into plasmids, Sanger sequencing was carried out using the services provided by LGC Genomics or Microsynth. The instructions of the companies were followed exactly regarding plasmid concentrations, volumes, sequencing primers requirements and used buffers for elution. The DNASTAR software (SeqMan Pro) and Chromos were then used to assess the sequencing quality and results.

3.3 Microbiology

3.3.1 Bacterial work

Expression vectors were amplified using chemically competent *E. coli* TOP10, XL1-Blue and TOP10 One Shot strains through transforming them as follows:

2-5 µl of the plasmid or ligation product (after cloning process) were added to the bacterial vial. The mixture was incubated on ice for 5 minutes followed by a heat shock at 42°C for 45 seconds followed immediately by 2 minutes on-ice incubation. Next, the following procedure was done:

For *E. coli* TOP10 or XL1-Blue strains, 500 µl of LB medium was added and the mixture was incubated further for 1 hour at 37 °C with 200 RPM shaking. Afterward, the mixture was centrifuged at 2500 RPM (Table-centrifuge 5424) for 5 minutes. The supernatant was discarded, except for approximately 20 µl that was used to re-suspend the bacterial pellet. The re-suspended bacterial pellet was then plated on LB-plate with antibiotic marker (ampicillin 100 µg/ml) and allowed to grow overnight at 37°C.

For TOP10 One Shot strain, 200 µl of SOC medium at room temperature was added, very gently mixed and then 100 µl was plated on LB-plate with antibiotic marker (ampicillin 100 µg/ml) and allowed to grow overnight at 37°C.

Growing the bacteria in liquid LB-medium was carried out using volumes of 5 ml or 200 mL of LB medium with suitable antibiotic marker. The bacteria were allowed to grow overnight at 37°C with continuous shaking at 200-250 RPM.

The long-term storage of liquid bacterial culture was carried out by adding an equal amount of Glycerol to the bacterial medium followed by immediate freezing using liquid nitrogen and then stored at -80°C.

3.3.2 Virus work

3.3.2.1 HCoV-229E propagation

Producing stocks of HCoV-229E was carried out as follows: 2.8×10^7 Huh7 cells were seeded into T145 dishes. 24 hours later the cells were transferred in an incubator adjusted to 33°C half an hour before the addition of 100 µl of a previous virus stock. The cells infected with the virus were then further incubated at 33°C for two more days, until cytopathic effects were observable. The medium was then collected and centrifuged for 10 minutes at 500 RPM (4°C, TJ-25 centrifuge). The supernatant, representing the new virus stock, was then aliquoted as desired and stored at -80°C. The titer of this new stock was then determined using TCID₅₀ or plaque assays.

3.3.2.2 Determining virus titer using TCID₅₀

Determining the functional titer (i.e. actual number of viruses that are able to infect target cells) is an essential part of any work that involves studying viruses. In this study, TCID₅₀ (median tissue culture infectious dose) was one of the methods used to assess the functional titer. The assay relies on creating a serial dilution of the virus sample and infecting target cells seeded in 96-well-plate with these dilutions. The target cell should be known to show observable cytopathic effect (CPE) after a certain incubation period with the virus of interest. At the end of this incubation time, CPE in each well are assessed using variety of methods including staining the cells for direct visual readout of dead cells. The TCID₅₀ of the sample can be then calculated using the dilution in which 50% of the wells displayed visible CPE. The calculation is carried out using different mathematical approaches including Reed and Muench method (REED and MUENCH 1938, 12; LaBarre and Lowy 2001; Smither et al. 2013).

The TCID₅₀ assay for HCoV-229E was carried as follows:

Three 96-well plates (for three technical replicas) were seeded with 12000 Huh7 cells per well and allowed to grow for 24 hours before infection with the virus serial dilution. Each well contained 100 µl of full DMEM medium. The HCoV-229E serial dilution used was from 10^2 up to 10^8 . One row of each plate was left without infection (or mock infection) as control. Each row of wells received 100 µl from specific dilution (added to each well in the row). The plates were then incubated at 33°C for 6 days. At the end of the incubation period supernatant was removed from the wells and 100 µl of 0.1% crystal violet dye (diluted from 1% stock beforehand in 20% ethanol solution) was added to each well and incubated for few minutes. Subsequently, the dye was decanted by tabbing the plates carefully inside a plastic bag. The stained wells (i.e. alive cells) and the unstained wells (i.e. dead cells) were counted. Providing that all wells in the control row survived (i.e. were stained) the TCID₅₀ was then calculated for each plate using Reed–Muench method (REED and MUENCH 1938; LaBarre and Lowy 2001).

The Reed–Muench calculation method goes as follow (C. Lei et al. 2021; Ramakrishnan 2016):

The ideal case would be to have a row (representing a dilution) that has exactly 50% of the wells stained and the other 50% unstained. Nevertheless, this is a very rare occurrence and hence, the so-called proportional distance (PD) to 50% has to be calculated according to the following formula:

$$PD = \frac{(\text{the percentage of dead cells directly above 50\%}) - 50\%}{\{(\text{the percentage of dead cells directly above 50\%}) - (\text{the percentage of dead cells directly below 50\%})\}}$$

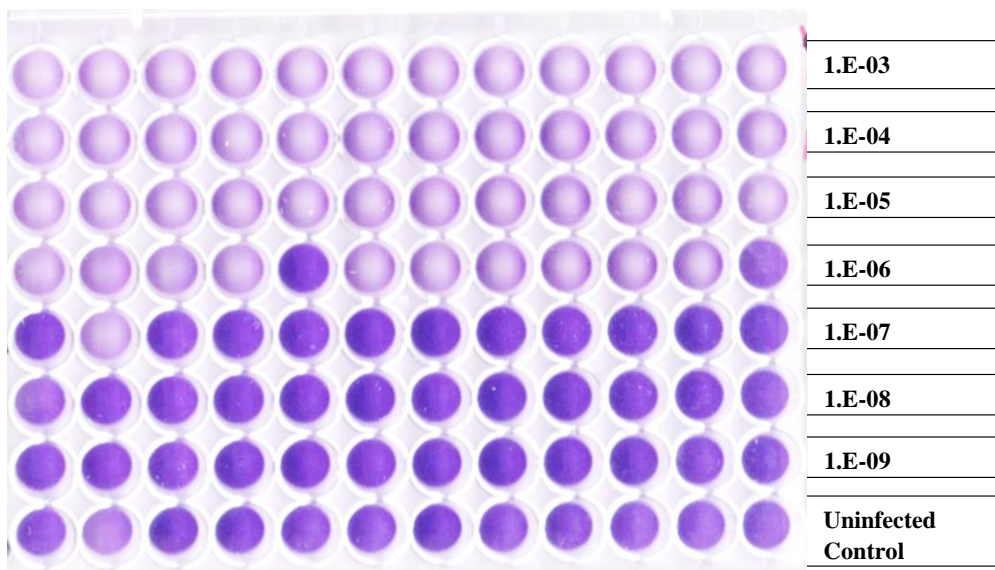
Next, the 50% endpoint dilution (Log lower dilution) should be calculated as follows:

$$\text{Log lower dilution} = \log (\text{the dilution in which the percentage of dead cells directly above 50\%})$$

Next, the PD value should be added to the Log lower dilution and expressed as $10^{(PD + \text{Log lower dilution})}$. This number is the TCID₅₀ of the sample.

The TCID₅₀ is then expressed per ml. This can be done through dividing it by the ml of virus added to the rows (100 µl in this case) to obtain TCID₅₀/ml.

Finally, one can convert this value to MOI (multiplicity of infection) through assuming that 3 TCID₅₀ corresponds to an MOI of 1 (LaBarre and Lowy 2001). Hence, an MOI of one means that theoretically one cell receives one infectious virus. Following is an illustrative example (Fig.7):



Virus Dilution	Died	Survived	Mortality per cent
1.E-03	12	0	100
1.E-04	12	0	100
1.E-05	12	0	100
1.E-06	10	2	83.33
1.E-07	1	11	8.33
1.E-08	0	12	0
1.E-09	0	12	0

Figure 7: An illustrative example taken from this study of the TCID₅₀ calculations using the Reed–Muench method.

See text above for details.

Alternatively, one can use plaque assay to determine MOI directly.

3.3.2.3 Determining virus titer using plaque assay

This assay relies on creating a serial dilution of the virus sample and infecting target cells seeded in, typically, 6-well-plate with these dilutions. The target cells are seeded in appropriate numbers to form a monolayer. The idea behind this method is to allow an infectious particle to infect a cell in the cell monolayer. This infection event will cause the cell to die and produce more infectious particles that would infect nearby cells, eventually (after appropriate incubation period) producing a visible hole (plaque) in the cell monolayer. To ensure a localized area of infection (where the plaque will form) and to prevent the virus from spreading outside this area, a semi-solid overlay is added to the cell monolayer. After an appropriate incubation period, the cell monolayer is then stained to visualize and count the plaques. The obtained number of plaques for each dilution (in each well) is then divided by that dilution to obtain plaque forming units (pfu)/Well. This number is then averaged across the different dilutions and divided by the added volume of virus dilution to obtain the sample titer expressed in pfu/ml (Smither et al. 2013; Baer and Kehn-Hall 2014). An illustrative example of these calculations has been delineated in figure 8.

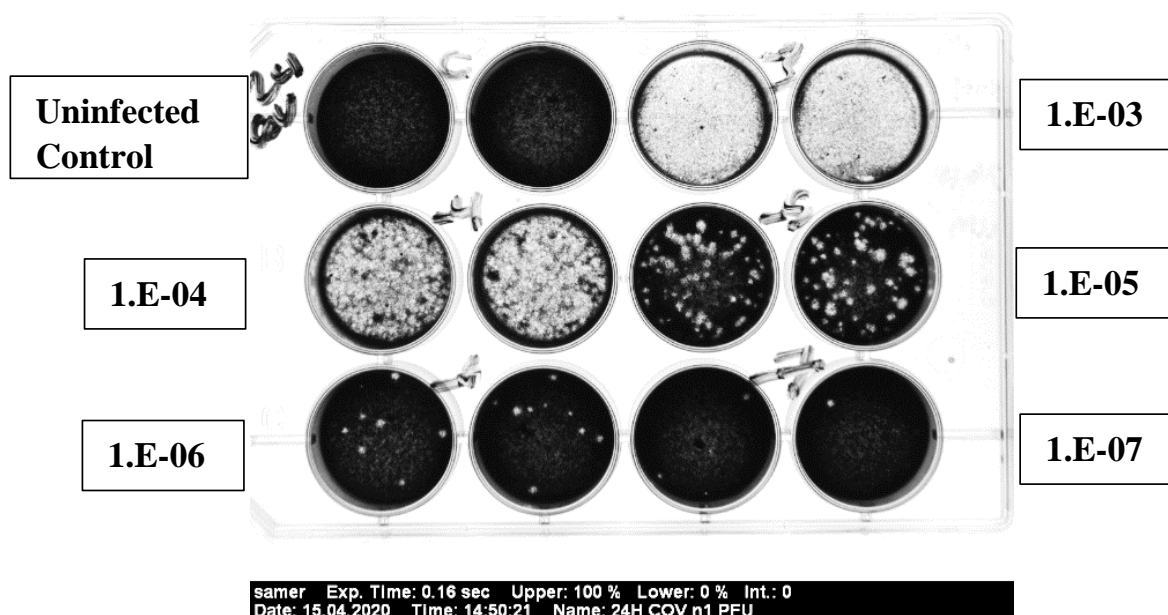
The plaque assay for HCoV-229E was carried out as follows:

6-well plate were seeded with 200,000 Huh7 cells per well and allowed to grow for 24 hours before infection with the virus serial dilution. The virus serial dilution used was from 10² up to 10⁸. The assay was carried out as two technical duplicate where two wells were infected with the same dilution. The first two wells were used as control (mock infection). Each well received 500 µl from specific dilution. The plates were incubated for one hour at 33°C. The supernatant was then removed and the wells were coated by the 1.25% semi-solid Avicel® mixed with MEM medium (100 U/ml penicillin, 100 µg/ml streptomycin, and 10% FBS) and incubated at 33°C for 3 days. At the end of the incubation period, Avicel®/MEM overlay was very carefully removed. The wells were then incubated for few minutes with 500 µl of 0.1% crystal violet dye (diluted from 1% stock beforehand in 20% ethanol solution) for staining. Subsequently, the dye was decanted and plaques were counted and documented.

The plaque assays for MERS-CoV and SARS-CoV-2 were carried out by Dr. Christin Mueller in the BSL 3 facility as follows:

Huh7 cells and VERO-E6 cells were used to titer MERS-CoV and SARS-CoV-2 respectively. The cells monolayers were then infected with virus serial dilution from 10¹ up to 10⁷. Dishes were then incubated at 33 °C for SARS-CoV-2 and at 37 °C for MERS-CoV for one hour. The supernatant was

then removed and the wells were coated with MEM medium containing 1.25% Avicel® (100 U/ml penicillin, 100 µg/ml streptomycin, and 10% FBS). At the end of the incubation period (2 days for MERS-CoV and 3 days for SARS-CoV-2), Avicel®/MEM overlay was discarded and the cells were washed with PBS and fixed in freshly prepared 3.7% PFA in PBS overnight. After the removal of the fixing solution next day, the cells were washed again with PBS and stained with 0.15% (w/v) crystal violet (diluted in 20% Ethanol). Plaques were documented and counted.



Virus Dilution	Plaques # Well-1	Plaques # Well-2	Average plaques #	pfu/well
1.E-03	All dead	All dead	-	-
1.E-04	All dead	All dead	-	-
1.E-05	48	46	47	5E+06
1.E-06	7	9	8	8E+06
1.E-07	No plaques	No plaques	-	-

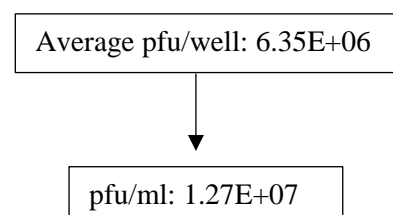


Figure 8: An illustrative example taken from this study of the MOI calculations using plaque assay. See text above for details.

For all viruses, the plaque numbers were used to calculate the EC₅₀ values, referenced to the virus + DMSO-only treated control, using non-linear regression method on GraphPadPrism 5.0 or 8.4.3 (GraphPad Software).

3.3.2.4 Working with lenti-virus

The lenti viral titer, used as a viral delivery system to transduce Huh7 cells with CRISPR-CAS-9 system, was determined together with B.Vincent Albert as follows:

6-well plates were seeded with 3×10^6 Huh7 cells. Each well had 3 ml full DMEM medium with 8 μg /ml of polybrene (to increase the efficiency of transduction). In each well, the following amount of lenti-virus-containing supernatant was added: 1 ml, 750 μl , 600 μl , 500 μl , 250 μl , 100 μl , 50 μl , 25 μl , or 0 μl . The content of each well was then thoroughly mixed by pipetting up and down. The plates were then centrifuged at 1000 RPM for 90 min at 33 °C (so called spinfection) and then incubated for further 24 hours. Thereafter, the medium was removed, cells were very gently washed with 400 μl TrypLE™ Express Enzyme per well. Next, 100 μl of TrypLE™ was added to each well and incubated at 37 °C for 5 min to detach the cells. The cells were then re-suspended by adding 2 ml of full DMEM medium per well with pipetting up and down. Cells in all conditions grew to the same level of confluency and hence the cell concentration for only the 0 μl lenti-virus supernatant condition was then determined. For each of the other lenti-virus supernatant conditions, 4 wells of a 96-well clear bottom black tissue culture plate were seeded with 4×10^3 of the transduced Huh7 cells (i.e. four wells for one transduction condition). 100 μl of full DMEM medium was used for the seeding. An additional 100 μl of DMEM medium with the corresponding selection antibiotic (puromycin 1 μg /ml) for the virus at an appropriate final concentration was added to 2 wells and 100 μl of regular DMEM medium to the other 2 wells. After 72–96 h, mock-infected cells should be all dead and cells incubated with no antibiotic should reach confluency of 80 to 90%. When this was the case, the cell viability for the rest of the conditions were quantified using CellTiter-Glo Luminescent Cell Viability Assay according to the manufacturer's protocol. This assay quantifies the presence of ATP and uses it as a proxy for metabolically active (alive) cells. The MOI was then calculated as the average luminescence, representing cell viability, of the 2 wells containing antibiotic marker divided by the average luminescence of the 2 wells without antibiotic. This resulted in a linear relationship between the added volume of the lenti-virus supernatant and the MOI at lower volumes and saturation at higher volumes.

3.3.2 Testing for mycoplasma

Mycoplasmas are type of bacteria that lack a cell wall. They are part of Mollicutes class and are the smallest known self-replicating organisms (Drexler and Uphoff 2002). Contamination with Mycoplasmas is a wide spread issue that can compromise the integrity of any experiment that involves eukaryotic cell culture (Drexler and Uphoff 2002). Hence, it was very important to control for Mycoplasmas contamination regularly and before embarking on large or small-scale experiments throughout this study. For this purpose, the PCR-Test kit A3744 from AppliChem was used to test the supernatant of cultured cells reaching confluency of about 90% for any contamination with Mycoplasmas. The tests were carried out regularly in collaboration with the technician Petra Kronich from the Kracht working group in accordance with the kit provider protocol.

3.4 Biochemistry

Several biochemical methods have been utilized in this study mainly to investigate proteins levels, interactions or translation rate. In all cases, the first step was harvesting and lysing the cells.

3.4.1 Lysing the cells

Cells were lysed in different lysis buffers using different procedures depending on the sample and the downstream application. In this section, focus will be on lysing procedures for Western blotting while for other downstream applications (such as BioID), the lysing procedures are delineated in the corresponding sections.

After harvesting the cells, the pellets were re-suspended in an appropriate amount (based on the pellet size, usually a pellet to buffer ratio of 1:50) of the Triton-based lysis buffer (called special-lysis buffer in the lab). The cells were then incubated on ice for 15 minutes followed by centrifugation for 15 minutes at 10000 RPM, 4°C. The “Table-centrifuge 5415 R” was used in this and in the following steps unless otherwise stated. The supernatant after the centrifugation step was then transferred to new tubes and the concentrations of the proteins were determined using Bradford assay.

Alternatively, cells were also lysed using SDS-buffer as follows: cell pellets were re-suspended in 90 μ l of ice-cold $\text{Ca}^{2+}/\text{Mg}^{2+}$ -free PBS and transferred to fresh tubes. Afterward, 10 μ l of 10% SDS buffer was added to the samples. Subsequently, the samples were heated for 10 min at 100 °C followed by centrifugation at 600 RPM for 1 min at room temperature. Supernatants were then transferred to new tubes and heated again for 10 min at 100 °C followed by centrifugation at 600 RPM for 1 min at room temperature.

Cells infected with either MERS or SARS-CoV-2 were lysed using the SDS-buffer as indicated above at BSL 3 facility by Dr. Christin Mueller.

3.4.2 Bradford assay

The Bradford assay is a colorimetric protein assay that is used frequently to determine protein concentration in a sample. The principle of the method relies on the dye Coomassie brilliant blue G-250 changing absorbance from 465 to 595 nm upon binding to limited number of amino acids (namely phenylalanine, lysine, histidine, arginine, tryptophan, and tyrosine) of proteins in the sample (Brunelle et al. 2017). A change in color from red to blue can be observed and the optical density can be quantified. The binding of the dye to proteins is fast and the color change is stable for about an hour (Bradford 1976).

The assay was carried out for samples lysed with special-lysis buffer as follows: cell lysates were diluted 1:300 in PBS. BSA standard series in PBS with the following concentrations were already prepared: 0 µg/ml, 5 µg/ml, 10 µg/ml, 15 µg/ml, 20 µg/ml, 25 µg/ml, 30 µg/ml, 35 µg/ml. Next, 100 µl from the diluted samples and the standards were pipetted into a 96-well plate as a technical triplicate or duplicate. Additional 100 µl of 40% Roti-Quant staining solution diluted in water was subsequently added to the unknown samples and to the standards. Microplate Spectrophotometer reader was used to measure the optical density at 595 nm of all samples and protein concentrations were calculated using the standards concentrations fitted to a linear curve.

For samples lysed with SDS buffer, the assay was carried out as follows: cell lysates were diluted 1:150 in PBS. Same BSA standard concentrations as explained above were used and 100 µl from the diluted samples and the standards were pipetted into a 96-well plate as a technical triplicate or duplicate. 100 µl of Pierce™ Detergent Compatible Bradford was added to the unknown samples and to the standards. A Microplate Spectrophotometer reader was used to measure the optical density at 595 nm of all samples and protein concentrations were calculated using the standards concentrations fitted to a quadratic curve.

3.4.3 SDS-PAGE

Sodium dodecyl sulfate–polyacrylamide gel electrophoresis (SDS-PAGE) is an electrophoretic method that was developed by Laemmli (Laemmli 1970). The method is used to separate proteins based on their molecular weights through eliminating the influence of the protein structure and differences in total charge. The SDS (which is a detergent) binding to proteins hydrophobic regions promotes their denaturation and the establishment of a uniform overall net negative charge causing the proteins to migrate toward the positive terminal of the electrical chamber, the anode, when subjected to electrical field. Hence, the migration of the proteins will be solely based on their molecular weights. The polyacrylamide (polymerized acrylamide, gel) forms a mesh-like matrix through which proteins of different sizes migrate.

The gels used in this study were prepared shortly before loading the samples and consisted of two parts: a stacking gel and a separating gel. The stacking gel had a constant acrylamide concentration of 5% while that of the separating gel varied (7-12%) according to the investigated proteins molecular weights or specific research question. The following table shows the recipes to make 5 ml stacking gel and 27 ml separating gel with an acrylamide concentration of 10% (used very frequently in this study):

Components	stacking gel (5% acrylamide; 5 ml)	Separating Gel (10% acrylamide; 27 ml)
Stacking gel buffer	0.63ml	-
Separating Gel Buffer	-	10.3ml
Rotiphoresis Gel 30	0.84ml	9ml
Glycerol 50% (v/v)	0.45ml	2.4ml
SDS 2% (w/v)	0.25ml	1.35ml

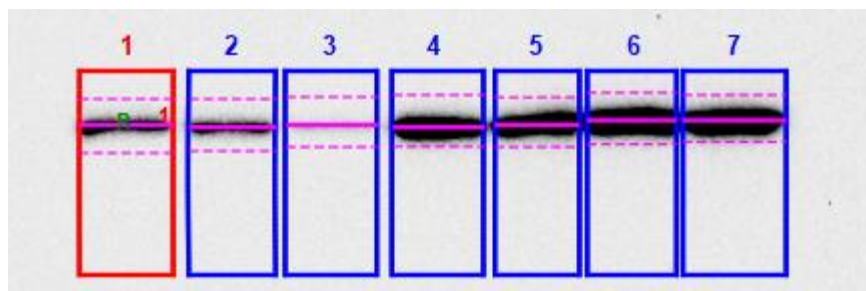
Water	2.8ml	3.8ml
APS 40% (w/v)	15 μ l	41 μ l
TEMED	10 μ l	27 μ l

The separating gel was then casted and allowed to solidify. Subsequently the stacking gel was poured and a comb with appropriate well numbers was inserted into it until it solidified. The comb was removed and the protein samples were mixed with ROTI®Load 1 (4 times concentrated) and then heated at 95°C for 10 min. After loading the samples and the PageRuler™ prestained protein ladder, the electrophoresis was then carried out in 1x Laemmli running buffer with constant current values of 35 to 50 mA per gel.

3.4.4 Semi-dry Western blotting

After separating proteins in a sample based on their molecular weights using SDS-PAGE, detecting a particular protein of interest (or a post-translation modification of that protein) can be carried out using Western blotting followed by incubation with specific antibodies that allow detection based on enhanced chemiluminescence light reaction (ECL). The method goes as follows: the SDS-PAGE gel containing separated proteins was stacked together with a PVDF (polyvinylidene fluoride) membrane and four filter papers soaked in 1x blotting buffer. The order of the components of this “sandwich” is very important and should be as follows (top to bottom): two filter papers, the gel, the PVDF membrane, and two filter papers. With this exact order, the “sandwich” was then placed on the positive terminal of the transfer chamber to allow the negatively charged proteins to migrate out of the gel to the PVDF membrane towards the plus pole. The transfer was then allowed to proceed for 2 hours 15 minutes at a constant current of 0.75 mA per cm² of the membrane. After the end of the transfer, the proteins on the PVDF membrane were stained with Ponceau S to control/troubleshoot any possible technical failures of the transfer process. The stained membrane was then documented and subsequently de-stained using TBS-T buffer. In order to block the non-specific binding sites on the membrane, it was incubated with 5% (w/v) skimmed milk powder dissolved in TBS-T buffer (blocking buffer) for 1 hour at room temperature. Afterward, the blocking solution was discarded and primary antibodies targeting protein of interest diluted according to providers’ instructions was added to the membrane and incubated overnight at 4°C. The next day, the primary antibody solution was subsequently collected to be re-used again and the membrane was washed four times with TBS-T buffer with 5 minutes shaking period in-between washes to remove any free unbound antibodies. Then, an incubation period of 2 hours at room temperature of the membrane with horseradish peroxidase (HRP)-coupled secondary antibodies at a dilution of 1:2500 in 5% (w/v) milk powder dissolved in TBS-T buffer was performed. Afterwards, the membrane was washed again as described above four times. Finally, the membrane was incubated with Amersham ECL Western Blotting Detection Reagent or Immobilon Western Chemiluminescent HRP substrates according to the manufacturer's instructions to detect the chemiluminescence signal of the secondary antibodies using the ChemiDoc™ Touch Imaging System. All incubation periods mentioned above were

done with continuous shaking. Protein bands were then quantified using ImageLab software as illustrated in the following example (Fig. 9):



Lane	Band No.	Relative Front	Adj. Volume (Int)	Volume (Int)	Relative quantification (using Adj. Volume)	Band %	Lane %
1	1	0.264368	610080	1418520	1	100	94.241226
2	1	0.275862	498464	1216486	0.817047	100	94.157115
3	1	0.264368	128193	879216	0.210125	100	78.900624
4	1	0.275862	1566903	2338323	2.568357	100	97.304432
5	1	0.264368	1546416	2269728	2.534776	100	96.732497
6	1	0.241379	2549154	3322910	4.178393	100	97.674723
7	1	0.241379	2334376	3157748	3.826344	100	97.223698

Figure 9: An illustrative example taken from this study of quantifying protein bands using ImageLab software.

Number of lanes (blue boxes) and bands (vertical violet lines) were determined/selected manually. Bands boundaries (discontinuous, vertical violet lines) were adjusted to be as comparable (covering the same area) as possible between different conditions. A reference band was then selected (usually the untreated or otherwise stated, indicated here by R and red box). Thereafter, the software will generate the table shown below.

3.4.4 BioID

The protocol for the BioID experiments (miniTurbo or BirA constructs) goes as follows:

Huh7 cells were seeded into appropriate dish sizes using tetracycline-free medium to prevent unwanted activation of the tet-on system controlling the expression of the constructs. The number of cells used (and hence dish sizes) depended on the downstream application; 3×10^6 Cells in T145 dishes for pulling down biotinylated proteins and mass spectrometry, and 3×10^5 in 60 mm dishes for whole-cell extracts investigation on Western blot. Cells were allowed to grow for 24 hours and then transfected with the miniTurbo or BirA constructs using calcium phosphate (CaCl_2) method as previously delineated. After the transfection procedure, cells were then treated with doxycycline to induce the tet-on with final concentrations as indicated in the results section. $50 \mu\text{M}$ of exogenous biotin was added to experimental conditions as indicated. Dishes were then incubated at 33°C or at 37°C for further 24 hours. For BioID experiments that involved virus infection, the dishes were incubated at 33°C for half an hour after the addition of doxycycline and biotin. Thereafter, cells were infected with HCoV-229E (MOI of 1) and incubated for further 24 hours. Cells from dishes used only to obtain whole-cell extracts for western blot

analysis were harvested, lysed using BioID lysis buffer and subjected to Western blotting as previously delineated.

Cells from dishes used for pulling down biotinylated proteins (and subsequent mass spectrometry analysis) were washed twice with ice-cold PBS after the removal of the medium. The cells were then harvested by scraping them in 10 ml of ice-cold PBS followed by 5 minutes, 4°C centrifugation at 900 RPM (Table-centrifuge 5415 R, for the following steps as well). The PBS was then removed and cells were re-suspend in 475 µl 50 mM Tris (pH 7.5/HCl) and 50 µl 10% Triton X-100. The cells resuspensions were then transferred to either 15 ml sonication tube or 1.5 ml sonication Eppendorf tubes. To each cell resuspension, 250 µl of room temperature BioID lysis buffer was added and the mixture was incubated on ice for 10 minutes. To reduce the viscosity, samples were sonicated at 4°C using Bioruptor machine with the following power settings: three cycles, ON: 30 sec, OFF: 30 sec, power high. The samples were then centrifuged at 16000 RPM for 15 minutes at 4°C to obtain cell lysates. 1% of the cell lysates was saved to test on Western blotting. Next, the affinity purification of biotinylated proteins was carried out as follows: 30 µl streptavidin agarose beads were added to 1.5 ml tubes filled with 1 ml of BioID lysis buffer. The beads were then centrifuged at 1000 RPM for 2 minutes at room temperature. The supernatant was then carefully removed without disturbing the beads and 30 µl of the BioID lysis buffer was added to each tube. Afterward, 700 µl of cell lysates were added to the beads and the mixture was incubated overnight at 4°C with continuous rotation. The next day, beads + lysates mixture was centrifuged at 1000 RPM for 2 minutes at room temperature. 1% of the supernatant was saved to test for unbound biotinylated proteins on Western blotting. The beads were then washed by adding 500 µl of the following wash buffers (see Materials for recipes):

Washing buffer	Times	Temperature
Wash Buffer I	1	Room temperature
Wash Buffer II	2	4°C
Wash Buffer III	2	4°C
Wash Buffer IV	1	4°C

In-between the washing steps, centrifuging at 1000 RPM for 2 minutes and the removal of the supernatant of the previous wash was carried out. After the last washing step, the beads were re-suspended in 1 ml of Wash Buffer V at 4°C. 20% of beads were transferred to fresh tubes for western blotting or sliver staining while the remaining 80% were sent mass spectrometry. For Western blotting or sliver staining, the supernatant was removed by 2 minutes of centrifugation at 1000 RPM, 4°C. The proteins were eluted through adding 30 µl of ROTI@Load 1 (2 times concentrated) followed by heating the samples at 95 °C for 10 minutes.

3.4.5 Silver staining

The silver staining of gels after SDS-PAGE to visualize the amount of proteins, especially in a pulldown experiment, was carried out as follows: After the completion of the SDS-PAGE run, the gel was incubated in the fixing solution (see Materials for recipes), overnight at 4°C with continuous shaking. Next day, the fixing solution was discarded and the gel was washed 4 times with water. Afterward, the gel was incubated with incubation solution for 1 hour followed by 6 times washing with water. Each of the washing steps mentioned above were done for 10 minutes with shaking at room temperature. The gel was then incubated with the staining solution for 1 hour followed by 2 times washing with water for 1 minute each time. The developer solution was then added to the gel and the progress of the staining (appearance of bands and their intensities) was monitored. The process was stopped when the bands intensities reached a good visible level by adding the stop solution. The stained gel was then documented and stored in 1% acetic acid solution at 4°C, away from light or discarded.

3.4.6 L-HPG labelling using click chemistry

The labelling of nascent polypeptide chains with L-HPG using click chemistry was done as follows: 3×10^6 cells were seeded in T145 dishes. The cells were allowed to grow for 24 hours at 37 °C and then infected/treated as described for further 24 hours at 33°C. At 2.5 hours before the end of the 24 hours infection/treatment period, cells were incubated in a methionine-free medium fortified with 6 mM of L-glutamine and 0.5 mM L-cysteine for half an hour followed by incubation with L-HPG for the remaining 2 hours, all at 33°C. Cells were then harvested as previously described and cell pellets were stored at -80°C. Subsequently, cell pellets were lysed with 1 ml click-chemistry lysis buffer and incubated on ice for 15 minutes with intermittent vortexing. The mixture was then centrifuged at 16000 RPM (Table-centrifuge 5415 R, for the following steps as well unless otherwise stated) for 30 minutes at 4°C. The supernatant was then transferred to new tubes. The concentrations of proteins in the samples were then determined using Pierce Bradford-Assay with a dilution of 1:300 in PBS. At this point, 25 µg of the lysate was saved to be investigated on Western blot. The next step was for pre-clearing of the lysates (to remove endogenously biotinylated proteins) and conjugation of biotin-azide using click reaction. For this, the following was done: 60 µl of well-mixed high capacity streptavidin agarose resin were added to 1.5 ml tubes filled with 500 µl click-chemistry lysis buffer. The mixture was then centrifuged at 1000 RPM for 2 min at 4°C. The supernatant was discarded carefully and the beads were then incubated with volume of lysates corresponding to 1.8 mg proteins (as calculated from Bradford assay). The tubes were then filled up to 1 ml with click-chemistry lysis buffer and allowed to rotate overnight at 4°C. Next day, the supernatants (representing the pre-cleared lysates) were collected through centrifugation at 1000 RPM for 2 min at 4°C and the beads were discarded. The following reaction mixture for the conjugation of the biotin-azide to the L-HPG was prepared as follows (final volume of 4.5 ml in this example):

Reagents	Stock concentration	Final concentration	dilution	4.5 ml
biotin-azide	15.3 mM DMSO (+Argon)	0.625 mM	1: 24.5	184 μ l
TCEP	174.3 mM H ₂ O	6.25 mM	1: 27.9	161 μ l
TBTA	56.5 mM DMSO (+Argon)	0.625 mM	1:90.4	49.8 μ l
CuSO ₄ *5H ₂ O	1 M in H ₂ O	6.25 mM	1:160	28.1 μ l
SDS	20%	6.25%	1:3.2	1406 μ l
Add H ₂ O				2671 μ l

160 μ l of the above reaction mixture was added per 1 ml pre-cleared lysate. The new mixture was then allowed to rotate for 1.5 hour at room temperature. The click-lysate is now ready for the next step of protein precipitation and purification: In this step the click-lysate was transferred to 5 ml Greiner tubes and 4 ml acetone cooled down to -20 ° C was added. The mixture was incubated overnight at -20°C.

Next day, the mixture inside the Greiner tubes was centrifuged at 3500 RPM (TJ-25 centrifuge) for 5 minutes at 4°C using appropriate centrifuge adapters. Acetone was removed and the pellet was washed two times with 2 ml methanol cooled down to 4°C with vortexing in-between washes and centrifugation at 3500 RPM (TJ-25 centrifuge) for 5 minutes at 4°C. In the final washing step, the remaining methanol was carefully removed and the pellet was left 5 minutes to dry out any remaining methanol. Afterward, the pellet was re-suspended in 120 μ l PBS with 1% SDS at room temperature and a desalting and re-buffering of the solution step was carried out using Zebra Spin Columns (Thermo 89882 7k MWCO) according to the manufacturer's guide. This step also removes excess biotin-azide, which might saturate the streptavidin beads later on. The columns were washed 2 times with 300 μ l of the washing buffer (PBS with 1% NP-40 & 0.1% SDS). The flow through was discarded each time through centrifugation at 1500 RPM (Table-centrifuge 5415 R) for 1 minute. The columns were then transferred to new collecting tubes and the samples were loaded into the column. The samples were then allowed to pass through the columns through centrifugation at 1500 RPM (Table-centrifuge 5415 R) for 2 minutes. The flow through is now the click-eluate and should be kept on ice. The protein concentrations in the click-eluate were measured using Pierce Bradford assay with dilutions of 1:400 in PBS. At this point, 25 μ g of the click-eluate was saved to be investigated on Western blot as a proof of a successful click reaction. The final stage was the streptavidin agarose beads pulldown and it was carried as follows: 60 μ l of well-mixed high capacity streptavidin agarose beads were added to 1.5 ml tubes filled with 500 μ l 1% NP-40, 0.1% SDS in PBS. The mixture was then centrifuged at 2000 RPM (Table-centrifuge 5415 R) for 1 min at 4°C. The supernatant was discarded carefully and the beads were then incubated with volume of click-eluate corresponding to 600 μ g of proteins (as calculated from Bradford assay). The tubes were then filled up to 700 ml with 1% NP-40, 0.1% SDS in PBS and allowed to rotate overnight at 4°C. The next day, supernatants were discarded (can also be saved as a diagnostic point if needed) through centrifugation at 1000 RPM (Table-centrifuge 5415 R) for 2 minute. The beads were then washed as follows:

Washing buffer	Times	Temperature
PBS with 1% NP-40, 0.1% SDS/ 500 μ l	2 with 10 minutes rotation	4°C
Ice-cold PBS with 6 M Urea/ 500 μ l	3 with 10 minutes rotation	4°C
Ice-cold PBS/ 500 μ l	3 with 10 minutes rotation	4°C

After the washing steps, 50 μ l ROTI@Load 1 (2 times concentrated) was added and the samples were heated at 95°C for 20 minutes. Eluted samples were either stored at -20°C or loaded directly on SDS-PAGE for Western blot analysis.

3.4.7 Mass spectrometry

3.4.7.1 MERS-CoV and SARS-CoV-2 samples processing for mass spectrometry

Samples for MERS-CoV and SARS-CoV-2 processing was described in Shaban et al (Shaban et al. 2021) as follows:

After measuring their protein concentrations using reagent compatible Bradford assay, samples (lysed in SDS lysis buffer) were sent to the “Mass spectrometry facility of the Department of Chemistry, Philipps University, Marburg, Germany”, headed by Dr. Uwe Linne, to perform the measurements. In there, samples were processed as follows: The filter-aided sample preparation (FASP) protocol was carried out using Microcon YM-30 filter devices to exchange the SDS buffer to an 8 M urea buffer (Sielaff et al. 2017). To allow optimal accessibility of trypsin to cleavage sites within the protein through the disruption of disulfide bonds formation, iodoacetamide was used to alkylate cysteines residues. Preparing for the tryptic digestion, the 8 M urea buffer was then exchanged to 50 mM ammonium-bicarbonate buffer (pH of 8.0). Subsequently, the samples were digested in filter-units using trypsin, followed by overnight incubation at 37 °C. Digested peptides were then eluted from the filter-units in fresh tubes by the addition of 50 μ L 0.5 M NaCl solution followed by centrifugation at 14.000 \times g for 10 min. Vacuum concentrator was then used to dry out the pellets before re-suspending them in 25 μ l of 0.1% formic acid. Thereafter, chromabond C18WP spin columns (Macherey-Nagel) were used to desalt and concentrate the peptides that were then dissolved in 25 μ l water with 5% acetonitrile and 0.1% formic acid.

200 ng of the peptides was injected on the separation column of the timsTOF Pro mass spectrometer (Bruker Daltonic) connected to a nanoElute HPLC system, at a constant pressure of 800 bar.

The separation of the digested peptides was carried out at 50 °C column temperature. The following solutions were used for the separation: water/0.1% formic acid (solvent A) and acetonitrile/0.1% formic acid (solvent B). The flow rate was 400 nl per minute and the separation gradients were as follows: Linear increase in B from 2% to 17 % in 60 minutes. Afterward, linear gradient of B to 25% in

30 minutes, followed by a linear increase in B to 37% in 10 minutes. Following that, B was increased to 95% in 10 minutes and remained at that level for another 10 minutes. The Data-dependent acquisition mode (DDA PASEF-standard_1.1sec_cycletime, developed by Bruker Daltonics) was used for mass spectrometric measurement.

3.4.7.2 BioID-ATF3 samples processing for mass spectrometry

For the BioID experiment the samples were sent to the Mass spectrometry facility (mentioned above) bound to beads in BioID Wash Buffer V (see Materials section). In there the samples were processed as follow: Samples-bound beads were washed with 100 μ L of ammonium-bicarbonate buffer (0.1 M) for three times. Thereafter, Sequencing Grade Modified Trypsin (Serva) was added to the samples (to perform on-bead digestion) for an incubation period of 45 minutes at 37 °C. The supernatant was then collected in fresh tubes and incubated overnight at 37°C. Thereafter, chromabond C18WP spin columns (Macherey-Nagel) were used to desalt and concentrate the peptides that were then dissolved in 25 μ l water with 5% acetonitrile and 0.1% formic acid. The rest was carried out the same as delineated in the previous section.

3.5 Cell biology

3.5.1 Assessing cells viability

To assess the viability of cells infected with HCoV-229E, and/or treated with different pharmacological compounds (as indicated in the results section), MTS assay from The CellTiter 96® AQueous One Solution Cell Proliferation Assay kit was carried out according to the manufacturer's user manual. Huh7 cells (1.2×10^4) or MRC-5 (1×10^4) cells were seeded in 96-well plates and allowed to grow for 24 hours. The wells containing the cells were then treated and/or infected as shown in the figure legends of the results section. At the end of the corresponding incubation periods, 4 μ l or 20 μ l CellTiter 96® AQueous one solution reagent was mixed with fresh medium to a volume of 100 μ l and added to the wells after discarding the old medium. The cells were then incubated for 1 hour at 33 °C. Microplate Spectrophotometer reader was used then to measure the absorbance of the different samples at 490 nm. The absorbance of the medium per se (i.e. with no cells) at 490 nm was used to correct for background absorbance and was subtracted from all values. The values of cell viability were calculated as a ratio of mean values of all technical replicates of an experimental condition to the mean values of the untreated controls. The mean values of the untreated controls were set to 100%.

Assessing the viability of VERO-E6 cells was carried out using ATPlite and MTT assays by Dr. Christin Mueller, Institute of Medical Virology, Justus Liebig University, Giessen, as follows: The cells were

seeded in a 96-well format to near confluency. Afterward the cells were treated with a serial dilution of thapsigargin for 24 hours, as indicated in the results section. At the end of the incubation period, the cell culture supernatans were removed and 100 µl of ATPlite assay was added to the cells and incubated for 10 minutes. The luminescence was then measured using a Spark 10 M instrument (Tecan).

For the MTT assay, 200 µl of MTT mix (DMEM supplemented with 10% FCS containing 250 µg/ml tetrazolium bromide, Sigma) was added to the cells and samples were incubated for 90-120 minutes at 37°C. In the same step, the cells were fixed using 3.7% PFA in PBS solution. 200 µl of isopropanol was added to each well to dissolve the Formazan crystals (the insoluble product of the reduction of the MTT reagent by viable cells dehydrogenase enzymes). ELISA reader (BioTek) was then used to measure the absorbance at 490 nm.

For both assays, the readout values (luminescence and absorbance values) were used to calculate the CC₅₀ values, referenced to the untreated control (set to 100%), using non-linear regression method on GraphPadPrism 5.0 (GraphPad Software).

3.5.2 Indirect immunofluorescence (IF)

9000 cells per slot were seeded in µ-slides VI (Ibidi). The cells were then allowed to adhere and grow for 24 hours at 37°C. Slots were treated/infected, as indicated in the results section, for 24 hours at 33°C. At the end of the incubation period, Ibdids were taken out to room temperature and the following IF protocol was carried out:

The slots were washed two times with 150 µl Hank's buffer salt solution (HBSS) for 5 minutes at each wash. The cells were then fixed with 100 µl of 4% paraformaldehyde in PBS for 5 minutes. Thereafter, the cells were washed two times with 150 µl HBSS for 10 minutes at each wash and then permeabilized and blocked with 100 µl of 10% normal donkey serum (diluted in HBSS with 0.005% saponin) for 20 min. After blocking, the cells were incubated with 100 µl of primary antibodies (diluted in HBSS with 0.005% saponin) for 2 hours at room temperature. Control slots received 100 µl of HBSS with 0.005% saponin only. The cells were then washed three times with 150 µl HBSS with 0.005% saponin for 10 minutes each wash. Thereafter, 100 µl of secondary antibodies diluted in HBSS with 0.005% saponin were added and incubated for 2 hours at room temperature in darkness. Secondary antibodies conjugated to the following dyes were used with the indicated dilutions and final concentrations:

Secondary antibody	Final concentration	Dilution
Cy3-mouse	1.25 µg/ml	1:100
DyLight488-rabbit	5 µg/ml	1:100
Cy3-rabbit	1.25 µg/ml	1:100
DyLight488-mouse	5 µg/ml	1:100

After the end of the incubation period with the secondary antibodies, the cells were washed three times with 150 μ l HBSS with 0.005% saponin for 10 minutes each wash. Thereafter, nuclei were stained using 100 μ l Hoechst 33342 solution (diluted 1:1000 in Hank's BSS) for 5 minutes, followed by two times washing with 150 μ l HBSS with 0.005% saponin for 5 minutes each wash. Finally, slots were covered with 50 μ l of 30% Glycerol (diluted in HBSS) and stored overnight at 4°C. Immunofluorescence was analyzed the next day using a Leica DMI8, and the Leica LASX software. The following filter cubes were used: Dylight488: excitation 480/40 and emission 527/30, Cy3: excitation 560/40 and emission 630/75, and Hoechst 33342: excitation 405/60 and emission 470/50. Exposure times were kept equal between samples of the same experiment.

3.6 Bioinformatics analysis

3.6.1 Data analysis of MERS-CoV and SARS-CoV-2 mass spectrometry samples

Experiments with each virus (with conditions indicated in the results section) were performed as two biological and three technical replicas. The raw data acquired after the end of the mass spectrometric runs were analyzed using MaxQuant software. The built-in Andromeda search engine was used to annotate and assign protein identifiers. The following Uniprot databases were used as reference for the annotation and assignment process:

Organism	Uniprot ID
Homo sapiens (Huh7 cells)	UP000005640 (Release 2019_06 of 03-Jul-2019)
Chlorocebus sabaeus (VERO-E6 cells), Green monkey, Cercopithecus sabaeus	UP000029965 (Release 2020_02 of 22-Apr-2020)
MERS-CoV	UP000139997 and UP000171868
SARS-CoV-2	UP000464024

The following parameters were used in the MaxQuant software for the two viruses' experiments:

Parameter	Value
Version	1.6.17.0
User name	-
Machine name	-
Date of writing	-
Include contaminants	True
PSM FDR	0.01
PSM FDR Crosslink	0.01
Protein FDR	0.01
Site FDR	0.01
Use Normalized Ratios For Occupancy	True
Min. peptide Length	7
Min. score for unmodified peptides	0
Min. score for modified peptides	40
Min. delta score for unmodified peptides	0

Min. delta score for modified peptides	6
Min. unique peptides	0
Min. razor peptides	1
Min. peptides	1
Use only unmodified peptides and	True
Modifications included in protein quantification	Oxidation (M);Acetyl (Protein N-term)
Peptides used for protein quantification	Razor
Discard unmodified counterpart peptides	True
Label min. ratio count	2
Use delta score	False
iBAQ	True
iBAQ log fit	True
Match between runs	True
Matching time window [min]	0.7
Match ion mobility window [indices]	0.05
Alignment time window [min]	20
Alignment ion mobility window [indices]	1
Find dependent peptides	False
Fasta file	
-Decoy mode	revert
Include contaminants	True
Advanced ratios	True
Fixed andromeda index folder	
Combined folder location	
Second peptides	True
Stabilize large LFQ ratios	True
Separate LFQ in parameter groups	True
Require MS/MS for LFQ comparisons	True
Calculate peak properties	False
Main search max. combinations	200
Advanced site intensities	True
Write msScans table	False
Write msmsScans table	True
Write ms3Scans table	True
Write allPeptides table	True
Write mzRange table	True
Write DIA fragments table	False
Write pasefMsmsScans table	True
Write accumulatedPasefMsmsScans table	False
Max. peptide mass [Da]	4600
Min. peptide length for unspecific search	8
Max. peptide length for unspecific search	25
Razor protein FDR	True
Disable MD5	False
Max mods in site table	3
Match unidentified features	False
Epsilon score for mutations	
Evaluate variant peptides separately	True
Variation mode	None
MS/MS tol. (FTMS)	20 ppm
Top MS/MS peaks per Da interval. (FTMS)	12
Da interval. (FTMS)	100
MS/MS deisotoping (FTMS)	True

MS/MS deisotoping tolerance (FTMS)	7
MS/MS deisotoping tolerance unit (FTMS)	ppm
MS/MS higher charges (FTMS)	True
MS/MS water loss (FTMS)	True
MS/MS ammonia loss (FTMS)	True
MS/MS dependent losses (FTMS)	True
MS/MS recalibration (FTMS)	False
MS/MS tol. (ITMS)	0.5 Da
Top MS/MS peaks per Da interval. (ITMS)	8
Da interval. (ITMS)	100
MS/MS deisotoping (ITMS)	False
MS/MS deisotoping tolerance (ITMS)	0.15
MS/MS deisotoping tolerance unit (ITMS)	Da
MS/MS higher charges (ITMS)	True
MS/MS water loss (ITMS)	True
MS/MS ammonia loss (ITMS)	True
MS/MS dependent losses (ITMS)	True
MS/MS recalibration (ITMS)	False
MS/MS tol. (TOF)	40 ppm
Top MS/MS peaks per Da interval. (TOF)	10
Da interval. (TOF)	100
MS/MS deisotoping (TOF)	True
MS/MS deisotoping tolerance (TOF)	0.01
MS/MS deisotoping tolerance unit (TOF)	Da
MS/MS higher charges (TOF)	True
MS/MS water loss (TOF)	True
MS/MS ammonia loss (TOF)	True
MS/MS dependent losses (TOF)	True
MS/MS recalibration (TOF)	False
MS/MS tol. (Unknown)	20 ppm
Top MS/MS peaks per Da interval. (Unknown)	12
Da interval. (Unknown)	100
MS/MS deisotoping (Unknown)	True
MS/MS deisotoping tolerance (Unknown)	7
MS/MS deisotoping tolerance unit (Unknown)	ppm
MS/MS higher charges (Unknown)	True
MS/MS water loss (Unknown)	True
MS/MS ammonia loss (Unknown)	True
MS/MS dependent losses (Unknown)	True
MS/MS recalibration (Unknown)	False
Site tables	Oxidation (M)Sites.txt

Perseus software (versions 1.6.10.50 for Huh7 and 1.6.14.0 for Vero-E6 proteomes) was then used to further analyze the data and perform statistical tests as delineated in Shaban et al 2021. Briefly:

The output of MaxQuant analysis is several txt files including a file named “proteinGroups.txt” that contains proteins intensities. This file was then processed using Excel 2016 to a spreadsheet table format that is readable and acceptable by Perseus software. In Perseus, proteins intensities were log₂-transformed and normalized using width adjustment method. IDs flagged or deemed as contaminants or reverse sequences were excluded. For each condition, the two biological and three technical replicas

were categorized as one group. This allowed then the calculation of ratio values amongst the different groups (conditions). Student's t-test analysis was used to identify DEPs. The lists of DEPs were then further processed and filtered using Excel 2016 to produce heatmaps (using the conditional formatting function) as described in the results section. Venn diagrams were generated using the tools available from <http://bioinformatics.psb.ugent.be/webtools/Venn/>. Metascape software was fed with the majority protein IDs (for Huh7 cells) or gene IDs (for Vero E6 cells) to perform overrepresentation analyses of the DEPs using the express settings in the software. The NCBI gene ID annotation matching that of the majority protein IDs was used to discover co-regulated proteins in Huh7 and VERO-E6 cells. The STRING database (version 10, <https://string-db.org/>) was fed with indicated DEP lists (gene IDs) to obtain protein-protein interaction networks that were then imported and visualized using Cytoscape 3.8.0 software.

4.6.2 Data analysis of BioID-ATF3 mass spectrometry samples

BioID experiment with the miniTurbo-ATF3 construct (with conditions indicated in the results section) was performed as three biological and two technical replicas. The raw data acquired after the end of the mass spectrometric runs were analyzed using MaxQuant software. The built-in Andromeda search engine was used to annotate and assign protein identifiers. The following Uniprot databases were used as reference for the annotation and assignment process:

Organism	Uniprot ID
Homo sapiens (Huh7 cells)	UP000005640 (Release 2019_06 of 03-Jul-2019)
HCoV-229E	UP000006716

The following parameters were used in the MaxQuant (version 2.0.3.0) software for the BioID-ATF3 experiment:

Parameter	Value
Version	2.0.3.0
User name	Bioinformatik
Machine name	DESKTOP-78071T6
Date of writing	
Include contaminants	True
PSM FDR	
PSM FDR Crosslink	
Protein FDR	
Site FDR	
Use Normalized Ratios For Occupancy	True
Min. peptide Length	
Min. score for unmodified peptides	
Min. score for modified peptides	
Min. delta score for unmodified peptides	
Min. delta score for modified peptides	
Min. unique peptides	
Min. razor peptides	

Min. peptides	
Use only unmodified peptides and	True
Modifications included in protein quantification	Oxidation (M);Acetyl (Protein N-term)
Peptides used for protein quantification	Razor
Discard unmodified counterpart peptides	True
Label min. ratio count	
Use delta score	False
iBAQ	True
iBAQ log fit	True
Match between runs	True
Matching time window [min]	
Match ion mobility window [indices]	
Alignment time window [min]	
Alignment ion mobility window [indices]	
Find dependent peptides	False
Decoy mode	revert
Include contaminants	True
Advanced ratios	True
Fixed andromeda index folder	
Combined folder location	
Second peptides	False
Stabilize large LFQ ratios	revert
Separate LFQ in parameter groups	True
Require MS/MS for LFQ comparisons	True
Calculate peak properties	False
Main search max. combinations	
Advanced site intensities	True
Write msScans table	False
Write msmsScans table	True
Write ms3Scans table	True
Write allPeptides table	True
Write mzRange table	True
Write DIA fragments table	False
Write DIA fragments quant table	False
Write pasefMsmsScans table	True
Write accumulatedMsmsScans table	True
Max. peptide mass [Da]	
Min. peptide length for unspecific search	
Max. peptide length for unspecific search	
Razor protein FDR	True
Disable MD5	False
Max mods in site table	
Match unidentified features	False
Epsilon score for mutations	
Evaluate variant peptides separately	True
Variation mode	None
MS/MS tol. (FTMS)	20 ppm
Top MS/MS peaks per Da interval. (FTMS)	
Da interval. (FTMS)	
MS/MS deisotoping (FTMS)	True
MS/MS deisotoping tolerance (FTMS)	
MS/MS deisotoping tolerance unit (FTMS)	ppm
MS/MS higher charges (FTMS)	True

MS/MS water loss (FTMS)	True
MS/MS ammonia loss (FTMS)	True
MS/MS dependent losses (FTMS)	True
MS/MS recalibration (FTMS)	False
MS/MS tol. (ITMS)	0.5 Da
Top MS/MS peaks per Da interval. (ITMS)	
Da interval. (ITMS)	
MS/MS deisotoping (ITMS)	False
MS/MS deisotoping tolerance (ITMS)	
MS/MS deisotoping tolerance unit (ITMS)	Da
MS/MS higher charges (ITMS)	True
MS/MS water loss (ITMS)	True
MS/MS ammonia loss (ITMS)	True
MS/MS dependent losses (ITMS)	True
MS/MS recalibration (ITMS)	False
MS/MS tol. (TOF)	40 ppm
Top MS/MS peaks per Da interval. (TOF)	
Da interval. (TOF)	
MS/MS deisotoping (TOF)	True
MS/MS deisotoping tolerance (TOF)	
MS/MS deisotoping tolerance unit (TOF)	Da
MS/MS higher charges (TOF)	True
MS/MS water loss (TOF)	True
MS/MS ammonia loss (TOF)	True
MS/MS dependent losses (TOF)	True
MS/MS recalibration (TOF)	False
MS/MS tol. (Unknown)	20 ppm
Top MS/MS peaks per Da interval. (Unknown)	
Da interval. (Unknown)	
MS/MS deisotoping (Unknown)	True
MS/MS deisotoping tolerance (Unknown)	
MS/MS deisotoping tolerance unit (Unknown)	ppm
MS/MS higher charges (Unknown)	True
MS/MS water loss (Unknown)	True
MS/MS ammonia loss (Unknown)	True
MS/MS dependent losses (Unknown)	True
MS/MS recalibration (Unknown)	False
Site tables	Oxidation (M)Sites.txt

Perseus software (versions 1.6.15.0) was then used to further analyze the data and perform statistical tests as follows:

The output file of MaxQunt “proteinGroups.txt” that contains proteins intensities was processed using Excel 2016 to a format that is acceptable by Perseus software. In Perseus, proteins intensities were log₂-transformed and no normalization was used as these were enrichment experiments with possibly very different data distributions in the individual conditions. IDs flagged or deemed as contaminants or reverse sequences were excluded. For each condition, the three biological and two technical replicas were categorized as one group and technical replicas were averaged. This allowed then the calculation of ratio values amongst the different groups (conditions). Lowest value in the log₂-transformed

intensities table was determined to be 7.7. Based on this value, missing values were imputed by 7 within the entire data matrix. The built-in Student's t-test analysis option with the default settings was used to identify DEPs. Figure 10 provides an overview of these steps ordered as carried out and the default settings used for the built-in Student's t-test analysis (Fig. 10). The lists of DEPs were then further processed and filtered using Excel 2016 to produce heatmaps and extract filtered ID lists for Venn diagrams as described in the results section. Venn diagrams were generated using the tools available from <http://bioinformatics.psb.ugent.be/webtools/Venn/>.

For pathway-enrichment analyses (Figs. 26, 28, 29, 30, 61 & 62), the Metascape software was fed with the majority protein IDs to perform overrepresentation analyses of the DEPs using the express settings in the software. The software uses the ontology sources of GO Biological Processes, CORUM, KEGG Pathway, WikiPathways, Canonical Pathways, Reactome Gene Sets, TRRUST, DisGeNET, PaGenBase, COVID, PANTHER Pathway, Transcription Factor Targets, and all genes in the genome as the enrichment background. P-value calculations were carried out using cumulative hypergeometric distribution. q-values calculations were based on the Benjamini–Hochberg procedure to account for multiple testings. The following criteria was then used to select terms: p-value < 0.01, a minimum count of 3, and an enrichment factor > 1.5.

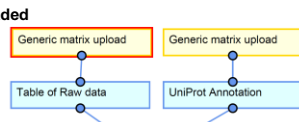
For hierarchical clustering (Fig. 28) of enriched terms, Kappa scores were used as the similarity measure. Sub-trees with a similarity of more than 0.3 were categorized as clusters. The terms with the highest statistical significance in a cluster were chosen to represent the cluster.

The STRING database (version 10, <https://string-db.org/>) was fed with the indicated DEP lists to obtain protein-protein interaction networks with settings indicated in figure legends. These networks (and individual nodes) were then imported to Cytoscape 3.8.0 software for further visualization and processing. Details of each network are included in the figure legends.

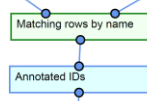
Two matrices (tables) were uploaded into Perseus:

1) The raw data table

2) The annotation matrix from Uniprot.



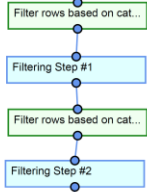
Applying the "Matching rows by name" function to the two matrices will update the raw data matrix to include selected annotation info from the second matrix.



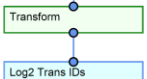
The now annotated raw data matrix can be filtered:

1) Filtering step #1: removes rows flagged as "Only identified by site".

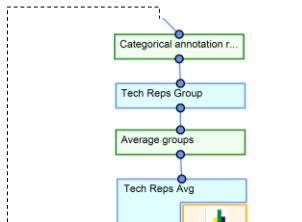
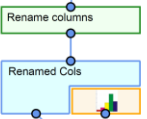
2) Filtering step #2: removes rows flagged as "Reverse".



Applying the "Transform" function to the previous matrix will log2-transform proteins intensities.

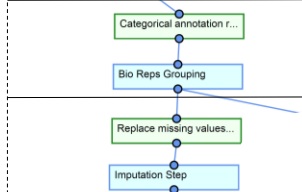


Applying the "Rename columns" function to give each column a more meaningful name in preparation for the next step.



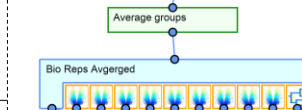
Applying the "Categorical annotation rows" function to group technical replicas together. This is made possible based on the correct naming in the previous step.

Applying the "Average groups" function to the previous grouping will output the mean of the technical replicas.

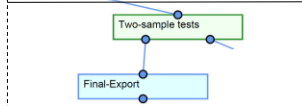


Applying the "Categorical annotation rows" function to group biological replicas together.

Carrying out the imputation step using "Replace missing values by constant" function.



Applying the "Average groups" function to the previous matrix to output the mean of the biological replicas. The "Keep original data" option was selected here.



Applying the "Two-sample tests" function to the previous matrix will update the results of the t-test (settings are shown below). The resulting matrix can be then exported.

Test	Student's T-test
S0	0
Side	Both
Valid value filter	<input checked="" type="checkbox"/>
Min. number of valid values	1
Min. number mode	In total
Min. percentage of valid values	0
Min. percentage mode	In total
Use for truncation	Permutation-based FDR
FDR	0.05
Report q-value	<input checked="" type="checkbox"/>
Number of randomizations	250
Preserve grouping in randomizations	<None>
Calculate combined score	<input type="checkbox"/>
-Log10 p-value	<input checked="" type="checkbox"/>
Suffix	

Figure 10: Example of a workflow of raw data processing in Perseus.

The raw data from the BioID-ATF3 mass spectrometry experiments were processed in multiple steps as shown and explained in the upper part of the figure. The lower part indicates the default settings used for the built-in Student's t-test analysis. Yellow boxes indicate uploaded matrices, blue boxes indicate processed matrices, and green boxes indicate functions carried out. The workflow was designed and carried out together with Dr. Axel Weber (Prof. Kracht working group).

Chapter 4: Results

4.1 Activation and pharmacological modulation of the ER stress response in CoV-infected cells

Coronaviruses (CoV) replicate in specialized, newly formed subcellular structures called double-membrane vesicles. These replicative organelles derive from the ER and remain in close spatial proximity to the ER (Cortese et al., 2020; Knoops et al., 2008; Snijder et al., 2020). Therefore it was expected that coronavirus infection will cause some form of ER stress and activation of the unfolded protein response (UPR), but it was unknown if this would occur in a virus-specific fashion.

To determine the ER stress response under these conditions, initially, the expression and activation status of several components of the canonical ER stress pathways were assessed using several methods comparing uninfected with infected cells.

Furthermore, pharmacological modulation of ER stress pathways, either in form of their inhibition or activation, was carried out to elucidate the effect of these pathways on viral replication and host response.

4.1.1 The activation status of the ER stress sensors PERK and IRE1 α in HCoV-229E-infected cells and the consequences of their inhibition for the host response and the viral replication.

To understand the involvement of two of the three main UPR sensors, namely PERK and IRE1 α , in the replication of HCoV-229E, the expression and phosphorylation patterns of the two kinases and their substrates were assessed and small molecule inhibitors were applied in these experiments. GSK2606414 and a newer, optimized version of the same inhibitor, called GSK2656157 (discussed in section 4.1.9), were used to inhibit PERK, while KIRA6 was used to inhibit IRE1 α as schematically shown in Figure 11.

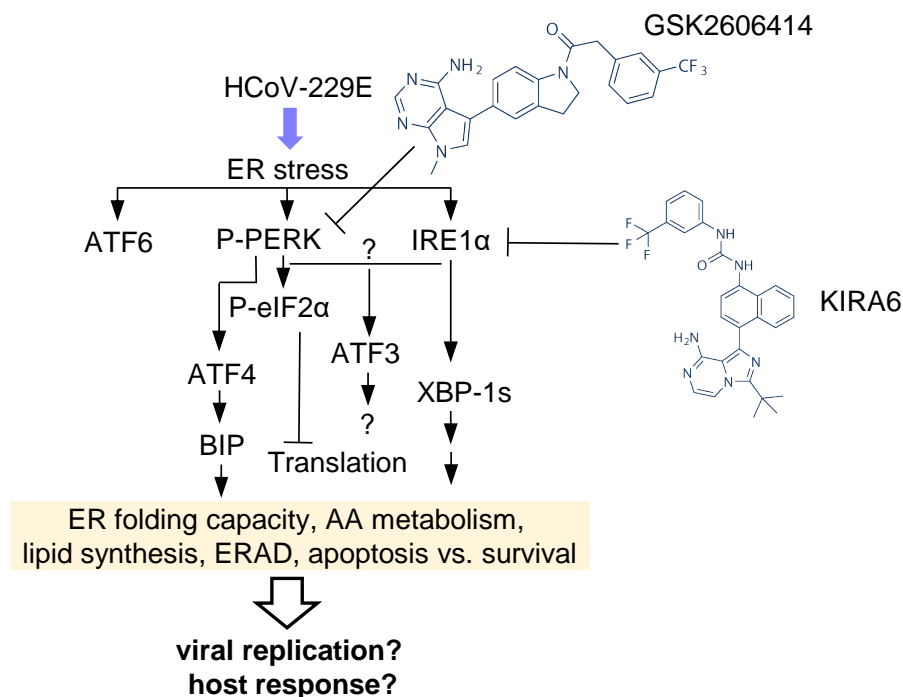
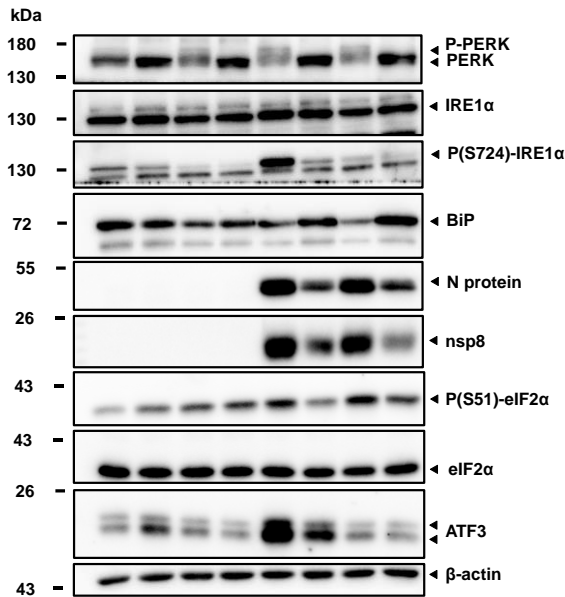


Figure 11: The putative roles of the canonical UPR pathways in the host response to CoV replication.

A schematic representation of ER stress sensors, downstream pathways and parameters activated by HCoV-229E infection that were investigated in this thesis. The shaded box indicates several functional and (patho-) physiological outcomes of ER stress responses. Structures show cell-permeable ATP-competitive agents such as GSK2606414 and KIRA6 that were applied in this study to inhibit the ER stress sensors PERK or IRE1 α , respectively. The scheme was adapted from Fig. 2a, Shaban et al. under a Creative Commons Attribution 4.0 International License (Shaban et al. 2021).

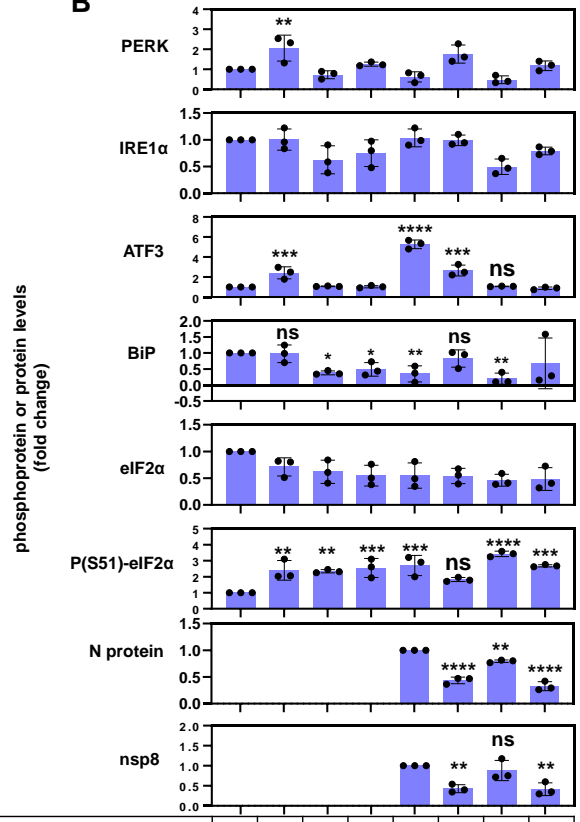
Western blot analysis revealed that HCoV-229E causes the activation of the UPR sensors PERK and IRE1 α . The activation of PERK was seen as a mobility shift of the PERK protein band and by the inducible phosphorylation of its substrate, eIF2 α , at serine 51, a modification well known for its role in translational shutdown (Clemens 2001). The activation of IRE1 α was indicated by the phosphorylation of the serine residue 724. In addition, infection resulted in the downregulation of the major ER chaperone BiP (also called GRP78 or HSPA5) and in the upregulation of the transcription factor ATF3, whose role in the ER stress response is not well defined (Fig. 12 A & B).

A



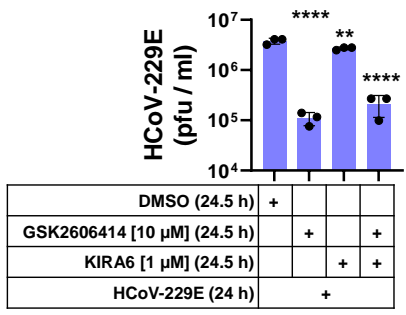
DMSO (24.5 h)	+				+			
GSK2606414 [10 μM] (24.5 h)		+		+		+		+
KIRA6 [1 μM] (24.5 h)			+	+			+	+
HCoV-229E (24 h)					-			+

B



DMSO (24.5 h)	+				+			
GSK2606414 [10 μM] (24.5 h)		+		+		+		+
KIRA6 [1 μM] (24.5 h)			+	+			+	+
HCoV-229E (24 h)					-			+

C



DMSO (24.5 h)	+			
GSK2606414 [10 μM] (24.5 h)		+		+
KIRA6 [1 μM] (24.5 h)			+	+
HCoV-229E (24 h)				+

Figure 12: Differential effects of the PERK inhibitor GSK2606414 and the IRE1α inhibitor KIRA6 on the ER stress response and replication of HCoV-229E.

Huh7 cells were pre-treated with 10 μM GSK2606414, 1 μM KIRA6, or solvent (0.1% DMSO) for 30 minutes either individually or in combination as indicated. Then, cells were left either uninfected or infected with HCoV-229E (MOI of 1) for additional 24 hours. Thereafter, total cell extracts were prepared using Triton-based buffer (the special lysis buffer, see Materials) and analyzed by Western blotting.

(A) The panels show representative immunoblots of the investigated host and viral proteins of one of the three biological replicas.

(B) The panels indicate corresponding phospho-protein or protein levels quantified from the 3 independent biological replicas relative to the untreated/uninfected control. Antibodies against β-actin were used as a loading control.

(C) Supernatants from the experiments shown in (A) were used to determine the production of infectious viral particles by plaque assay. The Y-axis shows plaque-forming units per milliliter (pfu/ml).

Bars show means ± s.d., while dots show the results from biologically independent experiments. Asterisks indicate p values (*p ≤ 0.05, **p ≤ 0.01, ***p ≤ 0.001, ****p ≤ 0.0001) obtained by one-way ANOVA test where the mean of each column was compared to the mean of the untreated column, except for the viral proteins and viral titer where they were compared to the mean of the infected sample + DMSO. For BiP panel, the last column was excluded from the comparison.

Infection of the cells was evident from viral protein synthesis of the nucleocapsid (N) protein, an essential structural protein, and of nsp8, a non-structural protein that is an essential component of the viral replication/transcription complex (vRTC) (Fig. 12 A & B).

GSK2606414 treatments of both infected and uninfected cells resulted in the deactivation of PERK. This deactivation was seen by the retraction of the PERK mobility shifts, whereby the various post-translationally modified forms of this protein collapsed to a faster-migrating band on the SDS-PAGE (Fig. 12 A).

KIRA6 treatment resulted in the downregulation of the serine-724 phosphorylation band induced by the virus infection. Intriguingly and somewhat counterintuitively (at least for PERK), treatments of the infected and uninfected cells with both inhibitors (individually or combined) resulted in the upregulation of basal eIF2 α serine 51 (S51) phosphorylation. On the other hand, GSK2606414 treatment alone of infected cells reduced the CoV-induced upregulation of S51 phosphorylation as seen in the quantification in figure 12 B. KIRA6 treatment of the uninfected cells resulted in the activation of the PERK band with a shift pattern of the protein band that is different from the one induced by CoV infection (Fig. 12 A).

The CoV-induced expression of ATF3 was significantly reduced by GSK2606414 and completely diminished by KIRA6 treatments. GSK2606414 treatment of the uninfected cells resulted in an upregulation of the ATF3 band compared to the steady-state levels. In both infected and uninfected cells, BiP levels were reduced with KIRA6 treatments. On the other hand, GSK2606414 treatment of infected cells reversed the CoV-induced downregulation of BiP and did not affect its levels in the uninfected cells.

On the viral side, PERK inhibitor treatment either alone or combined with KIRA6 resulted in about 50% reduction of the viral N protein as well as the viral NSP8. In contrast, the KIRA6 treatment resulted in a slight reduction, although statistically significant, in the levels of N protein but not in the levels of nsp8. To investigate whether a drop in the infectious particles accompanied this drop in the levels of the viral proteins, plaque assays were performed. In comparison to the DMSO + HCoV-229E control, Infected cells treated with GSK2606414, either alone or combined with KIRA6 showed a statistically significant drop of approximately 1.5 log₁₀ scales in the viral titer. On the other hand, only a very slight reduction in the viral titer was observed when infected cells were treated with KIRA6 alone (Fig. 12 C).

The data above alluded to a possible important role of PERK in the replication of HCoV-229E through a cross-talking network of (ER-related) host factors, while IRE1 α possibly only played a marginal role for the viral replication, but was required for the regulation of at least one inducible host factor, namely ATF3.

Both, the regulation of viral replication and host response were therefore further investigated and the results are described in the subsequent sections.

4.1.2 Effect of inhibiting ER stress sensors, PERK and IRE1 α , on the host de-novo protein synthesis levels in cells infected or uninfected with CoV

Throughout multiple kinases and pathways, the cell regulates the phosphorylation of eIF2 α on serine 51, which in turn modulates the level of translation (see the introduction for more details). To follow up on the regulation of eIF2 α phosphorylation levels seen in figure 12, a so called “puromycilation assay” was carried out. Given that puromycin is structurally similar to tyrosyl-tRNA, the cellular translation machinery will incorporate it into the nascent polypeptide chain. This incorporation will prevent further elongation and a drop of the polypeptide from the translating ribosome at the A side, resulting in size-diverse, truncated (depending on the place of incorporation into the peptide sequence) polypeptide chains labeled with puromycin (Fig. 13 A) and (Aviner 2020). These truncated polypeptides can then be detected with anti-puromycin antibodies rendering this method suitable to assess the levels of protein de-novo synthesis on western blot (Fig. 13 A). Using the same conditions described in figure 12, uninfected or infected cells, treated with GSK2606414 or with KIRA6 or with both inhibitors, were treated with 3 μ M of puromycin for 30 minutes (a puro pulse) before harvesting the cells. As a negative control for the method, an additional uninfected sample, treated with the solvent DMSO was left without puromycin treatment. Total cell extracts were then subjected to Western blotting. Coomassie blue brilliant (CBB) staining of the membrane was used to visualize the entire population of cellular proteins in each sample and to indicate equal loading. Expectedly, the control sample (without the puro pulse) showed no signal. In contrast, the uninfected sample, treated with DMSO and pulsed with puromycin showed a strong signal across the entire lane indicating the steady-state levels of translation. Cells infected with HCoV-229E showed a stark reduction in the translated proteins indicating the translational shutdown imposed on the cells by the virus (Fig. 13 B & C).

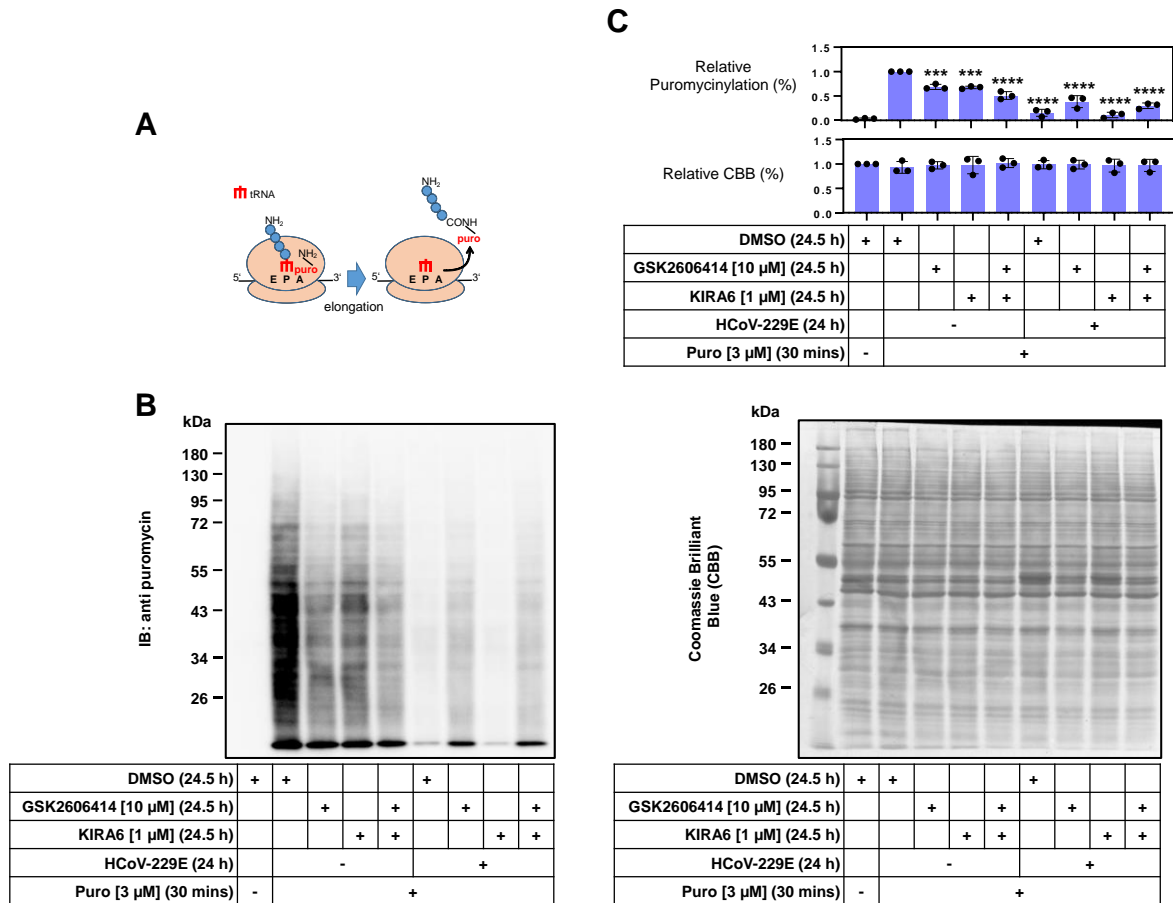


Figure 13: Differential regulation of host proteins de-novo synthesis in the presence or absence of HCoV-229E infection by PERK inhibitor GSK2606414 and the IRE1 α inhibitor KIRA6.

Huh7 cells were treated/infected as described in figure 12. Half an hour before the end of the infection/treatment period, cells were pulsed with 3 μ M of puromycin (puro). Uninfected, 0.1% DMSO-treated cells were either pulsed or left without the puro pulse as a negative control. Whole-cell extracts using the special lysis buffer were then subjected to western blot analysis.

(A) A schematic representation of the incorporation of puromycin in the nascent polypeptide chain and the subsequent premature chain termination.

(B) Anti-puromycin antibodies immunoblot of one representative replica (out of three biological replicas) (right) and CBB staining (left) of the corresponding immunoblot as a loading control and for the visualization of the levels of the steady-state proteins.

(C) The corresponding quantification of the experiment shown in (B) for three independent biological replicas relative to the puro-pulsed, DMSO-treated, uninfected control (i.e. steady-state level control).

Bars show means \pm s.d., while dots show the results from biologically independent experiments. Asterisks indicate p values (* $p \leq 0.05$, ** $p \leq 0.01$, *** $p \leq 0.001$, **** $p \leq 0.0001$) obtained by one-way ANOVA test where the mean of each column was compared to the mean of the untreated column (pulsed with puromycin).

In accordance with the increased phosphorylation of eIF2 α on serine 51 seen in the uninfected samples treated with GSK2606414, KIRA6, or both, translational levels in these samples were moderately, but in a statistically significant manner, reduced. Samples infected with HCoV-229E and treated with PERK inhibitor showed partial restoration of translation (around 50%) while KIRA6 treatment did not affect the virus-induced translational shutdown (Fig. 13 B & C).

These data for the one hand demonstrate the profound suppression of global protein synthesis within 24 h of CoV replication and on the other hand reiterate the intimate, yet complicated, connection between PERK and translation, in the absence or presence of an external stimulus (ex: virus infection or pharmacological compound). This connection was investigated at a deeper level using a more sophisticated method, the results for which were delineated in section 4.3.1.

4.1.3 Effect of the chemical compound thapsigargin on the activation of ER stress in the context of host response and virus replication

The inhibitor studies from this work (shown above) along with other published literature indicated an important, differential yet elusive role of different UPR sensors and components in CoV replication and host response (Sims et al. 2021.; Echavarría-Consuegra et al. 2021). These results also pointed out the possibility of modulating the UPR pathways as a way to interfere with CoV replication.

To investigate the role of ER stress and UPR activation in CoV replication a well-known chemical inducer of ER stress and UPR pathways, called thapsigargin, was utilized (Fig. 14).

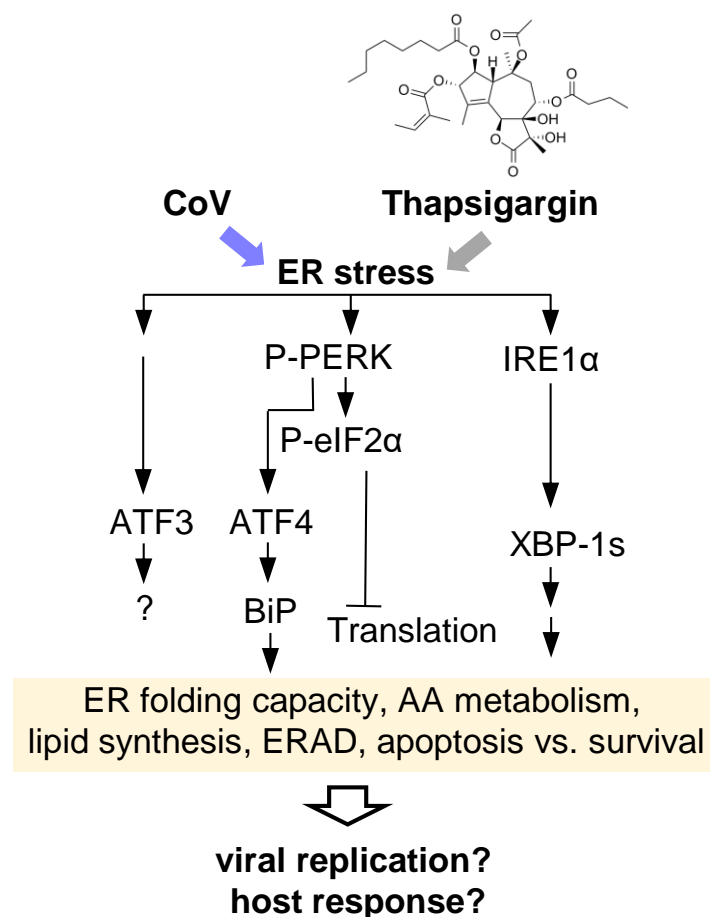


Figure 14: CoV and thapsigargin activation of ER stress and UPR pathways.

The same scheme as shown in Figure 11 is used to demonstrate the potential effects of thapsigargin that were studied in this thesis.

The scheme was adapted from Fig. 2a, Shaban et al. under a Creative Commons Attribution 4.0 International License (Shaban et al. 2021).

Thapsigargin induces ER stress by inhibiting the sarco/endoplasmic reticulum Ca^{2+} ATPase pump (SERCA). The depletion of ER calcium results in impairments of normal ER functioning and subsequent activation of ER stress and UPR pathways (see introduction for more details) (Shaban, Mayr-Buro, et al. 2022).

Initial experiments that were performed comparing 1 hour or 24 hours of thapsigargin treatment of Huh7 cells to 24 hours of HCoV-229E infection indicated a differential activation of UPR by both stimuli. This led to the question of whether chemically activating UPR is beneficial, detrimental, or irrelevant to HCoV-229E replication. Subsequently, a full-scale investigation of this compound was launched in the context of three human coronaviruses replication.

For this purpose, Huh7 cells were infected for 24 hours with HCoV-229E (MOI of 1) or left uninfected. The cells (both infected and uninfected) were treated with 1 μM of thapsigargin for 24 hours or 16 hours. Uninfected control samples were either treated for 1 hour with 1 μM of thapsigargin or left untreated (Fig. 15 A). Cell pellets were used either for RNA extraction followed by RT-qPCR analysis or for Western blotting using the special lysis buffer. Supernatants from virus-infected conditions were collected and assessed for infectious particles using plaque assay.

The western blot analysis showed that the viral N protein, nsp8, and nsp12 were all completely undetectable after the simultaneous treatment (thapsigargin and CoV for 24 hours). On the other hand, residual traces of these viral proteins can still be seen when thapsigargin was added 8 hours after the infection (Fig. 15 C). PERK activation pattern differed between 1 hour of thapsigargin treatment and the 24 or 16 hours treatments. In the latter two cases (prolonged treatments), a more prominent smear (corresponding to multiple bands of PERK) can be seen while in the 1 hour treatment a single, strongly shifted (i.e. slower migration) PERK band can be observed (Fig. 15 C). Both BiP and IRE1 α protein levels increased with the prolonged thapsigargin treatment, while ATF3 levels remained similar to the level seen in HCoV-229E infection though a slight decrease can be observed in 24 hours CoV+16 hours thapsigargin condition (Fig. 15 C & D). Notably, thapsigargin treatment countered the HCoV-229E-induced downregulation of BiP. On the other hand, the 1 hour of thapsigargin treatment alone did not significantly increase the levels of any of these factors (ATF3 or BiP) (Fig. 15 C & D).

To find out whether the disappearance of viral proteins observed on the western blot is reflected by a drop in the infectious particles production, a plaque assay was performed. 24 hours after the simultaneous thapsigargin + CoV condition, an approximately 100-fold drop (two \log_{10} scales) in the viral titer was observed (Fig. 15 B upper panel). Adding thapsigargin 16 hours after the beginning of the

infection resulted in a comparable drop (trending upward) to the simultaneous treatment (Fig. 15 B upper panel).

The intracellular viral RNA levels assessed by RT-qPCR showed a profound decrease in the spike RNA levels when infected cells were treated with thapsigargin for 24 or 16 hours as compared to the virus-alone condition (Fig. 15 B lower panel).

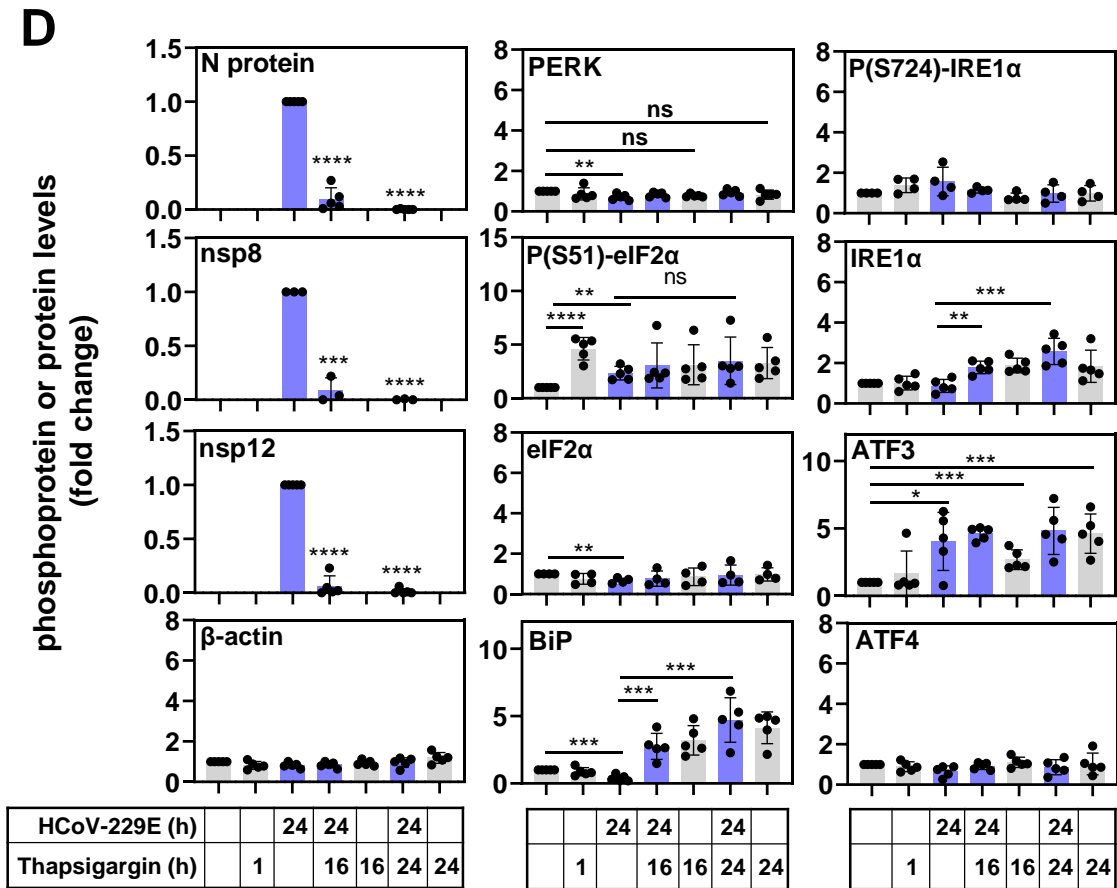
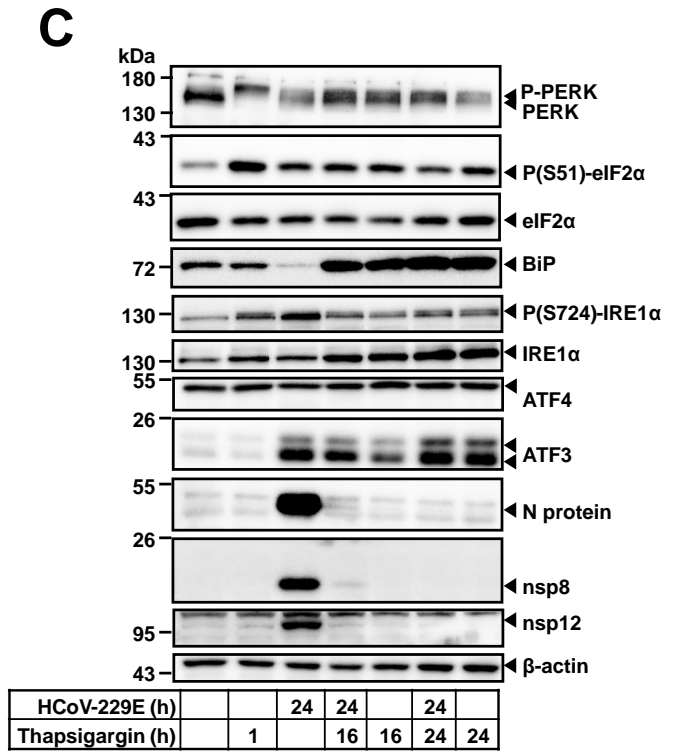
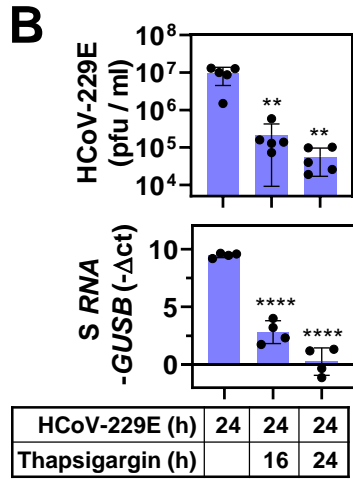
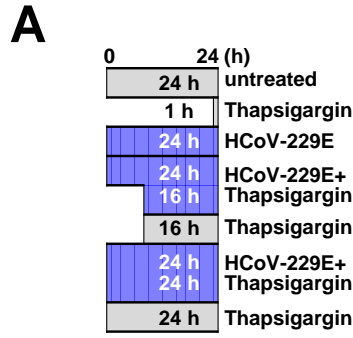


Figure 15: Thapsigargin profoundly inhibits the replication of HCoV-229E in Huh7 cells.

Huh7 cells were infected for 24 hours with HCoV-229E (MOI of 1) or left uninfected. The cells (both infected and uninfected) were treated with 1 μ M of thapsigargin for 24 hours or 16 hours. Uninfected samples were either treated for 1 hour with thapsigargin or left untreated. Cell pellets were used either for RNA extraction followed by RT-qPCR analysis or for Western blotting using the special lysis buffer. Supernatants from virus-infected conditions were collected and assessed for the production of infectious particles using plaque assay. The experiment was performed together with the technician Hendrik Weiser (Prof. Kracht working group). Hendrik Weiser helped perform the biological replicas.

The figure was adapted from Fig. 2, Shaban et al. under a Creative Commons Attribution 4.0 International License (Shaban et al. 2021).

(A) A schematic representation of the different experimental conditions described above.

(B) Upper panel shows the titer change of HCoV-229E by plaque assay expressed as pfu/mL with five biological replicas. The lower graph indicates the levels of the viral spike RNA, extracted from infected cells, with four biological replicas. The housekeeping gene GUS β was used for normalization.

(C) Immunoblots of one representative replica (out of five biological replicas) of investigated host and viral proteins with the conditions indicated in (A). β -actin was used as a loading control.

(D) Corresponding protein and phospho-protein levels from (C), quantified from at least four independent biological replicas relative to the untreated/uninfected control.

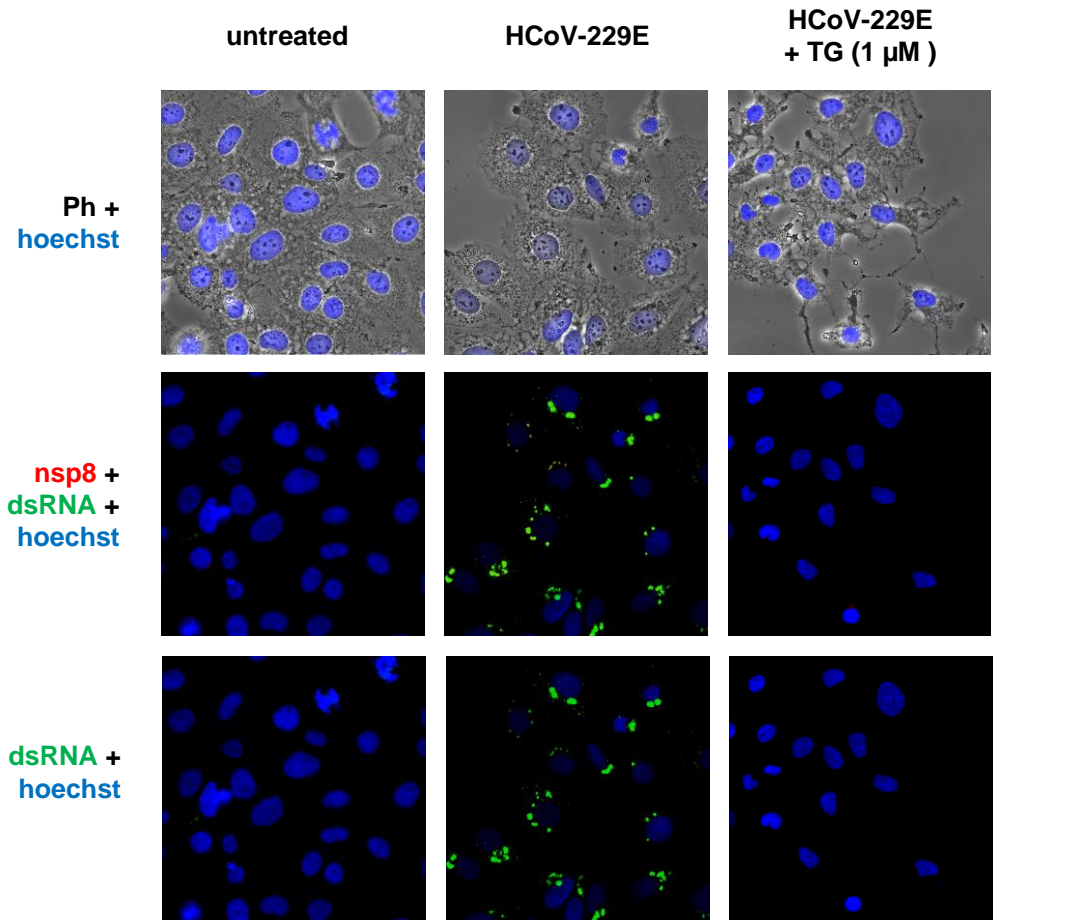
All bar graphs show means \pm s.d.; asterisks indicate p values ($*p \leq 0.05$, $**p \leq 0.01$, $***p \leq 0.001$, $****p \leq 0.0001$) obtained by two-tailed unpaired t-tests.

To follow up on the profound inhibition of HCoV-229E replication seen on multiple levels in the 24 hours simultaneous thapsigargin + CoV condition with an orthogonal cell imaging method, an indirect immuno-fluorescent assay (IFA) was carried out.

For this assay, Huh7 cells were infected with HCoV-229E alone, simultaneously treated and infected with thapsigargin and HCoV-229E, or left without treatment or infection. IFA was then performed as described in the Methods section using nsp8 (red fluorescence) and double-strand (ds) RNA (green fluorescence) antibodies to visualize viral replication and Hoechst staining to visualize the nuclei of the cells.

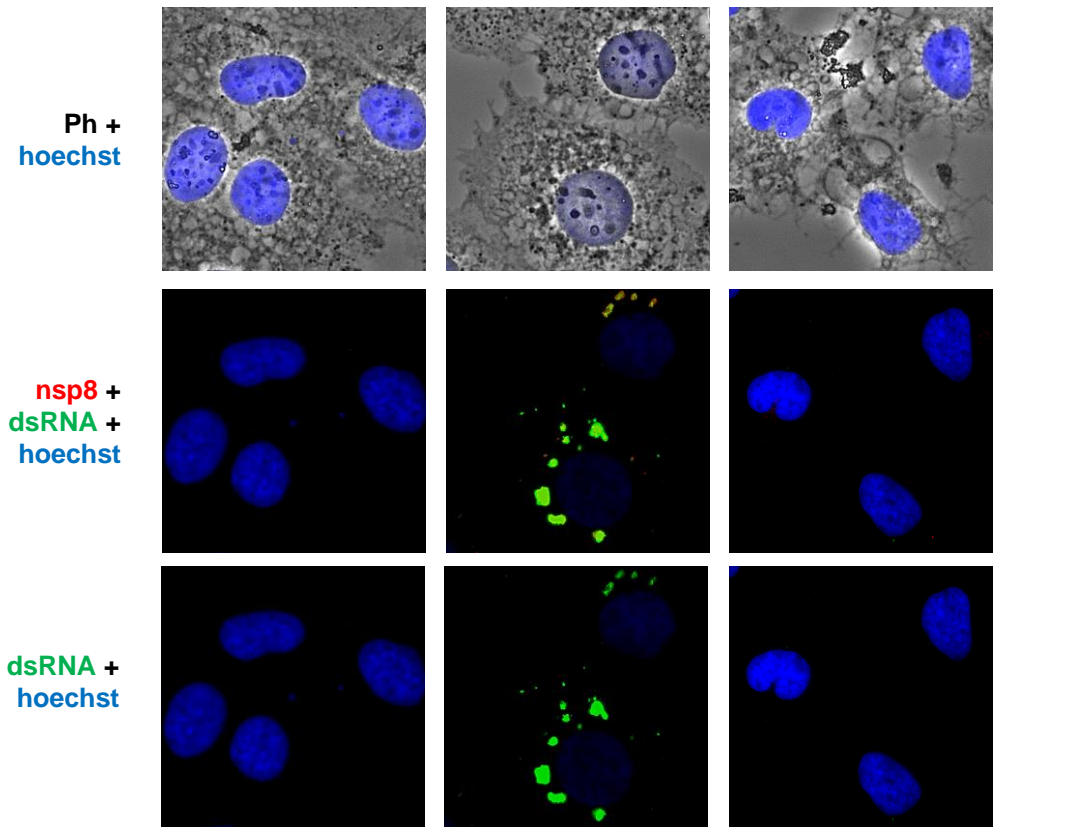
Infected samples showed a red and green fluorescent signal around the nucleus indicating active viral replication sites. Confirming the observations on the Western blot (Fig. 15), infected cells simultaneously treated with thapsigargin showed no red or green fluorescent signals (Fig. 16).

20x magnification



40x magnification zoom in

50 μ m



50 μ m

Figure 16: The anti-viral effect of thapsigargin observed by immuno-florescence analysis.

Huh7 cells were seeded into Ibidi 6 channel μ -Slides and subsequently either left untreated, infected with MOI of 1 of HCoV-229E for 24 hours, or simultaneously infected with HCoV-229E and treated with 1 μ M of thapsigargin (TG) for 24 hours. Cells were then subjected to IFA protocol as described in the method section.

Images of one representative replica (out of two biological replicas) of fluorescently labeled Huh7 cells with nsp8 and double-strand RNA antibodies to visualize the HCoV-229E replication sites. Phase-contrast (Ph) light microscopy images were used to indicate the morphology of the cells. Hoechst 33342 was used to stain the nuclei (blue). The experiment was performed together with Dr. Christin Mayer-Buro (Prof. Kracht working group). Dr. Mayer-Buro helped perform the biological replicas and analyzing the data.

Taken together, these data indicated a strong anti-viral effect of thapsigargin on HCoV-229E replication in Huh7 cells that can be seen on multiple levels of the viral life cycle.

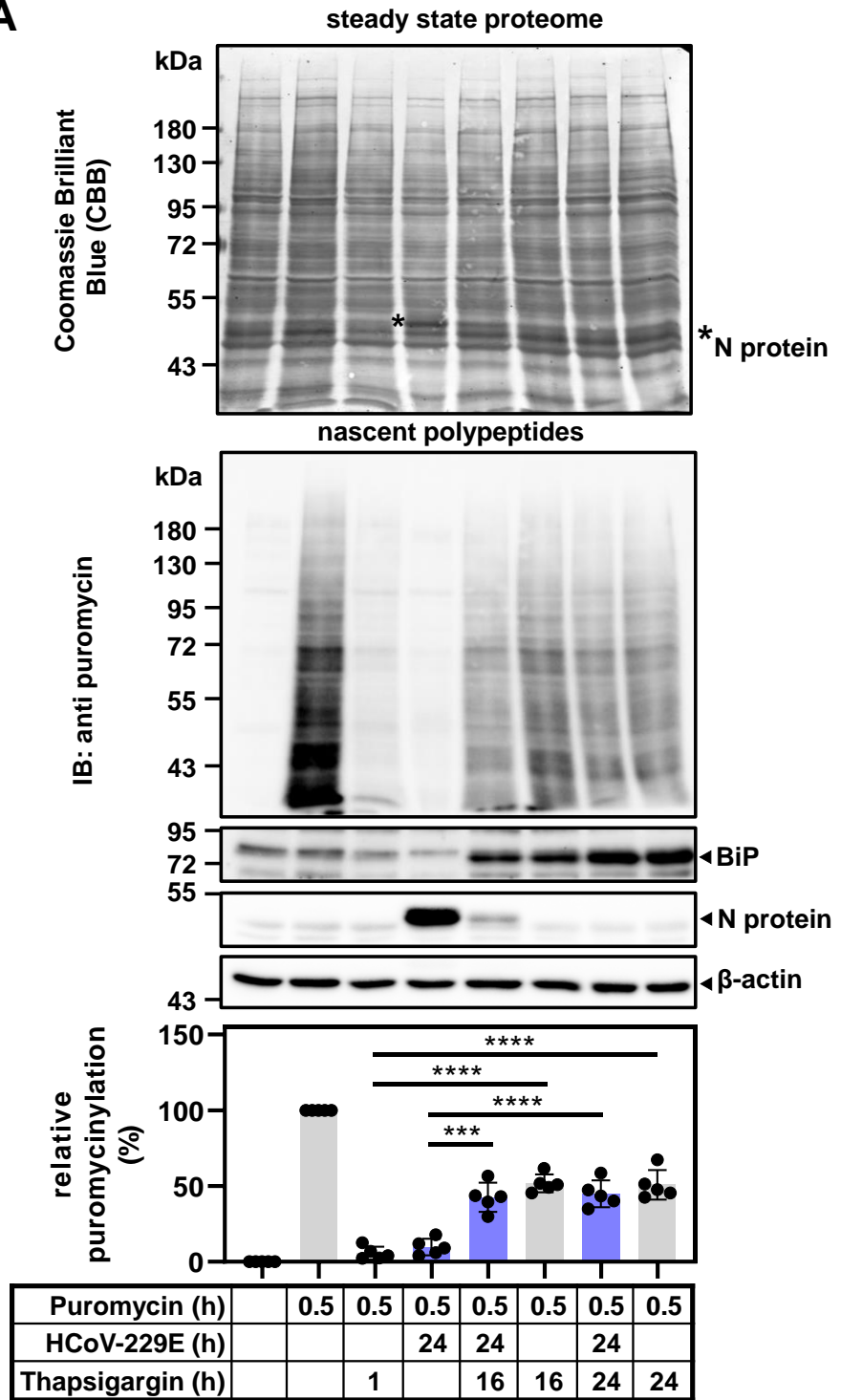
4.1.4 Effect of prolonged activation of ER stress pathways by thapsigargin on virus-induced translational shutdown

The phosphorylation of eIF2 α on serine 51 remained multiple folds higher than the steady-state level in all thapsigargin-treated conditions with 1 hour of thapsigargin showing the highest activation (Fig. 15 C & D). To investigate whether this continuous activation is paralleled by a continuous inhibition of the de-novo synthesis of proteins, a puromycinylation assay was carried out using the same conditions described in figure 15 A.

Samples treated with thapsigargin for 1 hour and samples infected with HCoV-229E alone for 24 hours showed a profound drop in newly translated polypeptides. On the other hand, long-term treatments with thapsigargin (16 and 24 hours) of both uninfected or infected cells resulted in a partial reversal of the translational shutdown. This indicated a possible attempt to restore normal cellular functioning induced after the long thapsigargin treatment. Interestingly, this partial reversal of the translational shutdown excluded the investigated viral proteins in infected samples (Fig. 17 A). It also did not coincide with a reduction in the phosphorylation of eIF2 α on serine 51 if compared to the phosphorylation levels induced by CoV alone condition (Fig. 15 C & D).

With the same conditions described above, a puromycinylation assay was carried out using an indirect immunofluorescence assay. To visualize the levels of puromycin labelling and viral replication, puromycin (green fluorescence) and NSP8 (red fluorescence) antibodies were used respectively. In comparison to the control sample without the puromycin pulse, cells pulsed with puromycin displayed a strong green fluorescent signal. The 1 hour thapsigargin treatment led to a reduction in the cells displaying the green signal. To a lesser extent, cells infected with HCoV-229E or simultaneously infected and treated with thapsigargin showed a variety of green signal strengths ranging from reduced to disappearing or even increased in some cells (Fig. 17 B).

A



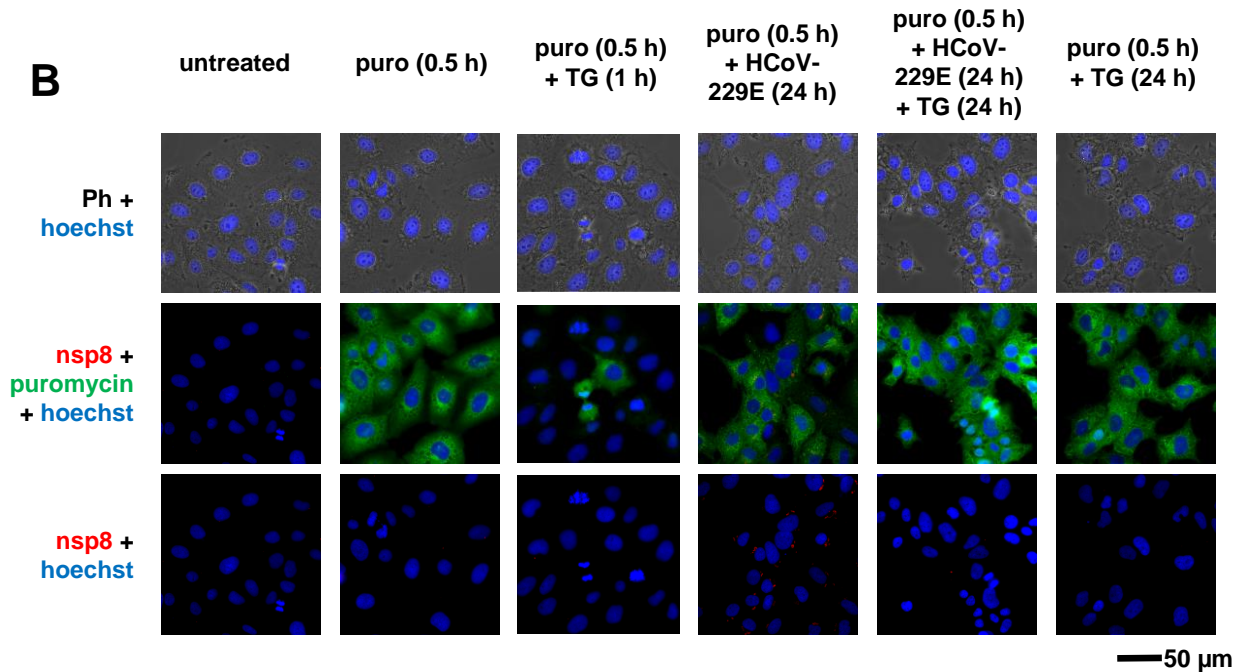


Figure 17: Prolonged treatment of infected cells with thapsigargin partially reverses the HCoV-229E-induced translational shutdown.

Huh7 cells with the same conditions described in figure 15 were pulsed with 3 μ M of puromycin for 30 minutes before the end of the experiment. As a control, a sample with no treatment or infection was left without the puromycin pulse. Thereafter, cells seeded on dishes were harvested and whole-cell extracts using the special lysis buffer were subjected to Western blotting, while cells seeded in Ibidi were subjected to IFA protocol.

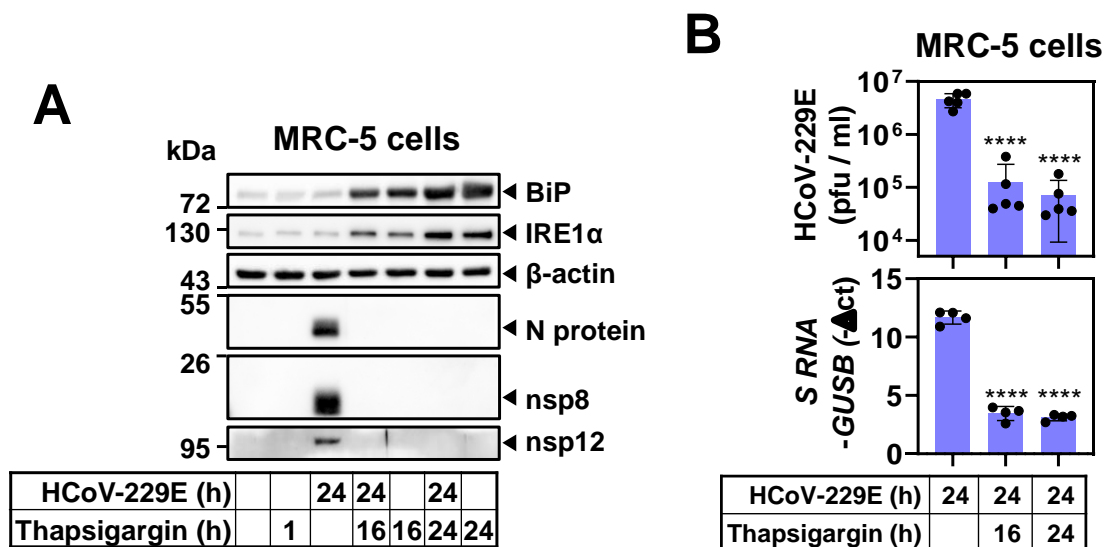
(A) Immunoblot of a representative replica (out of five biological replicas) using indicated antibodies. CBB staining of the corresponding immunoblot was used for loading control and visualization of steady-state protein level. The lower graph shows the corresponding quantification from the five independent biological replicas relative to the puromycin-pulsed untreated/uninfected control. β -actin was used as a loading control. The experiment was performed together with the technician Hendrik Weiser. Hendrik Weiser helped perform the biological replicas. The figure was adapted from Fig. 3e, Shaban et al. under a Creative Commons Attribution 4.0 International License (Shaban et al. 2021).

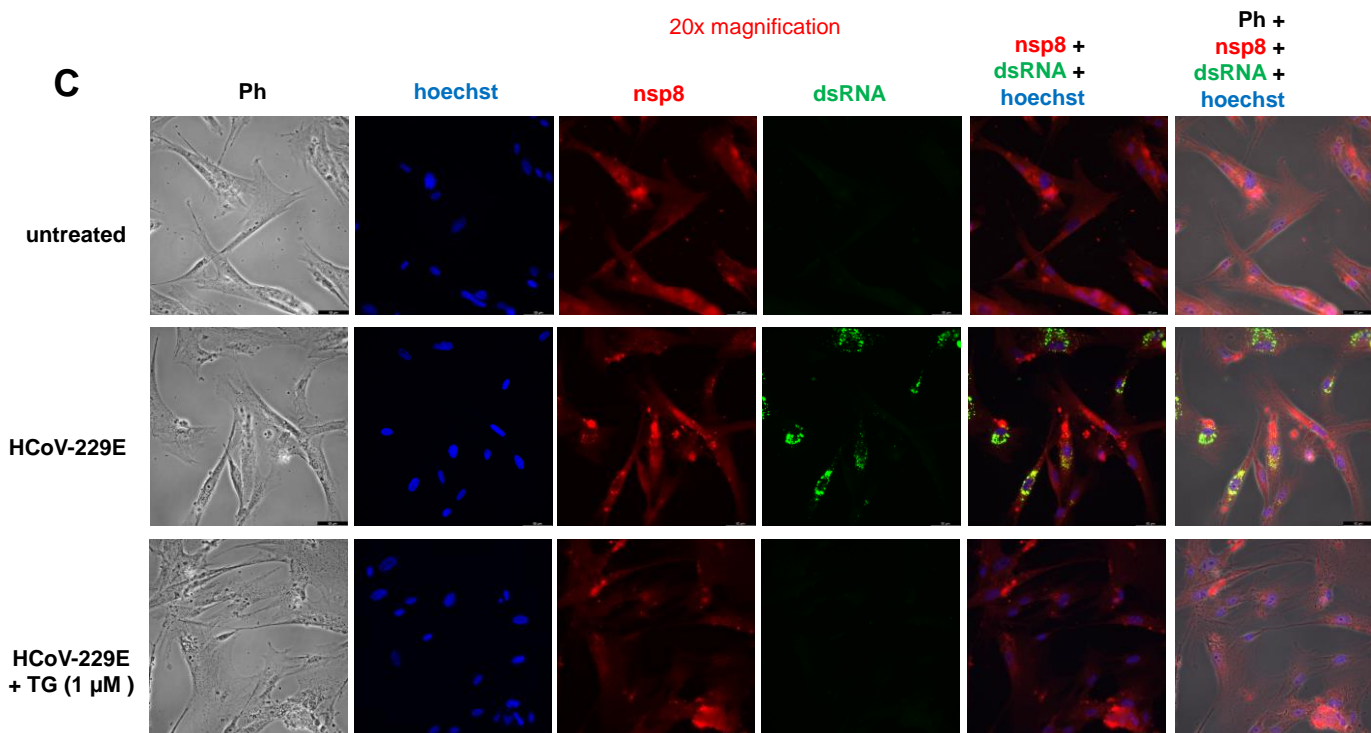
(B) Images of one representative replica (out of two biological replicas) of fluorescently labeled Huh7 cells with NSP8 (red) and puromycin (green) antibodies along with phase-contrast (Ph) light microscopy images indicating the HCoV-229E replication sites, translation levels, and the morphology of the cells respectively. The first set of images (vertically) was left without the puromycin pulse as negative control. Hoechst 33342 was used to stain the nuclei (blue). TG: thapsigargin. The experiment was performed together with Dr. Christin Mayer-Buro. Dr. Mayer-Buro helped perform the biological replicas.

Together, these data indicated a possible adaptive response induced by prolonged exposure of the cells to thapsigargin while concurrently maintaining a strong anti-viral state. Nevertheless, the discrepancy in the level of signal reduction in CoV-infected samples between the IFA and the western blot necessitates further investigation. Possible reasons for such discrepancy can be partially attributed to heterogeneity in infection/treatment that is hard to see on Western blotting, the different number of cells used, or the nature of each assay/readout itself.

4.1.5 Reproducibility of thapsigargin anti-viral effect in a different cellular model

To test the reproducibility of the main findings mentioned in section 4.1.3, in a physiologically more relevant cellular model, MRC-5 cells were used. MRC-5 is an embryonic lung-derived, diploid fibroblast cell line that can be readily infected with HCoV-229E. Cells uninfected or infected with MOI of 1 of HCoV-229E were either treated with 1 μ M of thapsigargin for 24 hours or for 16 hours. For control samples, uninfected cells were either treated with 1 hour of thapsigargin (1 μ M) or left without any treatment. Supporting the results obtained in Huh7 cells, all investigated viral proteins were undetectable on Western blot in infected samples treated with thapsigargin (Fig. 18 A). These results were further supported by IFA, intracellular viral RNA levels assessed by RT-qPCR, and the viral titer assessed by plaque assay (Fig. 18 B & C). Moreover, increase in the levels of IRE1 α and BiP proteins in cells treated with 24 or 16 hours of thapsigargin has also been observed (Fig. 18 A).





40% increase in contrast
and brightness

Figure 18: Thapsigargin anti-viral effect is reproducible in MRC-5 cells.

MRC-5 cells with the same conditions described in figure 15 were harvested and cell pellets used for RNA extraction followed by Western blotting (using the special lysis buffer), RT-qPCR and immuno-fluorescence analysis. Supernatants from virus-infected conditions were collected and assessed for the production of infectious particles using plaque assay.

(A) Immunoblot of indicated host and viral proteins of one representative replica (out of two biological replicas). β -actin was used as a loading control.

(B) The corresponding titer change of HCoV-229E assessed using plaque assay of five independent biological replicas (upper graph). RT-qPCR was used to assess the levels of the viral spike RNA extracted from infected cells of four biological replicas (lower graph). The housekeeping gene GUS β was used for normalization.

(C) Cells seeded on Ibidi were subjected to IFA protocol. Images of one representative replica (out of two biological replicas) of fluorescently labeled MRC-5 cells with nsp8 (red) and double-strand RNA (green) antibodies along with phase-contrast (Ph) light microscopy images indicating the HCoV-229E replication sites and the morphology of the cells respectively. Hoechst 33342 was used to stain the nuclei (blue).

The panels A and B were adapted from Fig. 4a & b, Shaban et al. under a Creative Commons Attribution 4.0 International License (Shaban et al. 2021). The experiment was performed together with the technician Hendrik Weiser and Dr. Christin Mayer-Buro. They both helped perform the biological replicas.

Taken together, these results indicated a cell-type independent anti-viral effect of thapsigargin on HCoV-229E replication.

4.1.6 Cytotoxic and effective concentrations of thapsigargin in Huh7 cells for HCoV-229E inhibition

The phase contrast (light) microscopy images of Huh7 cells treated with 24 hours of thapsigargin indicated a change in cell morphology and an increase in cellular death (Fig. 16). It was therefore essential, to quantify and correlate the anti-viral effects of thapsigargin with cell viability. To investigate the effect of thapsigargin on Huh7 cells viability, MTS assay was performed.

The MTS assay principle relies on the reduction of the MTS tetrazolium compound by NAD(P)H-dependent dehydrogenase enzymes present in viable, metabolically active cells. This reduction generates a colored formazan dye that is soluble in cell culture media. The concentration of reduced dye is then quantified by directly measuring the absorbance at 490-500 nm in miniaturized cell culture systems such as 96-well plates.

The viability of Huh7 cells treated with DMSO (as solvent control) was compared to cells treated with increasing doses of thapsigargin with or without HCoV-229E (MOI of 1) infection, for 24 hours. The infection of the cells for 24 hours with HCoV-229E did not result in any appreciable drop in cellular viability (mean $90.02 \pm 12.32\%$). Contrarily, 50 μM of thapsigargin for 24 hours resulted in nearly complete death of both infected and uninfected samples. At concentrations of 0.1 μM and 1 μM of thapsigargin, a reduction to $76.6 \pm 7.9\%$ of cellular viability has been observed. From these MTS data, a half-maximum cellular cytotoxic concentration (CC_{50}) of 5.9 μM for thapsigargin-alone treatment and a slightly lower CC_{50} of 4.6 μM of the combined thapsigargin + CoV condition has been calculated. This placed the used 1 μM concentration well below the CC_{50} of thapsigargin cytotoxic effect (Fig. 19 A).

To determine the half-maximum effective concentration (EC_{50}) of HCoV-229E inhibition by thapsigargin in Huh7 cells, infected cells were treated with increasing concentrations of thapsigargin. A plaque assay was then performed. Interestingly, the inhibitory effect of thapsigargin plateaued after a concentration of 0.01 μM (10 nM). The calculated EC_{50} from these data was 1 nM (Fig. 19 B).

Remdesivir is a well-known nucleotide analog, frequently used to inhibit multiple RNA viruses including coronaviruses (Kokic et al. 2021; Tchesnokov et al. 2019). To compare the efficacy and cytotoxicity of thapsigargin in inhibiting HCoV-229E to remdesivir, Huh7 cells infected with HCoV-229E were treated with increasing concentrations of remdesivir. MTS and plaque assays were then carried out as indicated above. The calculated CC_{50} from these data was higher than 100 μM while the EC_{50} amounted to 10 nM (Fig. 19 C). The relatively high CC_{50} of Remdesivir can be partially explained by the specificity of this drug to the viral RNA-dependent RNA polymerase, excluding its usage by the host DNA-dependent RNA polymerase or other enzymes and hence, less cytotoxic effects.

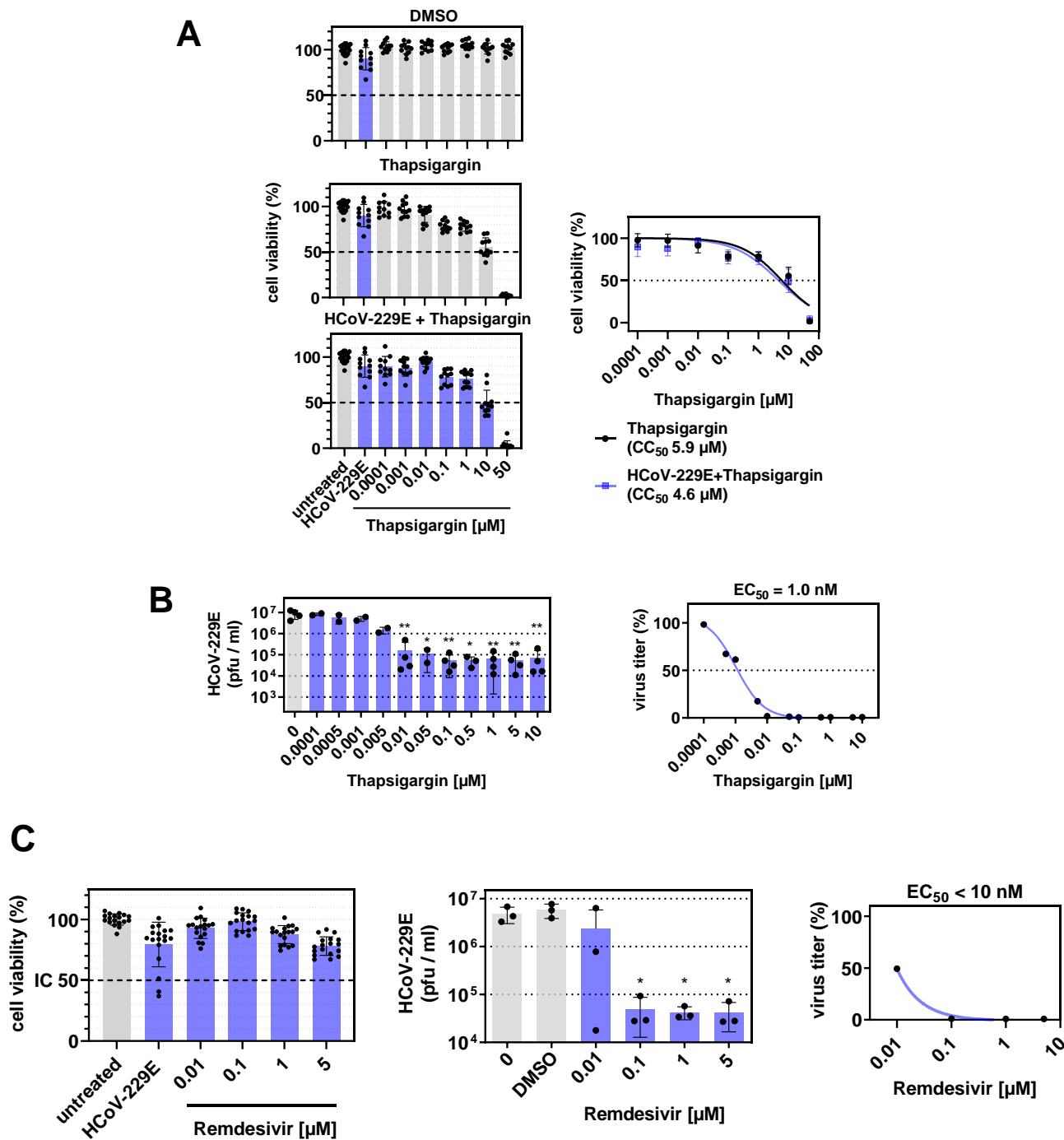


Figure 19: Thapsigargin inhibits HCoV-229E replication in Huh7 cells with an EC_{50} in the lower nanomolar range while exerting cytotoxicity with a CC_{50} in the micromolar range.

Huh7 cells were left either untreated or treated with the indicated concentrations of DMSO as control. Cells uninfected or infected for 24 hours with HCoV-229E (MOI of 1) were treated with the indicated concentrations of thapsigargin or remdesivir for 24 hours. Cells seeded on 96-well plates with these conditions were then subjected to the MTS protocol according to the manufacturer's recommendation. For plaque assay, cells were seeded in dishes. Supernatants from virus-infected conditions with different thapsigargin or remdesivir concentrations were collected and assessed for the production of infectious particles.

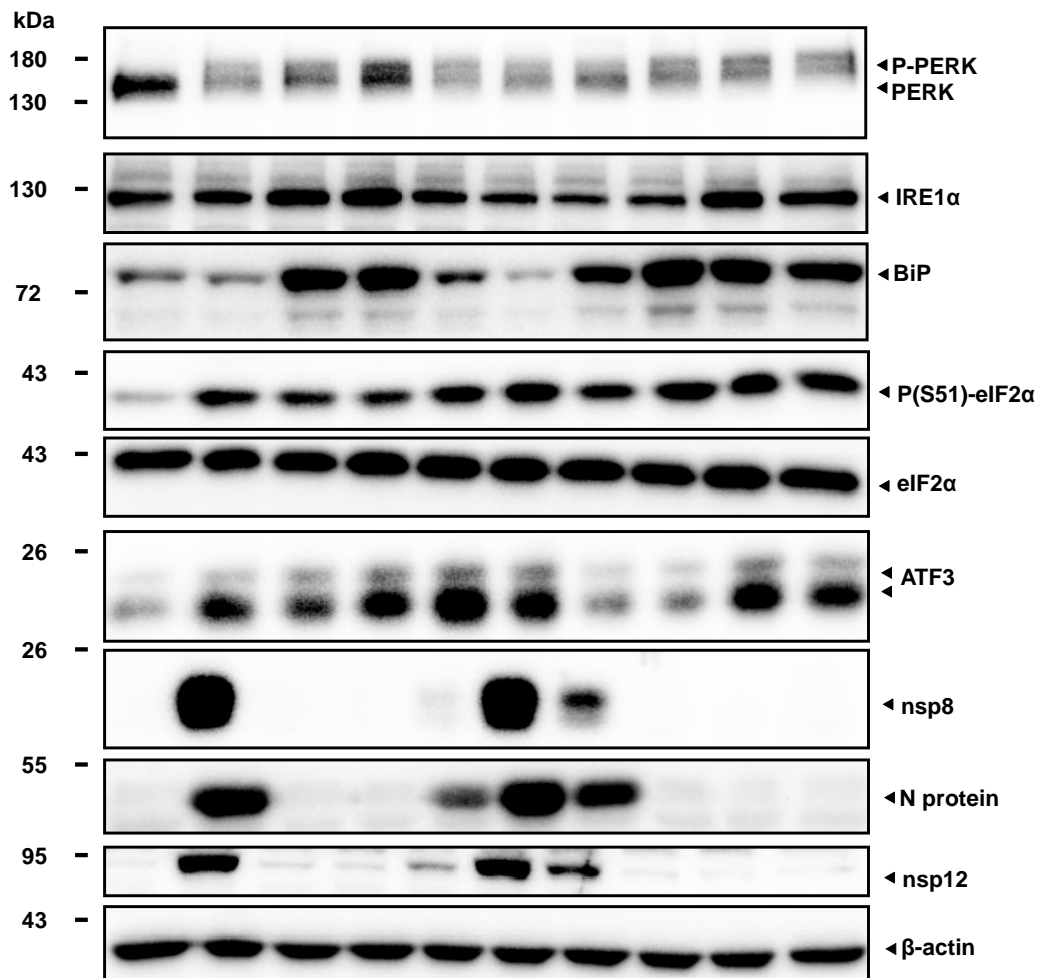
(A) MTS assay quantifications of five biologically independent replicas showing the effect of increasing concentrations of thapsigargin on Huh7 cells survivability when left uninfected (middle graph) or infected (lower graph) with HCoV-229E as compared to DMSO control treatment (upper graph). The right subpanel indicates cytotoxic concentration (CC_{50}) calculations derived from the left subpanels.

(B) Plaque assay quantification of at least two biological replicas showing the dose-dependent inhibition of HCoV-229E by thapsigargin (left graph) and the derived effective concentration (EC_{50}) value (right graph).

(C) Left graph indicates MTS assay quantification of the effect of increasing concentrations of remdesivir on Huh7 cell's survivability compared to cells infected with HCoV-229E or untreated/uninfected control. The middle graph indicates plaque assay quantification of three biological replicas showing the dose-dependent inhibition of HCoV-229E by remdesivir. The right panel shows the derived effective concentration (EC_{50}) from the middle panel.

The experiment was performed together with the technician Hendrik Weiser and Dr. Christin Mayer-Buro. They both helped perform the biological replicas. Hendrik Weiser performed the experiment shown in panel B. The figure was adapted from Fig. 3 a, b & c and supplementary figure 5 Shaban et al. under a Creative Commons Attribution 4.0 International License (Shaban et al. 2021).

To investigate the levels of host and viral proteins as function of thapsigargin concentration or time of addition, Huh7 cells were infected with MOI of 1 of the virus and either simultaneously treated with varying concentrations of thapsigargin or treated with 1 μ M of thapsigargin at 4, 8, or 14 hours post-infection, the results were then visualized on western blots. Expectedly, from a concentration of 10 nM (0.01 μ M) the viral N protein, nsp8, and nsp12 were undetectable on the blot, where a concentration of 1 nM resulted in approximately 50% reduction in the levels of these viral proteins. Interestingly, adding 1 μ M of thapsigargin even 14 hours after the start of the infection still resulted in a profound (though not complete) reduction in the levels of the investigated viral proteins indicating a fast switch to an anti-viral state in the host upon thapsigargin treatment. Host factors of BiP and IRE1 α showed the already described increase in their protein levels at the higher, anti-viral concentrations of thapsigargin. In line with results shown before (Fig. 15), the phosphorylation of eIF2 α on serine 51 remained higher than the untreated control level throughout all the investigated conditions (Fig. 20).



HCoV-229E (24 h)		+	+	+	+	+	+	+	+	+
Thapsigargin (X h, Y μM)			4 hPI, 1 μM	8 hPI, 1 μM	14 hPI, 1 μM	0 hPI, 0.1 nM	0 hPI, 1 nM	0 hPI, 10 nM	0 hPI, 100 nM	0 hPI, 1 μM

Figure 20: Thapsigargin inhibition of HCoV-229E is readily visible at lower concentrations and up to 14 hours post-infection.

Huh7 cells were left untreated or infected with HCoV-229E (MOI of 1) for 24 hours and either simultaneously treated with the indicated concentrations of thapsigargin for 24 hours or treated with 1 μM of thapsigargin at 4, 8, or 14 hours post-infection (hPI). Whole-cell extracts using the special lysis buffer were then subjected to western blot analysis. Cellular and viral factors were investigated using the indicated antibodies. β-actin was used as a loading control.

Altogether, the data above indicated a strong, fast, and possibly virus-entry independent anti-viral effect of thapsigargin on HCoV-229E replication within the non-toxic range of the compound concentrations.

4.1.7 Durability of thapsigargin inhibition of HCoV-229E beyond 24 hours

Given the robustness of thapsigargin inhibition of HCoV-229E replication observed within the investigated 24 hours experimental condition, the durability of this effect over prolonged experimental time points beyond this initial condition was investigated, to address the question of a single application of the compound may lead to an irreversible suppression of the virus. For this, the viability of Huh7 cells treated with thapsigargin and/or infected with HCoV-229E over a period of 96 hours was tested by MTS assay. At this time point, infected cells showed a sharp decrease in viability with only 20% of the cells surviving while uninfected or infected cells treated with 1 μ M of thapsigargin showed a higher survivability rate of around 50% hinting back at the possible adaptive/protective effect of thapsigargin (Fig. 21 A).

The production of infectious particles in infected cells, treated with thapsigargin at the 96-hour time point showed a stark decline amounting to zero plaques in the lowest tested virus dilution in 2 out of 3 biological replicas when assessed by plaque assay. The intracellular viral RNA levels (tested through RT-qPCR) showed a comparably strong drop (Fig. 21 B).

Furthermore, to confirm whether the continuous presence of thapsigargin in the medium after the initial treatment is important for the durability of the anti-viral effect, Huh7 cells uninfected or infected with HCoV-229E for 48 hours were treated with thapsigargin for 48 hours (simultaneous infection/treatment) or 47 hours (treatment 1 hour after infection). Eight hours after the beginning of the 48 hours experiment, the cell-culture medium was removed, cells were washed and a new fresh medium was added. Cells were further incubated for 36 hours (totaling 48 hours since the start of the experiment). Whole-cell extracts were then subjected to western blot analysis. Investigated viral protein levels indicated no reversal of the anti-viral effect as a result of the medium exchange supporting the conclusion of the long-lasting anti-viral effect of thapsigargin (Fig. 21 C).

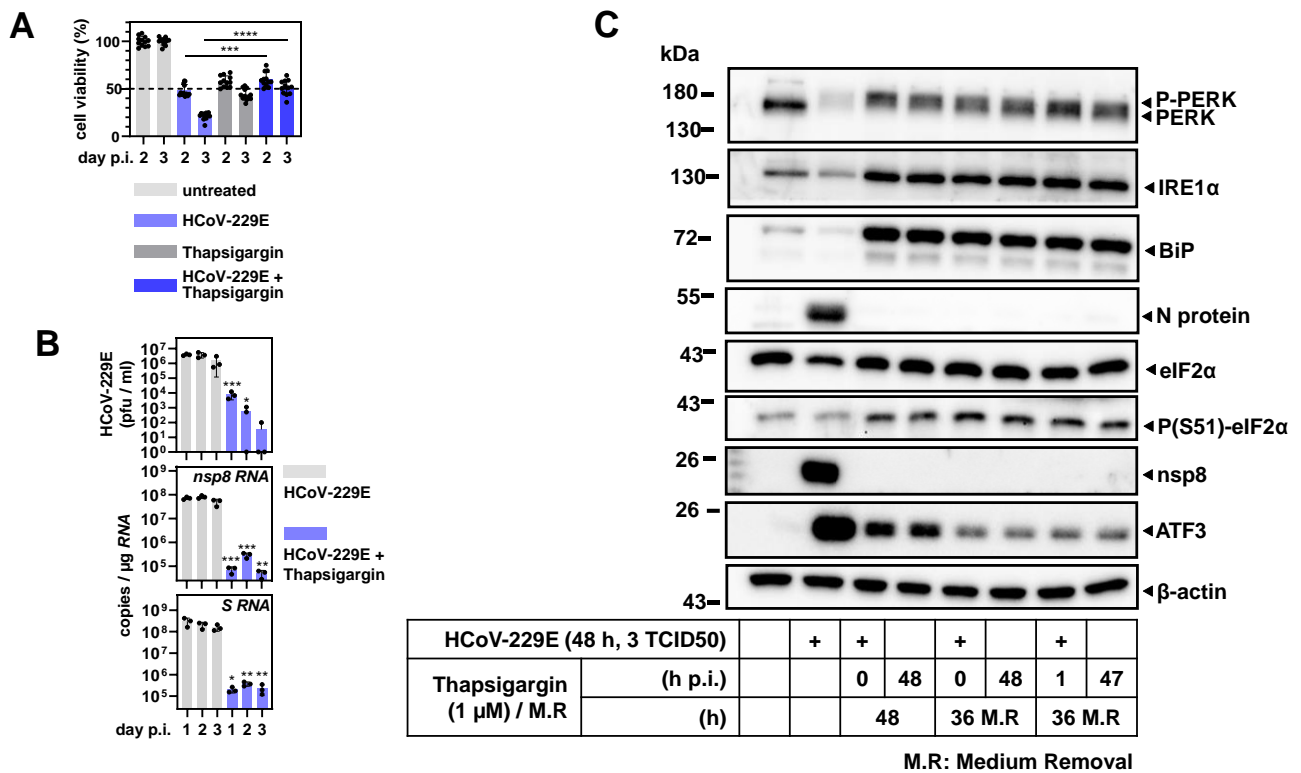


Figure 21: Thapsigargin inhibition of HCoV-229E is durable over prolonged incubation periods and after medium exchange.

Huh7 cells seeded in 96-well plates were left either untreated, infected with HCoV-229E (MOI of 1), treated with 1 μM of thapsigargin, or simultaneously infected and treated. MTS protocol according to the manufacturer's recommendation was then carried out at each of the indicated time points (in days post-infection, day p.i.). For plaque assay and RT-qPCR, cells were seeded in dishes. Cell pellets at indicated time points were used for RNA extraction followed by subsequent RT-qPCR and absolute quantification of viral RNA copies. Supernatants from virus-infected conditions were collected at indicated time points and assessed for the production of infectious particles. For Western blotting, Huh7 cells uninfected or infected with MOI of 1 of HCoV-229E for 48 hours were treated with 1 μM of thapsigargin for 48 hours (simultaneous infection/treatment) or 47 hours (treatment 1 hour after infection). Eight hours after the beginning of the experiment, the cell-culture medium was removed, cells were washed and a new fresh medium was added. Cells were further incubated for 36 hours (totaling 48 hours since the start of the experiment). Whole-cell extracts using the special lysis buffer were then subjected to western blot analysis.

(A) Survivability of Huh7 cells treated with 1 μM of thapsigargin and/or infected with HCoV-229E over a period of 3 days compared to the untreated control, assessed by MTS assay.

(B) The viral titers assayed by plaque assay (upper panel) and copy numbers of intracellular viral *nsp8* and *S* RNAs assessed by RT-qPCR (three biologically independent experiments).

(C) Immunoblots analysis with indicated viral and host antibodies.

The experiments shown in panels A & B were performed together with the technician Hendrik Weiser and Dr. Christin Mayer-Buro. They both helped perform the biological replicas. Dr. Mayer-Buro performed the qPCR absolute quantification shown in panel B. The panels A and B were adapted from Fig. 3d, Shaban et al. under a Creative Commons Attribution 4.0 International License (Shaban et al. 2021).

Taken together, these data indicated a strong, beyond 24 hours durable anti-viral effect of thapsigargin on inhibiting HCoV-229E replication.

4.1.8 Inhibitory effect of thapsigargin on the highly pathogenic MERS-CoV and SARS-CoV-2 replication

The above-mentioned experiments indicated a strong anti-viral effect of thapsigargin on HCoV-229E replication in Huh7 and MRC-5 cells. To address whether this anti-viral effect can also be observed for two other, highly pathogenic, coronaviruses namely MERS-CoV and SARS-CoV-2, a new set of experiments with these two viruses was carried out.

Huh7 cells uninfected or infected with MERS-CoV for 12 and 24 hours were treated with either 1 or 0.4 μM of thapsigargin. For both time points of infection and both concentrations of thapsigargin, a strong reduction in the viral N protein was observed on the western blot. This reduction was mirrored by at least 3 \log_{10} folds drop in the production of infectious particles observed using the plaque assay. As previously described, the levels of both host factors, BiP and IRE1 α , strongly increased with thapsigargin treatments (Fig. 22 A).

To determine the half-maximum effective concentration (EC_{50}) of MERS-CoV inhibition by thapsigargin in Huh7 cells, infected cells were treated with increasing doses of thapsigargin concentrations. A plaque assay was then performed. The calculated EC_{50} from these data amounted to 4.8 nM (Fig. 22 C).

The same set of experiments was performed for SARS-CoV-2 in VERO-E6 cells (African green monkey kidney cell line used extensively as a cellular model to study SARS-CoV-2 replication). For both indicated concentrations of thapsigargin, a drop in the viral titer and strong reduction of the viral N protein can be observed, though to a lesser degree than the effects observed in Huh7 cells infected with MERS-CoV or HCoV-229E. The calculated EC_{50} of thapsigargin inhibition of SARS-CoV-2 was 260 nM. The viability of VERO-E6 cells treated with the indicated gradient of thapsigargin concentrations was assessed by MTT or ATPLit assays and CC_{50} of 18.25 μM was accordingly calculated (Fig. 22 B & D).

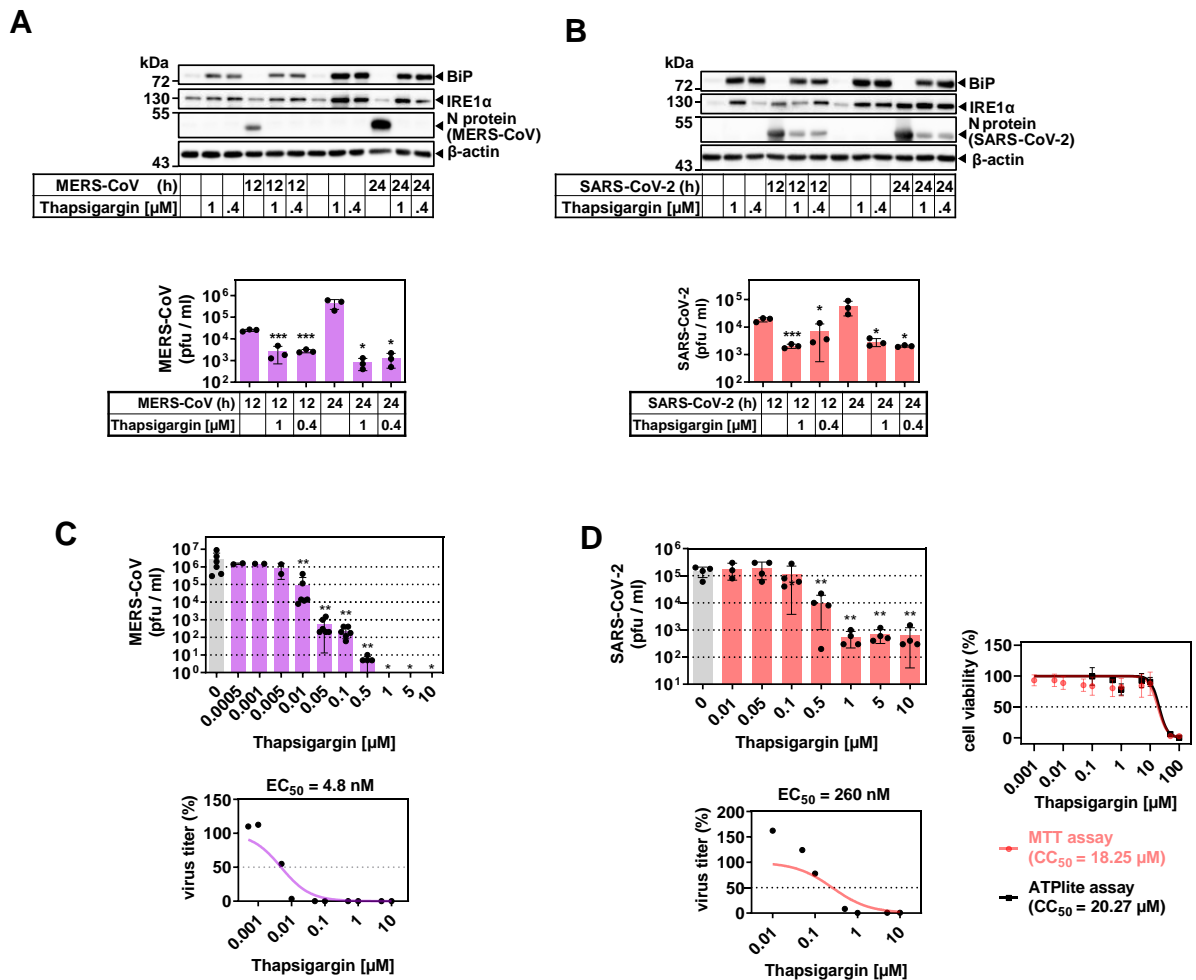


Figure 22: Thapsigargin inhibits the replication of MERS-CoV and SARS-CoV-2 in cellular models.

Analysis of the effect of different concentrations of thapsigargin on Huh7 or VERO-E6 cells uninfected or infected with 12 or 24 hours of MOI of 0.5 of MERS-CoV or MOI of 0.5 of SARS-CoV-2 respectively.

(A) Uninfected or infected Huh7 cells with 12 or 24 hours of MOI of 0.5 of MERS-CoV were treated with 1 or 0.4 μ M of thapsigargin. Upper panel shows immunoblots of a representative replica (out of three biological replica) of whole-cell extracts using SDS buffer of Huh7 cells with the mentioned conditions. Lower panel shows the corresponding changes in viral titer assessed by plaque assay of three independent biological replicas.

(B) Upper, and lower panels show similar analysis to panel A for VERO-E6 cells uninfected or infected with MOI of 0.5 of SARS-CoV-2 that were treated with 1 or 0.4 μ M of thapsigargin.

(C) Dose-dependent inhibition of MERS-CoV (MOI of 0.5) by thapsigargin assessed by two to six independent biological replicas using plaque assay (upper panel) and the corresponding calculated EC₅₀ (lower panel).

(D) Similar analysis to panel C for VERO-E6 cells infected with MOI of 0.5 of SARS-CoV-2 (upper and lower, three to four independent biological replicas). The right graph indicates the CC₅₀ of thapsigargin in VERO-E6 assessed by MTS or ATPLite assays (of at least three independent biological replicas).

The infection experiments were performed together with Hendrik Weiser and Dr. Christin Mueller (Prof. Ziebuhr working group). Dr. Mueller performed all SARS-CoV-2 and MERS-CoV infections, plaque assays and cell viability assays in the BSL3 laboratory of the Institute of Medical Virology, Justus Liebig University Giessen. Cell pellets from infected cells were then transferred to the Rudolf Buchheim Institute of Pharmacology and Western blot experiments were performed together with Hendrik Weiser. The figure was adapted from Fig. 4 e, f, g, h, i, j & k, Shaban et al. under a Creative Commons Attribution 4.0 International License (Shaban et al. 2021).

The data above indicated a strong, cell-type independent anti-viral effect of thapsigargin against three different coronaviruses with EC_{50} in the lower nanomolar range and a CC_{50} well above the used anti-viral concentration.

4.1.9 PERK role in the thapsigargin-induced anti-viral effect

PERK is a major UPR and ER stress sensor that is activated upon infection with HCoV-229E and whose inhibition by pharmacological means resulted in a significant drop in the virus replication as described in previous sections.

To investigate whether inhibiting PERK in the context of thapsigargin treatment would affect the anti-viral state induced by thapsigargin, GSK2656157 (a newer optimized version of the same PERK inhibitor GSK2606414 mentioned previously, see Fig. 12 above) was utilized. For this purpose, Huh7 cells uninfected or infected with HCoV-229E were treated with increasing concentrations of GSK2656157 or 1 μ M of thapsigargin. As a control, uninfected or infected cells were treated with DMSO (solvent control) or left without any treatment or infection (steady-state control). Whole-cell extracts were then subjected to Western blot analysis. Cells treated with 1 or 10 μ M of GSK2656157 showed an “inactivated” PERK band (as evidenced by the loss of slower migrating, phosphorylated forms of PERK) and reduced phosphorylation of eIF2 α on the corresponding immunoblots. The viral N protein showed a dose-dependent reduction of its levels (Fig. 23 A left). The corresponding viral titer showed a drop of approximately 1 \log_{10} fold at a concentration of 10 μ M (Fig. 23 A right). Interestingly, lower concentrations of the inhibitor did not result in any significant drop although the corresponding viral N protein was reduced by around 50% on the immunoblot. The cell viability assay did not show any significant increase in cytotoxicity at the indicated concentrations of the inhibitor (Fig. 23 B). Plaque assay of viral particles production in Huh7 cells infected with MERS-CoV and treated with 10 or 50 μ M of GSK2656157 showed a significant decrease of about 2 \log_{10} folds (Fig. 23 D).

Combinatory treatment of thapsigargin and GSK2656157 of HCoV-229E-infected cells with indicated conditions in figure 23 C did not show any significant additive inhibitory effect when whole-cell extracts were analyzed on western blot or supernatants of infected samples assessed for infectious particles using plaque assay.

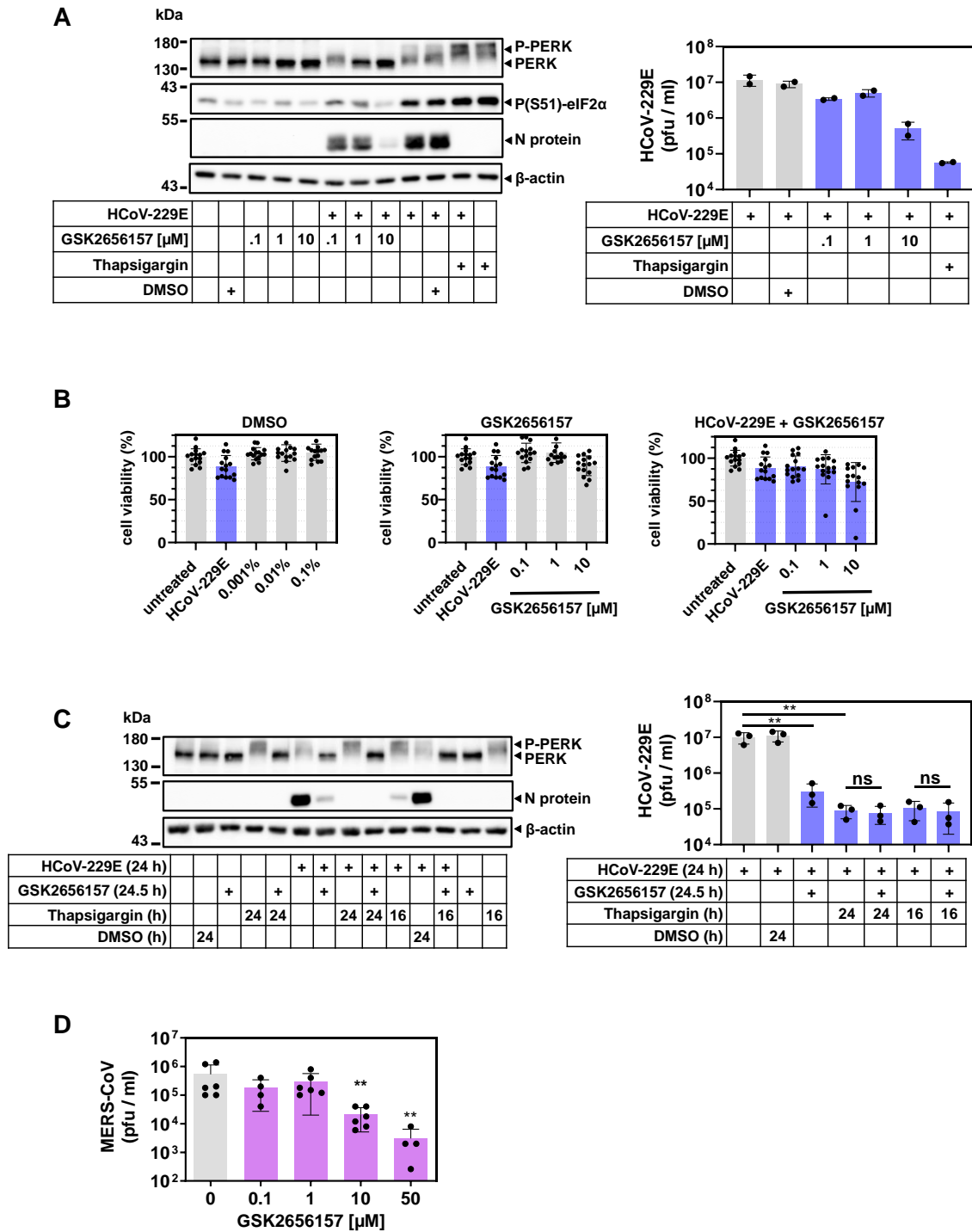


Figure 23: PERK inhibition does not affect the anti-viral state induced by thapsigargin.

Analysis of the effect of different concentrations of GSK2656157 and/or 1 μ M of thapsigargin on Huh7 cells uninfected or infected with 24 hours of HCoV-229E (MOI of 1) or 24 hours of MERS-CoV (MOI of 0.5) and on the replication of the two investigated viruses. GSK was added half an hour before infection/treatment.

(A) Left panel indicates Western blot analysis of Huh7 cells uninfected or infected with 24 hours of HCoV-229E. The cells were treated with the indicated concentrations of GSK2656157 or 1 μ M of thapsigargin. As a control, uninfected or infected cells were treated with DMSO (solvent control) or left without any treatment or infection (steady-state control). Whole-cell extracts using the special lysis buffer were then subjected to Western blot analysis using the indicated host and viral antibodies. Right panel shows the corresponding change in viral titer from supernatants of infected samples with indicated conditions assessed by two biological replicas.

(B) Huh7 cells viability assessed using MTS assay. The cells were treated three different concentrations of GSK2656157 and/or infected with 24 hours of HCoV-229E (MOI 1) as indicated (middle and right panels). Cells treated with corresponding DMSO concentrations were used as control (left panel).

(C) Left panel shows Western blot analysis of whole-cell extracts of Huh7 cells uninfected or infected with HCoV-229E (MOI of 1) that were treated with 10 μ M of GSK2656157 and/or 1 μ M of thapsigargin (see figure for details of the conditions). Right panel indicates the corresponding viral titer of infected samples as assessed using plaque assay of three biologically independent experiments.

(D) Huh7 cells infected with MERS-CoV (MOI of 0.5) were treated with indicated concentrations GSK2656157 for 24 hours. Supernatants from these conditions were then used to assess the viral titer by plaque assay (at least four biological replicas).

The experiments were performed together with Hendrik Weiser and Dr. Christin Mueller. Dr. Mueller performed all MERS-CoV infections and plaque assays in the BSL3 laboratory of the Institute of Medical Virology, Justus Liebig University Giessen. Hendrik Weiser performed all the biological replicas shown in panels A, B & C. The figure was adapted from supplementary figure 2, Shaban et al. under a Creative Commons Attribution 4.0 International License (Shaban et al. 2021).

The data above indicated that inhibiting PERK did not affect the strong anti-viral state imposed on the cellular models by thapsigargin, suggesting that the thapsigargin anti-viral effect is occurring downstream of PERK. These data also indicated no improvement in the anti-viral effect of the newer version of PERK inhibitor compared to the older one (Fig. 12). However, a strong reduction in the phosphorylation of eIF2 α on serine 51 in infected cells, treated with 10 μ M of the inhibitor (when compared with the infection-only control) might hint at an indeed improved specificity of the newer inhibitor.

4.1.10 Alterations in the cellular proteomic landscapes induced by thapsigargin treatments and/or CoV infection

The Western blot analysis of Huh7 cells infected with HCoV-229E and/or treated with thapsigargin (Fig. 15) indicated a significant change in the expression levels of the investigated specific host proteins. These alterations incited the question of whether they are the “tip of an iceberg” of more profound changes in the host proteomes that can also offer a mechanistic explanation of the anti-viral effect of thapsigargin.

For this purpose, a liquid chromatography-tandem mass spectrometry (LC-MS/MS) approach to characterize the cellular proteomes was implemented and the results are included in this section, as they led to the identification of several thapsigargin-regulated factors and pathways whose (de)regulation was further studied during this thesis.

Figure 24 summarizes the experimental conditions used and offers an overview of the data analysis strategy that is subsequently delineated in the text below. Given their current relevance and pathogenicity, corresponding cellular models infected with MERS-CoV and SARS-CoV-2, with or without thapsigargin treatment were used for this study. Whole-cell extracts were digested by trypsin

and the resulting complex peptide mixtures were separated by nano HPLC and subjected to mass-spectrometry for identification of proteins by means of the precursor ion masses and peptide amino acid sequence information (for details see methods part). Raw data obtained from these samples were then analyzed through a label-free quantification approach using the MaxQuant software to obtain a list of expressed proteins and their relative abundance in each sample. From this list, a list of differentially expressed proteins (DEPs) was obtained by applying different statistical tools and methods available in the software Perseus including calculating p-values and fold changes (using two samples t-tests). The data were then visualized as a pairwise comparison between the indicated experimental conditions using volcano blots with a p-value of $-\log_{10}(p) \geq 1.3$ as a cut-off (Fig. 25).

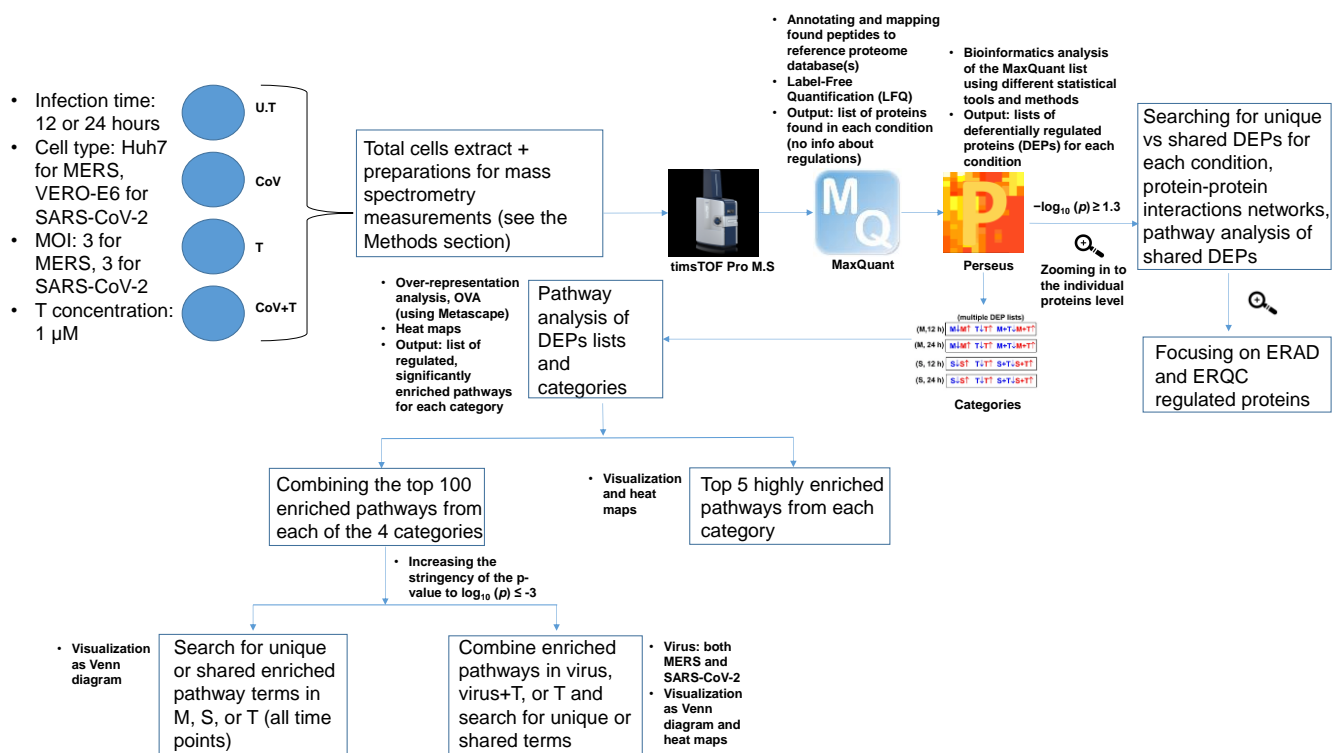


Figure 24: Proteome-wide investigation of thapsigargin's anti-viral effects.

The Diagram outlines the large-scale proteomic approach starting from experimental design; sample preparations, mass spectrometry measurements, raw data processing, and bioinformatics strategy used to analyze the data (see text and subsequent figures for details and results). Altogether, raw data from 96 LC-MS/MS runs (representing two independent experiments per time point and three technical replicates per sample) were performed and analyzed. U.T: untreated condition (reference control), M: MERS-CoV, S: SARS-CoV-2, T: thapsigargin, ERAD: ER-associated degradation, ERQC: ER quality control.

The Proteome-wide experiment was carried out with extensive contributions from multiple people. Dr. Christin Mueller performed all MERS-CoV and SARS-CoV-2 infections. Hendrik Weiser pre-prepared the samples. LC-MS/MS mass spectrometry measurements were done in the mass spectrometry facility of the Department of Chemistry, Philipps University, Marburg (headed by Dr. Uwe Linne). Raw data were mapped to the human and viral proteomes by Dr. Uwe Linne and Dr. Axel Weber (Prof. Kracht working group) using the MaxQuant framework. The bioinformatics strategy and the entire subsequent analyses (figures 25, 26, 27, 28, 29 & 30) were devised, carried out and visualized by Prof. Michael Kracht. M.Samer Shaban extensively discussed, checked, re-analyzed the entire data set and created this scheme.

When compared to the untreated condition, the 12 hours and the 24 hours of MERS-CoV or SARS-CoV-2 infection of Huh7 and VERO-E6 cells respectively resulted in the suppression and upregulation of multiple proteins as indicated in figure 25. Thapsigargin treatment alone of the cells also resulted in its own large number of deregulated host proteins (Fig. 25). The simultaneous treatment and infection at both investigated time points, when compared to infection alone, resulted in a new pattern of up and downregulated proteins as well as a strong downregulation of viral proteins for both MERS-CoV and SARS-CoV-2 confirming the results obtained using Western blot analysis.

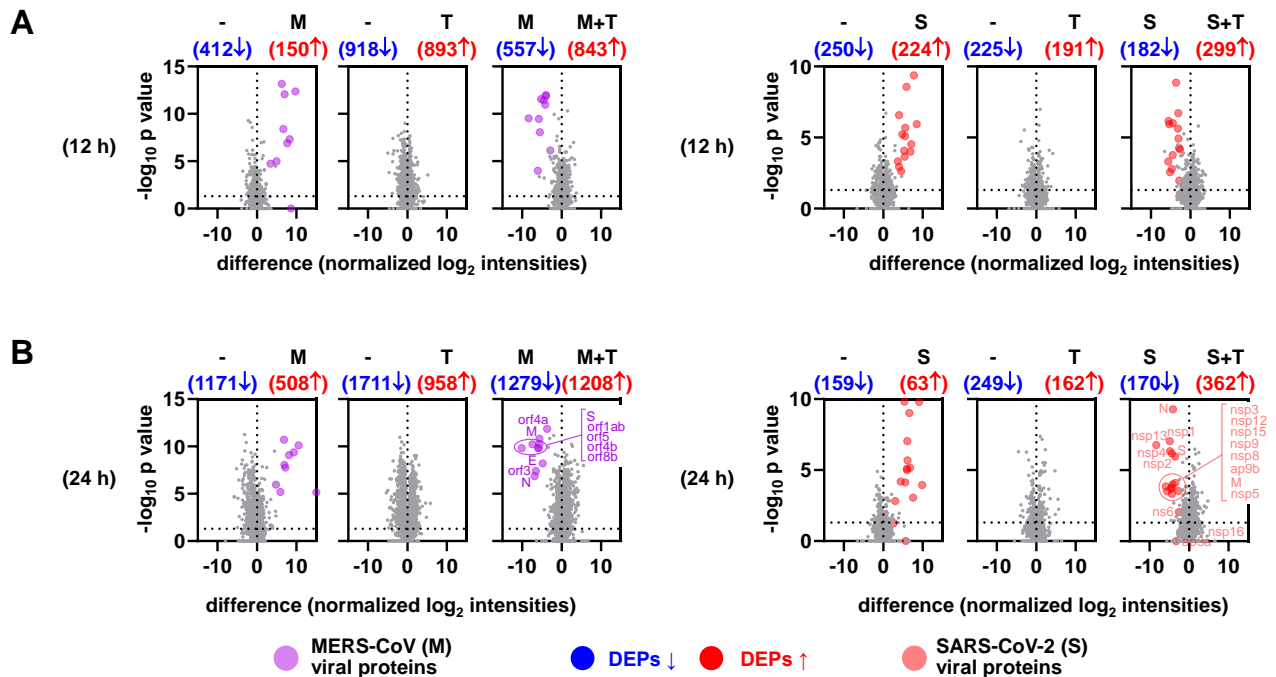


Figure 25: Overview of all deregulated proteins in response to thapsigargin treatment in the presence or absence of CoV infection.

Total cell extracts analyzed by LC-MS/MS from Huh7 or VERO-E6 cells uninfected (-), treated with thapsigargin (T), infected with MERS-CoV (M) or SARS-CoV-2 (S) respectively for 12 h or 24 h or thapsigargin-treated and CoV-infected simultaneously (M+T, S+T). MOI of 3 of both viruses and 1 μ M of thapsigargin were used. The intensities of the majority of protein IDs identified (5,367 from Huh7 and 5,066 from Vero E6 cells) were normalized between samples and DEPs were then visualized with volcano plots using pairwise ratio comparisons of indicated conditions. For each condition, two independent biological replicates and three technical measurements were carried out. Subsequently, p values were calculated using Student's t -tests from the means of the replicates. Numbers of differentially expressed proteins (DEPs, ratio > 0, p -value of $-\log_{10}(p) \geq 1.3$) are highlighted with blue (downregulation) and red (upregulation) while purple and light red dots visualize individual viral proteins. h: hour

(A) MERS-CoV experiments

(B) SARS-CoV-2 experiments

The figure was adapted from Fig. 6 a, b, c, & d, Shaban et al. under a Creative Commons Attribution 4.0 International License (Shaban et al. 2021). See Fig. 24 legend for contributions.

The lists of deregulated proteins were then used for further analysis on the individual protein levels to uncover shared or unique DEPs amongst the experimental conditions.

To make a meaningful comparison between the deregulated DEPs for both viruses and thapsigargin treatments, it is important to note that the two cellular models used for infection/treatment (Huh7 for MERS-CoV and VERO-E6 for SARS-CoV-2) share 57.5% of their proteomes considering all proteins that were identified by LC-MS/MS (Fig. 26 A). This most likely reflects the difference in cell identities (liver versus kidney) rather than the different species (homo sapiens versus *Chlorocebus sabaeus* (Green monkey, *Cercopithecus sabaeus*)), as the human and green monkey genomes are almost identical (>97%) (Warren et al. 2015; M.-L. Zhang et al. 2019).

With this in mind, Venn diagrams analysis revealed that the two viruses upregulated 38 and downregulated 5 identical DEPs in both cell types. The virus + thapsigargin conditions (M+T, S+T) showed a larger set of common deregulated proteins encompassing, 120 upregulated and 63 downregulated identical proteins (Fig. 26 B).

By examining the top 50 DEPs, a strong similarity in the regulation patterns between proteins affected in thapsigargin-alone and virus + thapsigargin conditions was observed. This finding might indicate the dominance of thapsigargin-induced molecular events in the virus + thapsigargin condition and diminishing of virus-only regulated pathways. Indeed, the virus-only conditions showed the downregulation of many of these DEPs including HERPUD1, BiP and SEQSTM1 (p62) while thapsigargin treatment prevented this downregulation, or even caused an (active) upregulation. Worth noting here, that this observation was more readily visible in MERS-CoV than in SARS-CoV-2 experiments (Fig. 26 C). One possible explanation is that under the chosen conditions, the MERS-CoV infection was affecting more cells simultaneously compared to SARS-CoV-2.

Pathway analysis of the 120 upregulated DEPs shared between the virus + thapsigargin conditions revealed terms related to ER stress, Golgi vesicle transport, fiber organization, and apoptosis. While the list of 63 shared, downregulated DEPs indicated terms belonging to the metabolic, viral life cycle, and translation-related pathways amongst others (Fig. 26 D). Of these 120 DEPs, 71 were involved in protein-protein network interactions (Fig. 26 E left) while only 26 out of 63 downregulated DEPs showed a network interaction as assessed by analysis based on STRING database (Fig. 26 E right).

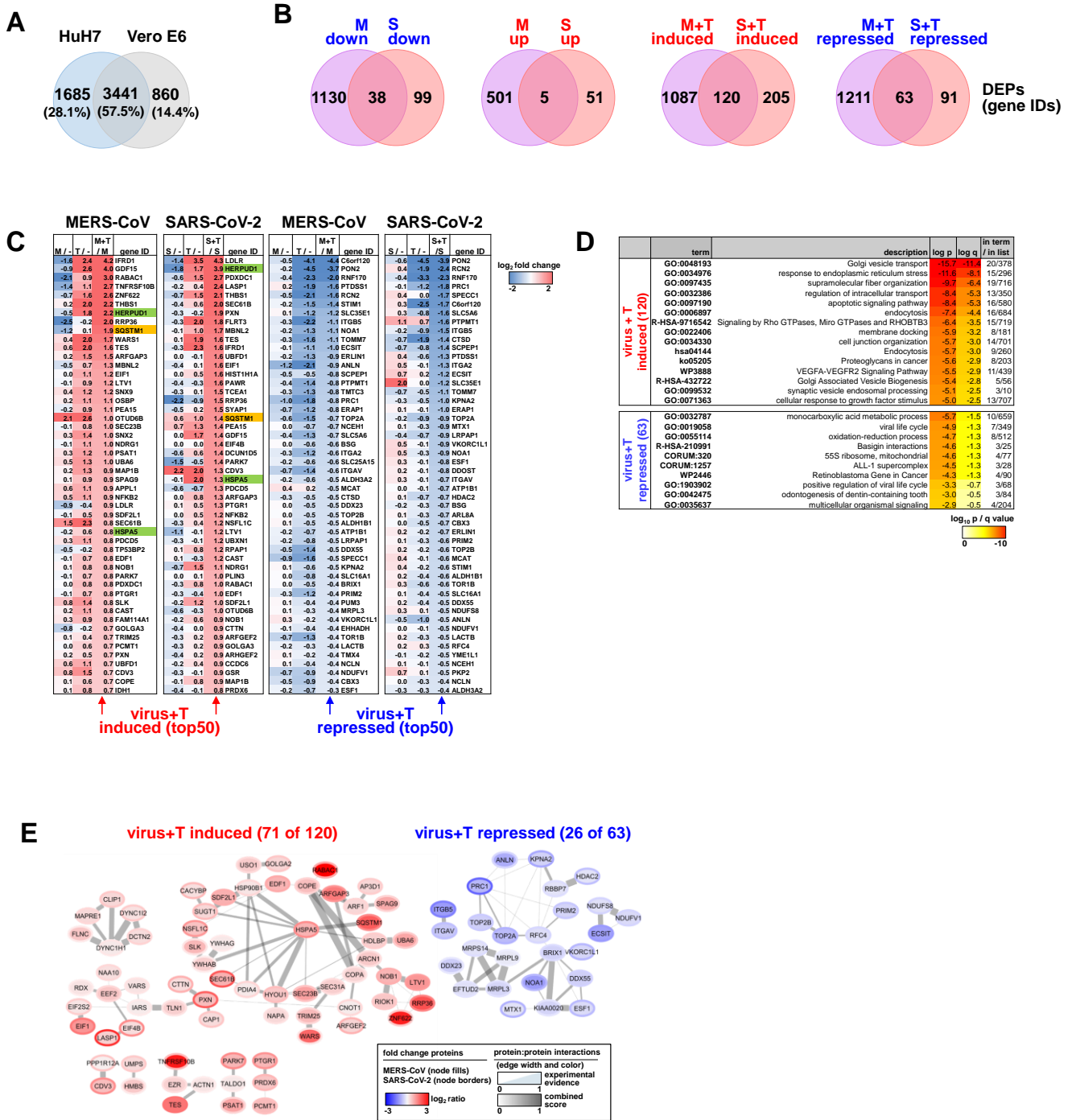


Figure 26: Thapsigargin-induced regulations of proteins dominate over CoV-induced regulations.

(A) Venn diagram revealing unique vs shared expressed proteins in Huh7 and their orthologues in VERO-E6 cells.

(B) Venn diagrams revealing unique vs shared DEPs between indicated conditions (DEPs, ratio > 0, p -value of $-\log_{10}(p) \geq 1.3$).

(C) Top 50 deregulated proteins in indicated conditions shown as heatmaps displaying the individual mean ratio values of normalized intensities. The lists are sorted according to virus + thapsigargin conditions. (-) refers to the untreated control. Green and yellow colors highlight indicated proteins.

(D) Using Metascape analysis, top pathways corresponding to shared (induced or repressed, as indicated in the figure) DEPs between virus + thapsigargin referenced to virus infection alone (ratios shown in C) are displayed as heatmaps sorted according to indicated p -values

(E) Using the STRING database, protein-protein interactions of shared (induced or repressed, as indicated in the figure) DEPs between virus + thapsigargin referenced to virus infection alone (ratios shown in B) are displayed as networks based on experimental evidence, co-occurrence, co-expression, and confidence scores. In this analysis, STRING experimental evidence and combined score indicated that 49 upregulated and 37 downregulated shared DEPs did not engage in any known networks. Cytoscape software was used for the visualization of the networks.

M: MERS-CoV, S: SARS-CoV-2, T: thapsigargin

The figure was adapted from Fig. 7 a, b, c, d & e, Shaban et al. under a Creative Commons Attribution 4.0 International License (Shaban et al. 2021). See Fig. 24 legend for contributions.

Of the top 50 DEPs shown in figure 26 C, two were of particular interest given their functions and their thapsigargin-induced upregulation in MERS-CoV and SARS-CoV-2 infected cells. HERPUD1 and p62/SQSTM1 are both involved in intracellular degradation pathways namely ERAD and autophagy respectively. These two pathways are major contributors in dealing with unfolded proteins and disposing of bulky components through proteasomal (HERPUD1) or autophagosomal (p62) degradation (Paredes et al. 2016, 1; Chen et al. 2020). They are also relevant to innate immunity and ER membrane remodeling. Hence, a search into the DEPs lists to reveal additional ERAD/ERQC factors was carried out. While more experiments to investigate the role of autophagy in CoV replication were subsequently done, details of which are in section 4.2.

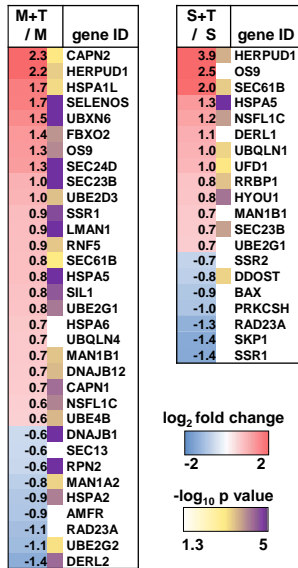
The search for differentially expressed ERAD/ERQC factors of the entire lists of components of KEGG pathway hsa04141 “protein processing in endoplasmic reticulum” in the virus + thapsigargin conditions (referenced to virus-only condition) resulted in 33 and 20 related DEPs for MERS-CoV and SARS-CoV-2, respectively (Fig. 27 A). The majority, but not all of these changes were statistically significant, which is why some factors were excluded during the filtering steps applied for analyses leading to the results shown below.

A further intersection of shared DEPs between the virus + thapsigargin condition with data of a genome-wide sgRNA screen, which uncovered new ERAD factors important for protein degradation in non-viral system, revealed 30 additional regulated factors. These factors included the E1 ubiquitin ligase UBA6 and the zinc finger protein ZNF622 (also called ZPR9), which were recently described either as negative regulators of autophagy or of some DNA viruses infection (Fig. 27 B).

A

core ERQC / ERAD components

MERS-CoV SARS-CoV-2



B

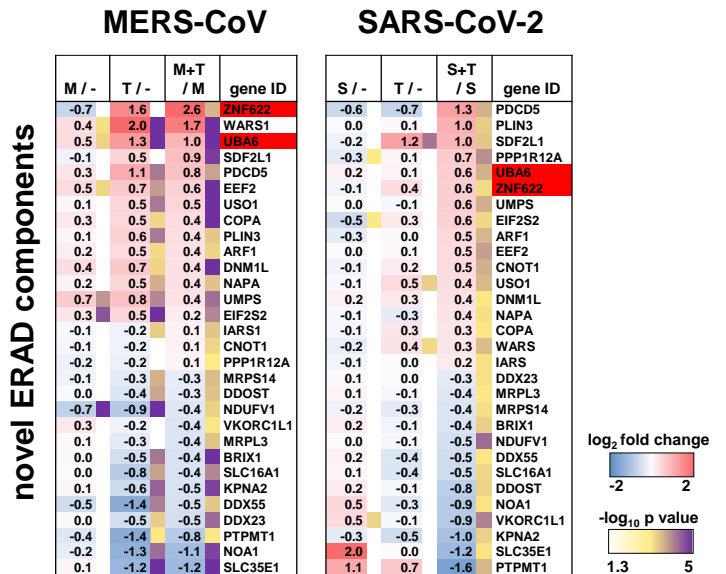
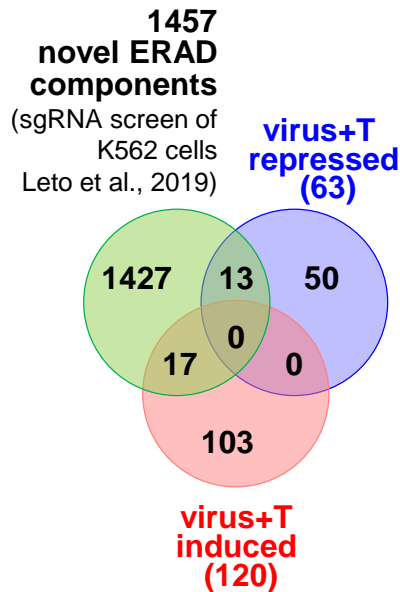


Figure 27: Thapsigargin regulation of several ERAD/ERQC factors.

(A) ERAD/ERQC factors (extracted from KEGG hsa04141) regulation in virus + thapsigargin conditions (referenced to virus-only condition) are shown as heatmaps displaying the individual mean ratio of fold changes.

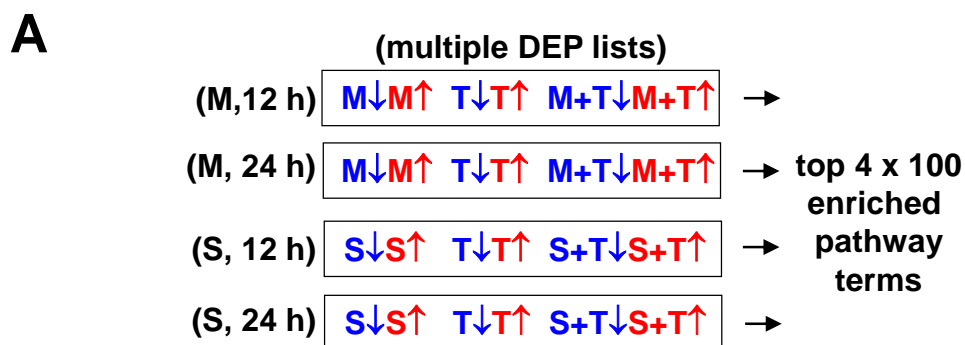
(B) Left: Venn diagram revealing the intersection between DEPs in the indicated conditions and novel ERAD factors uncovered through a genome-wide CRISPR-CAS9 approach from Leto et al, 2019. Right: regulation of the intersected novel components under the indicated conditions.

M: MERS-CoV, S: SARS-CoV-2, T: thapsigargin

The figure was adapted from Fig. 7 f & g, Shaban et al. under a Creative Commons Attribution 4.0 International License (Shaban et al. 2021). See Fig. 24 legend for contributions.

The data analysis above indicated the need for a deeper understanding of the regulation of the uncovered DEPs on the level of pathways and networks. For this purpose, an enriched pathway analysis approach was implemented to uncover the unique or shared regulated molecular events and pathway terms upon CoV infection and/or thapsigargin treatment. This approach was also used to uncover possible mechanistic insights into the two viruses' replication and the thapsigargin-imposed anti-viral state.

To facilitate meaningful analysis of the data, the uncovered DEPs were classified into four different categories according to the virus (MERS-CoV or SARS-CoV-2) and length of infection (12 h or 24 h). Each category contained lists of up-and down-regulated DEPs (kept separate) for each experimental condition (Fig. 28 A & Fig. 24). Using Overrepresentation analysis (ORA) through Metascape software, the gene IDs of the corresponding DEPs lists were annotated to biological pathways and hierarchically clustered heatmaps of the top 100 differentially enriched pathways were generated (Fig. 28 B & C). The heatmaps revealed that many of the differentially enriched pathways were shared among different conditions while also condition-unique pathways were observed. They also indicated that although many of these pathways were shared between the two viruses, individual regulated proteins were not identical. This pointed out the particularity of each virus in regulating the same pathway using different effectors, an observation most likely stemming from divergent viral evolution and adaptations.



B**12 h MERS-CoV****24 h MERS-CoV**

C

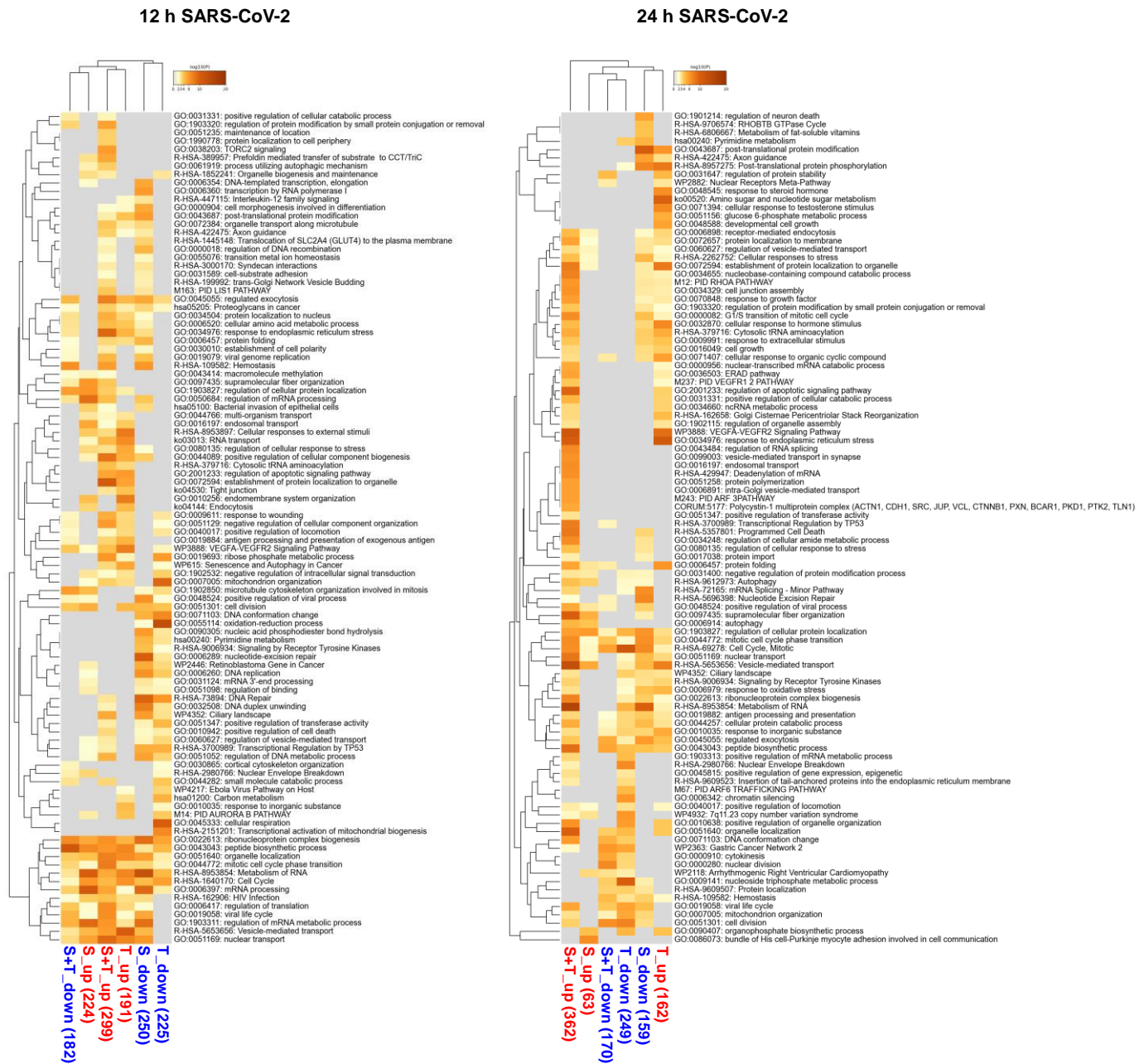


Figure 28: heatmaps of the top 100 differentially enriched pathways in MERS-CoV infected Huh7 and SARS-CoV-2 infected VERO-E6 cells for 12 or 24 hours.

(A) Shows a schematic representation of the four different categories according to the virus (MERS or SARS-CoV-2) and length of infection (12 h or 24 h). Using Overrepresentation analysis (ORA) through Metascape software, the gene IDs of the corresponding DEPs (ratio > 0, p-value of $-\log_{10}(p) \geq 1.3$) lists were annotated to biological pathways and hierarchically clustered heatmaps of the top 100 differentially enriched pathways were generated for MERS-CoV experiments (B) and SARS-CoV-2 experiments (C).

Upward arrows with red color indicate upregulation. Downward arrows with blue color indicate downregulation

T: thapsigargin, M: MERS-CoV, S: SARS-CoV-2

The figure was adapted from Fig. 6 e and supplementary figures 6 and 7, Shaban et al. under a Creative Commons Attribution 4.0 International License (Shaban et al. 2021). See Fig. 24 legend for contributions.

Concentrating on the top five (for both viruses at both time points) and top 10 (for thapsigargin treatments at both time points) pathways of up-or downregulated DEPs revealed many highly enriched pathways that are related to RNA, DNA, metabolic functions, and localization (Fig. 29).

condition	time	GO	description	DEPs↑	DEPs↓	
MERS-CoV	12h	GO:0009117	nucleotide metabolic process	-7.9	-5.0	
		GO:0016236	macroautophagy	-5.9		
		GO:0022411	cellular component disassembly	-5.7	-10.1	
		WP3888	VEGFA-VEGFR2 Signaling Pathway	-5.4	-8.1	
		hsa04144	Endocytosis	-4.8		
MERS-CoV	24h	R-HSA-8957275	Post-translational protein phosphorylation		-14.8	
		R-HSA-8953854	Metabolism of RNA		-13.9	
		GO:0051129	negative regulation of cellular component organization		-13.0	
		GO:0072594	establishment of protein localization to organelle		-13.0	
		GO:0010638	positive regulation of organelle organization		-12.8	
SARS-CoV-2	12h	GO:0006397	mRNA processing	-11.0	-9.2	
		R-HSA-8953854	Metabolism of RNA	-10.1	-12.7	
		GO:1903311	regulation of mRNA metabolic process	-9.2	-8.7	
		GO:0050684	regulation of mRNA processing	-8.7	-3.9	
		GO:0043043	peptide biosynthetic process	-7.0		
	SARS-CoV-2	24h	R-HSA-8953854	Metabolism of RNA	-10.1	-12.7
			GO:0006289	nucleotide-excision repair		-10.0
			R-HSA-73894	DNA Repair		-9.6
			GO:0006397	mRNA processing	-11.0	-9.2
			GO:0022613	ribonucleoprotein complex biogenesis	-5.2	-9.0
SARS-CoV-2	24h	GO:0086073	..His cell-Purkinje myocyte adhesion in communication	-6.83		
		GO:1903827	regulation of cellular protein localization	-5.9	-6.3	
		R-HSA-5653656	Vesicle-mediated transport	-5.2	-4.6	
		GO:0097435	supramolecular fiber organization	-5.0		
		GO:0090407	organophosphate biosynthetic process	-4.19		
	SARS-CoV-2	24h	GO:0043687	post-translational protein modification		-10.5
			R-HSA-8953854	Metabolism of RNA		-10.0
			R-HSA-8957275	Post-translational protein phosphorylation		-7.2
			R-HSA-5696398	Nucleotide Excision Repair		-7.1
			R-HSA-69278	Cell Cycle, Mitotic		-7.0
Thapsigargin	HuH7	GO:0006520	cellular amino acid metabolic process	-49.0		
		GO:0051186	cofactor metabolic process	-43.3	-7.2	
		R-HSA-5653656	Vesicle-mediated transport	-42.7	-6.4	
		GO:0009117	nucleotide metabolic process	-38.9	-17.5	
		R-HSA-5357801	Programmed Cell Death	-28.9	-4.8	
		GO:0006397	mRNA processing		-24.7	
		R-HSA-8953854	Metabolism of RNA	-13.7	-23.7	
		GO:0007005	mitochondrion organization	-8.5	-20.5	
		R-HSA-72766	Translation	-13.5	-17.5	
		GO:0009117	nucleotide metabolic process	-38.9	-17.5	
Thapsigargin	HuH7	R-HSA-5653656	Vesicle-mediated transport	-59.1	-6.0	
		GO:0006520	cellular amino acid metabolic process	-34.5	-6.8	
		GO:0051186	cofactor metabolic process	-34.5	-14.7	
		ko04144	Endocytosis	-31.1		
		WP3888	VEGFA-VEGFR2 Signaling Pathway	-30.9	-6.7	
		R-HSA-72203	Processing of Capped Intron-Containing Pre-mRNA		-100.0	
		GO:0022613	ribonucleoprotein complex biogenesis	-3.1	-71.0	
		GO:0006403	RNA localization		-49.6	
		GO:0050684	regulation of mRNA processing		-46.6	
		R-HSA-1640170	Cell Cycle	-14.9	-40.6	
Thapsigargin	Vero E6	R-HSA-5653656	Vesicle-mediated transport	-10.4		
		R-HSA-8953897	Cellular responses to external stimuli	-8.1		
		GO:0010256	endomembrane system organization	-8.0		
		WP3888	VEGFA-VEGFR2 Signaling Pathway	-7.8		
		GO:0051169	nuclear transport	-7.4		
		GO:0055114	oxidation-reduction process		-13.5	
		GO:0045333	cellular respiration		-10.2	
		GO:0007005	mitochondrion organization	-3.1	-9.4	
		GO:0071103	DNA conformation change		-7.1	
		R-HSA-2151201	Transcriptional activation of mitochondrial biogenesis		-6.9	
Thapsigargin	Vero E6	GO:0034976	response to endoplasmic reticulum stress	-11.3		
		ko00520	Amino sugar and nucleotide sugar metabolism	-9.8		
		WP3888	VEGFA-VEGFR2 Signaling Pathway	-8.9		
		R-HSA-8957275	Post-translational protein phosphorylation	-8.2		
		GO:0072594	establishment of protein localization to organelle	-8.2		
		R-HSA-69278	Cell Cycle, Mitotic		-11.9	
		GO:0009141	nucleoside triphosphate metabolic process		-10.2	
		GO:0051301	cell division		-7.44	
		R-HSA-2980766	Nuclear Envelope Breakdown		-6.9	
		WP4932	7q11.23 copy number variation syndrome		-6.1	

top10 pathways

- DNA
- RNA
- metabolism
- localization

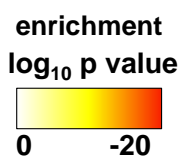


Figure 29: Top 5 (for both viruses at both time points) and top 10 (for thapsigargin treatments at both time points) pathways of up- or downregulated DEPs extracted from the top 100 deregulated pathways.

The figure was adapted from supplementary figure 8a, Shaban et al. under a Creative Commons Attribution 4.0 International License (Shaban et al. 2021). See Fig. 24 legend for contributions.

The 400 enriched pathways categories shown as heatmaps in figure 28 were then pooled together and filtered down to 229 pathways through an increase of p-values stringency ($\log_{10}(p) \leq -3$) and search for shared or unique GO terms for MERS-CoV, SARS-CoV-2, infections, and thapsigargin alone treatments. The results were then visualized using Venn diagrams (Fig. 30 A).

The Venn diagram analysis showed 36 pathways were shared by both viruses and by thapsigargin. Amongst the top deregulated of these pathways, many were related to the cellular response to stress, regulation of mRNA processing (GO:0006397), ribonucleoprotein complex biogenesis (GO:0022613) and vesicle-mediated transport (R-HSA-5653656). While, interestingly, the top deregulated pathways unique to thapsigargin represented mostly metabolic and biosynthetic pathways (such as cellular amino acid metabolic process, GO:0006520, or nucleotide metabolic process, GO:0009117) hinting at a thapsigargin-unique metabolic response (Fig. 30 A, lower heatmap).

The unique set of deregulated metabolic pathways in thapsigargin-treated cells incited investigating their regulation in cells infected with CoV and simultaneously treated with thapsigargin. For this purpose, all virus + thapsigargin, enriched pathways were pooled and compared to pooled pathways from virus infection (both viruses) alone or compared to pathways pooled from all thapsigargin alone treatments (this resulted in 249 out of 400 pathways with p-values of $\log_{10}(p) \leq -3$). Unique and shared terms amongst these new categories were then visualized using Venn diagram (Fig. 30 B). The analysis revealed 147 shared pathways amongst the three mentioned new categories and 20 unique pathways in the virus + thapsigargin category. These 20 unique pathways mainly mapped to splicing, signaling (TORC, RHOA, ARF3), and transport/localization. Thapsigargin alone and virus + thapsigargin shared 37 categories most of which represented metabolic pathways including amino acid metabolism pathways. Pathways unique or shared between virus and thapsigargin conditions (but not present in virus + thapsigargin) mapped to diverse terms of entirely different biological categories including DNA-related processes (Fig. 30 B lower heatmap).

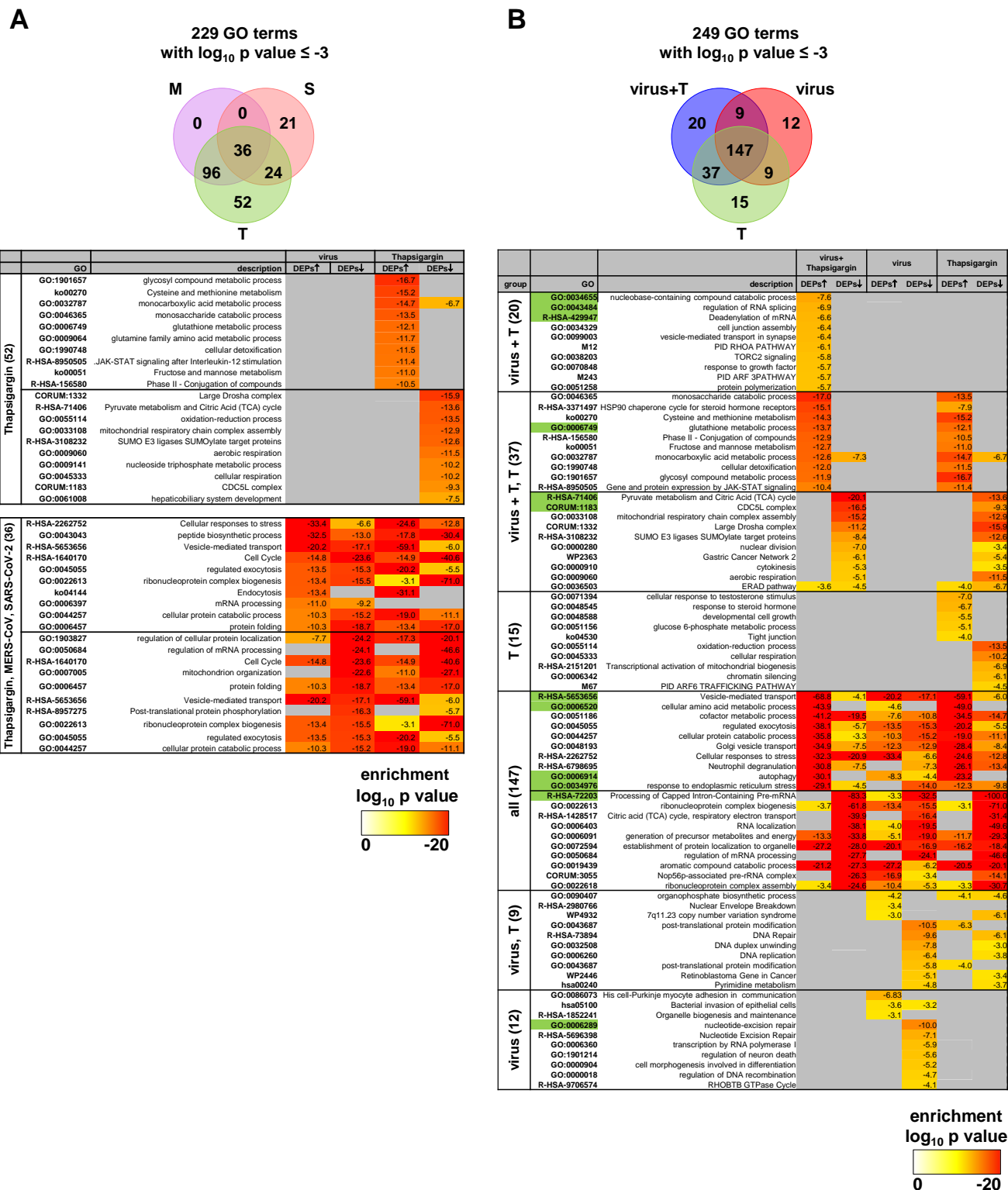


Figure 30: Thapsigargin treatments of cellular models invoked a unique metabolic response that coincided with an anti-viral effect.

(A) Upper: Venn diagram indicating unique vs shared GO terms amongst the indicated conditions generated from the 400 enriched pathways categories shown as heatmaps in figure 28 after they were pooled together and filtered down to 229 pathways through an increase of p values stringency ($\log_{10}(p) \leq -3$). Lower: details of top pathways are displayed as a heatmap.

(B) Upper: Venn diagram indicating unique vs shared GO terms amongst the indicated conditions generated from the 400 enriched pathways categories shown as heatmaps in figure 28 after they were pooled together and filtered down to 249 pathways through an increase of p values stringency ($\log_{10}(p) \leq -3$). Lower: details of top pathways are displayed as a heatmap

T: thapsigargin, M: MERS-CoV, S: SARS-CoV-2

The figure was adapted from Fig. 6 f, g & h and supplementary figure 8b, Shaban et al. under a Creative Commons Attribution 4.0 International License (Shaban et al. 2021). See Fig. 24 legend for contributions.

Taken together, the proteomic data indicated a coinciding of the anti-viral effect of thapsigargin with strong regulation of multiple metabolic programs, ERAD/ERQC and autophagy pathways. It also showed that although the same pathway can be regulated under different experimental conditions, individual DEPs involved could differ.

Given its consistent upregulation and multiple biological functions, in the next section, a series of experiments were carried out to expand more on the role of p62/SQSTM1 and autophagy flux in the context of CoV infection and/or thapsigargin treatment.

4.2 Pharmacological modulation of autophagy flux in cells infected with CoV

Autophagy is a dynamic process through which the cell disposes of and recycles bulky intracellular components including aggregates of proteins, invading pathogens, and up to entire cellular organelles (e.g. ERphagy) (Parzych and Klionsky 2014). Given the contribution of autophagy to the innate and adaptive immune responses evoked by viral invasion (Y. Xu and Eissa 2010; Levine and Deretic 2007; Tao and Drexler 2020), it was expected that viruses have evolved different mechanisms to evade or even harness this process to their advantage. Of the many host factors involved in this process (see introduction for more details), p62/SQSTM1 and LC3B-II are of particular importance given their well-established functions as cargo receptors for selective autophagy and autophagosome formation respectively, and their involvement in almost all the steps of this process. Consequently, in a given experimental condition (e.g. CoV infection) the protein levels of these factors, determined by Western blotting in the presence or absence of an autophagy flux blocker (ex: bafilomycine A1, BafA1, as a lysosomal inhibitor), are used to estimate the levels of protein degradation (or turn over) that would have occurred if the flux was not blocked. An estimation of degradation rate (i.e. the flux) through referencing it back to the steady-state (untreated) condition can be then calculated. These blockers (e.g. BafA1) can also be used to elucidate the effect of autophagy on viral replication, host response, and possible cross talk with other UPR pathways.

4.2.1 Selective and basal autophagy flux are differentially regulated when investigated at the late stage of the 24 hours HCoV-229E infection

The initial step was to measure autophagy flux in Huh7 cells infected with HCoV-229E and/or treated with thapsigargin in reference to the steady-state flux without interfering with the course of the infection itself. For this purpose, cells were left uninfected or infected with HCoV-229E (MOI of 1). The cells were then treated with thapsigargin (1 μ M) or left without the treatment. 4 hours before the end of the 24 hours experiment, the cells were then either treated with 0.1 μ M (standard in the literature) of BafA1 or left without BafA1 treatment. As solvent control, which is samples treated with DMSO, were either left uninfected or infected with the virus. Whole-cell extracts were then analyzed using Western blotting and the protein levels of LC3B-II and p62 were quantified. From these data, ratios of autophagy flux for each indicated condition were then calculated (Fig. 31 A & B).

The Western blot analysis indicated no change in the levels of the viral N protein and the activation pattern of PERK band in the presence or absence of BafA1. The levels of p62 and LC3B-II, on the other hand, varied strongly amongst the different conditions and BafA1 treatments. For instance, the level of p62 in CoV-infected cells without BafA1 treatment showed a pronounced reduction in comparison to the untreated control while the addition of BafA1 increased the band intensity, pointing out the accumulation of this protein. The calculated change in autophagy flux reflected these changes (Fig. 31

B) indicating a reduction in basal autophagy flux (LC3B-II based) in all tested conditions while induction of specific autophagy flux (p62 based) occurred in HCoV-229E infected cells only. Interestingly, thapsigargin treatment of cells infected with HCoV-229E diminished the virus-induced specific autophagy flux.

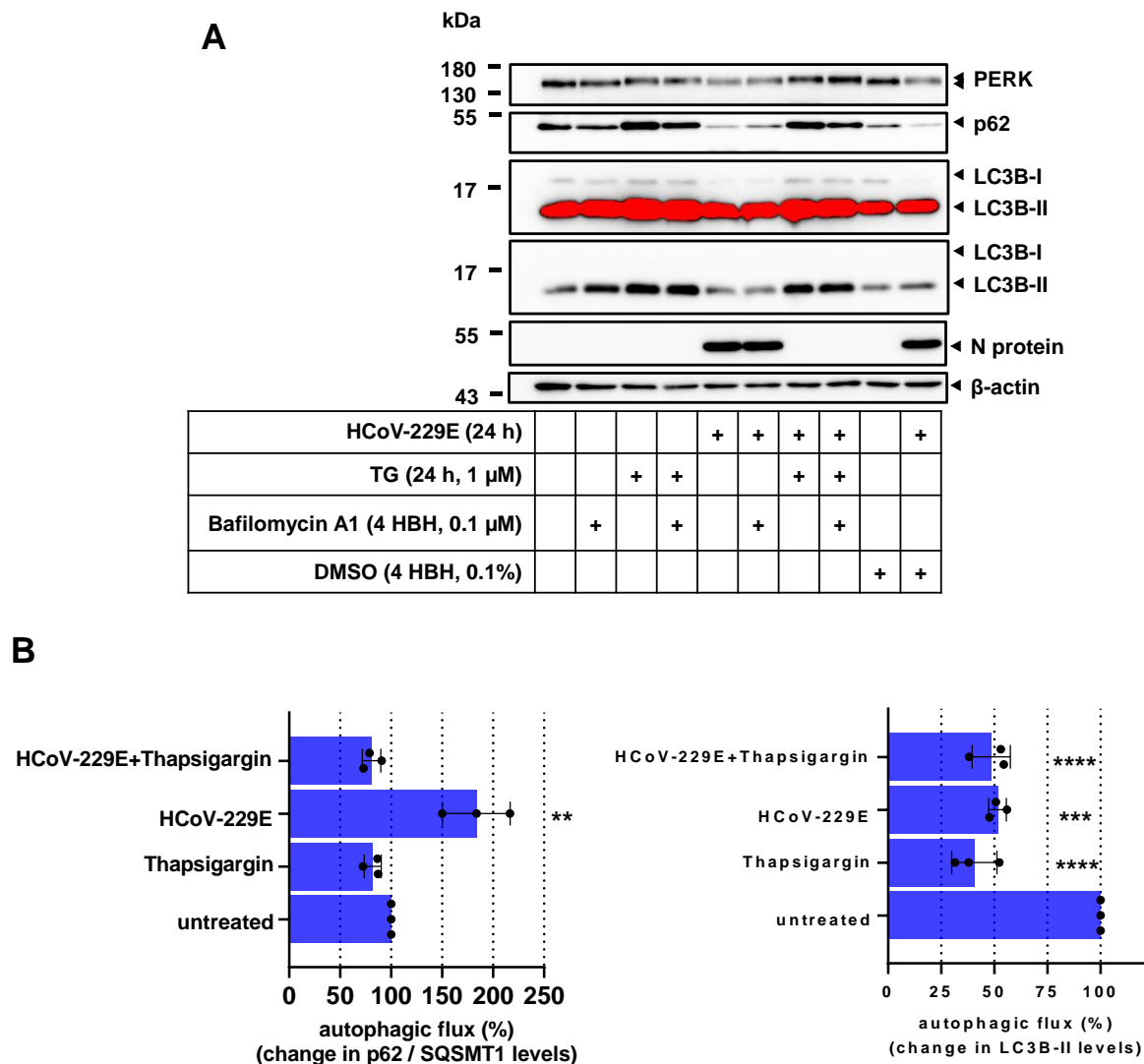


Figure 31: HCoV-229E infection induces specific (p62 based) autophagy flux, while thapsigargin inhibits it.

Huh7 cells were left uninfected or infected with MOI of 1 of HCoV-229E. The cells (uninfected or infected) were then treated with 1 μ M of thapsigargin or left without the treatment. 4 hours before the end of the 24 hours experiment, the cells were then either treated with BafA1 (0.1 μ M) or left without the treatment. DMSO was used as solvent control. HBH: hours before harvesting. Untreated: steady-state control. TG: thapsigargin

(A) Whole-cell extracts using the special lysis buffer were subjected to Western blotting analysis and probed with indicated host and viral proteins antibodies. β -actin was used as an equal loading control. The experiment was performed as three independent biological replicas.

(B) Autophagy flux calculations relative to the untreated control (steady-state) based on the protein levels of LC3B-II and p62 from data shown in (A).

Bars show means \pm s.d., while dots show the results from biologically independent experiments. Asterisks indicate p values (* $p \leq 0.05$, ** $p \leq 0.01$, *** $p \leq 0.001$, **** $p \leq 0.0001$) obtained by one-way ANOVA test where the mean of each column was compared to the mean of the untreated column.

4.2.2 Bafilomycine A1 inhibition of CoV is pathogen- and time of addition- dependent

The downregulation of basal and the upregulation of specific autophagy flux seen in the late stage of 24 hours of HCoV-229E infection prompted the question of whether blocking the lysosome at an earlier stage or even before the infection would interfere with replication of the virus or would change the status of the autophagy flux.

For this purpose, Huh7 cells infected with HCoV-229E and/or treated with thapsigargin were either treated with BafA1 or left without the BafA1 treatment. The BafA1 treatments were either 4 hours before the start of the 24 hours infection/treatment or 8 hours after (i.e. 28 hours or 16 hours of BafA1 respectively) (Fig. 32 A). Blocking the lysosome (and hence autophagy flux) 4 hours before the CoV infection resulted in a significant drop in the level of the viral N protein. The 28 hours of BafA1 treatment resulted in a strong downregulation of basal autophagy flux in all thapsigargin treated conditions as compared to the steady state flux. This downregulation was also observed in HCoV-229E infected cells but to a lesser degree. As seen previously, the selective autophagy flux was strongly induced with virus infection while the simultaneous infection and thapsigargin treatment resulted in a strong reversal of this induction. Adding BafA1 for 16 hours resulted in a similar pattern of basal and selective autophagy flux inhibition and activation (respectively) to adding BafA1 for 28 hours for all conditions. Interestingly the level of the viral N protein remained unchanged when BafA1 was added 8 hours after the infection (Fig. 32 B, C & D). Investigation of the levels of ubiquitinated proteins using Western blotting under the experimental conditions mentioned above revealed a unique pattern of ubiquitinated proteins in virus-infected cells. Some of the prominent bands seen on the blot might correspond to ubiquitinated viral proteins or ubiquitinated host factors in response to the infection. Generally, blocking the lysosome at any of the indicated time points increased ubiquitinated proteins, especially in the upper region of the blot. This effect was particularly strong in thapsigargin-treated conditions and may be explained by a suppression of lysosomal degradation of bulky protein aggregates marked for recycling by classical K48-linked polyubiquitination (Fig. 32 E).

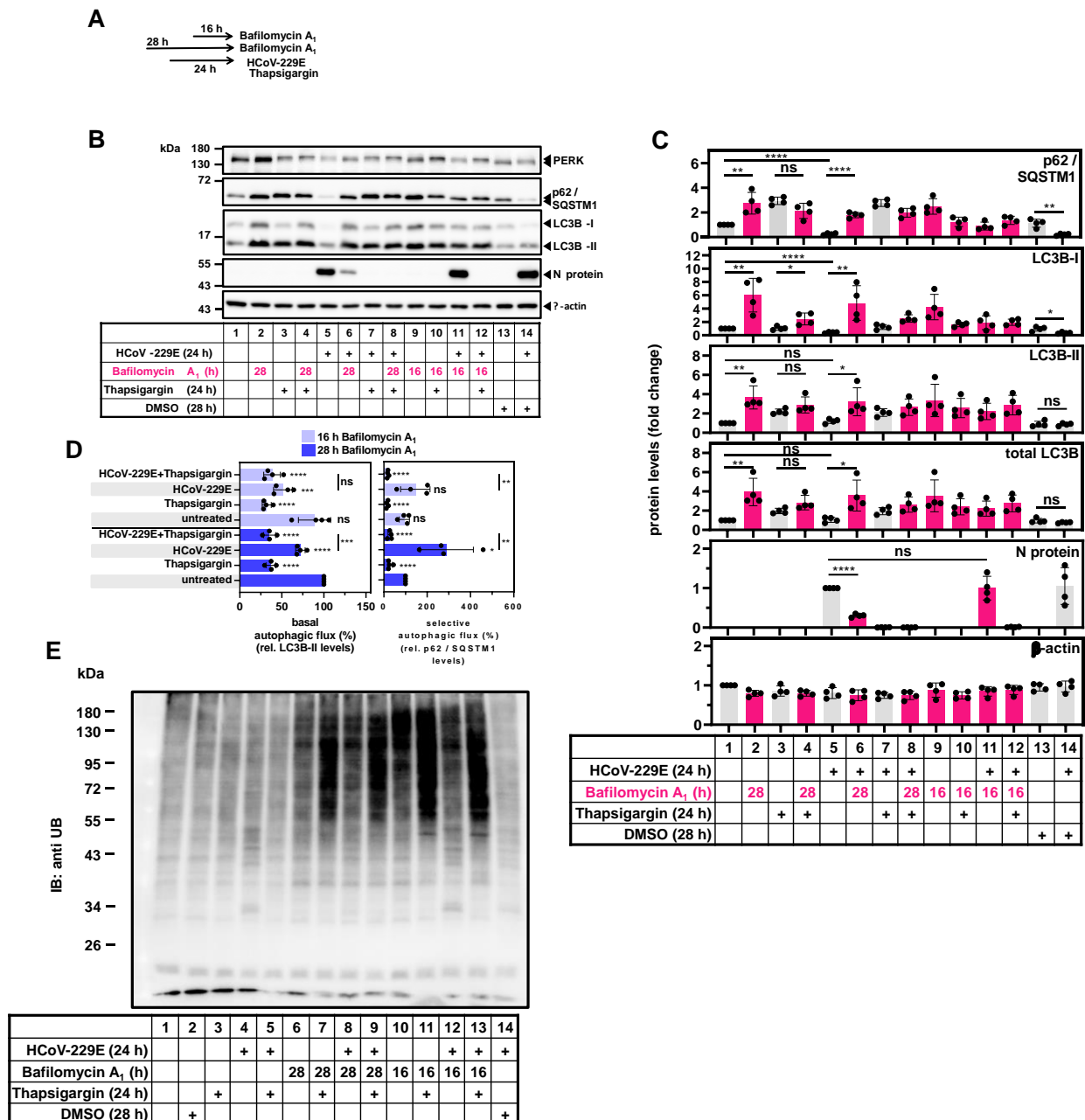


Figure 32: Bafilomycine A1 inhibition of HCoV-229E is time of treatment dependent.

Huh7 cells infected with HCoV-229E (MOI of 1) and/or treated with 1 μ M thapsigargin were either treated with BafA1 or left without the BafA1 treatment. The BafA1 treatments were applied either for 28 hours or for 16 hours as indicated in the text.

(A) Schematic representation of BafA1 time of addition.

(B) Whole-cell extracts using the special lysis buffer were subjected to western blot analysis and probed with indicated viral and host proteins antibodies. β -actin is used as an equal loading control.

(C) Quantification of the levels of proteins investigated in (B) from four independent biological replicas relative to the untreated/uninfected control.

(D) LC3B-II and p62 Autophagy flux calculations relative to the untreated A₁ control (steady-state) levels from data shown in (C).

(E) Immunoblot generated from lysate from (B) was probed using anti-ubiquitin antibodies

All bar graphs show means \pm s.d.; asterisks indicate p values (* $p \leq 0.05$, ** $p \leq 0.01$, *** $p \leq 0.001$, **** $p \leq 0.0001$) obtained by two-tailed unpaired t-tests.

The experiments shown in panels B, C & D were performed together with the technician Hendrik Weiser. Hendrik Weiser helped perform the biological replicas. The figure (except panel E) was adapted from figure 8 a, d, e & f Shaban et al. under a Creative Commons Attribution 4.0 International License (Shaban et al. 2021).

The data above indicated a possible role of basal autophagy flux and lysosomal pathways in earlier steps of HCoV-229E replication. The data also indicated a role of selective autophagy in this CoV replication that might be needed throughout the investigated 24 hours of infection. Hence, the downregulation of CoV-induced specific autophagy flux by thapsigargin can offer a possible anti-viral mechanism.

Assessing the status of autophagy flux under the above-mentioned conditions using IFA revealed the following: the steady-state level of selective autophagy flux can be observed as an increase in the cytoplasmic p62 (red) puncta (corresponding to autophagosomes) in presence of BafA1 as compared to untreated cells. Cells infected with the virus and treated with BafA1 4 hours before infection showed an expected sharp decrease in the nsp8 (green) signal and a massive increase in the p62 puncta when compared to infection without BafA1. The simultaneous virus infection and thapsigargin treatment resulted in a strong increase of p62 puncta that remained relatively the same when BafA1 was added for 16 or 28 hours (Fig. 33). All of which corresponded to the autophagy flux quantification in figure 32 D.

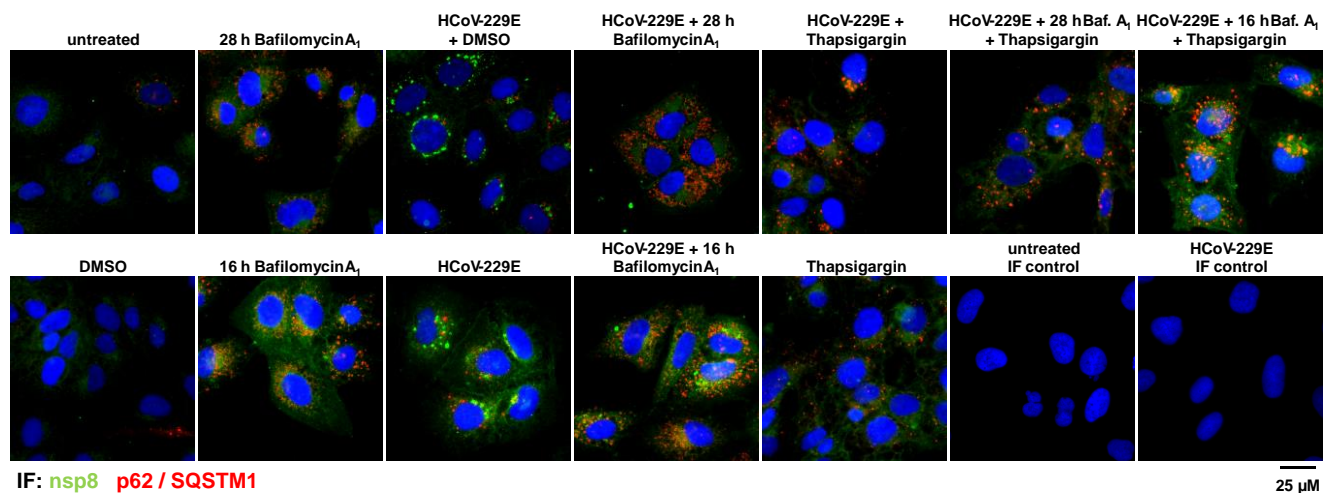


Figure 33: Representative images of one out of two biological replicas of fluorescently labeled Huh7 cells with nsp8 (green) and p62 (red) antibodies along with phase-contrast (Ph) light microscopy images. Green signal indicates the HCoV-229E replication sites while red signal shows p62-positive puncta under indicated conditions.

Method details as indicated in figure 16 & 17. DMSO was used as solvent control. Hoechst 33342 was used to stain the nuclei (blue).

The experiment was performed together with Dr. Christin Mayer-Buro. Dr. Mayer-Buro helped perform the biological replicas and analyzing the data. The figure was adapted from figure 8 c, Shaban et al. under a Creative Commons Attribution 4.0 International License (Shaban et al. 2021).

The sharp drop in the viral N protein level in the 28 hours of BafA1 treatment in contrast to the unchanged levels of this protein in the 16 hours of BafA1 treatment of HCoV-229E infected cells as

observed on Western blot promoted deeper investigation. For this, the viral titers of these conditions were investigated using plaque assay (Fig 34). A titer drop of 2 log₁₀ fold was observed when the cells were treated with 28 hours of BafA1. Intriguingly, the 16 hours of BafA1 treatment resulted in a significant drop of the titer of about one log₁₀ fold contradicting the results obtained on the Western blot and suggesting a possible parallel inhibition of the degradation of this viral protein or decoupling between the production of infectious particles and the viral protein translation. 16 hours of BafA1 treatment of cells under thapsigargin + virus condition resulted in an additive, additional drop of the viral titer when compared to the 16 hours of BafA1 + virus only condition. Contrary to that, the 28 hours of BafA1 treatment of thapsigargin + virus condition did not show any accumulative anti-viral effect (Fig. 34 left).

Concerning other coronaviruses, treatment of MERS-CoV-infected cells with BafA1 for 28 hours or 16 hours did not result in any drop in the virus titer hinting at the insensitivity of this CoV to lysosomal blockade (Fig. 34 middle). On the other hand, SARS-CoV-2-infected cells, treated with BafA1 showed a significant drop in the virus titer at both time points of BafA1 addition (Fig. 34 right). Notably (and independent from BafA1 treatment), 28 hours of thapsigargin treatment of SARS-CoV-2-infected cells resulted in a much stronger drop of the virus titer previously seen in the 24 hours of simultaneous treatment/infection pointing to a possible mechanism of virus-entry inhibition by thapsigargin in VERO-E6 cells.

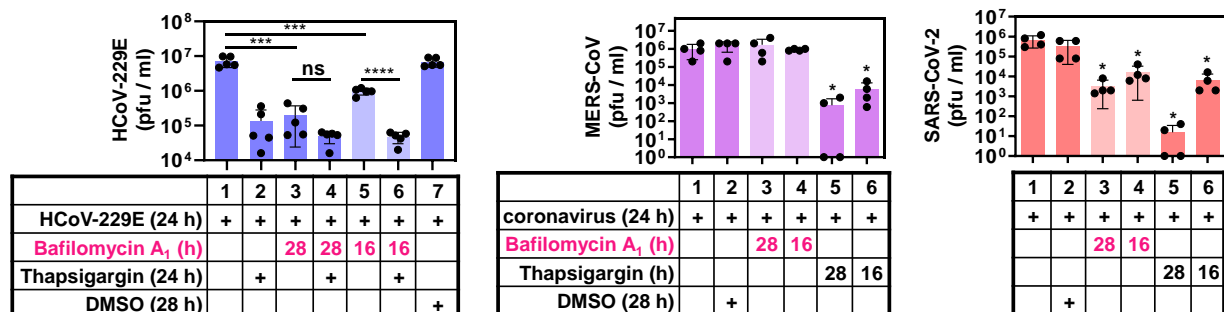


Figure 34: Bafilomycin A1 inhibition of CoV replication is pathogen- and time of treatment-dependent.

Supernatants from Huh7 cells infected with MERS-CoV or HCoV-229E and from VERO-E6 cells infected with SARS-CoV-2 under the indicated experimental conditions were analyzed through plaque assay to determine the corresponding viral titer. MOIs used were 1, 0.5, and 0.5 for HCoV-229E, MERS-CoV, and SARS-CoV-2 respectively. The infection lasted 24 hours. DMSO was used as solvent control. The experiment was performed as at least four independent biological replicas. Dots show individual replicates, all bars show the means \pm s.d.; asterisks indicate *p* values ($*p \leq 0.05$, $**p \leq 0.01$, $***p \leq 0.001$, $****p \leq 0.0001$) obtained by two-tailed unpaired t-tests.

The experiments were performed together with Hendrik Weiser and Dr. Christin Mueller. Dr. Mueller performed all MERS-CoV and SARS-CoV-2 infections and plaque assays. Hendrik Weiser helped perform the biological replicas of the HCoV-229E experiment. The figure was adapted from figure 8 a & b Shaban et al. under a Creative Commons Attribution 4.0 International License (Shaban et al. 2021).

Overall, the data above hinted at an intricate, virus-specific relation between autophagy flux and CoV replication that varies with the progression of the infection and that was completely disrupted by thapsigargin.

4.2.2 Pharmacological modulations of autophagy flux and PERK pathway in cells infected with CoV

Pathways regulated by PERK have been shown to induce/contribute to autophagy flux upon UPR activation (Avivar-Valderas et al. 2011; Ogata et al. 2006; Zheng et al. 2019). To explore the cross talk between ER stress and UPR through PERK activation in the context of CoV infection, PERK, and lysosomal pathways were blocked using GSK2606414 and BafA1 respectively, alone or in combination,. Subsequently, the autophagy flux was measured as previously described and viral replication was assessed in supernatants of infected conditions using plaque assay.

This cross talk was first explored in the context of HCoV-229E infection of Huh7 cells with experimental conditions schematically indicated in figure 35 A. Whole-cell extracts were then subjected to Western blot analysis and probed with indicated viral and host proteins antibodies (Fig. 35 B). Expectedly, infected samples treated with GSK2606414 showed single inactivated (fast-migrating) PERK band. The viral N protein showed a reduction of about 50 percent in presence of 10 μ M of the PERK inhibitor, recapitulating the results in section 4.1.1. Likewise, BafA1 treatment for 28 or 16 hours of infected samples recapitulated the results seen in figure 32.

Combined treatment of both GSK2606414 and BafA1 of infected cells resulted in a strong reduction of the N protein band. Compared to GSK2606414 alone or BafA1 alone treatments, this reduction was stronger when BafA1 was added 4 hours before the infection. On the other hand, adding BafA1 8 hours after infection resulted in a reduction of the N protein that was similar to the reduction seen in GSK alone condition. The measured viral titer for the combinatory treatments of GSK2606414 + 16 hours BafA1 showed an additive inhibitory effect when compared to 16 hours of BafA1 alone treatment. Intriguingly, the GSK2606414 + 28 hours of BafA1 did not show any significant drop of the viral titer when compared to 28 hours of BafA1 alone treatment despite the stronger reduction of the N protein levels seen on Western blot. This last observation might be hinting at the activation of an alternative (more efficient?) degradation mechanism of the viral N protein when both pathways are blocked.

Analysis of p62 and LC3B protein level changes amongst the experimental conditions and the subsequent calculations of specific and basal autophagy flux showed that the PERK inhibitor slightly downregulated specific autophagy flux and had little to no influence on basal flux. This might indicate a decoupling of virus replication inhibition from autophagy flux as opposed to the strong inhibition of both fluxes seen in the thapsigargin treatment of infected cells.

(E) Supernatants of infected conditions from (B) were used to assess virus replication using plaque assay. Viral titer expressed as pfu/ml.

The experiment was performed as three independent biological replicas. All bar graphs show means \pm s.d.; asterisks indicate *p* values (**p* \leq 0.05, ***p* \leq 0.01, ****p* \leq 0.001, *****p* \leq 0.0001) obtained by two-tailed unpaired t-tests.

Similar to HCoV-229E, the same set of experiments, under the same set of conditions shown in figure 35 A, was carried out in Huh7 cells infected with MERS-CoV. Intriguingly, neither PERK inhibitor nor BafA1 treatment, at both time points, significantly affected the levels of the viral N protein as analyzed on Western blotting (Fig. 36 A & B). In contrast to that, 10 μ M of GSK2606414 and the combinatory treatment of GSK2606414 + 28 hours BafA1 resulted in a significant drop of the viral titer with about one log₁₀ fold difference for both cases (Fig. 36 D). This observation hints at the possibility that the PERK-mediated inhibition of MERS-CoV replication is not coupled with inhibition of the viral N protein translation. Alternatively, it might indicate a deactivation of the degradation mechanism of the viral protein.

Analysis of p62 and LC3B protein level changes amongst the experimental conditions and the subsequent calculations of specific and basal autophagy flux showed that both MERS-CoV infection and GSK2606414 treatment, alone or combined resulted in the downregulation of basal autophagy flux. MERS-CoV infection did not significantly influence specific autophagy flux when BafA1 was added for 28 hours. Contrary, adding BafA1 for 16 hours resulted in a significant reduction of specific autophagy flux. PERK inhibitor downregulated specific autophagy flux at both time points of BafA1 addition (Fig. 36 C).

Similar to HCoV-229E and MERS-CoV, the same set of experiments, under the same set of conditions shown in Fig 35 A, was carried out in VERO-E6 cells infected with SARS-CoV-2. In contrast to the data obtained from HCoV-229E, the PERK inhibitor did not result in any significant changes in the two visible bands of SARS-CoV-2 N protein when analyzed on western blot. BafA1 treatment at 4 hours before infection led to the complete disappearance of both bands of the viral N protein. Intriguingly, the 16 hours of BafA1 treatment of infected cells (i.e. 8 hours after infection) lead to the complete disappearance of the lower band of the viral N protein and a significant increase in the upper band when compared to the infection-only condition. However, the overall intensity of the two bands of the viral N protein in infection-only condition was similar to the 16 h BafA1 + infection solo band. These observations might indicate a possible merging of the viral N protein bands as a result of PTMs induced by the presence of BafA1. The combinatory treatments of GSK2606414 + BafA1 resulted in a similar pattern of viral N protein bands to the BafA1 only treatment of infected cells at each respective time point of BafA1 addition (i.e. GSK2606414 + 16 h BafA1 was similar to 16 h BafA1 and GSK2606414 + 28 h BafA1 was similar to 28 h BafA1).

Assessing basal and specific autophagy flux through quantifying the levels of LC3B and p62, respectively, revealed a strong downregulation of basal autophagy flux by GSK2606414 that was further downregulated by SARS-COV-2 at both time points of BafA1 addition. On the other hand, GSK2606414 treatment resulted in a slight reduction of specific autophagy flux. SARS-CoV-2 infection significantly downregulated specific autophagy flux. This last observation might indicate a possible anti-viral role of this arm of autophagy in SARS-CoV-2 replication contrary to the observations in HCoV-229E (Fig. 37 C).

Supernatants from infected conditions were then used to assess the virus replication using plaque assay. The analysis indicated that only conditions with BafA1 added 4 hours before the infection showed a significant drop in the titer (Fig. 37 D).

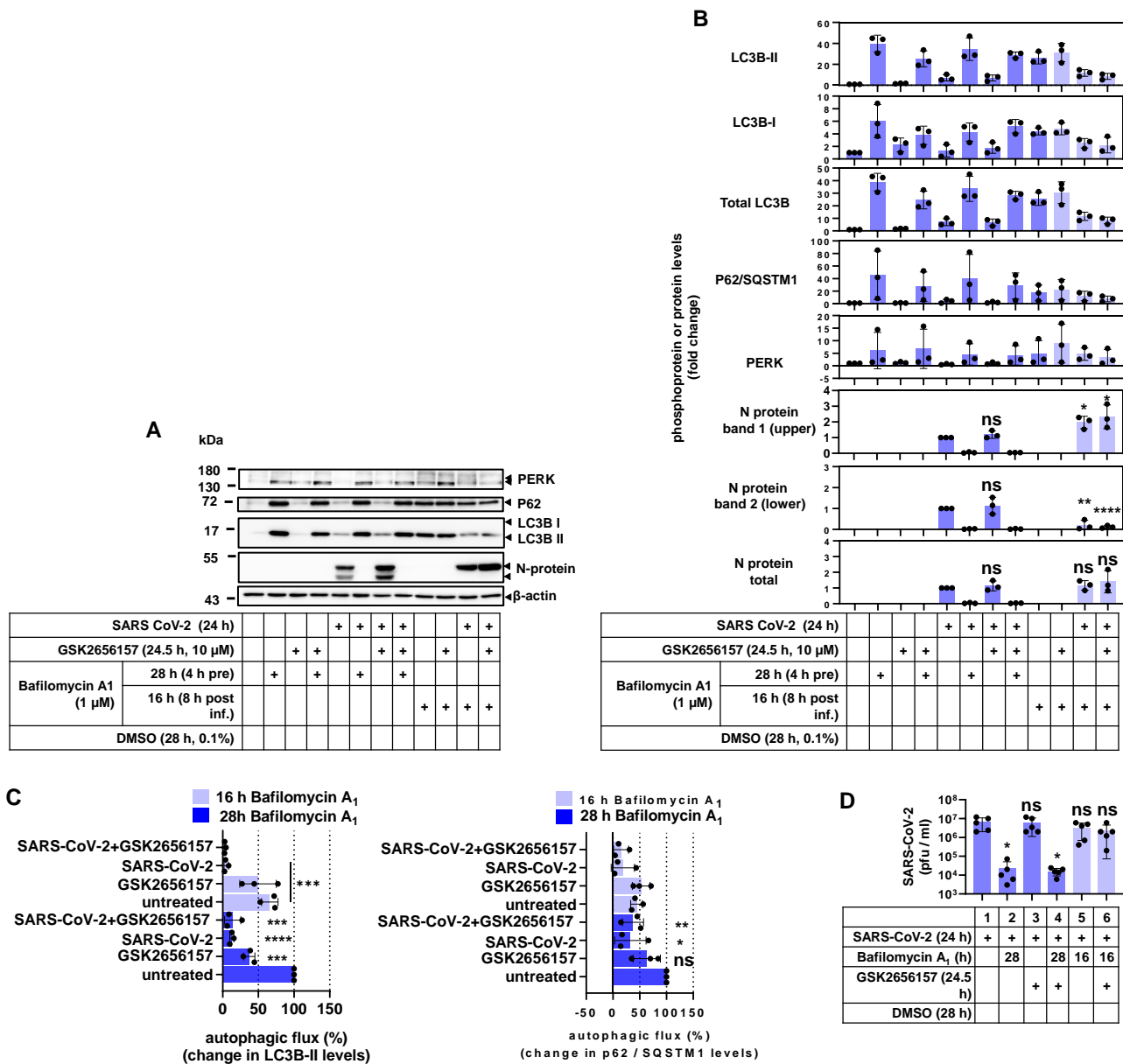


Figure 37: Regulation of autophagy flux and SARS-CoV-2 replication in the context of GSK treatments.

VERO-E6 cells were left uninfected or infected with SARS-CoV-2 (MOI=1) for 24 hours. The cells were treated with 10 μ M of GSK2606414 and 1 μ M of BafA1 in combination or alone. BafA1 was added either 4 hours before infection/treatment (28 h conditions) or 8 hours after (16 h conditions). GSK was added half an hour before the start of the 24 hours infection/treatment period, as indicated in figure 35 A.

(A) Whole-cell extracts using SDS lysis buffer were subjected to western blot analysis and probed with indicated viral and host protein antibodies. β -actin was used as an equal loading control.

(B) Quantification of protein levels investigated in (B) relative to the untreated/uninfected control.

(C) Autophagy flux calculations based on LC3B and P62 protein levels relative to the untreated control (steady-state) levels from data shown in (B) & (C).

(D) Supernatants of infected conditions from (B) were used to assess virus replication using plaque assay. Viral titer expressed as pfu/ml.

The experiment was performed as three independent biological replicas. All bar graphs show means \pm s.d.; asterisks indicate p values ($*p \leq 0.05$, $**p \leq 0.01$, $***p \leq 0.001$, $****p \leq 0.0001$) obtained by two-tailed unpaired t-tests.

The experiment was performed together with Dr. Christin Mueller. Dr. Mueller performed all SARS-CoV-2 infections and plaque assays.

Taken together, the data obtained from the three viruses indicated a possible strain-specific role of both investigated types of autophagy in their replication that is in need for further elucidation.

4.3 Genetic perturbations of several ER stress factors in Huh7 cells and their effect on CoV replication and host response

The results of the pharmacological manipulation of ER stress and UPR pathways presented in the previous sections indicated a possible important role of PERK in the replication of HCoV-229E and MERS-CoV. By contrast, IRE1 α inhibition did not result in any major changes in HCoV-229E replication. As with most protein kinase inhibitors (Bain et al. 2007; Davies et al. 2000), the ones used in this study can be prone to off-target inhibition, and lack of information on enzymatic-independent activities (for example; structural roles) of the inhibited protein kinases amongst others. Hence, a genetic approach was next followed to knockdown (KD) the two ER stress sensors, PERK and IRE1 α , and the downstream transcription factor ATF3 that is stress-induced but yet with an elusive role.

For this purpose, a CRISPR-CAS-9 approach that is based on single vector systems that allow transfer of all components to the recipient cell either by normal transfection or by lentiviral transduction was utilized. Both protocols require the delivery of an active CAS-9 enzyme along with target-specific single guide RNA (sgRNA). The two protocols differ in the vectors used for cloning and expressing the required components and the delivery method to the cells. The pX459 protocol utilizes the pX459 (sSpCas9 (BB)-2A-Puro) vector that expresses active CAS-9 enzyme. A target-specific sgRNA is then cloned in this vector and the resulting vector is then delivered to the cells (Huh7 cells in this case) via different methods including, for example, Calcium phosphate transfection. The selection marker for the integration of this vector is puromycin. Hence, cells resistant to puromycin's cytotoxic effect would be assumed to have successfully and stably integrated the CAS-9-sgRNA components.

On the other hand, the highly efficient, second-generation lentivirus transduction system used here as well depends on simultaneously delivering three plasmids to HEK293FT cells through a reagent-dependent method of transfection (for example; Lipofectamine 2000). Two of these plasmids, the packaging and the envelope vectors, are carrying essential components to produce replication-incompetent lentivirus particles. A third one, the transfer vector, contains CAS-9 enzyme and target-specific sgRNA. The co-transfection of these three plasmids will result in the production of lentivirus particles containing a gene of interest (CAS-9-sgRNA components) capable of infecting a wide range of host cells (Huh7 cells in this case) and subsequently stably integrating the gene of interest in the host genome with puromycin as selection marker.

As a control for any unintended deregulations of cellular pathways of the targeted cells by both methods, an empty vector (with no sgRNA) cell line has been established in parallel.

After applying any of these two methods, cells surviving the selection pressure are then tested and characterized using different methods. Example of such methods include host DNA extraction, PCR amplification of the targeted region in the genome followed by Sanger sequencing of the amplicon (to confirm the InDel mutations) or protein levels assessment (of the product of the targeted gene) on Western blots.

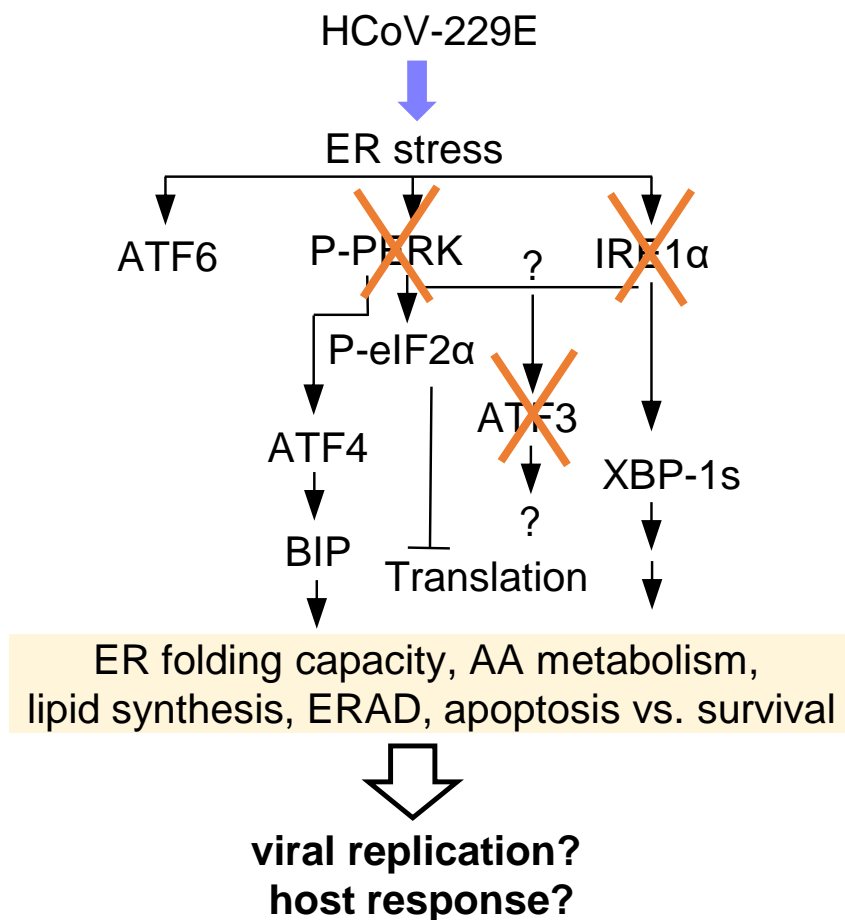


Figure 38: The schematic representation described in figure 11 is used here to illustrate the targets of the CRISPR-CAS-9-mediated genetic approach used in this study.

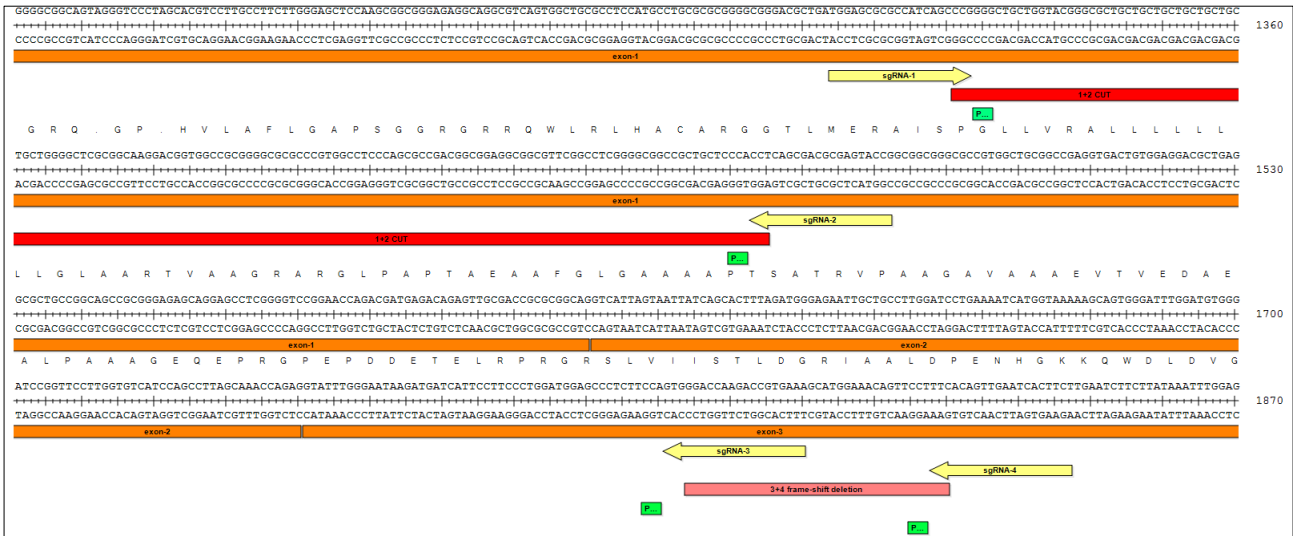
4.3.1 Establishing stable PERK and IRE1α knockdown cell lines

For knocking down PERK, four different sgRNAs targeting exons one and three of the *EIF2AK3* (PERK gene) DNA sequence were designed (see methods). In-silico, sgRNA 1 and 2 together resulted in 145 nucleotides removal from the sequence while sgRNA 4 and 5 resulted in a deletion leading to a frameshift (Fig. 39 A). The sgRNAs were cloned into the pX459 system and the resultant vectors were

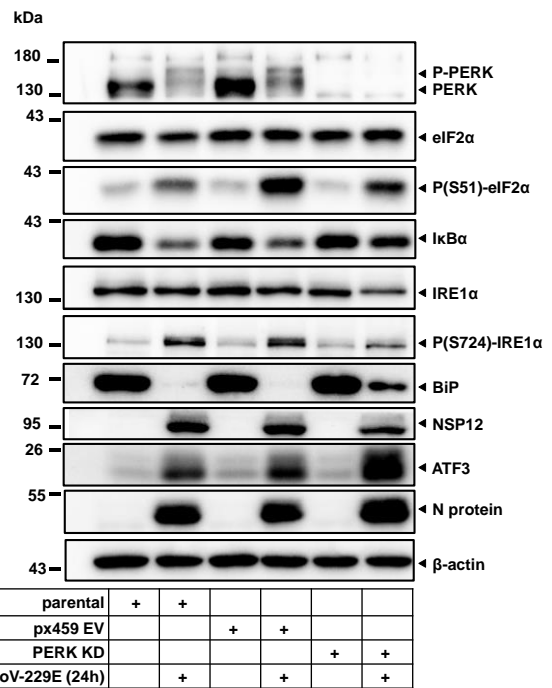
transfected in Huh7 cells either individually or in combination. After several weeks of puromycin selection (1 µg / ml), the PERK protein levels in the newly engineered cell lines were assessed on a Western blot with or without HCoV-229E infection (Fig. 39 B).

With parental Huh7 cells used as a reference, the Western blot analysis indicated a successful knockdown (KD) of PERK in all the tested, stable cell lines though to a varying degree of protein level reduction (Fig. 39 B). The cell line with sgRNAs 1+2 combination displayed the best PERK protein level reduction and hence was selected for further characterization. Next, the behavior of this stable PERK KD cell line was compared to the empty vector control and the parental cell lines with or without HCoV-229E infection on a Western blot (Fig. 39 C). In comparison to the parental cell line, the empty vector control cell line showed a very comparable pattern of regulation of the investigated host and viral proteins upon the virus infection. Based on this observation, this cell line was used as a sole reference control for further experiments and characterizations. On the other hand, factors investigated in the PERK KD cell line displayed multiple deviations (from both controls) including an increase in the viral N and ATF3 protein levels, and a reduction in IRE1α protein level. All of which were the subject of further investigation.

A



C



B



Figure 39: Establishing a stable PERK knockdown cell line.

(A) Schematic representation of the four different sgRNAs targeting exons one and three of the *EIF2AK3* (PERK gene) DNA sequence in-silico (using DNASTAR navigator). These sgRNAs were then cloned into the pX459 plasmid system and used to transfect parental Huh7 cells individually or in combination. The transfected cells were then subjected to puromycin selection (1 μg / ml). Yellow arrows represent the individual sgRNAs. The head of the arrow indicates the direction of sgRNA. Red rectangular marked with “1+2 cut” represents the expected (possible) 145 nucleotides removal as a result of sgRNA 1+2 cuts. Pink rectangular marked with “3+4 frameshift-deletion” represents the deletion and subsequent frameshift as a result of sgRNA 3+4 cuts. Green boxes indicate the PAM site.

(B) Whole-cell extracts of the newly engineered cell lines using special lysis buffer were subjected to Western blot analysis and the efficiency of PERK knockdown was then assessed using anti-PERK antibodies in the presence or absence of 24 hours of HCoV-229E (MOI of 1) infection.

(C) After further multiple passages under puromycin selection (1 μg / ml) a stable cell line carrying the combination sgRNAs 1+2 was selected and designated as the PERK KD cell line. Whole-cell extracts from PERK

KD, parental Huh7, and pX459 empty vector control cell lines with or without 24 hours of HCoV-229E (MOI of 1) infection were subjected to Western blotting. Using indicated antibodies, host and viral protein levels were then compared amongst the three cell lines.

β -actin was used as a loading control.

Worth noticing here is the improvement in the knockdown efficiency between the first test of the PERK KD cell line (Fig. 39 B) and the subsequent testing (Fig. 39 C). This improvement happened after several passages of the cells under the selection pressure. This improvement might indicate either a further elimination of cells that did not integrate the CRISPR-CAS-9 system or a further targeting of more alleles within cells already integrated the system. As the double strand break induced by the CAS-9 enzyme is irreversible, the reduction of PERK will then expectedly increase over time as more cells of the pool will acquire complete genome editing.

Furthermore, a CAS-9 recombination event is irreversible and is therefore usually referred to as a knockout (compared to classical RNA interference, which causes knockdowns). Nevertheless and given the strong reduction in protein levels seen on Western blotting, these experiments were performed with pools of cells (i.e. no clonal selection was carried out) and hence, the genome-edited cells examined here are referred to as knockdowns.

The next step was to knockdown IRE1 α . For this purpose, four different sgRNAs targeting exons one and eight of the *ERN1* (IRE1 α gene) DNA sequence were designed. In-silico, sgRNA 1 and 2 together or 3 and 4 together resulted in cuts with a subsequent frameshift (Fig. 40 A). As previously described for PERK KD, the sgRNAs were cloned into the pX459 system and the resultant vectors were used to transfect Huh7 parental cells either individually or in combination. After several weeks of puromycin selection (1 μ g / ml), the IRE1 α protein levels in the newly engineered cell lines were assessed on a Western blot with or without HCoV-229E infection. The parental and the empty vector cell lines were used as control references. All of the tested cell lines showed a reduction in the levels of IRE1 α with the cell line carrying the sgRNA 1+2 combination displaying the strongest reduction (Fig. 40 B). This cell line was then designated as IRE1 α KD and used for further experimentations. On a Western blot, the regulation of multiple host and viral proteins was then compared amongst the three cell lines, the empty vector control, the parental Huh7, and IRE1 α KD cell lines with or without HCoV-229E infection. Confirming the observations in figure 39 C, the empty vector control cell line displayed a very similar pattern of proteins regulation upon the virus infection to the parental cell line. Contrary, the IRE1 α KD cell line displayed multiple deviations including a slight reduction in the viral N protein and a strong reduction in ATF3 activation levels (Fig. 40 C).

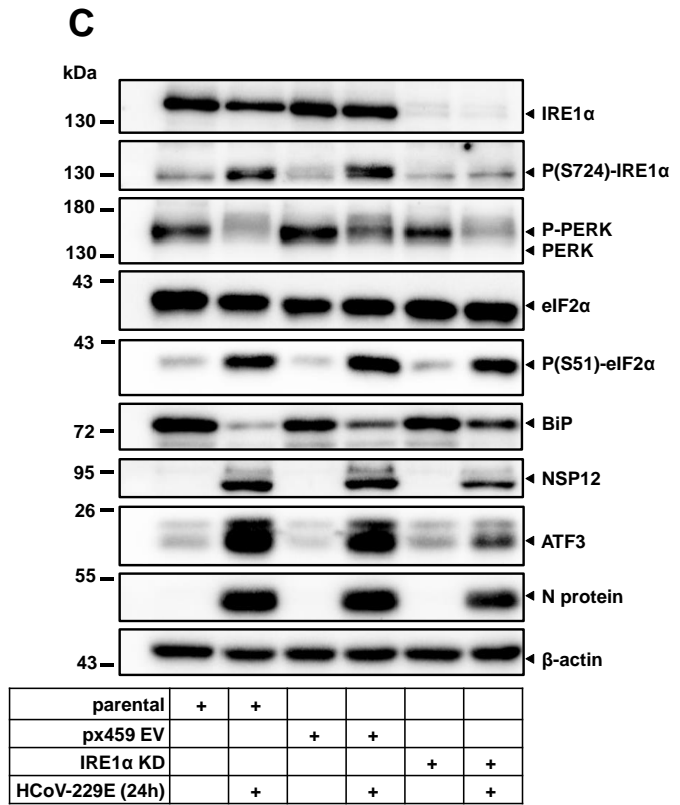
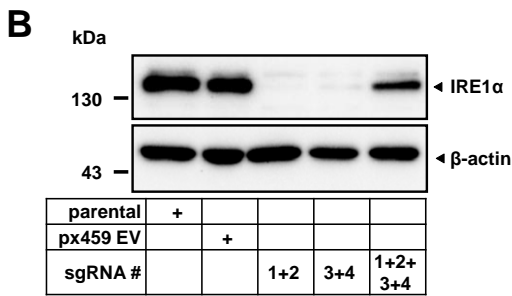
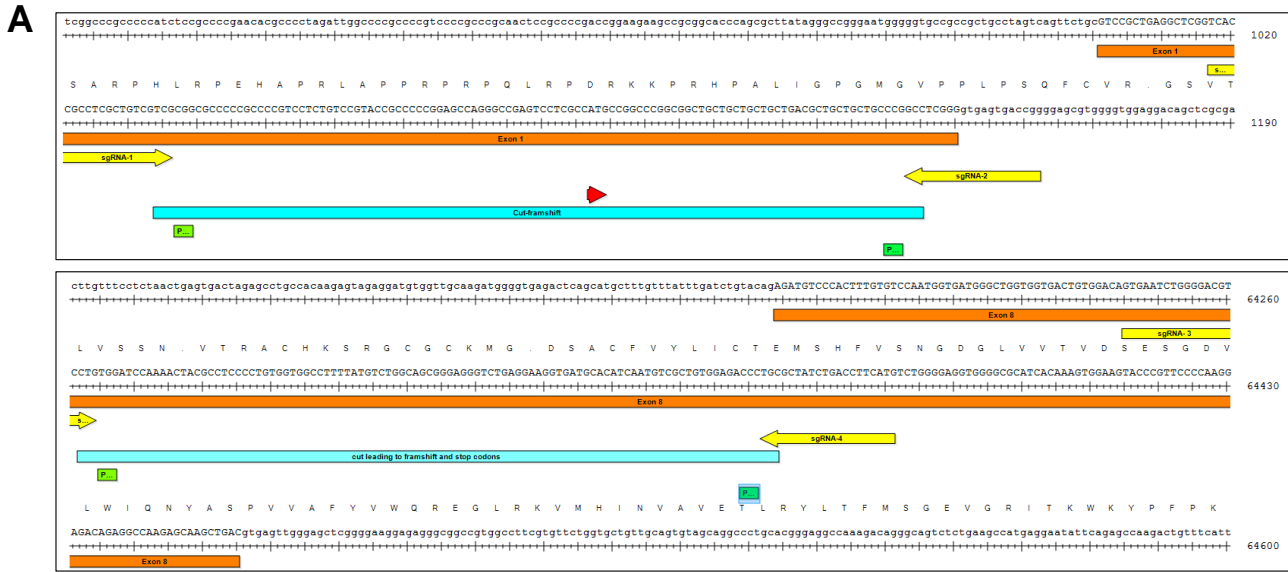


Figure 40: Establishing a stable IRE1α knockdown cell line.

(A) Schematic representation of the four different sgRNAs targeting exons one and three of the human *ERN1* gene (encoding IRE1α) DNA sequence in-silico (using DNASTAR navigator). These sgRNAs were then cloned into the pX459 plasmid system and used to transfect parental Huh7 cells individually or in combination. The transfected cells were then subjected to puromycin selection (1 μg / ml). Yellow arrows represent the individual sgRNAs. The head of the arrow indicates the direction of sgRNA. The two blue rectangular marked with “1+2 frameshift-deletion” and with “3+4 frameshift-deletion” represent the deletion and subsequent frameshift as a result of sgRNAs 1+2 and 3+4 cuts respectively. Green boxes indicate the PAM site. The red arrow indicates the start of coding sequence.

(B) Whole-cell extracts of the newly engineered cell lines using special lysis buffer were subjected to Western blot analysis and the efficiency of IRE1 α knockdown was then assessed using anti-IRE1 α antibodies in the presence or absence of 24 hours of HCoV-229E (MOI of 1) infection.

(C) After further multiple passages under puromycin selection (1 μ g / ml), a stable cell line carrying the combination sgRNAs 1+2 was selected and designated as the IRE1 α KD cell line. Whole-cell extracts from IRE1 α KD, parental Huh7, and pX459 empty vector control cell lines with or without 24 hours of HCoV-229E (MOI of 1) infection were subjected to Western blotting. Using indicated antibodies, host and viral protein levels were then compared amongst the three cell lines.

β -actin was used as a loading control

The data above indicated a successful establishment of engineered cell lines carrying PERK or IRE1 α knockdowns.

4.3.2 Characterizing PERK and IRE1 α knockdown cell lines in the context of HCoV-229E replication

To follow up on the initial observations seen in figures 39 C & 40 C, protein levels of several host and viral factors in PERK and IRE1 α KD cell lines in reference to the empty vector control cell line were compared on a Western blot (Fig. 41 A & B). PERK and IRE1 α protein levels showed a strong reduction corresponding to each of these cell lines' knockdown, confirming the stability of these selected cell lines. Interestingly, in the PERK KD cell line, thapsigargin-induced upregulation of IRE1 α was completely reversed. One hour of thapsigargin induced strong phosphorylation of eIF2 α on serine 52 in both IRE1 α KD and the empty vector cell lines. In comparison to these cell lines, no phosphorylation of eIF2 α on serine 52 was observed in PERK KD. On the other hand, prolonged exposure of all cell lines to thapsigargin activated eIF2 α serine 51 phosphorylation, indicating an independent mechanism for translation modulation in prolonged ER stress conditions in PERK KD (though there was no statistical significance using the indicated test and comparison, see figure legends).

The investigated viral factors showed a varying degree of regulation in the KD cells. PERK KD cells infected with 24 hours of HCoV-229E (MOI of 1) showed a significant increase in the viral N protein while no change in the levels of nsp8. IRE1 α KD cells infected with the virus showed no changes in the levels of either viral factors. Assessing the level of infectious particles production in these cell lines using plaque assay indicated a slight change in the viral titer in IRE1 α KD cell line while surprisingly, in the light of the aforementioned effects on intracellular N viral protein, a decrease in the titer has been observed in PERK KD cell line (Fig. 41 C).

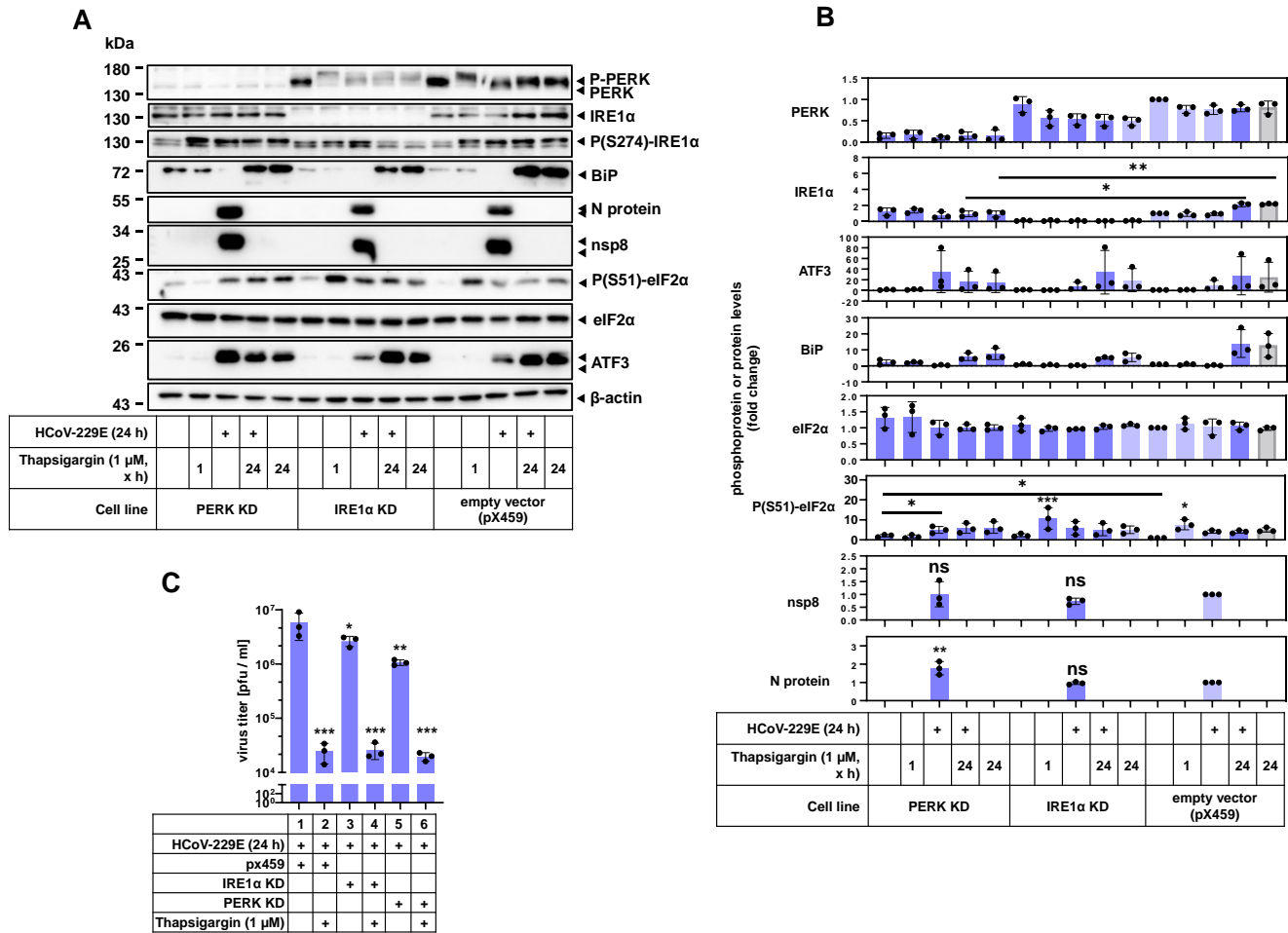


Figure 41: Differential effects of CRISPR-CAS-9 engineered cell lines lacking PERK or IRE1 α on the ER stress response and HCoV-229E replication.

Huh7 cells with CRISPR-CAS-9 engineered PERK or IRE1 α knockdown or the empty vector control cell line were either left untreated, infected with HCoV-229E (MOI of 1), treated with 1 μ M of thapsigargin, or infected and treated simultaneously as indicated. After 24 h, whole-cell extracts were prepared using the special lysis buffer and subjected to Western blotting. Supernatants from the indicated conditions were collected and assayed for infectious particles production using plaque assay.

(A) Shows a representative immunoblot of the investigated host and viral proteins of one out of the three biological replicas.

(B) Quantification of proteins or protein phosphorylation levels shown in (A) from three independent biological replicas relative to the untreated control. Antibodies against β -actin were used as a loading control.

(C) Supernatants from the experiments shown in (A) were used to determine the production of infectious viral particles by plaque assay. The Y-axis shows plaque-forming units per milliliter (pfu /ml).

Bars show means \pm s.d., while dots show the results from biologically independent experiments. Asterisks indicate p values (* $p \leq 0.05$, ** $p \leq 0.01$, *** $p \leq 0.001$, **** $p \leq 0.0001$) obtained by one-way ANOVA test where the mean of each column was compared to the mean of the empty vector untreated column, except for the vrial proteins and viral titer where they were compared to the mean of the empty vector infected sample. Two-tailed unpaired t-test was also used for the indicated pairs in IRE1 α and eIF2 α panels (B).

Overall, the data indicated a PERK-independent regulation of eIF2 α serine 52 phosphorylation along with a possible decoupling between the viral N protein translation and/or degradation and infectious

particles production. Overall, and in contrast to PERK, the data showed only a minor role of IRE1 α in HCoV-229E replication.

To follow up on the differential regulation of eIF2 α phosphorylation in PERK KD cells compared to the empty vector control cell line and the impact of this regulation on the de-novo protein synthesis landscape in this cell line, a puromycilation assay was utilized. As previously described for parental Huh7 cells, one hour of thapsigargin treatment of the empty vector control cells resulted in a strong reduction in translation levels. In stark contrast, PERK KD cells showed a complete reversal of the translation shutdown. On the other hand, the virus-induced translational shutdown seen in the control cell line was only partially reversed in the PERK KD cell line. A strong reversal of the partial translation shutdown induced by 24 hours of thapsigargin was observed in PERK KD cells compared to the control. In contrast, IL-1 treatment, which was used as an additional reference, did not induce changes in translational levels in either cell lines, confirming the specificity of the effects (Fig. 42 A & B).

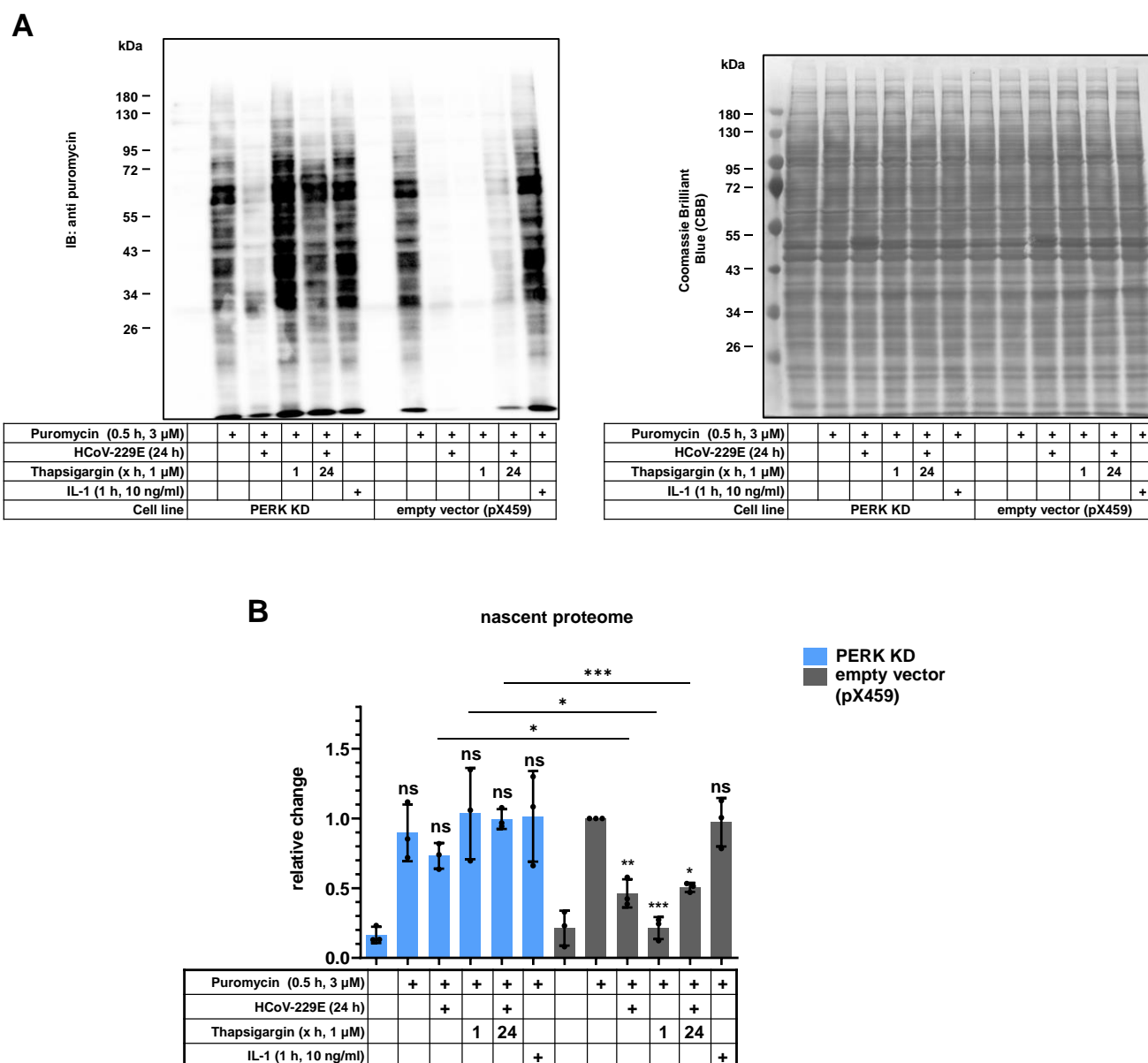


Figure 42: Differential effects of CRISPR-CAS-9 engineered PERK KD cell line on de novo protein synthesis.

Huh7 cells with CRISPR-CAS-9 engineered PERK knockdown or the empty vector control cell line were either left untreated, infected with HCoV-229E (MOI of 1), treated with 1 μ M of thapsigargin for 1 h or 24 h, infected and treated with 24 hours of thapsigargin and HCoV-229E or treated with 1 h of IL-1 as indicated. Half an hour before harvesting the cells, a pulse of 3 μ M of puromycin was added to the medium of all conditions except one untreated/uninfected control (as indicated in the legend). Thereafter, total cell extracts were prepared using special lysis buffer and analyzed on western blot.

(A) Representative immunoblot of anti-puromycine antibodies (left) and CBB staining of the corresponding immunoblot as a loading control and steady-state protein levels visualization (right) of one out of three biological replicas.

(B) The corresponding quantification from (A) from the three independent biological replicas relative to the puromycine-only condition (puro-pulsed, untreated/uninfected control of the empty vector).

Bars show means \pm s.d., while dots show the results from biologically independent experiments. Asterisks indicate p values (* $p \leq 0.05$, ** $p \leq 0.01$, *** $p \leq 0.001$, **** $p \leq 0.0001$) obtained either by one-way ANOVA test where

the mean of each column was compared to the mean of the empty vector untreated (puromycin-pulsed) column, or using two-tailed unpaired t-tests for the indicated pairs.

The same puromycylation assay experiment, under the same experimental conditions, was then carried out for the IRE1 α KD cell line. The western blot analysis indicated no major changes in the pattern of translation regulation as compared to the empty vector control though the intensities of lanes in the IRE1 α KD cell line were stronger (Fig. 43). Therefore, the role of IRE1 α in these effects was not followed any further.

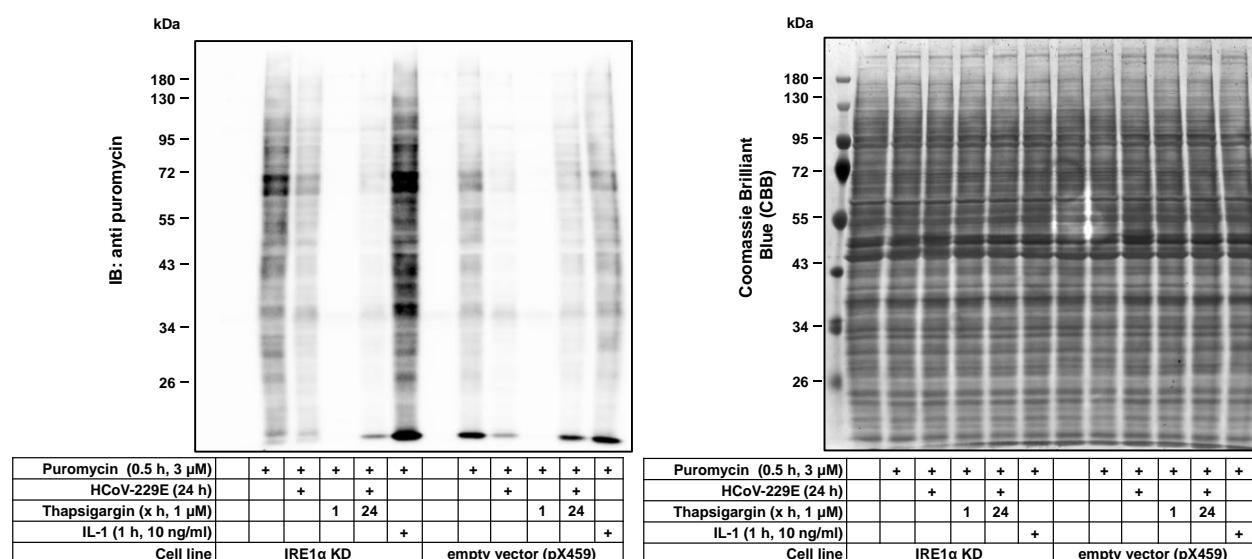


Figure 43: Differential effects of CRISPR-CAS-9 engineered IRE1 α knockdown cell line on de novo protein synthesis.

Huh7 cells with CRISPR-CAS-9 engineered IRE1 α knockdown or the empty vector control cell line were either left untreated, infected with HCoV-229E (MOI of 1), treated with 1 μ M of thapsigargin for 1 h or 24 h, infected and treated with thapsigargin and HCoV-229E for 24 hours or treated with 1 h of IL-1. Half an hour before harvesting the cells, a pulse of 3 μ M of puromycin was added to the medium of all conditions except one untreated/uninfected control (as indicated in the legend). Thereafter, total cell extracts were prepared using the special lysis buffer and analyzed on western blot.

The panel shows an immunoblot of anti-puromycine antibodies (left) and CBB staining of the corresponding immunoblot as a loading control and steady-state proteins levels visualization (right) of a single experiment.

The data above reflected the role of PERK in the differential regulation of eIF2 α phosphorylation and its effect on translation. The data also pointed out possible, additional involvement of other eIF2 α protein kinases (PKR, GCK2 and HRI) that might be activated by the virus to induce and maintain the translational shutdown throughout the infection.

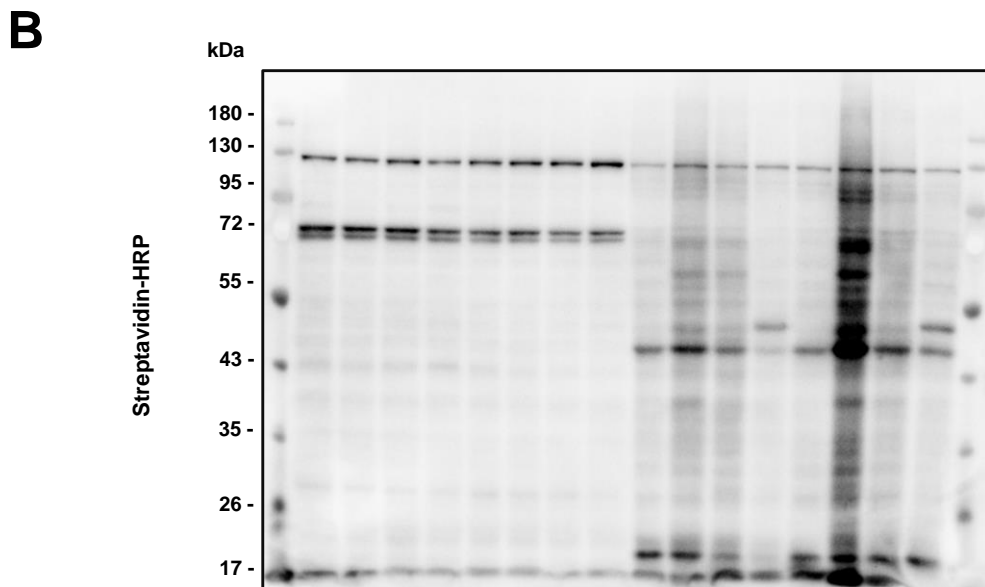
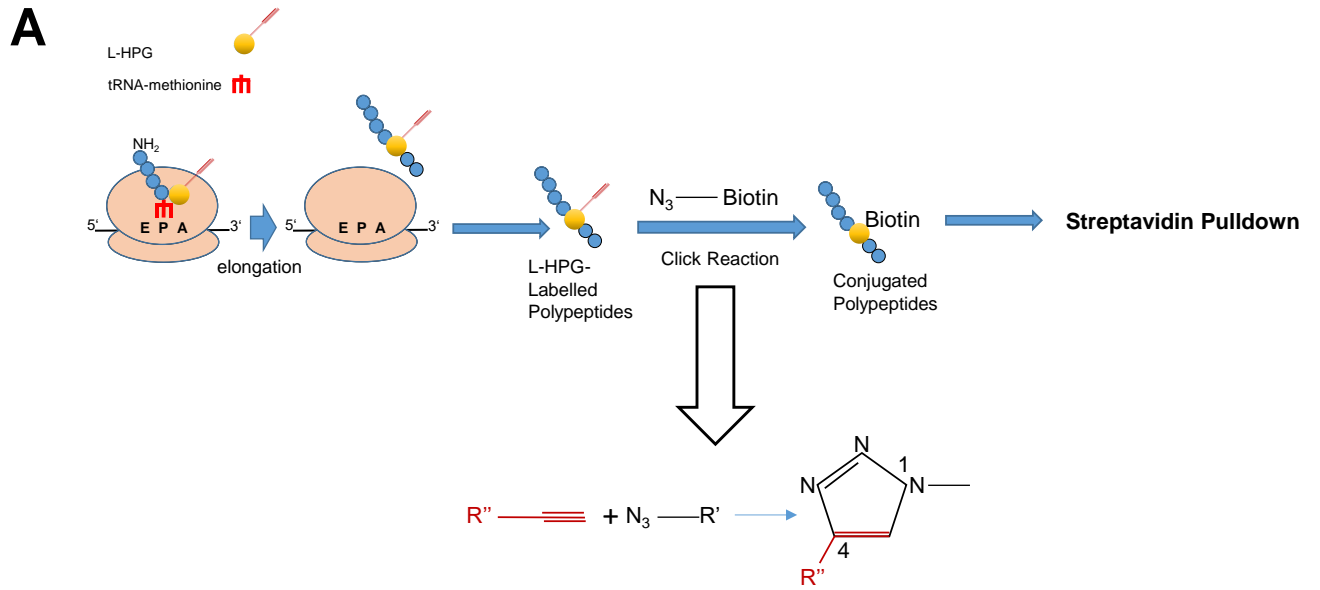
To follow up on the increase of the viral N protein in the PERK KD cells accompanied by a reduction in the titer, a click chemistry approach was implemented to label the nascent polypeptides with methionine analog, L-Homopropargylglycine (L-HPG). L-HPG can be then conjugated to biotin, pulled down and probed for the protein of interest on a western blot. This method has two main advantages over classical puromycin labelling mentioned previously. First, it does not result in a premature stop of translational elongation that is associated with puromycin and therefore, is suited to detect any artifacts associated with t-RNA analogues such as puromycin or its derivatives. The second one, it allows the

purification of the full length nascent proteins using the biotin-streptavidin system and the subsequent analysis of the translation rates of individual proteins using specific antibodies.

The method relies on the addition of L-HPG to a methionine-free medium two hours before the end of the experiment. The added L-HPG will be incorporated into the newly synthesized polypeptides without causing premature translation termination. Proteins extracted from these cells will then be subjected to a click reaction to add a biotin azide to the alkyne group on the L-HPG that can be then captured using streptavidin beads and analyzed on Western blot or sent to mass spectrometry analysis (Fig. 44 A).

For this purpose, PERK KD and empty vector control cell lines were left untreated, infected with 24 hours of HCoV-229E (MOI of 1), or simultaneously infected and treated with 1 μ M of thapsigargin for 24 hours. Whole-cell extracts containing polypeptides labeled with L-HPG were then conjugated to biotin and analyzed on a western blot using the click chemistry step. The analysis was done by first comparing whole-cell lysates before and after the click reaction using streptavidin covalently conjugated to Horseradish peroxidase enzyme (i.e. lysates vs click lysates). This comparison indicated the successful conjugation of the biotin azide to the alkyne group on the L-HPG of the newly synthesized polypeptides as the click-lysates side of the blot showed the expected smear patterns while lysates side showed no smear. The efficiency of labeling, however, was different between the two cell lines with the empty vector control cells showing stronger intensities of the smear (Fig. 44 B).

Labeled polypeptides from both cell lines were then pulled down using streptavidin beads. Click-lysate and pulled down proteins were probed for biotin and several host, and viral factors. PERK and BiP were shown to be strongly newly synthesized in the empty vector control condition treated with thapsigargin. The downregulation of the BiP and PERK upon HCoV-229E infection can also be seen on the level of translation in this cell line. Under all conditions, PERK KD cells exhibited a general downregulation of all investigated factors. Nevertheless, under the virus infection condition, the viral N protein was massively translated in PERK KD cells when compared to the empty vector control cell line, which was in agreement with the increase of the steady state level of this protein seen in the lysate blots (Fig. 41 A and Fig. 44 C).



	lysate (25 µg)								Click-lysate (25 µg)								
Sample #	1	2	3	4	5	6	7	8	1	2	3	4	5	6	7	8	
EV control					+	+	+	+						+	+	+	+
PERK KD	+	+	+	+					+	+	+	+					
Met-free medium		+	+	+		+	+	+		+	+	+		+	+	+	
HCoV-229E (24 h)			+	+			+	+			+	+				+	+
Thapsigargin 24 h [1 µM]			+				+				+					+	
L-HPG (25 µM, 2 h)	+	+	+			+	+	+		+	+	+		+	+	+	

C

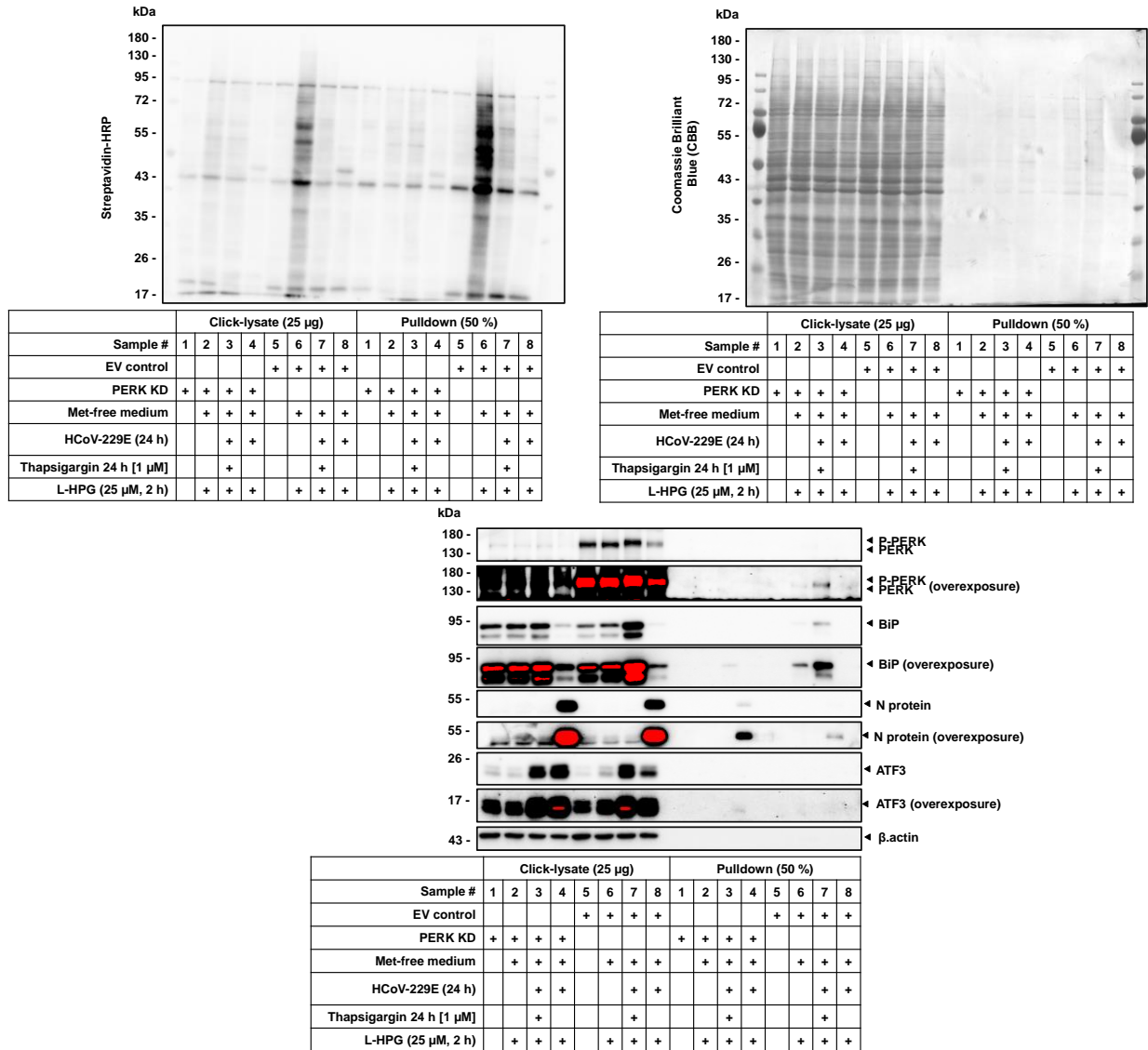


Figure 44: Upregulation of de novo synthesis of the viral N protein in CRISPR-CAS-9 engineered PERK cell lines.

CRISPR-CAS-9 engineered PERK knockdown and the empty vector control cell lines were left untreated, infected with 24 hours of HCoV-229E (MOI of 1), simultaneously infected and treated with 1 µM of thapsigargin for 24 hours. At 21.5 hours before the end of the infection/treatment period, cells were washed with warm PBS and then incubated in a methionine-free medium for half an hour, and then 25 µM of L-HPG was added for further 2 hours. As a negative control for the method, additional untreated cells were left without medium change or L-HPG addition. Total cell extracts using click-chemistry lysis buffer (details in the materials section) were pre-cleared and then conjugated to biotin through click reaction. Proteins were then precipitated with acetone, re-suspended in PBS with 1% SDS and separated from the reaction buffer using Zebra Spin Columns (Thermo 89882 7k MWCO). Finally, biotinylated nascent proteins were pulled down using Streptavidin-Agarose beads, and then analyzed on Western blot

(A) Schematic representation of labeling nascent polypeptides with L-HPG, the subsequent click reaction to conjugate it to biotin, and thereafter pulling down the labeled proteins using streptavidin beads. R: side group.

(B) Western blot analysis comparing lysate vs click-lysate using HRP-Conjugated streptavidin.

(C) Western blot analysis comparing click-lysate vs pull-down using HRP-Conjugated streptavidin (upper left) and the indicated host and viral proteins antibodies (lower). CBB staining of the corresponding immunoblot was used as a loading control and steady-state proteins levels visualization (upper right).

The data above demonstrated the strong translational induction of viral N protein, and the virus-induced downregulation of BiP at the translational level in infected cells. The data further showed that thapsigargin suppresses N protein synthesis and restores BiP synthesis against the global translational shutdown. The data also indicated a decoupling between the viral N protein translation and the production of infectious particles in cells lacking PERK.

Together, the data shown so far in chapters 4.1 and 4.3 highlight the complex and diverging roles of the two major ER stress sensors IRE1 α and PERK in CoV- infected cells and in the response to thapsigargin. Therefore, additional experiments were performed to study downstream effector molecules in these pathways.

4.3.3 Establishing stable ATF3 knockdown cell line using lentivirus system

ATF3 is a transcription factor involved in multiple ER stress pathways. As previously indicated in figure 12, ATF3 is induced upon HCoV-229E infection as well as by long-term thapsigargin treatment. The induction of this factor was suppressed when cells were treated with either PERK or IRE1 α inhibitors. However, no functional role of this transcription factor in CoV replication nor in thapsigargin-mediated effect has been reported or investigated yet.

For this purpose, two ATF3 knockdown cell lines were generated using the pX459 system, each having one sgRNA designed to target the coding sequence of ATF3 as described previously. After puromycin selection, none of these cell lines showed any reduction in the levels of ATF3 in the presence or absence of HCoV-229E infection (Fig. 45 A). Given these negative results, the lentivirus transduction system, a more efficient and comprehensive approach, was utilized. Six sgRNAs taken from the GECKO version 2.0 sgRNA library (Sanjana, Shalem, and Zhang 2014) were cloned in the transfer vector of the second-generation lentivirus transduction system and the protocol was carried out as described in the Methods to generate six engineered cell lines (see Methods for more details). After puromycin selection, the six resultant cell lines were either left untreated or infected with HCoV-229E for 24 hours. An empty vector control cell line was used as a reference. Out of the six cell lines, only the cell line with sgRNA number 3 (LentiViruse-sgRNA3) showed a knockdown of the protein in both steady-state and induced (with infection) conditions. This cell line was then chosen for further analysis (Fig. 45 B).

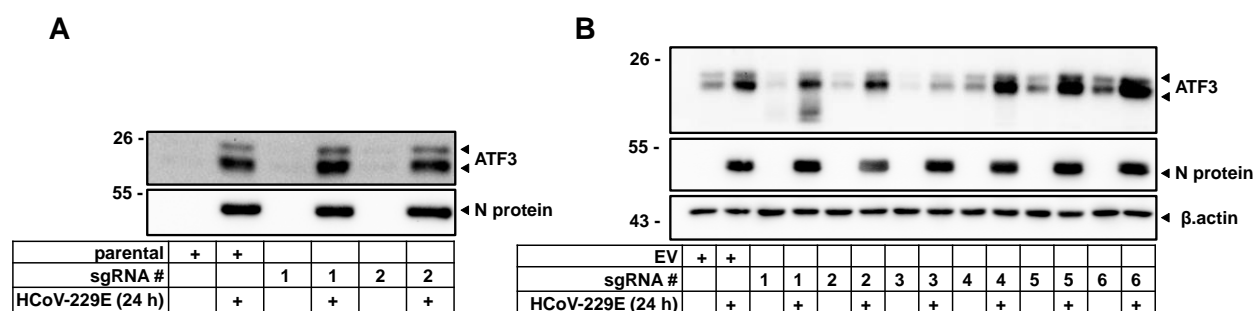


Figure 45: Attempts to establish stable ATF3 knockdown cell lines.

(A) Parental Huh7 cells were individually transfected with two pX459 plasmids containing either sgRNA 1 or 2 each targeting a different region in the coding sequence of ATF3, as previously described. After multiple passages under puromycin (1 µg / ml) selection, the efficiency of ATF3 knockdown in the resultant two cell lines was assessed using whole-cell extracts from these cell lines on Western blotting in the presence or absence of 24 hours of HCoV-229E (MOI of 1) infection. The parental cell line was used as a reference control.

(B) For a second attempt to knockdown ATF3 using the lentivirus transduction system, parental Huh7 cells were individually infected with six lentiviral populations targeting diverse regions in the sequence of ATF3 (details and sequences are in the materials and methods sections). After multiple passages under puromycin selection (1 µg / ml), the efficiency of ATF3 knockdown in the resultant six cell lines was then assessed using whole cell extracts from these cell lines on Western blotting in the presence or absence of 24 hours of HCoV-229E (MOI of 1) infection. The cell line infected with Lentivirus-sgRNA3 was selected for further experimentation. Lentiviruses carrying no sgRNA insert were used as a reference control (Lentivirus-Empty-Vector, EV).

Antibodies against β-actin were used as a loading control.

Further analysis using western blot and plaque assay of the stable ATF3 knockdown cell line indicated no changes in the levels of the investigated viral and host proteins nor in the levels of the viral titer (Fig. 46).

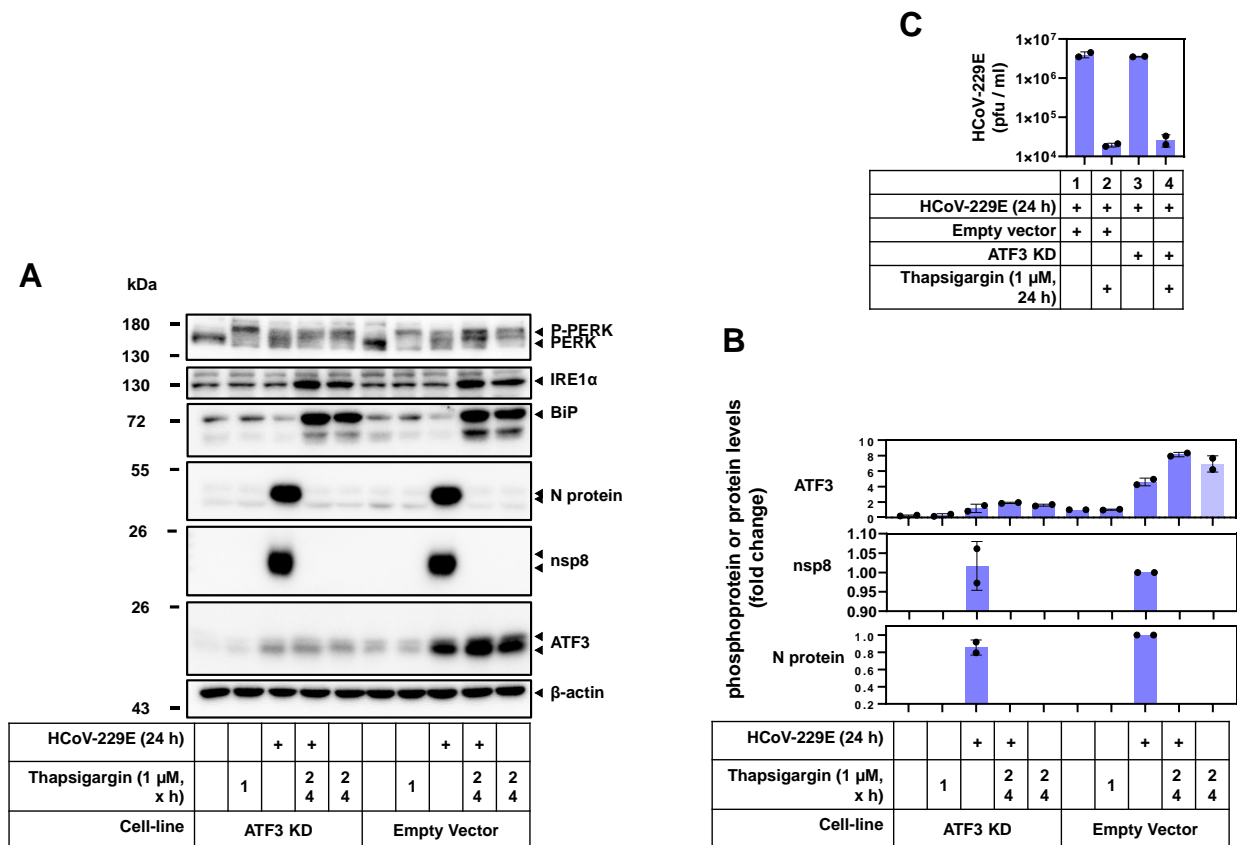


Figure 46: Analysis of the effects of CRISPR-CAS-9 engineered ATF3 knockdown cell line on the ER stress response and the replication of HCoV-229E.

Huh7 cells with CRISPR-CAS-9 engineered ATF3 knockdown (Lentivirus-sgRNA3) or the Lentivirus-Empty-Vector control cell line were left untreated, infected with HCoV-229E (MOI of 1), treated with 1 µM of thapsigargin for 24 hours or infected and treated simultaneously. Thereafter, total cell extracts using the special lysis buffer were prepared and analyzed via Western blotting. Supernatants from infected conditions were used for plaque assay.

(A) Representative immunoblot showing the detection of the indicated host and viral proteins of one out of two biological replicas.

(B) Corresponding protein levels from (A) were quantified from the two independent biological replicas relative to the untreated/uninfected control of the empty vector cell line. Antibodies against β -actin were used as a loading control.

(C) Supernatants from the two biological replicas shown in (B) were used to determine the production of infectious viral particles by plaque assay. The Y-axis shows plaque-forming units per milliliter (pfu /ml).

The data above indicated no phenotypic role of this transcription factor in the replication of HCoV-229E or thapsigargin- or viruse-induced effects on PERK, IRE1 α or BiP levels in Huh7 cells under the indicated conditions and left the question open of whether an alternative method of investigation can reveal a functional involvement of this factor which will be the topic of the next chapter.

4.4 The interactome of major UPR effectors

ER stress pathways are effectuated through the activation of multiple cascades of signaling and genetic programs that involve extensive transient or prolonged protein-protein interactions at the up- and downstream levels of these pathways. Viral infections can significantly alter the landscape of protein-protein interactions either because of an anti-viral mechanism, global effects on protein expression (such as the translational shutdown) or as a specific exploitation of these pathways by the virus to foster its replicative cycle.

To determine putative interactors of major ER stress sensors PERK and IRE1 α and the up- and downstream effectors, BiP and ATF3 in the context of HCoV-229E infection, a biotinylation assay approach named BioID was utilized (Sears, May, and Roux 2019). The assay depends on generating a chimeric protein consisting of a biotin ligase part and a protein of interest (bait) part. The chimeric protein is generated through cloning the DNA sequence of the bait protein next to the DNA sequence of the ligase, either on the C- or on the N- terminal side, in an appropriate expression vector. After transfecting the resultant expression vector in a suitable model (in cells or organisms), if expressed and folded correctly the interactions and behavior of this chimeric protein should mimic those of the endogenous one. Interactors that come within a defined distance to this chimeric protein will be labeled with exogenous biotin. Given the uncommonness of biotin as an endogenous protein modification, these proteins can be enriched for by pulling them down and then analyzed using Western blotting or mass spectrometry (Fig. 47 A). The advantage of this method is to capture a snapshot of interactions that occur only transiently, at low frequency, substoichiometrically, with low affinity, or in insoluble cellular compartments (Sears, May, and Roux 2019).

Multiple options are available to be used as a biotin ligase for this method. For instance, BirA biotin ligase derived from *Escherichia coli* or the smaller, genetically engineered (humanized) biotin ligase derived from *A. aeolicus* capable of biotinylating lysine residues on an acceptor peptide (D. I. Kim et al. 2016). Several limitations of BirA have been described that include temperature sensitivity, varying

biotinylation efficiency depending on cellular compartment and slow kinetic activities. To overcome these limitations, a directed evolution approach was implemented by Bannon et al to produce a smaller, faster, and more efficient version called miniTurbo (Branon et al. 2018; Mair et al. 2019). The expression vectors designed for expressing the chimeric proteins with their respective ligase are schematically represented in figure 47 B.

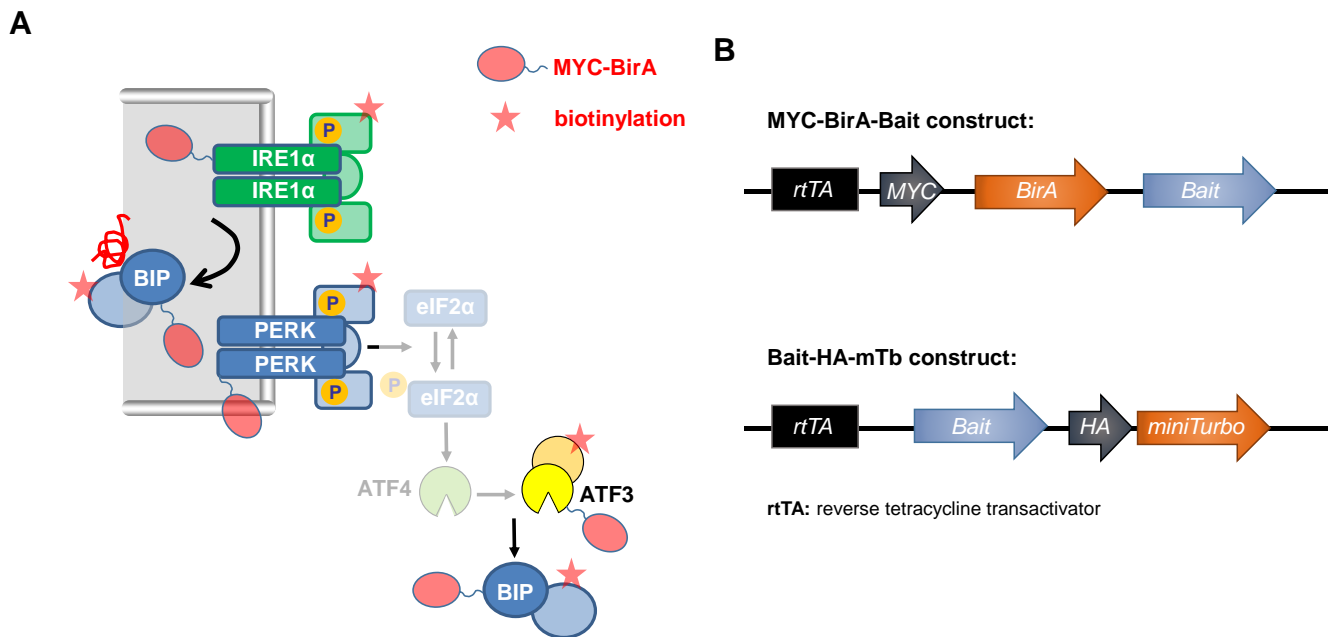


Figure 47: Revealing the interactomes of major ER stress factors using proximity-based biotinylation labelling strategies.

(A) Schematic representation of chimeric proteins consisting of major ER stress factors attached to them a biotin ligase. Increasing the intracellular biotin levels by addition of exogenous biotin will promote the ligase to biotinylate proteins coming in close contact within a radius of approximately 10 nm of the chimeric protein. This radius might be affected by the length of a linker peptide sequence between bait and biotin ligase. The stable biotin modification can then be used to purify or visualize proteins by adding streptavidin conjugates.

(B) Schematic representation of the two plasmid vectors used to express the chimeric proteins where the bait (protein of interest) cDNA will be ligated into the plasmid next to a tag (MYC or HA peptide sequences) and a biotin ligase (in this case, either BirA or miniTurbo). The expression of both of these constructs is under tet-on system control.

Both of these vectors contain a tetracycline-on (tet-on) system. Hence, the expression of these constructs is regulated by the addition of tetracycline or its derivative doxycycline. The tet-on system contains *rtTA* (reverse tetracycline-controlled trans-activator) which is an engineered construct that consists of a mutated tetracycline repressor (*tetR*) fused to it the transcriptional activation domain of the virion protein 16 (VP16). The binding of tetracycline (or doxycycline) to the mutated *tetR* results in the binding of the *rtTA* to the promoter and the activation of gene expression (Gossen et al. 1995).

In this study, the two biotin ligases (BirA and miniTurbo) were used and the resultant chimeric proteins were characterized and tested under multiple experimental conditions. The results are shown in the subsequent sections.

4.4.1 Characterization of BirA and miniTurbo constructs

The first step was to characterize the pTet-on_Puro_Myc-BirA (referred to interchangeably as Myc-BirA or BirA) constructs. For this purpose, the cDNAs of PERK, BiP, IRE1 α , or ATF3 were (separately) ligated into the Myc-BirA vector (see Methods section for more details). The resultant new vectors were used to transiently transfect parental Huh7 cells using the calcium phosphate method. Whole-cell extracts from these transfected cells were then analyzed on Western blot. The analysis indicated that all the chimeric proteins were expressed when the vectors were induced with 1 μ g/ml of doxycycline for 24 hours. Expectedly, the bands corresponding to the chimeric proteins were migrating slower (i.e. at a higher molecular weight) than the corresponding endogenous protein bands. The MYC tag bands were detectable on the blot (using anti-myc antibodies) for all of the constructs except for Myc-BirA-PERK. This can be possibly explained because of the three-dimensional folding of the chimeric protein that might have masked the tag polypeptide (Fig. 48).

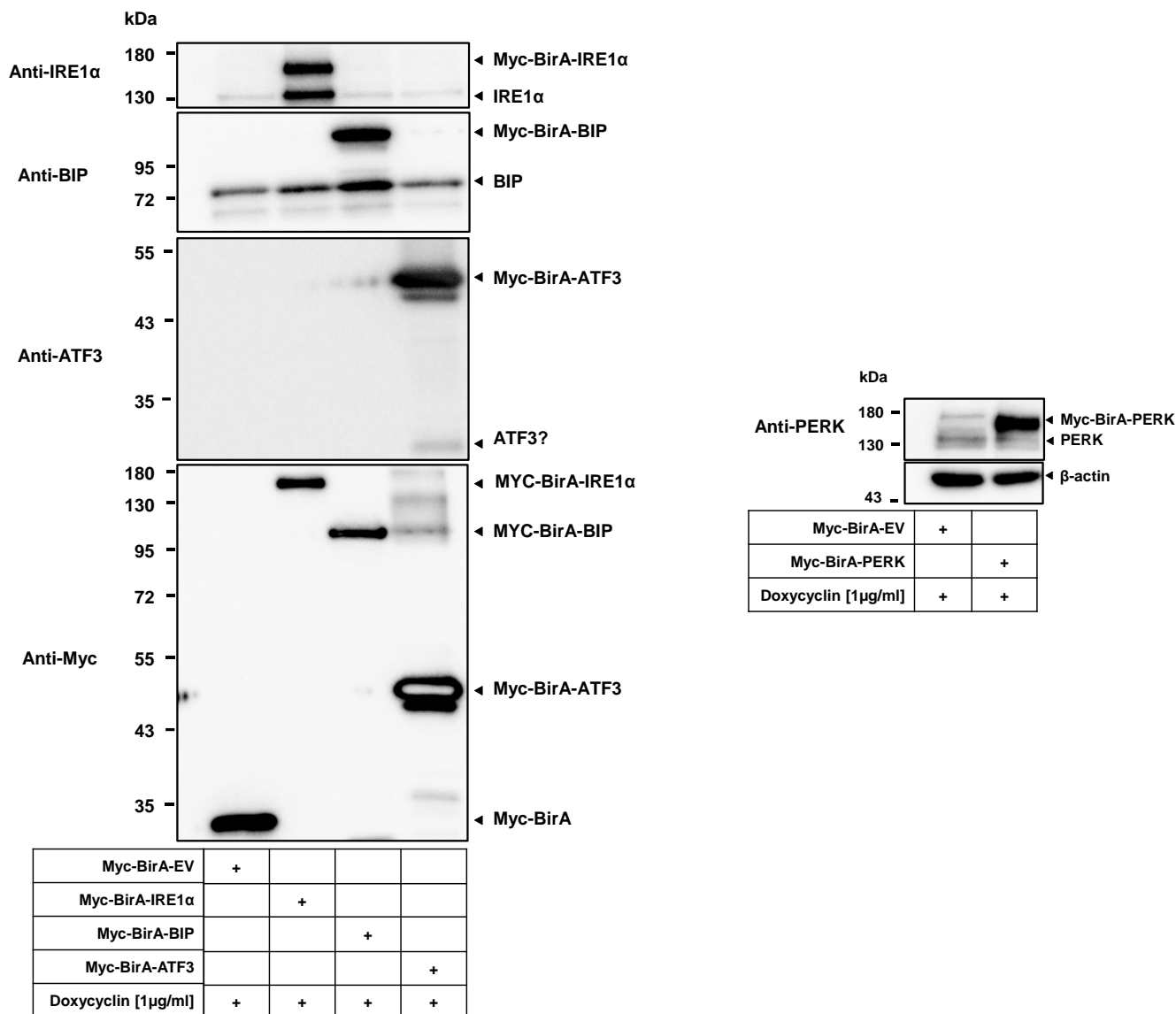


Figure 48: Expression of Myc-BirA-Empty-Vector and Myc-BirA- PERK, -BiP, -IRE1α, -ATF3 constructs.

Parental Huh7 cells transiently transfected with BirA-Empty-Vector (ligase only) and BirA- PERK, -BiP, -IRE1α, -ATF3 using the calcium phosphate method. 1 μg/ml of doxycycline was added immediately after the transfection to induce the expression of these constructs for 24 hours at 37°C. Whole-cell extracts from these cells using the special lysis buffer were then analyzed on a Western blot using the indicated antibodies (on the left). Labeling on the right indicates constructs/proteins detected. Antibodies against β-actin were used as a loading control.

With the expression of the four chimeric proteins shown in figure 48 being confirmed, the next step was to assess their biotinylation efficacy in Huh7 cells at normal cell culturing temperature (37°C).

After transfecting parental Huh7 cells with the vectors BirA-BiP, -ATF3, -IRE1α, -PERK or the empty vector control (expressing only BirA ligase) using calcium phosphate, cells were immediately induced with doxycycline along with exogenous biotin (50 μM) addition for 24 hours (D+, B+). As a control for leaky expression of the constructs, additional transfected cells (for each construct) were left without doxycycline induction after transfection (D-, B+). Thereafter, the BioID protocol as described by Roux

et al was followed (details in Methods, (Roux et al. 2012)), and pulled down proteins with streptavidin beads were compared to whole-cell extracts lysate on Western blot.

In the D+, B+ conditions, the streptavidin-horseradish peroxidase conjugates revealed a smear pattern in the lane corresponding to the BirA-EV (ligase only control) transfected cells, indicating random biotinylation of cellular proteins by the ligase. The lane also showed a relatively big band in the region of 34 kDa most likely corresponding to auto-biotinylation of the ligase itself. On the other hand, D+, B+ lanes corresponding to cells transfected with BirA-BiP, -ATF3, -IRE1 α , or -PERK showed a varying degree of smear intensities and auto-biotinylation bands. Contrary, in the D-, B+ conditions, all lanes displayed a strong reduction in the smear intensities (Fig. 49 A).

Silver staining of SDS gels is a sensitive method to visualize and assess the abundance of proteins and suitability to send them to mass spectrometry after a pulldown protocol, such as the BioID. Under the same conditions and expression vectors described above, corresponding gels were stained with silver nitrate. The smear patterns intensities seen in the streptavidin blots were reduced and in many instances, they were indistinguishable from the D-, B+ control level. On the other hand, the prominent bands thought to be corresponding to each of the expressed chimeric proteins auto-biotinylation remained visible (Fig. 49 B).

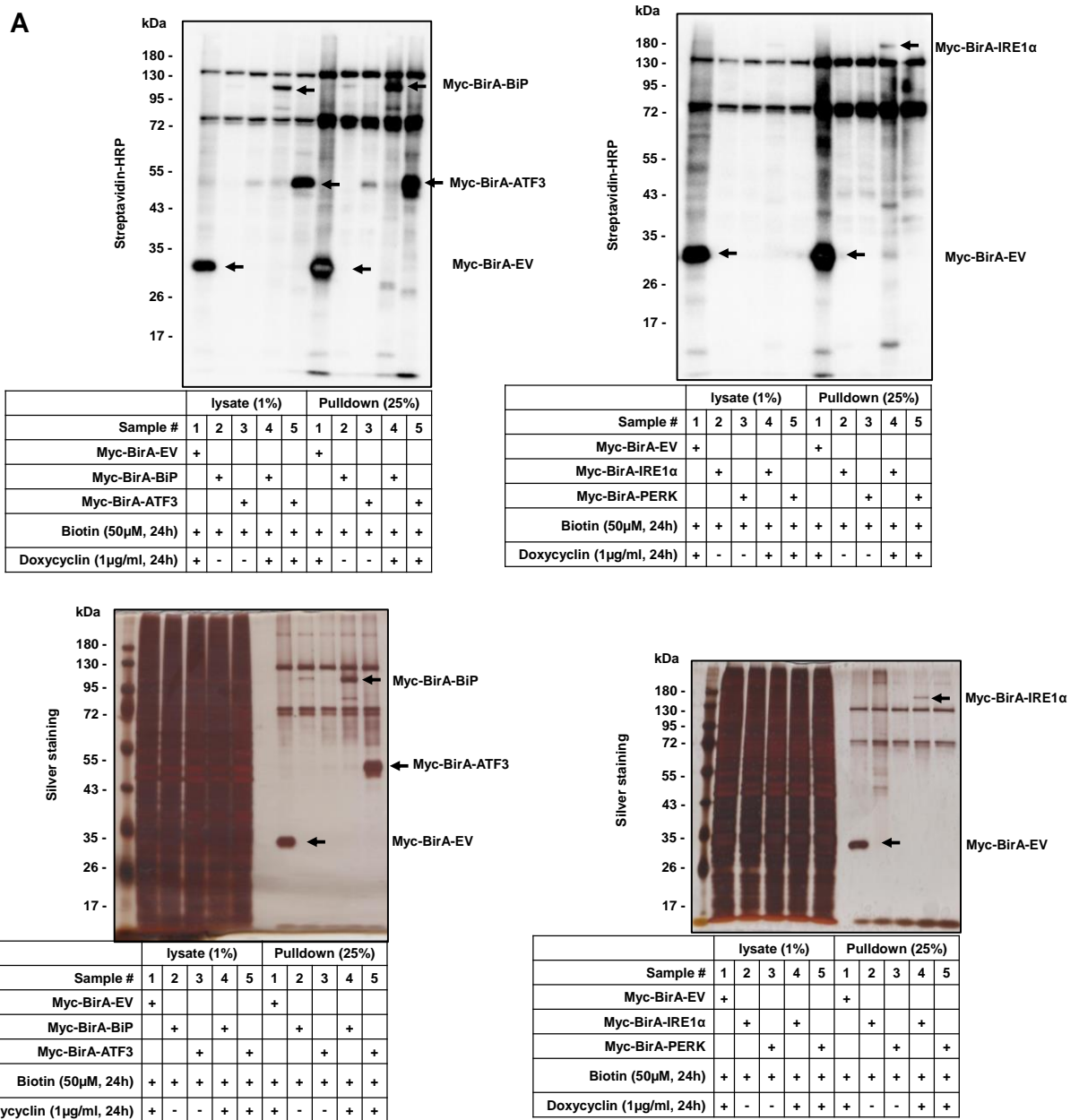


Figure 49: Biotinylation efficiency of Myc-BirA-EV (ligase only) and Myc-BirA-PERK, -BiP, -IRE1α, -ATF3 fusion proteins.

Parental Huh7 cells were transfected with vectors Myc-BirA-EV (ligase only) and Myc-BirA-PERK, -BiP, -IRE1α, -ATF3 using calcium phosphates methods. The expression of the vectors was induced by adding 1 μg/ml of doxycycline (D+) to indicated conditions. 50 μM of exogenous biotin (B+) was added to all conditions. Cells were then incubated at 37°C for 24 hours. BioID protocol (using BioID lysis buffer) as described in the methods (adapted from Roux et al. 2012) was then followed to obtain lysate and pulled down proteins.

(A) 1% of whole-cell extracts (lysate) were compared to 25% of pulled down proteins on a Western blot using HRP-Conjugated streptavidin or (B) on SDS gels using silver staining (details in the Methods section). For both (A) and (B), right half of the figure corresponds to cells transfected with Myc-BirA-BiP and -ATF3, while the left half represents cells transfected with Myc-BirA-IRE1α and -PERK. In both panels, lanes corresponding to empty vector control expressing only BirA ligase with doxycycline or BirA + bait without doxycycline induction were used as reference controls.

The levels of protein smear intestines observed on the silver staining between BirA-Bait with D+, B+ and BirA-Bait with D-, B+ conditions were comparable for all tested chimeric constructs. Given this observation, further investigation of the suitability and efficacy of this biotin ligase to biotinylate interactors was needed. Therefore, a series of experiments were performed to assess and compare BirA performance to the mutated, smaller and newer version miniTurbo.

For this purpose, the cDNAs of ATF3 and PERK were cloned into the pTet-on_Puro_HA-miniTurbo (referred to interchangeably as -HA-mTb or miniTurbo) vector. Thereafter, a three-pair comparison of BirA vs miniTurbo ligases (empty vectors), BirA-ATF3 vs miniTurbo-ATF3, or BirA-PERK vs miniTurbo-PERK at two different temperatures, namely 33°C vs 37°C was carried out. This was done by transfecting parental Huh7 cells with these constructs using calcium phosphate. Thereafter, all conditions received 50 µM of exogenous biotin for 24 hours. Induction with 24 hours of doxycycline was either included or omitted for the same condition as control. Untransfected cells were used as an additional control. Cells were then lysed (BioID protocol lysis buffer) and whole-cell extracts were analyzed on Western blot.

In doxycycline-induced conditions, lanes in streptavidin blot corresponding to cells transfected with miniTurbo ligase (empty vector) or miniTurbo-ATF3 revealed strong biotinylation patterns when compared to BirA ligase (empty vector) or BirA-ATF3 at both temperatures (Fig. 50 A). Both BirA ligase and BirA-ATF3 performed very poorly at 33 °C. Noticeably, when induced with doxycycline, the chimeric BirA-ATF3 construct was expressed to levels comparable or higher than that of the miniTurbo-ATF3 construct at both temperatures (Fig. 50 A & C). This pointed out the reduced efficiency of biotinylation of the BirA fusion proteins rather than suboptimal expression levels as primary cause for the inefficient biotinylation. Lanes in the MYC tag and ATF3 antibodies blots corresponding to cells transfected with BirA-ATF3 without doxycycline induction (D-) revealed a faint band of the chimeric protein indicating a leaky expression of this construct. No leaky expression band was observed for the miniTurbo-ATF3 construct on either the HA tag or ATF3 antibodies blots (Fig. 50 B & C).

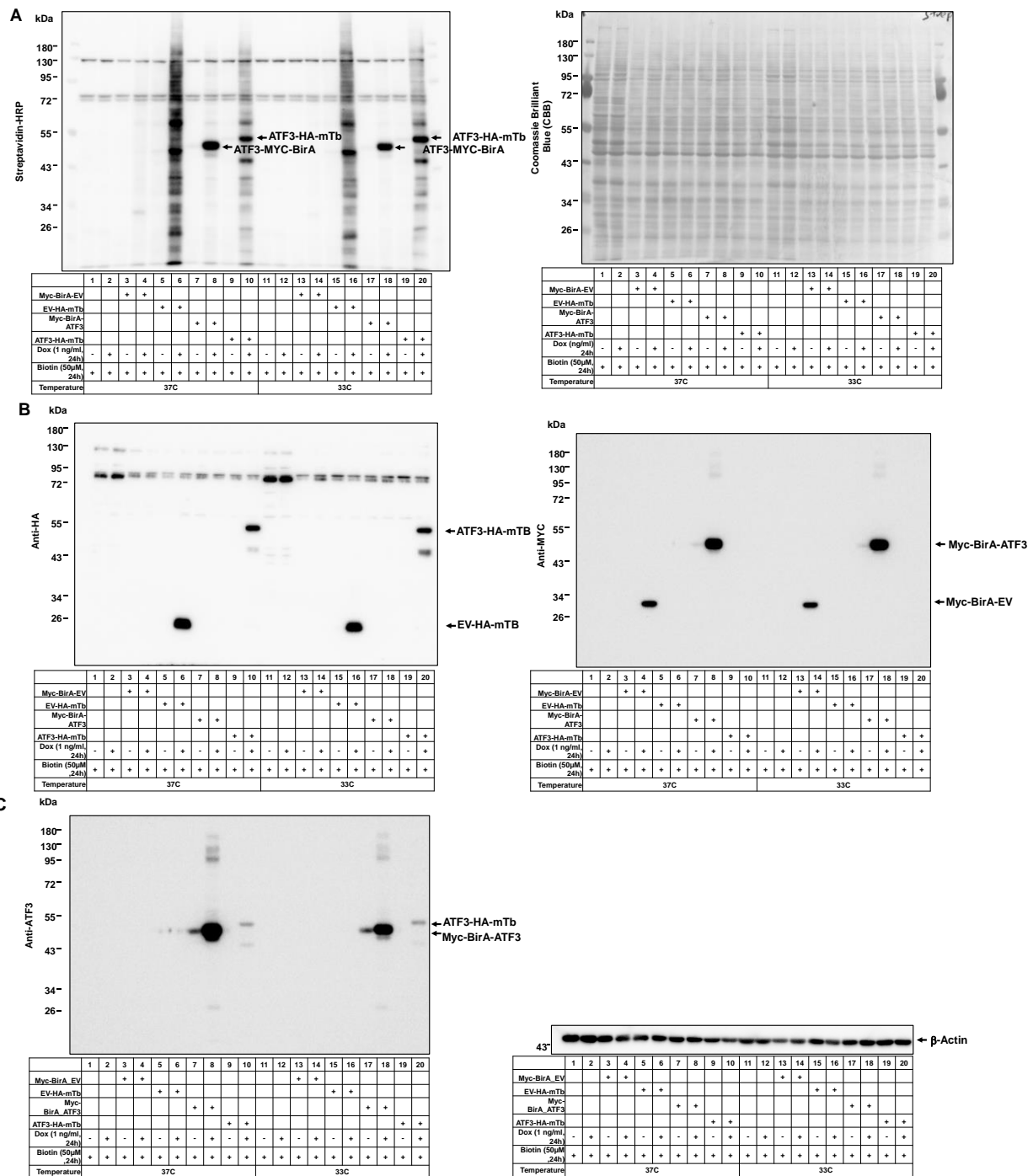


Figure 50: Biotinylation efficiency of miniTurbo-ATF3 construct is superior to that of BirA-ATF3 construct at 33°C and 37°C.

Huh7 cells were left without transfection or transfected with plasmids carrying either miniTurbo-ATF3, miniTurbo ligase (empty vector, EV), BirA-ATF3, or BirA ligase (empty vector, EV) constructs using the calcium phosphate method in two identical groups where each group contained 10 conditions. All conditions received 50 μM of exogenous biotin while induction with doxycycline was either included or omitted for the same condition. Doxycycline induction and biotin treatment were carried out immediately after the end of the transfection protocol. Groups were then incubated for further 24 hours at either 33°C or 37°C. Cells were then harvested and whole-cell extracts (using BioID lysis buffer) were subjected to western blot analysis. No pulldown was carried out. -HA-mTb: miniTurbo

(A) Streptavidin-HRP blot (left) with black arrows pointing to indicated constructs. CBB staining (right) of the same blot was used as a loading control.

(B) HA (left) and MYC (right) antibodies blots with black arrows pointing to indicated constructs.

(C) ATF3 antibodies blot (left). β -actin antibodies (right) were used to validate equal loading.

The same approach was then followed for PERK constructs. Streptavidin-HRP blots of lysates from Huh7 cells transfected with the BirA and the miniTurbo vectors recapitulated the same strong differences between the performances of the two ligases at either temperatures. On the other hand, with doxycycline induction, biotinylation efficiency of the miniTurbo-PERK was strongly reduced when compared to the miniTurbo ligase (empty vector) at 37°C. The biotinylation efficiency of the miniTurbo-PERK almost completely diminished to the levels of the non-induced control at 33°C. This pointed out the temperature sensitivity of this particular construct.

Doxycycline-induced Myc-BirA-PERK did not show any prominent auto-biotinylation band in the streptavidin-HRP blot at either temperature. At 37°C degrees, the doxycycline-induced and non-induced miniTurbo-PERK construct showed auto-biotinylation bands, with the latter (the leaky band) being very faint. Both of these bands were strongly reduced at 33°C degrees. The effect of temperature on the expression of BirA- and miniTurbo- PERK constructs induced with doxycycline can be seen on the PERK antibodies blot. In there, band levels corresponding to both constructs were strongly reduced at 33°C when compared to 37°C. Neither of the HA or MYC tags antibodies blots showed any band corresponding to their respective -PERK constructs with or without doxycycline induction (Fig. 51 A, B & C).

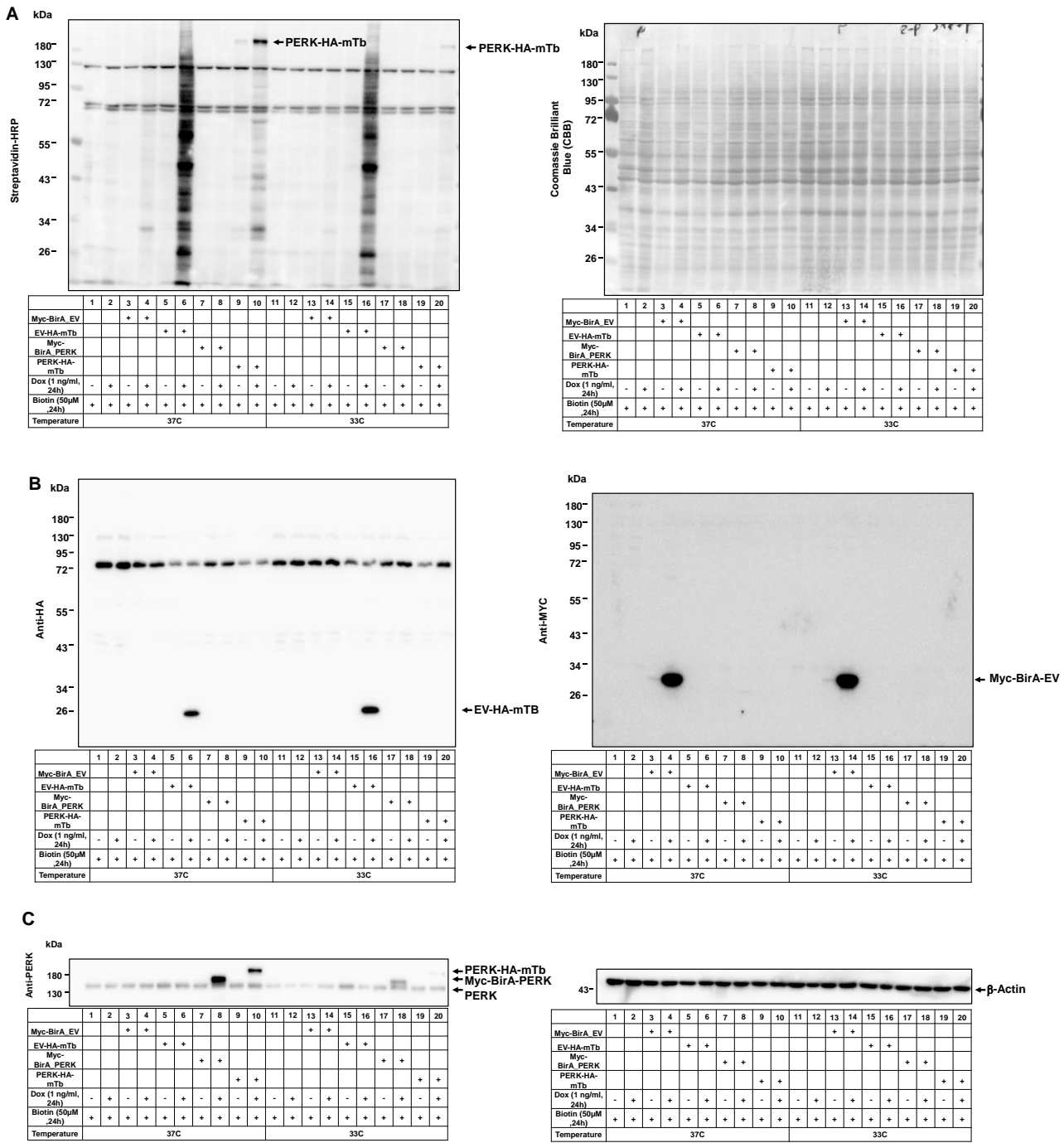


Figure 51: Biotinylation efficiency of miniTurbo-PERK construct is superior to that of MYC-BirA-PERK construct at 37 °C.

Huh7 cells were left without transfection or transfected with plasmids carrying either miniTurbo-PERK, miniTurbo ligase (empty vector, EV), BirA-PERK, or BirA ligase (empty vector, EV) constructs using the calcium phosphate method. The rest of treatments and conditions are the same as in figure 50.

(A) Streptavidin-HRP blot (left) with black arrows pointing to indicated constructs. CBB staining (right) of the same blot was used as a loading control.

(B) HA (left) and MYC (right) antibodies blots with black arrows pointing to indicated constructs.

(C) PERK antibodies blot (left). β -actin antibodies blot (right) was used as a loading control.

The data above indicated much better performance of all miniTurbo constructs over the BirA constructs in both tested temperatures. It also pointed out that the miniTurbo constructs biotinylation efficiency can be bait- and temperature-dependent as exemplified by the miniTurbo-PERK construct.

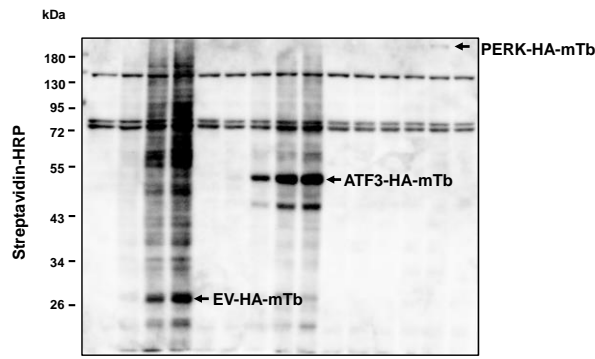
Given that all miniTurbo constructs over-performed the BirA ones at both tested temperatures, it was only logical to exclude the latter from further optimization and experimentation. Furthermore, the HCoV-229E optimal replication temperature in cell culture is 33°C, therefore, this temperature was chosen for subsequent experiments.

The next step of the optimization process was to compare the miniTurbo constructs expression and biotinylation levels at 33°C as a function of doxycycline concentration. For this purpose, Huh7 cells transfected with the miniTurbo ligase (empty vector, EV), miniTurbo-ATF3 and miniTurbo-PERK constructs (as previously described) were treated with increasing concentrations of doxycycline for 24 hours. All conditions were treated with 50 µM exogenous biotin for 24 hours except for one (B-) control condition for each construct. These control conditions were induced with 1 µg/ml of doxycycline. Cells were then harvested and whole-cell extracts using BioID lysis buffer were analyzed using Western blotting.

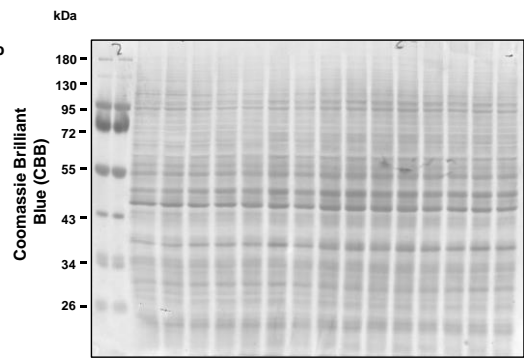
Streptavidin-HRP blots indicated biotinylation levels of the constructs auto-biotinylation bands that are increasing in intensity as a function of doxycycline concentration in the presence of exogenous biotin. This was observed for all constructs except miniTurbo-PERK. Control conditions induced with the highest concentration of doxycycline but lacking exogenous biotin did not show any protein smear or prominent bands in the Streptavidin-HRP blot. The miniTurbo-PERK construct biotinylation levels at any given doxycycline concentration were comparable to the non-induced or no biotin controls while a faint band corresponding to auto-biotinylation of this construct can be observed at the two highest concentrations of doxycycline (Fig. 52 A).

Both PERK and ATF3 antibodies blots showed a doxycycline-dependent increase in the level of the induced chimeric proteins. In the control lanes induced with doxycycline but without biotin addition, bands of the chimeric proteins were migrating slightly faster (i.e. at lower molecular weight marker) indicating the lack of auto-biotinylation in the absence of exogenous biotin. The HA tag antibodies blot showed the same doxycycline-dependent increase in the levels of the miniTurbo ligase only construct (empty vector control) and the miniTurbo-ATF3 construct while the miniTurbo-PERK construct was not detectable (Fig. 52 B & C).

A

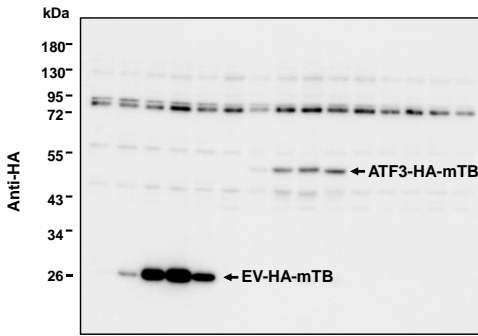


	1	2	3	4	5	6	7	8	9	10	11	12	13	14	15	
EV-HA-mTb	+	+	+	+	+											
ATF3-HA-mTb							+	+	+	+						
PERK-HA-mTb											+	+	+	+	+	
Dox (ng/ml, 24h)	0	10	100	1000	1000	0	10	100	1000	1000	0	10	100	1000	1000	
Biotin (50µM, 24h)	+	+	+	+	-	+	+	+	+	-	+	+	+	+	+	-
Temperature	33C															



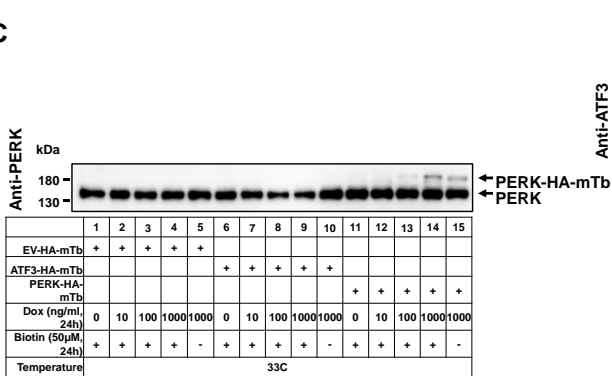
	1	2	3	4	5	6	7	8	9	10	11	12	13	14	15	
EV-HA-mTb	+	+	+	+	+											
ATF3-HA-mTb							+	+	+	+						
PERK-HA-mTb											+	+	+	+	+	
Dox (ng/ml, 24h)	0	10	100	1000	1000	0	10	100	1000	1000	0	10	100	1000	1000	
Biotin (50µM, 24h)	+	+	+	+	-	+	+	+	+	-	+	+	+	+	+	-
Temperature	33C															

B

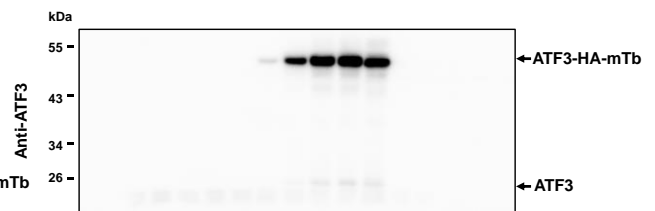


	1	2	3	4	5	6	7	8	9	10	11	12	13	14	15	
EV-HA-mTb	+	+	+	+	+											
ATF3-HA-mTb							+	+	+	+						
PERK-HA-mTb											+	+	+	+	+	
Dox (ng/ml, 24h)	0	10	100	1000	1000	0	10	100	1000	1000	0	10	100	1000	1000	
Biotin (50µM, 24h)	+	+	+	+	-	+	+	+	+	-	+	+	+	+	+	-
Temperature	33C															

C



	1	2	3	4	5	6	7	8	9	10	11	12	13	14	15	
EV-HA-mTb	+	+	+	+	+											
ATF3-HA-mTb							+	+	+	+						
PERK-HA-mTb											+	+	+	+	+	
Dox (ng/ml, 24h)	0	10	100	1000	1000	0	10	100	1000	1000	0	10	100	1000	1000	
Biotin (50µM, 24h)	+	+	+	+	-	+	+	+	+	-	+	+	+	+	+	-
Temperature	33C															



	1	2	3	4	5	6	7	8	9	10	11	12	13	14	15	
EV-HA-mTb	+	+	+	+	+											
ATF3-HA-mTb							+	+	+	+						
PERK-HA-mTb											+	+	+	+	+	
Dox (ng/ml, 24h)	0	10	100	1000	1000	0	10	100	1000	1000	0	10	100	1000	1000	
Biotin (50µM, 24h)	+	+	+	+	-	+	+	+	+	-	+	+	+	+	+	-
Temperature	33C															



	1	2	3	4	5	6	7	8	9	10	11	12	13	14	15	
EV-HA-mTb	+	+	+	+	+											
ATF3-HA-mTb							+	+	+	+						
PERK-HA-mTb											+	+	+	+	+	
Dox (ng/ml, 24h)	0	10	100	1000	1000	0	10	100	1000	1000	0	10	100	1000	1000	
Biotin (50µM, 24h)	+	+	+	+	-	+	+	+	+	-	+	+	+	+	+	-
Temperature	33C															

Figure 52: Biotinylation levels of miniTurbo constructs at 33 °C are doxycycline concentration dependent.

Parental Huh7 cells were transfected with plasmids carrying either miniTurbo-ATF3, miniTurbo-PERK, or miniTurbo ligase only (empty vector, EV) as previously described. Thereafter, transfected cells were treated with increasing doses of doxycycline as indicated along with 50 μ M exogenous biotin and further incubated at 33 °C for 24 hours. As a control, cells transfected with each of the aforementioned constructs were induced with 1 μ g/ml of doxycycline but left without the biotin treatment. Whole-cell extracts (using BioID lysis buffer) were then subjected to western blot analysis. The experiment was performed as two independent biological replicas. -HA-mTb: miniTurbo

(A) Streptavidin-HRP blot with black arrows pointing to indicated constructs (left). CBB staining of the same blot as a loading control (right).

(B) HA-tag antibodies blot with black arrows pointing to indicated constructs.

(C) Anti-PERK, -ATF3 and $-\beta$ -actin (as a loading control) antibodies blots (left to right).

With these optimization results in mind, the next step was to perform pulldown experiments with these chimeric constructs with or without HCoV-229E infection.

Parental Huh7 cells were transfected with either the miniTurbo ligase only or the miniTurbo-PERK using the calcium phosphate transfection method. Transfected cells were then treated with biotin, induced with doxycycline, and either infected with HCoV-229E (24 hours at MOI of 1) or left uninfected. As a control, cells transfected with miniTurbo-PERK were left either without doxycycline induction or without exogenous biotin addition. The adapted BioID protocol, as described by Roux et al (see Methods section) was then followed to obtain lysates and to purify biotin-tagged proteins. 25% of the pulldown was compared to 1% whole-cell extracts lysates on Western blot. The streptavidin blot indicated the usual strong smear associated with random biotinylation of host proteins by the miniTurbo ligase only (empty vector control) construct in both the lysate and the pulldown lanes. While, expectedly, the miniTurbo-PERK construct showed a strongly reduced biotinylation pattern, almost at the level of the controls lacking doxycycline induction or the exogenous biotin addition. The miniTurbo-PERK construct showed a faint band corresponding to the auto-biotinylation of this construct. Noticeably, the blot of pulled down proteins probed with anti-PERK antibody showed a band in the lanes corresponding to the miniTurbo ligase (empty vector control). This observation indicates a (non-specific?) interaction between this ligase and the endogenous PERK. The silver staining of SDS gel loaded with 25% of the pulldown recapitulated the same patterns seen in the streptavidin-HRP blot (Fig. 53).

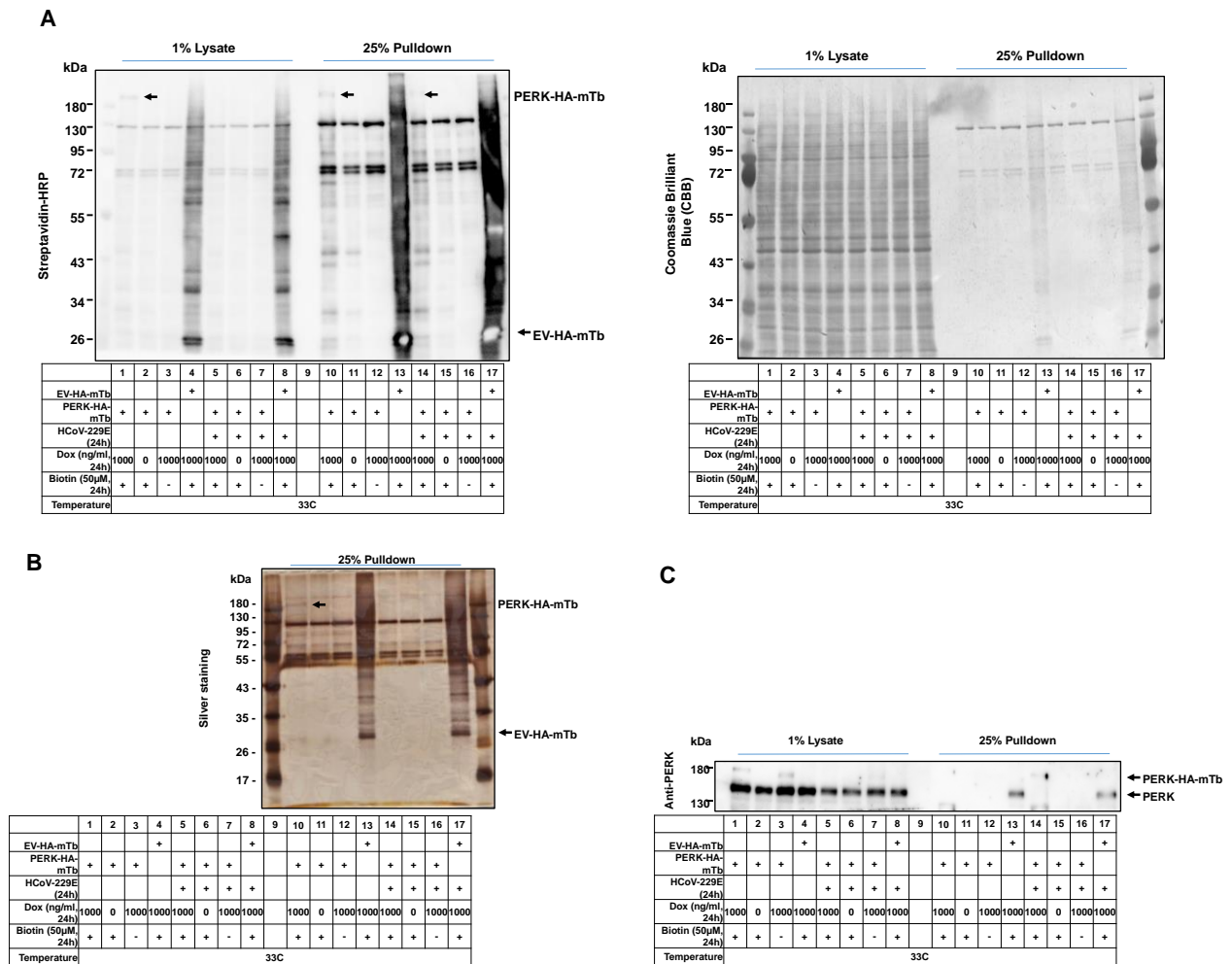


Figure 53: Pull-down of biotinylated proteins by miniTurbo-PERK or miniTurbo ligase only in the presence or absence of HCoV-229E infection.

Parental Huh7 cells were transfected with plasmids carrying either miniTurbo-PERK or miniTurbo ligase only (empty vector, EV) constructs using the calcium phosphate method followed by doxycycline induction (1 µg/ml) and exogenous biotin treatment (50 µM). As control conditions, cells transfected with miniTurbo-PERK were left either without the doxycycline induction but with exogenous biotin addition or vice versa (as indicated in the legends). An identical set of conditions (control and experimental) were infected with MOI of 1 of HCoV-229E. All cells were then incubated for further 24 hours at 33°C. Cells were then harvested and subjected to BioID protocol (see methods section) to obtain lysates and pulled down proteins and then subjected to Western blotting and SDS sliver staining. -HA-mTb: miniTurbo.

A) Streptavidin blot (left). CBB staining of the same blot as a loading control (right).

B) Sliver staining of 25% of pulled down proteins loaded on SDS gel.

C) Anti-PERK antibodies blot.

Black arrows are pointing to the indicated constructs.

The same methodology and conditions described in figure 53 were applied to the miniTurbo-ATF3 construct. The streptavidin blot showed the smear patterns associated with the biotinylation of host proteins by miniTurbo ligase only and miniTurbo-ATF3 constructs. The intensities of these patterns were well above the control conditions and can be observed in both the lysate and the pull-down lanes.

The corresponding silver staining of SDS gel recapitulated the same patterns seen in the streptavidin-HRP blot. The ATF3 antibodies blot of pulled down proteins showed bands of the chimeric miniTurbo-ATF3 protein in the expected conditions / lanes (Fig. 54 A, B & C).

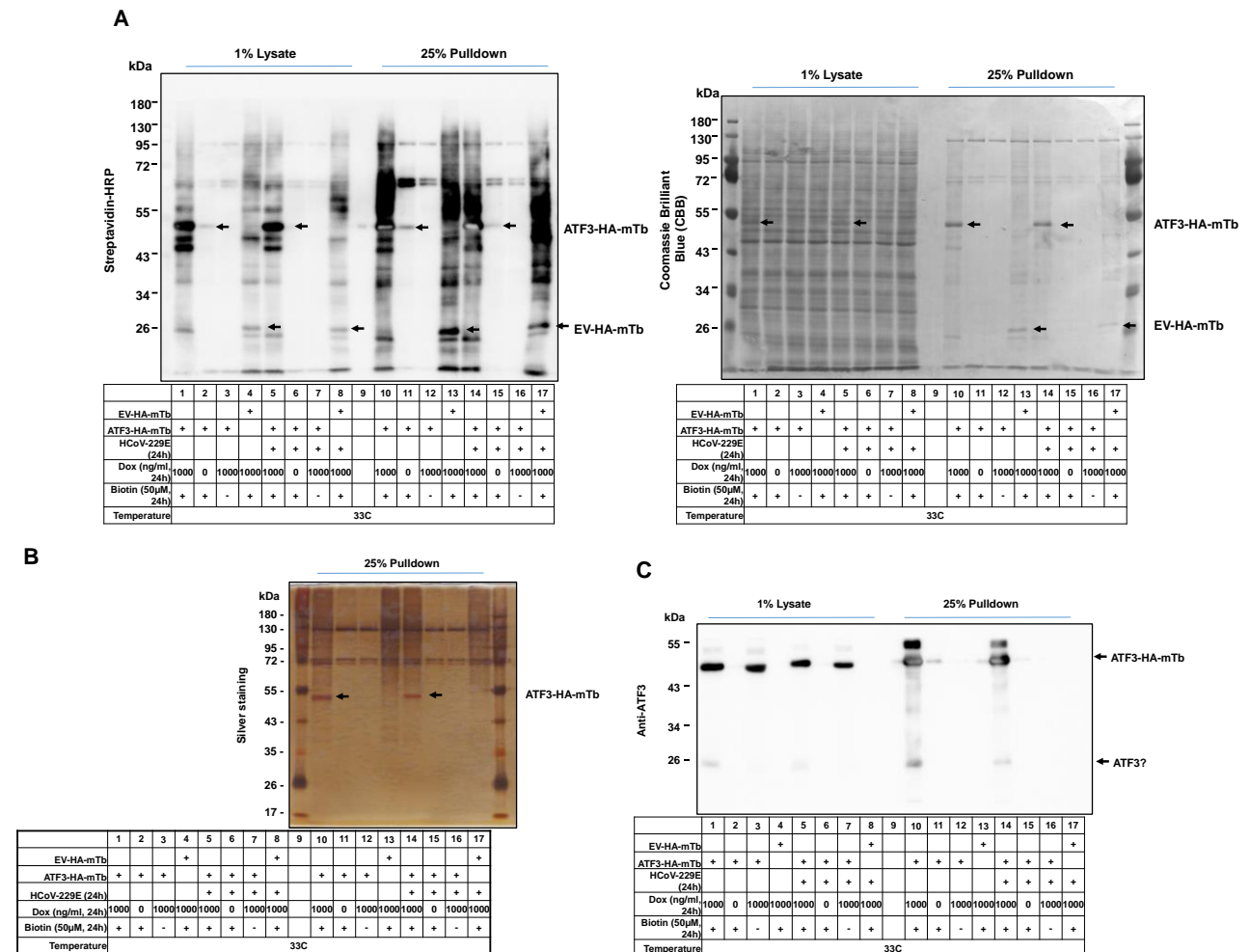


Figure 54: Pulldown of biotinylated proteins by miniTurbo-ATF3 or miniTurbo ligase only in the presence or absence of HCoV-229E infection.

Same procedure and conditions as in figure 53 but using miniTurbo-ATF3.

A) Streptavidin blot. CBB staining of the same blot as a loading control (right).

B) Silver staining of 25% of pulled down proteins loaded on SDS gel.

C) Anti-ATF3 antibodies blot.

Black arrows pointing to indicated constructs.

Taken together, the optimization and the pulldown data made a strong argument to exclude the miniTurbo-PERK construct from further experimentation in the context of HCoV-229E infection (at 33°C) and focus on the miniTurbo-ATF3 construct for more in-depth analysis of the ATF3 interactome using mass spectrometry.

4.4.2 The proximity-based interactome of ATF3 in the context of HCoV-229E infection

Under the same, optimized experimental and control conditions described in figure 54, samples from three biologically independent replicas were harvested, subjected to BioID protocol, and thereafter pulled down proteins were sent to mass spectrometry analysis. Raw data obtained from these samples were initially processed using MaxQuant and lists of expressed proteins and their relative abundancies in each sample were generated. These lists were then subjected to different statistical analysis methods available in Perseus including calculating p-values and fold changes to obtain lists of differentially enriched proteins (DEPs). The lists of DEPs were then visualized as pairwise comparisons using volcano plots. To control for the success of the protocol in pulling down proteins biotinylated by the miniTurbo-ATF3 construct multiple comparisons were carried out (Fig. 55). For the sake of simplicity, a list of abbreviations for conditions and vectors is included in table 2.

Abbreviation	Explanation
ATF3	Indicates Huh7 cells transfected with miniTurbo-ATF3.
EV	Indicates Huh7 cells transfected with miniTurbo ligase only (empty vector).
V	HCoV-229E (MOI of 1, 24 hours).
B	Biotin
D	Doxycycline
+	Addition
-	Omission

Table 2: List of abbreviations used in this section

To help the reader in following the upcoming text, list of conditions has been delineated in table 3.

Type of condition	Name abbreviation of the condition (see table 2)
Additional negative control for non-specific binders (omission of either doxycycline or biotin)	ATF3 D-B+ ATF3 D+B- ATF3 V+D-B+ ATF3 V+D+B-
Specific ATF3 interactomes	ATF3 D+B+ ATF3 V+D+B+
Main negative control for nonspecific binders (empty vector control)	EV D+B+ EV V+D+B+

Table 3: List of conditions used in the interactome experiment

Expectedly, ATF3 D+B+ showed massive enrichment of DEPs when compared to the negative control conditions of ATF3 D-B+ or ATF3 D+B-. Similar results can be seen when the same set of comparisons were made for conditions that included the virus infection (i.e. for ATF3 V+D+B+ vs its corresponding negative controls). Comparing the negative control conditions among themselves (i.e. ATF3 D-B+ vs

ATF3 D+B-) showed substantial enrichment of proteins in the condition lacking doxycycline induction but with exogenous biotin addition (D+ B-). The same pattern can be observed for the negative control conditions infected with the virus. The comparisons among the negative control conditions indicated that in the presence of exogenous biotin, leaky expression of the construct or biotinylation by endogenous biotin ligases is sufficient to produce some DEPs, which emphasizes the importance of both of these negative controls (Fig. 55 A).

On the other hand, the comparisons between the experimental conditions themselves and between the experimental conditions and their respective empty vector controls (i.e. with or without the virus infection) indicated a relatively equal enrichment of DEPs. The ATF3 D+B+ comparison to the EV D+B+ showed ATF3 and multiple of its well-known interactors (e.g. JUND, TP53) to be amongst the most enriched DEPs. The ATF3 V+D+B+ comparison to the EV V+D+B+ revealed enrichment of all viral proteins in the ligase-only (EV) construct. Contrary, the ATF3 D+B+ vs ATF3 V+D+B+ comparison displayed fewer DEPs and showed an enrichment of the viral proteins in the ATF3 V+D+B+ condition, indicating the importance of having EV V+D+B+ as an additional reference condition (Fig. 55 B).

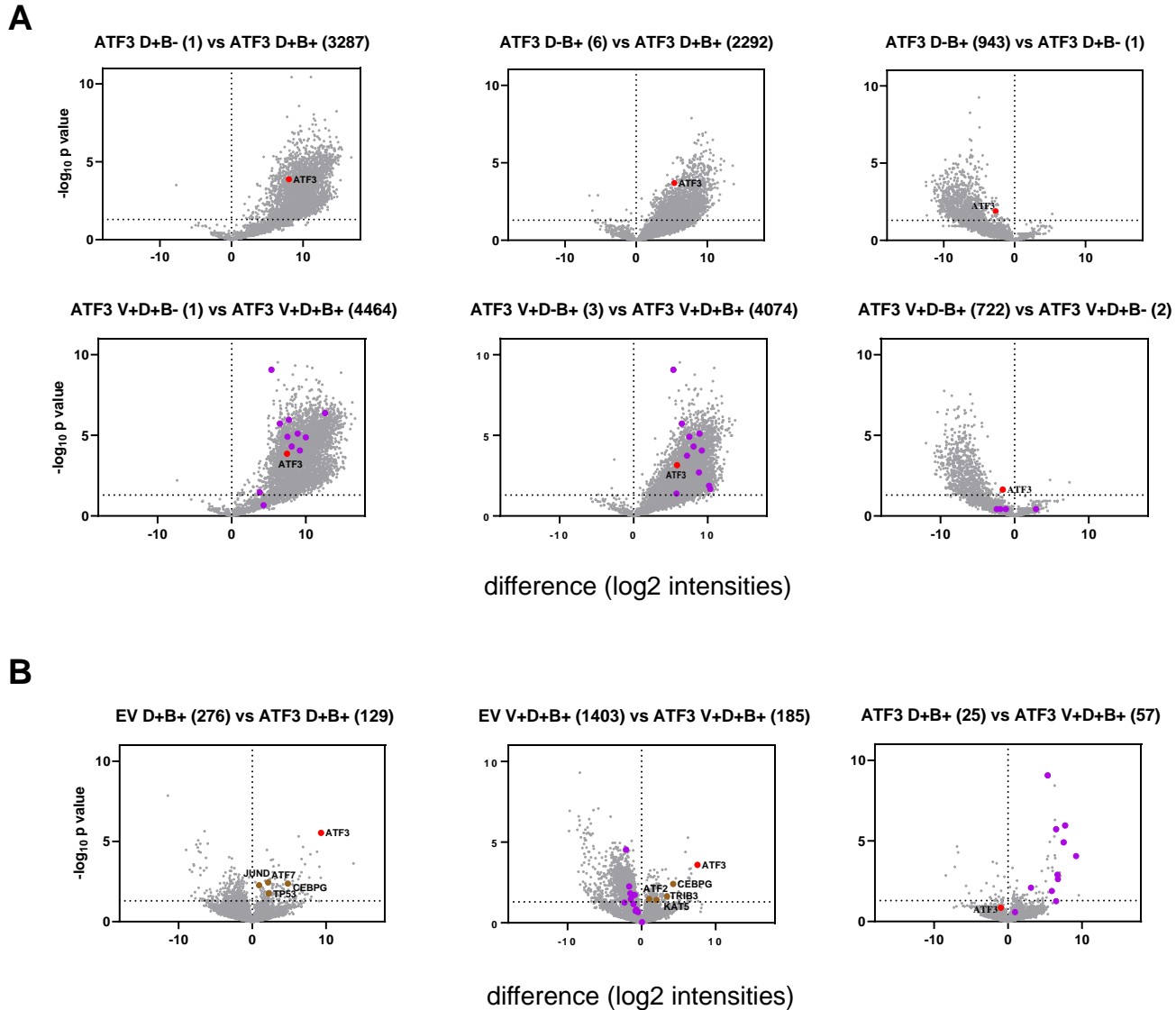


Figure 55: Volcano plot representations of all mass spectrometry data to identify proteins enriched with the miniTurbo-ATF3 fusion protein.

Total cell extracts from Huh7 cells transfected with the indicated constructs, treatments and infection conditions were analyzed by LC-MS/MS. The intensities of the majority protein IDs identified were used for all further analyses. In case no protein intensity was measured, an imputation strategy was implemented (see methods) in order to facilitate the calculation of enrichment values (ratios) between pairs of the conditions. Volcano plots indicate the distribution of mean ratios (differences) derived from pairwise comparisons on the x-axis and the significance of these changes (p values) at the y-axis. For each condition, three independent biological replicates and two technical measurements were carried out and subsequently, p values were calculated using Student's t-tests from the means of the technical measurements. The reference is always shown in the left half of the graph. Differentially enriched proteins (DEPs) were defined based on a ratio > 0 and p value of $-\log_{10}(p) \geq 1.3$. Total number of proteins found amounted to 5788. Number of uncovered DEPs is indicated in each volcano plot next to the stated conditions.

(A) Comparisons among the negative control conditions with or without infection upper and lower panels respectively.

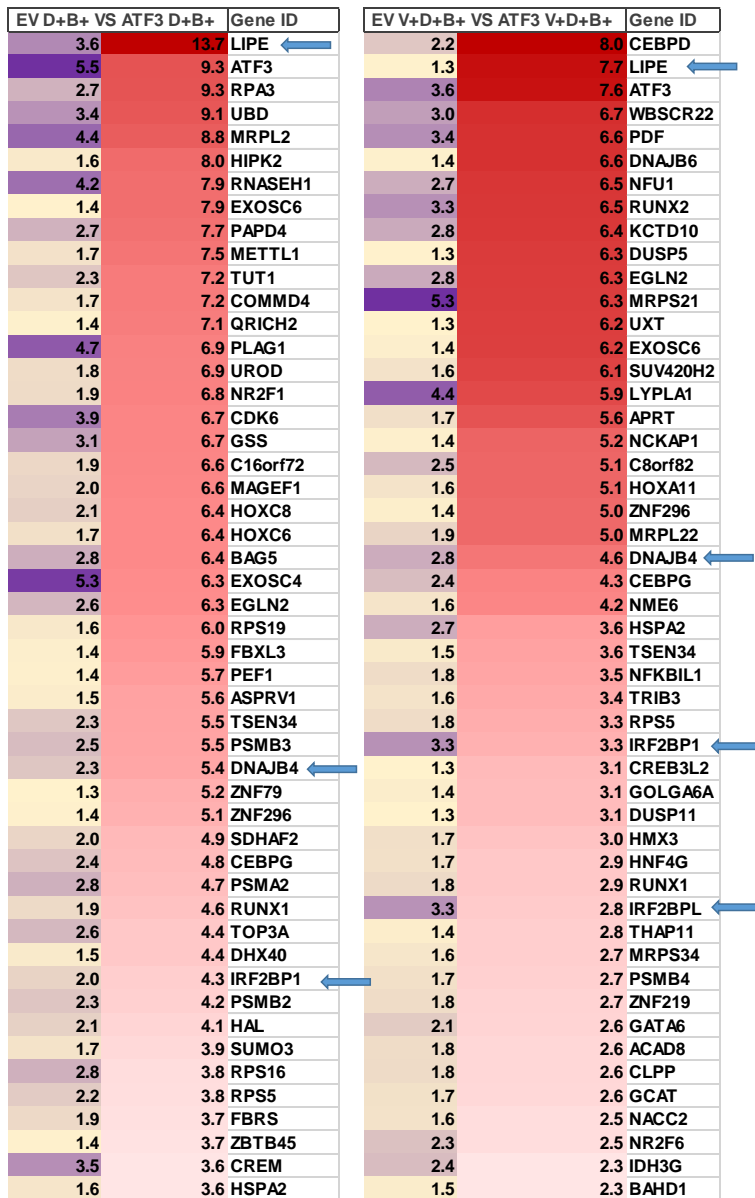
(B) Comparisons among experimental conditions and empty vector (EV) control conditions with or without infection as indicated.

Purple dots indicate HCoV-229E viral proteins. Well-known interactors of ATF3 (as identified by co-immunoprecipitation in previous studies) are indicated as brown dots with their names next to them.

A closer look at the top 50 DEPs from both ATF3 D+B+ and ATF3 V+D+B+ showed several DEPs in common including Lipase E, hormone Sensitive type (LIPE), chaperon proteins (DNAJB1 & DNAJB4), and interferon regulatory factors (IRF2BPL & IRF2BP2) (see blue arrows in Fig. 56 A & B).

Nevertheless, many DEPs were unique to each of these conditions. Venn diagram analysis revealed that the two conditions shared 34 DEPs, while ATF3 V+D+B+ had 150 unique DEPs and ATF3 D+B+ had 88. Interestingly, CEBPD, a bZIP transcription factor heavily involved in the regulation of multiple genes related to immune and inflammatory responses, was found to be the most enriched DEP in ATF3 V+D+B+ unique top 50 list (Fig. 56 A & B).

A



B

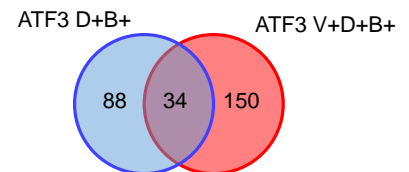
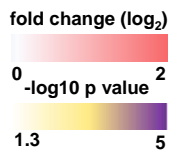
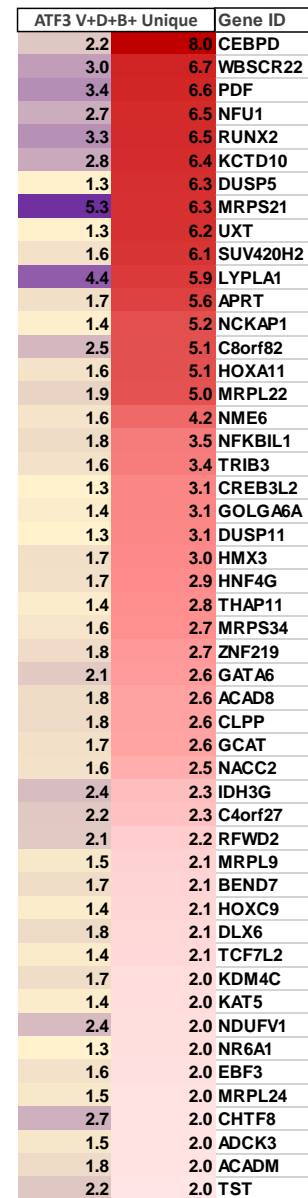


Figure 56: miniTurbo-ATF3 interacts with a variety of transcriptional regulators and factors, including those involved in immune response and inflammation.

(A) Heatmaps generated using mean intensity ratios of the top 50 enriched proteins of ATF3 D+B+, ATF3 V+D+B+ compared to their respective empty vector control (EV). Blue arrows indicate interactors in-common between the two conditions.

(B) Upper, the top 50 unique DEPs in the ATF3 V+D+B+ condition were displayed as a heatmap. Lower, Venn diagram showing common vs unique DEPs between the two lists in (A).

DEPs, ratio > 0, p values (p) of $-\log_{10}(p) \geq 1.3$.

An important additional layer of analysis was to study the DEPs on the level of protein-protein interactions and networks, and in terms of their subcellular localization. For this purpose, the top DEPs from each of the comparisons shown in figure 55 B were analyzed using the STRING database (version 11.5) (Szklarczyk et al. 2019) and the Cytoscape software (version 3.8.0 or 3.9.1). The STRING application embedded in Cytoscape were used to visualize the networks and their annotations.

In the EV D+ B+ vs ATF3 D+B+ comparison the top 100 DEPs in the ATF3 D+B+ (defined by DEPs, ratio > 0, p-values of $-\log_{10}(p) \geq 1.3$) condition showed a strongly interconnected main network, smaller sub-networks, and multiple unconnected individual nodes. These proteins localized to the nucleus as seen by GO cellular component terms and their corresponding FDR values. On the other hand, the top 100 enriched DEPs in the EV D+B+ condition did not show any GO cellular component terms (or others) that are related to the nucleus indicating a correct localization of the miniTurbo-ATF3 (Fig. 57).

EV D+B+ vs ATF3 D+B+

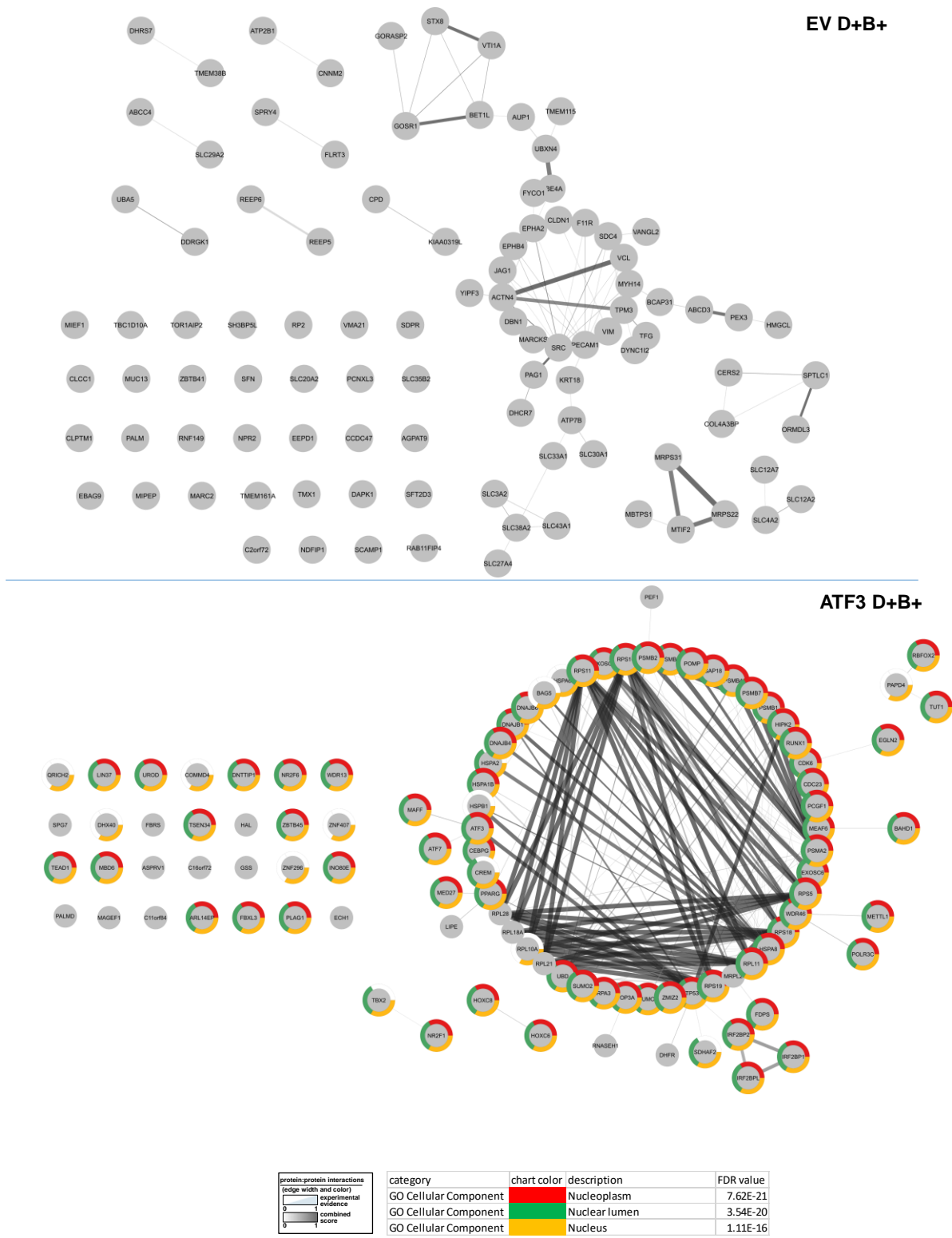


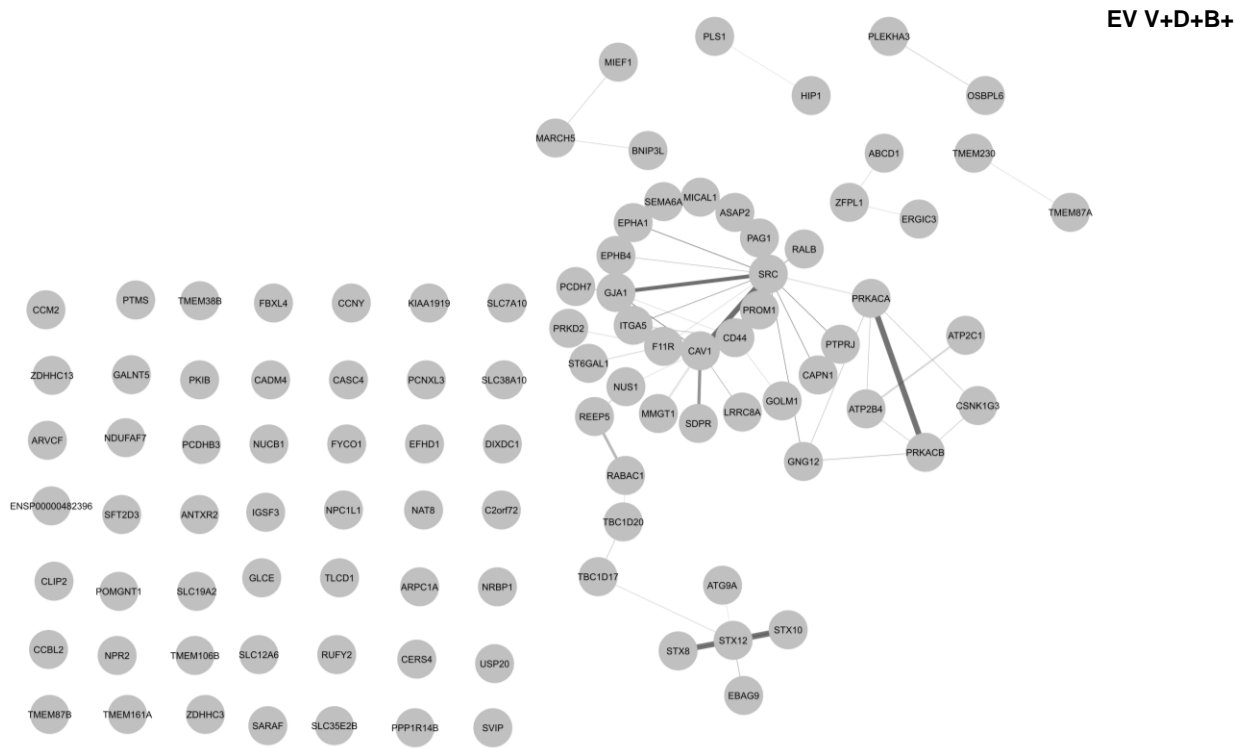
Figure 57: Compared to EV D+B the interactors of ATF3 D+B+ fusion protein predominantly localize to the nucleus and are partially engaged in known physical or functional protein: protein interaction (PPI) networks.

The top 100 DEPs from the ATF3 D+B+ (lower) or from the EV D+B+ (upper) conditions were used as inputs to the STRING database to look for protein-protein interactions based on experimental evidence, co-expression, and confidence. Networks (and individual nodes) were then imported to Cytoscape for functional enrichment analysis

and visualization. Proteins belonging to GO cellular component terms of Nucleoplasm, Nuclear lumen, and Nucleus were highlighted using red, green, or orange respectively. None of these GO terms were found in the functional enrichment analysis of the top DEPs of the EV D+B+ condition. Both networks were constructed based on experimental evidence and combined score. Both networks have 0.4 STRING score. The ATF3 D+B+ (lower) network has the following statistics: number of nodes (DEPs): 99, number of edges: 231, statistical significance of enrichment of Protein: Protein Interactions (PPI) by p value: 1.0E-16. The EV D+B+ (upper) network has the following statistics: number of nodes (nont DEPs): 100, number of edges: 83, PPI: 3.11E-12.

The same network and functional enrichment analysis were carried out for the infected conditions. The analysis of the top 100 DEPs in the ATF3 V+D+B+ and EV V+D+B+ conditions recapitulated the same pattern of proteins localization seen in the uninfected conditions (Fig. 58).

EV V+D+B+ vs ATF3 V+D+B+



ATF3 V+D+B+

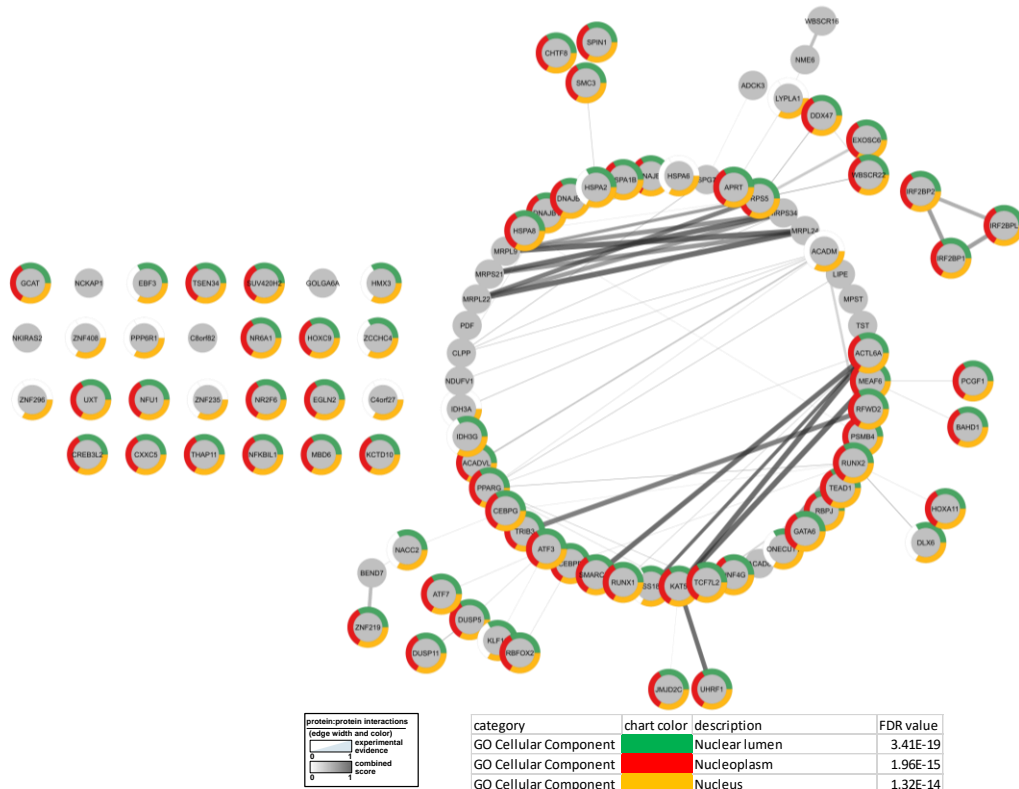


Figure 58: Compared to EV V+D+B+, DEPs from the ATF3 V+D+B+ condition overwhelmingly localize to the nucleus.

Same analysis described in figure 57 was implemented for top 100 DEPs in the ATF3 V+D+B+ (Right) or EV V+D+B+ (Left) conditions. Both networks were constructed based on experimental evidence and combined score. Both networks have 0.4 STRING score. The ATF3 V+D+B+ (lower) network has the following statistics: number of nodes (DEPs): 100, number of edges: 128, statistical significance of enrichment of Protein: Protein Interactions

(PPI) by p value: 1.0E-16. The EV V+D+B+ (upper) network has the following statistics: number of nodes (DEPs): 100, number of edges: 62, PPI: 7.18E-7.

For the ATF3 D+B+ vs ATF3 V+D+B+ comparison, the top DEPs in the ATF3 V+D+B+ condition showed a strong enrichment of GO cellular component terms related to the mitochondria (Fig. 59). This enrichment might indicate a translocation of ATF3 to the mitochondria upon virus infection.

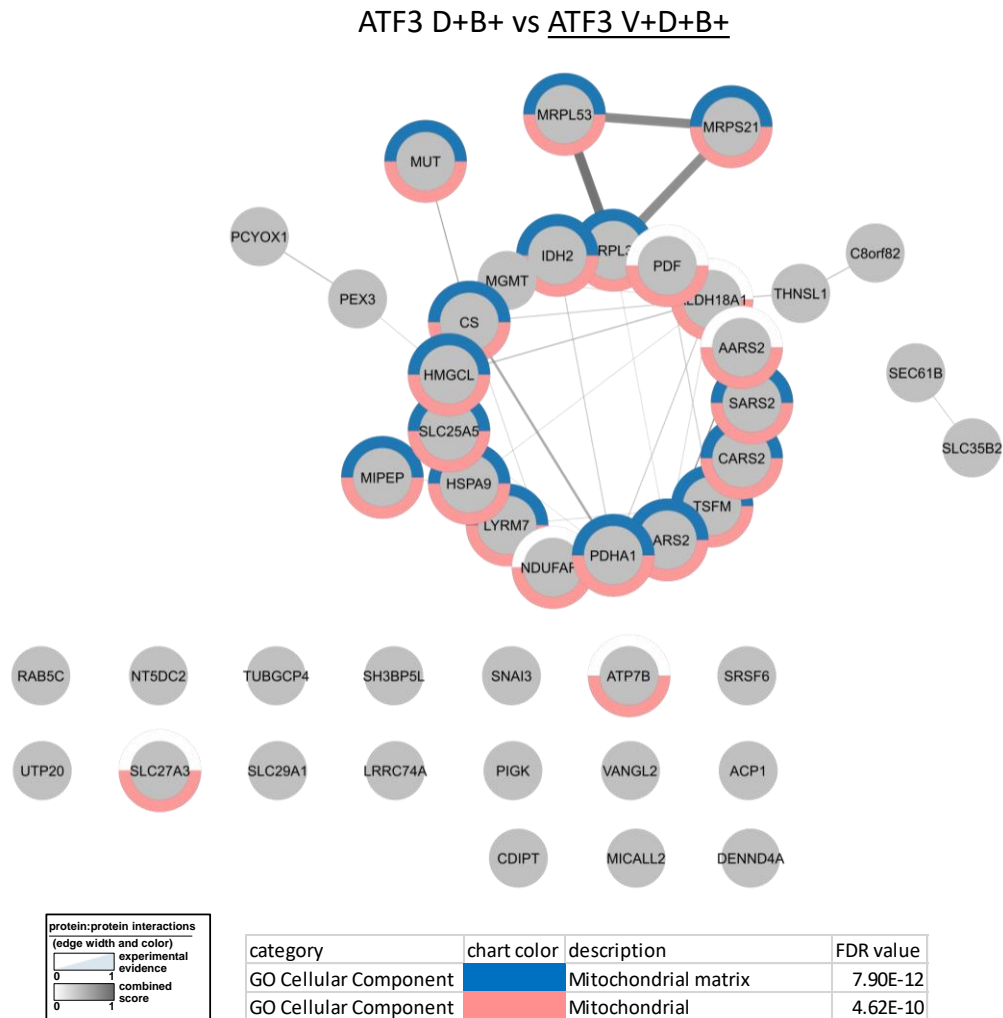


Figure 59: In the ATF3 D+B+ vs ATF3 V+D+B+ comparison, DEPs enriched in the latter condition showed a strong localization to the mitochondria.

The same analysis described in figure 57 was implemented for all non-viral DEPs in the ATF3 V+D+B+ (compared to ATF3 D+B+). Proteins belonging to GO cellular component terms of mitochondrial matrix or mitochondria were highlighted by blue and pink colors of the node borders, respectively. Network was constructed based on experimental evidence and combined score and has a 0.4 STRING score with the following statistics: number of nodes (DEPs): 44, number of edges: 46, protein: protein Interaction Enrichment (PPI): 1.0E-16.

Network and functional enrichment analysis of protein-protein interactions using STRING database in Cytoscape of the top 100 (out of 150) DEPs unique to the ATF3 V+D+B+ condition showed a strongly interconnected main network, smaller sub-networks, and multiple individual nodes. GO cellular component terms with the highest enrichment revealed a strong chromatin and mitochondrial localization of these proteins (Fig. 60).

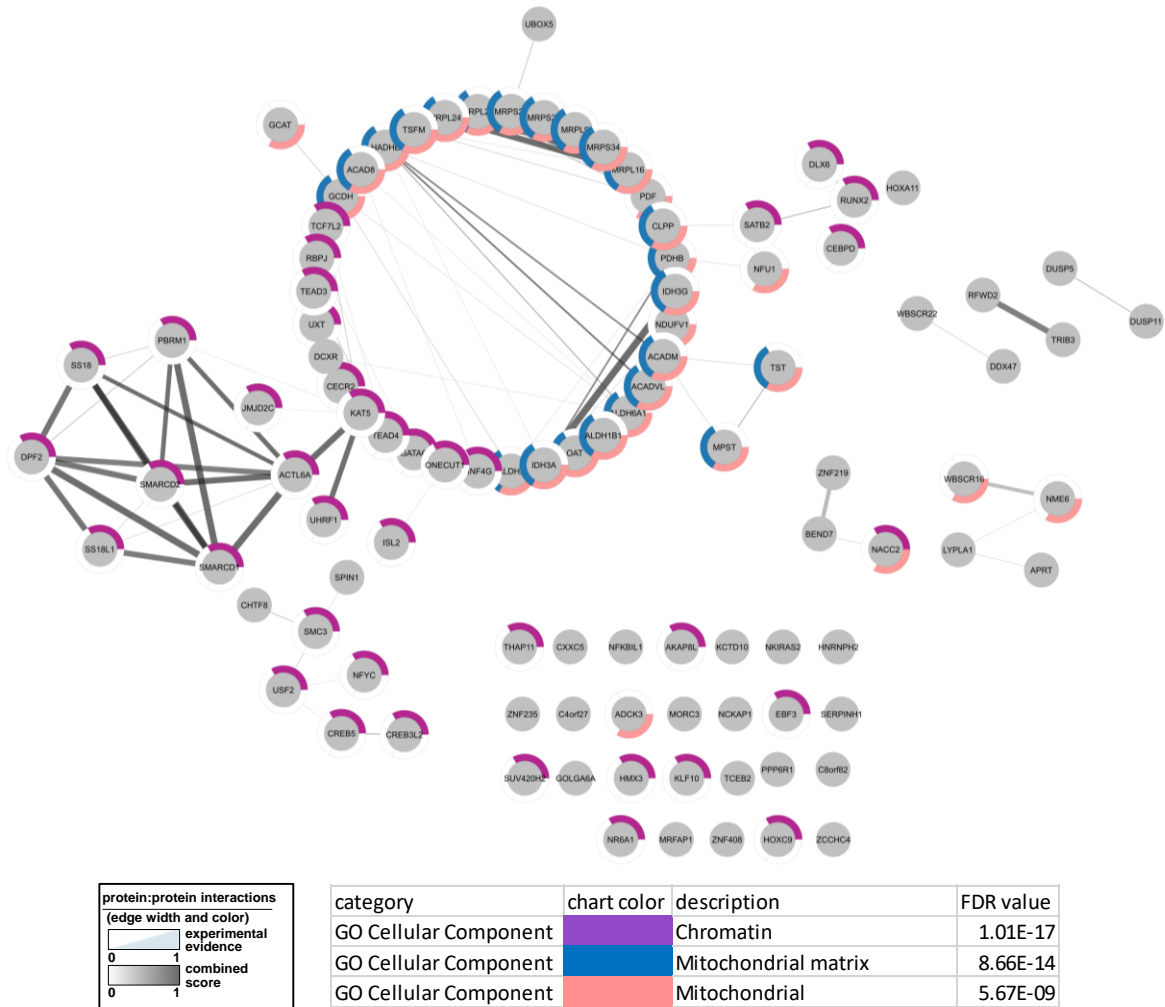


Figure 60: Top 100 DEPs of the ATF3 V+D+B+ unique list showed strong localization to the mitochondria.

The same analysis described in figure 57 was implemented for the top 100 unique DEPs in the ATF3 V+D+B+ from figure 56 B. Proteins belonging to GO cellular component terms of Chromatin, mitochondrial matrix, or mitochondria were highlighted using purple, blue, and pink colors for node borders, respectively. Network was constructed based on experimental evidence and combined score and has a 0.4 STRING score with the following statistics: number of nodes (DEPs): 100, number of edges: 130, protein: protein Interaction Enrichment (PPI): 1.0E-16.

The full lists of DEPs from each of the experimental conditions were then analyzed using metascape databases to generate lists of enriched pathways. The lists of DEPs used were as follow; ATF3 D+B+ (compared to EV D+B+), ATF3 V+D+B+ (compared to EV V+D+B+), ATF3 V+D+B+ (compared to ATF3 D+B+) and the unique list of DEPs from figure 56 B. The functional analysis of the ATF3 D+B+ DEPs list revealed pathways connected to stress response, Metabolism of RNA, Response of EIF2AK4 (GCN2) to amino acid deficiency, and many translation-related pathways. Pathway terms enriched in the analysis of the DEPs from the ATF3 V+D+B+ showed a strong signature of chromatin and mitochondria-related processes including chromatin organization, chromatin modifying enzymes, Mitochondrial translation elongation. Interestingly, the term Thermogenesis, a biological process that

leads to the generation of thermal energy through the metabolism of fat tissue, was amongst the top enriched pathway in ATF3 V+D+B+ (Fig. 61).

Term	Description	Log(q-value)	In term	In list	Term	Description	Log(q-value)	In term	In list
R-HSA-2262752	Cellular responses to stress	-25.3	38	757	GO:0006325	chromatin organization	-10.4	26	569
R-HSA-8953897	Cellular responses to stimuli	-25.3	38	771	WP4321	Thermogenesis	-10.3	14	108
R-HSA-9010553	Regulation of expression of SLITs and ROBOs	-18.8	20	171	hsa00280	Valine, leucine and isoleucine degradation	-10.3	11	48
R-HSA-8953854	Metabolism of RNA	-17.9	30	673	R-HSA-8939243	RUNX1 interacts with co-factors whose precise effect on RUNX1 targets is not known	-9.9	10	38
R-HSA-376176	Signaling by ROBO receptors	-16.9	20	218	R-HSA-3247509	Chromatin modifying enzymes	-9.4	18	274
R-HSA-9633012	Response of EIF2AK4 (GCN2) to amino acid deficiency	-16.8	16	101	R-HSA-4839726	Chromatin organization	-9.4	18	274
CORUM306	Ribosome, cytoplasmic	-15.0	14	80	WP4204	Tumor suppressor activity of SMARCB1	-9.0	9	33
GO:0002181	cytoplasmic translation	-14.5	15	112	CORUM713	BRG1-SIN3A complex	-8.6	7	14
R-HSA-156902	Peptide chain elongation	-14.5	14	89	CORUM714	BRM-SIN3A complex	-8.4	7	15
R-HSA-192823	Viral mRNA Translation	-14.5	14	89	CORUM555	BAF complex	-8.1	6	9
WP477	Cytoplasmic ribosomal proteins	-14.4	14	90	hsa00071	Fatty acid degradation	-8.0	9	43
R-HSA-156842	Eukaryotic Translation Elongation	-14.3	14	93	CORUM1239	EBAFPb complex	-7.9	6	10
R-HSA-240857	Selenocysteine synthesis	-14.3	14	93	CORUM1252	EBAFPa complex	-7.9	6	10
R-HSA-72764	Eukaryotic Translation Termination	-14.3	14	93	CORUM1254	PBAF complex (Polybromo- and BAF containing complex)	-7.9	6	10
R-HSA-6791226	Major pathway of rRNA processing in the nucleolus and cytosol	-14.3	17	184	CORUM808	BRM-associated complex	-7.9	6	10
R-HSA-975956	Nonsense Mediated Decay (NMD) independent of the Exon Junction Complex (EJC)	-14.3	14	95	GO:0016054	organic acid catabolic process	-7.9	15	224
R-HSA-168255	Influenza Infection	-14.1	16	156	hsa04714	Thermogenesis	-7.7	15	232
R-HSA-9711097	Cellular response to starvation	-14.1	16	156	CORUM806	BRM-SIN3A-HDAC complex	-7.3	6	12
R-HSA-8868773	rRNA processing in the nucleus and cytosol	-14.1	17	194	CORUM189	BAF complex	-7.0	6	13
R-HSA-71291	Metabolism of amino acids and derivatives	-14.1	21	374	GO:0044282	small molecule catabolic process	-7.0	17	354
R-HSA-72689	Formation of a pool of free 40S subunits	-14.0	14	101	R-HSA-5389840	Mitochondrial translation elongation	-6.8	10	87
R-HSA-72312	rRNA processing	-13.7	17	204	R-HSA-5368287	Mitochondrial translation	-6.5	10	93
R-HSA-156827	L13a-mediated translational silencing of Ceruloplasmin expression	-13.4	14	111	R-HSA-2262752	Cellular responses to stress	-6.5	23	757
R-HSA-1799339	SRP-dependent cotranslational protein targeting to membrane	-13.4	14	112	CORUM1251	BAF complex	-6.4	5	8
R-HSA-72706	GTP hydrolysis and joining of the 60S ribosomal subunit	-13.4	14	112	CORUM564	BAF complex	-6.4	5	8
R-HSA-927802	Nonsense-Mediated Decay (NMD)	-13.3	14	115	R-HSA-8953897	Cellular responses to stimuli	-6.4	23	771
R-HSA-975957	Nonsense Mediated Decay (NMD) enhanced by the Exon Junction Complex (EJC)	-13.3	14	115	CORUM1237	BAF complex	-6.2	5	9
R-HSA-2408522	Selenoamino acid metabolism	-13.1	14	118	CORUM1238	PBAF complex (Polybromo- and BAF containing complex)	-6.2	5	9
R-HSA-72619	Eukaryotic Translation Initiation	-13.1	14	119	CORUM556	PBAF complex (Polybromo- and BAF containing complex)	-6.2	5	9
R-HSA-72737	Cap-dependent Translation Initiation	-13.1	14	119	CORUM565	PBAF complex (Polybromo- and BAF containing complex)	-6.2	5	9
hsa03010	Ribosome	-12.8	15	158	CORUM566	BAF complex	-6.2	5	9
CORUM3055	Nop56p-associated pre-rRNA complex	-12.4	13	104	CORUM710	Brg1-associated complex I	-6.2	5	9
R-HSA-1682731	Influenza Viral RNA Transcription and Replication	-12.4	14	135	CORUM711	Brm-associated complex	-6.2	5	9
R-HSA-450531	Regulation of mRNA stability by proteins that bind AU-rich elements	-11.7	12	88	CORUM807	BRG1-associated complex	-6.2	5	9
R-HSA-9675108	Nervous system development	-11.6	22	577	CORUM778	LARC complex (LCR-associated remodeling complex)	-6.2	6	19
GO:0043043	peptide biosynthetic process	-11.0	18	359	GO:0006337	nucleosome disassembly	-6.2	6	19
R-HSA-424275	Axon guidance	-11.0	21	552	GO:0031498	chromatin disassembly	-6.2	6	19
R-HSA-450408	AUF1 (hnRNP D0) binds and destabilizes mRNA	-10.7	10	56	GO:0006338	chromatin remodeling	-6.2	14	267
GO:0006412	translation	-10.5	17	332	GO:0046395	carboxylic acid catabolic process	-6.2	13	220
CORUM308	60S ribosomal subunit, cytoplasmic	-9.7	9	47	CORUM320	55S ribosome, mitochondrial	-6.2	9	77

ATF3 D+B+

ATF3 V+D+B+

Figure 61: Top 40 enriched pathways mapping to DEPs from ATF3 D+B+ (compared to EV D+B+) (left) and ATF3 V+D+B+ (compared to EV V+D+B+) (right) revealed by Metascape analysis.

Blue arrows point to indicated terms.

Pathways enrichment analysis of the 150 DEPs unique to the ATF3 V+D+B+ (see figure 56 B) showed comparable enriched pathways to the analysis done with the list of DEPs from ATF3 V+D+B+ (compared to EV V+D+B+) in figure 61. Lastly, analysis of DEPs of the ATF3 V+D+B+ (compared to ATF3 D+B+) condition showed pathways mostly related to metabolism and mitochondria. This partially recapitulated some of the terms seen in the pathway analysis of the 150 DEPs unique to the ATF3 V+D+B+, although with weaker q-values reflecting the lower number of DEPs in this condition (Fig. 62).

Term	Description	Log(q-value)	in term	in list
hsa00280	Valine, leucine and isoleucine degradation	-10.9	11	48
GO:0006325	chromatin organization	-10.9	24	569
R-HSA-3247509	Chromatin modifying enzymes	-9.6	17	274
R-HSA-4839726	Chromatin organization	-9.6	17	274
WP4204	Tumor suppressor activity of SMARCB1	-9.6	9	33
R-HSA-8939243	RUNX1 interacts with co-factors whose precise effect on RUNX1 targets is not known	-9.1	9	38
CORUM:713	BRG1-SIN3A complex	-9.1	7	14
WP4321	Thermogenesis	-9.1	12	108
CORUM:714	BRM-SIN3A complex	-9.0	7	15
GO:0016054	organic acid catabolic process	-8.9	15	224
hsa00071	Fatty acid degradation	-8.8	9	43
CORUM:555	BAF complex	-8.7	6	9
CORUM:1239	EBAFb complex	-8.4	6	10
CORUM:1252	EBAFa complex	-8.4	6	10
CORUM:554	PBAF complex (Polybromo- and BAF containing complex)	-8.4	6	10
CORUM:808	BRM-associated complex	-8.4	6	10
GO:0044282	small molecule catabolic process	-8.4	6	10
CORUM:806	BRM-SIN3A-HDAC complex	-7.8	6	12
R-HSA-5389840	Mitochondrial translation elongation	-7.6	10	87
CORUM:189	BAF complex	-7.6	6	13
R-HSA-5368287	Mitochondrial translation	-7.4	10	93
GO:0006338	chromatin remodeling	-7.1	14	267
GO:0046395	carboxylic acid catabolic process	-7.0	13	220
GO:0006520	cellular amino acid metabolic process	-6.9	14	276
CORUM:1251	BAF complex	-6.9	5	8
CORUM:564	BAF complex	-6.9	5	8
hsa04714	Thermogenesis	-6.8	13	232
CORUM:320	55S ribosome, mitochondrial	-6.8	9	77
R-HSA-3214858	RMTs methylate histone arginines	-6.7	9	79
CORUM:1237	BAF complex	-6.7	5	9
CORUM:1238	PBAF complex (Polybromo- and BAF containing complex)	-6.7	5	9
CORUM:556	PBAF complex (Polybromo- and BAF containing complex)	-6.7	5	9
CORUM:565	PBAF complex (Polybromo- and BAF containing complex)	-6.7	5	9
CORUM:566	BAF complex	-6.7	5	9
CORUM:710	Brg1-associated complex I	-6.7	5	9
CORUM:711	Brg1-associated complex	-6.7	5	9
CORUM:507	BRG1-associated complex	-6.7	5	9
CORUM:778	LARC complex (LCR-associated remodeling complex)	-6.7	6	19
GO:0006337	nucleosome disassembly	-6.7	6	19
GO:0031498	chromatin disassembly	-6.7	6	19

ATF3 V+D+B+ unique (150 DEPs-See Fig. 56)

Term	Description	Log(q-value)	in term	in list
R-HSA-71406	Pyruvate metabolism and Citric Acid (TCA) cycle	-5.1	6	55
R-HSA-72766	Translation	-5.0	9	291
WP3925	Amino acid metabolism	-4.2	6	91
R-HSA-1428517	The citric acid (TCA) cycle and respiratory electron transport	-4.1	7	178
GO:0032543	mitochondrial translation	-4.1	5	50
R-HSA-379726	Mitochondrial tRNA aminoacylation	-3.9	4	21
hsa05230	Central carbon metabolism in cancer	-3.5	5	70
R-HSA-70268	Pyruvate metabolism	-3.3	4	31
hsa00640	Propanoate metabolism	-3.3	4	32
GO:0140053	mitochondrial gene expression	-3.3	5	82
GO:0006520	cellular amino acid metabolic process	-3.2	7	276
GO:0006418	tRNA aminoacylation for protein translation	-3.0	4	41
R-HSA-379724	tRNA Aminoacylation	-3.0	4	42
GO:0043039	tRNA aminoacylation	-2.9	4	44
GO:0043038	amino acid activation	-2.9	4	45
GO:0043604	amide biosynthetic process	-2.9	8	474
hsa00620	Pyruvate metabolism	-2.9	4	47
GO:0006412	translation	-2.9	7	332
GO:0006518	peptide metabolic process	-2.9	8	489
GO:0043043	peptide biosynthetic process	-2.7	7	359
GO:0043603	cellular amide metabolic process	-2.5	9	750
hsa00970	Aminoacyl-tRNA biosynthesis	-2.4	4	66
hsa00010	Glycolysis / Gluconeogenesis	-2.4	4	67
R-HSA-9609507	Protein localization	-2.2	5	163
GO:0072530	purine-containing compound transmembrane transport	-2.2	3	24
GO:0051503	adenine nucleotide transport	-2.0	3	27
GO:0015868	purine ribonucleotide transport	-2.0	3	28
R-HSA-5389840	Mitochondrial translation elongation	-2.0	4	87
GO:0015865	purine nucleotide transport	-2.0	3	29
R-HSA-5368287	Mitochondrial translation	-1.9	4	93
hsa00020	Citrate cycle (TCA cycle)	-1.9	3	30
GO:0006099	tricarboxylic acid cycle	-1.9	3	31
hsa04922	Glucagon signaling pathway	-1.7	4	107
hsa04066	HIF-1 signaling pathway	-1.7	4	109
GO:0006862	nucleotide transport	-1.7	3	37
hsa01200	Carbon metabolism	-1.6	4	115
R-HSA-425397	Transport of vitamins, nucleosides, and related molecules	-1.5	3	43
WP534	Glycolysis and gluconeogenesis	-1.5	3	45
GO:0007005	mitochondrion organization	-1.5	6	418
hsa00270	Cysteine and methionine metabolism	-1.4	3	50

ATF3 D+B+ vs ATF3 V+D+B+

Figure 62: Top 40 enriched pathways mapping to DEPs unique to the ATF3 V+D+B+ (see figure 56 B) and ATF3 V+D+B+ (compared to ATF3 D+B+) revealed by Metascape analysis. Blue arrows point to indicated terms.

Overall, the bioinformatics analysis of the miniTurbo-ATF3 construct showed several known interactors of ATF3 and revealed new potential ones. The interaction of miniTurbo-ATF3 with several proteins localized in the mitochondria upon HCoV-229E infection might offer a new insight into the role of this factor in CoV replication. With this informaton in hand, functional follow up experiments can now be designed in future studies to confirm these new interactions by orthogonal methods (e.g. co-immunoprecipitation, proximity ligation assays) during the virus-mediated up regulation of ATF3 and, as loss of ATF3 did not affect viral replication (Fig. 46), reveal their functional relevance for the host response.

Chapter 5: Discussion

5.1 The roles of the UPR in CoV replication

As delineated in the introduction, coronaviruses replicate their genome in specialized, virus-induced subcellular structures referred to as double-membrane vesicles (DMVs). One putative origin of these structures is the ER membrane (Klein et al. 2020; Cortese et al. 2020; Romero-Brey and Bartenschlager 2016). Hence, it is expected that their formation upon CoV infection and the subsequent accumulation of newly synthesized viral proteins can cause a form of ER stress and activation of the unfolded protein response (UPR). Molecular details and the biological role of this type of ER stress and the subsequent UPR activation in CoV replication are still largely poorly characterized.

In this work, the investigation of major UPR and ER stress factors in response to CoV infection showed a unique pattern of activation and attenuation of these factors. This indicated a virus-specific host response concerning both processes to the infection. Small molecule inhibitors and genetic loss of function (i.e. knockdown) strategies were implemented to investigate the roles of these factors in CoV replication and host response. The roles of UPR and ER stress induction in CoV replication and host response were also studied through activating these systems by the chemical compound thapsigargin. The results of these studies are discussed in the following sections.

5.1.1 The modulation of major UPR factors by CoV infection

The UPR sensors PERK and IRE1 α were both activated in response to CoV infection, which was in line with multiple other studies with different strains of CoV including SARS-CoV, MERS-CoV, SARS-CoV-2, and PHEV-CoV (Krähling et al. 2009; Chu et al. 2021; Echavarría-Consuegra et al. 2021; Shi et al. 2022; Xue et al. 2018; To S. Fung and Liu 2014; To Sing Fung, Liao, and Liu 2016).

The activation of PERK by a short pulse of chemical ER stress (i.e. 1 hour of thapsigargin) showed only one, hyper-shifted band of PERK. Interestingly, when compared to 1 hour of thapsigargin treatment, the PERK activation pattern seen on the Western blot due to 24 hours of virus infection showed multiple bands of PERK. The single band seen in 1 hour of thapsigargin treatment can be due to multisite-phosphorylation of PERK upon initial activation of UPR. The pattern of PERK activation seen after 24 hours of virus infection might be attributed to different levels of PERK phosphorylation or possibly other post-translational modifications (PTMs) such as K48-linked ubiquitination that might target the protein for degradation (Larhammar et al. 2017; Akimov et al. 2018). It can also be a reflection of degradation products of an initial single hyper-phosphorylated band. Hence, it is reasonable to speculate that a short pulse of chemical ER stress might not be enough to show the full range of the post-translationally modified products or degradation products on the Western blot. Indeed longer treatments of the cells with thapsigargin resulted in a somewhat similar pattern of activation of the PERK band to

the one seen in the virus-infected cells. Overall, these data hint at the dynamic pattern of PTMs in regulating PERK levels (and maybe functions) depending on the length of UPR activation. An interesting follow-up experiment would be to identify these modifications by mass spectrometry at different time points of UPR activation and under different stimuli (i.e. thapsigargin vs CoV). This experiment can be followed up by mutating any differential PTMs of PERK under these conditions and observing any subsequent phenotype.

In contrast, IRE1 α activation was observed as a single protein band phosphorylated at serine 724 with no effect on the overall levels of the protein in HCoV-229E-infected cells. This phosphorylation site is widely used to monitor the activation of IRE1 α in response to ER stress. A recent study in mouse embryonic fibroblast cells and primary hepatocytes has indicated that the phosphorylation of IRE1 α at Ser724 is crucial for the IRE1 α auto-phosphorylation and the activation of its RNase activity (Y. Li et al. 2022).

The mechanism of UPR sensors activations has been under study for a long time (Gardner and Walter 2011; Kopp et al. 2019; Verfaillie et al. 2012). An interesting assay developed by Kopp et al depends on the FRET signal that quantitatively assesses the association and dissociation of BiP from IRE1 α upon the activation of UPR (Kopp et al. 2018). The same group showed in a later study that BiP has dual functionality as a chaperon and as an ER stress sensor through its interactions with luminal domains of UPR sensors of IRE1 α and PERK (Kopp et al. 2019). The FRET assay mentioned above can also be extended to study the activation mode of PERK under different experimental conditions (including CoV infection) and at different time points of the UPR activation. This will give more insight into the subtle differences in UPR activation and mechanisms as a function of treatment or infection.

Interestingly, MERS-CoV infection of Huh7 cells resulted in the downregulation of IRE1 α protein levels while SARS-CoV-2 infection of VERO-E6 cells upregulated the protein levels. These data suggest a possible pathogen-specific involvement of IRE1 α in the replication of each of these viruses. Indeed a recent study has indicated that SARS-CoV-2 (unlike other betacoronaviruses, including MERS-CoV) only partially activates the IRE1 α pathway in human lung-derived cells (Nguyen et al. 2022). The paper argued that the inhibition of the RNase domain of auto-phosphorylated IRE1 α could be seen as a strategy to modulate the host's innate immune response through inhibiting the IRE1 α -dependent splicing of XBP1 mRNA.

The prominent ER stress marker BiP showed a reduction in protein levels after 24 hours of HCoV-229E and MERS-CoV infections of Huh7 cells. BiP is usually involved in chaperoning unfolded proteins and hence its upregulation, rather than its downregulation, would have been expected upon induction of UPR. Nevertheless, few other studies reported a similar downregulation of BiP as a result of a CoV infection (Echavarría-Consuegra et al. 2021). The observed downregulation might be attributed to a possible anti-viral role of BiP, which is discussed in more details in section 5.1.3.

Finally, the infection of Huh7 cells with HCoV-229E resulted in huge induction of ATF3, which is discussed in more detail in section 5.3.

5.1.2 The effects of attenuating the functions and protein levels of PERK and IRE1 α on CoV replication and host response

This present study utilized small molecule inhibitors and genome editing by CRISPR-CAS-9 as two independent and complementary loss of function approaches to investigate the effect of attenuating the functions and protein levels of both, PERK and IRE1 α , on CoV replication and the host response.

5.1.2.1 The “basal” host response to attenuating the functions and protein levels of PERK

The treatment of the uninfected cells with 10 μ M of PERK inhibitor for 24.5 hours resulted in a clear deactivation (i.e. contraction to one single fast-migrating band) of the slightly activated PERK bands. This slight activation is most likely due to treatment with the vehicle DMSO and/or residual stress resulting from harvesting the cells, a process that involves a change in temperature and mechanical scraping. The treatment also led to an unexpected, significant increase in the levels of eIF2 α phosphorylation and ATF3 induction. This paradoxical increase of eIF2 α phosphorylation was accompanied also by a reduction in translation levels as assessed by the puromycilation assay. One possible explanation of this observation can be attributed to a compensatory mechanism initiated by the cell upon PERK inhibition. This compensatory mechanism is carried out by other eIF2 α kinases leading to the induction of a moderate (or low) UPR, possibly without an underlying causative ER stress. Hence, the moderate induction of ATF3 seen under this condition might be understood as a “by-product” of such activation and ultimately point out to possible connection between ATF3 and other eIF2 α Kinases (discussed in section 5.3). Indeed a similar decorrelation between PERK inhibition and eIF2 α phosphorylation has been previously reported for PERK inhibitor GSK2656157 (Krishnamoorthy et al. 2014). In that study, the authors argued that GSK2656157 could indeed induce ER stress-mediated death of human fibrosarcoma cells and might be used to investigate pathways that compensate for PERK inhibition. Supporting the idea of compensatory pathways, a study done in human breast cancer cells indicated a reciprocal modulation of activities between PERK and GCN2 (Alasiri et al. 2020). In that study, the authors demonstrated that inhibiting PERK with GSK2606414 lead to an induction in GCN2 expression and activity.

Alternatively, Mendez et al reported a novel small ATP-competitive molecule (IPA) that inhibits PERK at a certain range of concentrations while it activates it at the lower range (Mendez et al. 2015). The authors argued for a model where the binding of this molecule at lower concentrations would lead to a predisposition of the kinase to switch to the active conformation state. This in turn would lead to a trans-

activation of an un-bound (to the inhibitor) second PERK molecule through dimerization, a process known as allosteric activation. Similar results from Dey et al were also reported for PKR kinase (Dey et al. 2014). Hence, a similar phenomenon with the current PERK inhibitor cannot be excluded.

In agreement with the results from the inhibitor studies discussed above, the knockdown of PERK in Huh7 cells led to a similar statistically significant increase in the phosphorylation of eIF2 α in the non-infected cells. This observation supports the argument of a compensatory response from other eIF2 α kinases in cases of PERK knockdown or inhibition. Nevertheless, this increase in eIF2 α phosphorylation was seen as only a slight decrease (statistically non-significant) in the translation levels as investigated through puromycilation assay. Contrary, when investigated using click-chemistry-mediated biotin labeling of the nascent proteins, the reduction was more readily seen on Western blot. This discrepancy might be attributed to a shortcoming of the puromycin-labeling method in PERK KD cells. Indeed a group of researchers reported similar disagreement between these two methods in energy-starved cells (Marciano, Leprivier, and Rotblat 2018). In that correspondence, the authors showed a significant reduction in the levels of mRNA translation using both puromycin labeling and methionine homolog L-azidohomoalanine (AHA) labeling under cycloheximide treatment. The results, however, were different under glucose or total starvation (both of which are known to induce translational shut-off). Under these conditions, puromycin labeling showed only a minor reduction in protein synthesis as compared to AHA labeling.

5.1.2.2 The effects of attenuating the functions and protein levels of PERK and IRE1 α on CoV replication

The effect of PERK inhibitor on HCoV-229E replication was readily seen as a significant reduction in the levels of the viral N protein and the production of infectious particles. This also led to a partial reversal in the virus-induced phosphorylation of eIF2 α and the virus-induced translational shut-off.

The data obtained from attenuating PERK genetically agreed with the inhibitor studies on a reduction in the production of HCoV-229E infectious particles. However, a key discrepancy between the two approaches was readily evident in the production of the viral N protein. Wherein the pharmacological attenuation of PERK resulted in a massive reduction of the N protein, the genetic approach resulted in a significant increase (two folds) in the levels of this viral protein. This increase in the N protein was orthogonally validated using the click-chemistry approach to assess de-novo synthesis levels of proteins of interest under infection conditions. The click-chemistry approach indicated that this increase is a result of active translation of the viral N protein rather than lack of its degradation.

Another interesting observation when comparing the two approaches (genetic vs pharmacological) can be seen in the levels of HCoV-229E infectious particles production. Although both approaches agreed on a reduction in the viral titer, the PERK KD cells showed a weaker (though still statistically

significant) reduction than that observed using pharmacological inhibition of PERK. The observation can either be interpreted as a piece of evidence supporting the idea that the presence of enzymatically inactive PERK has an anti-viral effect or that the inhibitor might be off-targeting other kinases that are relevant to the infection.

Arguably, the inhibition of the enzymatic activities of PERK pharmacologically does not necessarily prevent PERK from forming protein-protein complexes and engaging in non-enzymatic activities. These non-enzymatic activities might lead (directly or indirectly) to the activation of further anti-viral mechanisms or even targeting the N protein for degradation or reducing its translation. Hence, an additional layer of the structurally dependent (enzymatically independent) anti-viral role of PERK might be involved. Consequently, a systematic approach to studying the interactome of PERK protein under CoV infection conditions might shed light on new functions of this protein. Worth pointing out here that PERK consists of multiple domains including a transmembrane, luminal, and kinase domains (H. Wu, Ng, and Thibault 2014). Of these domains, the luminal one has been shown to form selective protein: protein interactions with misfolded proteins but not with their native forms (P. Wang et al. 2018).

Indeed many reports indicated a wide range of non-catalytic activities of multiple kinases. These activities included allosteric regulation, scaffolding, and interacting with nucleic acids (Kung and Jura 2016).

One prominent example of such “enzymatically independent” functioning is the α isoform of p38 MAP kinase. The activation of this protein leads to cell cycle arrest through the triggering of the G2/M checkpoint (Fan et al. 2005). RNA interference depletion of p38 α resulted in an expected inhibition of cell proliferation; however, the inhibition of the kinase using small molecules did not affect the cell cycle supporting the idea of a kinase-independent role of this protein in the cell proliferation (Fan et al. 2005).

Moreover, a study from Hett et al indicated an important, kinase-independent, role of PKR in pyroptosis (a process that leads to programmed cell death accompanied by high levels of inflammation) through the activation of caspase-1 (Hett et al. 2013)

A hypothesis that might integrate both of these observations (i.e. viral titer and N protein levels differences between inhibiting PERK pharmacologically and PERK KD) relies on multiple studies that showed an abundant amount (i.e. ectopic overexpression) of the viral N protein might enhance the production of CoV infectious particles (Casais et al. 2001; Mishra et al. 2021; Sungsuwan, Jongkaewwattana, and Jaru-Ampornpan 2020). Indeed, a recent study indicated that the ectopic overexpression of the N protein of both TGEV and PEDV coronaviruses led to an increase in the production of PEDV RNA and virions in cell culture (Sungsuwan, Jongkaewwattana, and Jaru-Ampornpan 2020). Hence, the weaker reduction of the viral titer in PERK KD cells can be also attributed to enhanced production of viral particles, due to the increased N protein translation. In other words, the

increased translation of the N protein might be able to compensate for the partial anti-viral state imposed by the absence of PERK.

A follow-up experiment to test this hypothesis would include the ectopic overexpression of the viral N protein in cells infected with HCoV-229E and simultaneously treated with PERK inhibitor. An increase in the production of infectious particles might be considered as supporting evidence for this hypothesis.

Additionally, the reconstitution of PERK KD cells with PERK construct encoding a kinase-dead mutant under HCoV-229E infection should result in further reduction in the titer and a decrease in the amount of the N protein if indeed PERK has an enzymatically independent role in CoV replication.

When investigating translation levels under CoV infection, both approaches (i.e. inhibitors and knockdown) led to only a partial reversal in the virus-induced translational shutdown. Contrary, the treatment of PERK KD cell line with 1 μ M of thapsigargin for 1 hour resulted in a complete reversal of the translational shut-off observed under this condition in the parental cells. These observations support the idea of active contribution of other eIF2 α kinases to the induction of translation shutdown upon CoV infection.

The treatment of both uninfected and HCoV-229E-infected cells with 1 μ M of KIRA6 (IRE1 α inhibitor) led to the activation of the PERK band and a significant increase in eIF2 α phosphorylation. The treatment also resulted in minor effect on the viral replication and N protein production. No effect was observed on the virally-induced translational shut-off after this treatment.

It is known that PERK signaling persists in prolonged ER activation while IRE1 α activation attenuates (Chang et al. 2018). It is possible that a prolonged IRE1 α inhibition by KIRA6 can be interpreted by the cell as a signal to switch between adaptive UPR (IRE1 α -dependent) into an apoptotic one (PERK-dependent) and hence the activation of the PERK band.

The activation of eIF2 α phosphorylation and the minor effect on the virus replication has been partially mirrored in the IRE1 α KD cells. Nevertheless, the activation of the PERK band itself has not been observed in IRE1 α KD cells which might argue again for similar issues regarding inhibitor vs KD discrepancies discussed above for PERK.

On the other hand, the double treatment of both PERK and IRE1 α inhibitors of infected cells leads to the deactivation of IRE1 α -induced activation of PERK. Hence, the dominance of the anti-viral effect resulting from the deactivation of PERK-phospho-eIF2 α pathways argues for an important partially pro-viral role of activated PERK in the replication of HCoV-229E. This may occur possibly, through a translation-shut-off mediated mechanism whereby global suppression of host translation favors the translation of (structural) viral proteins while concomitantly the production of some anti-viral host proteins is repressed.

5.1.3 Role of thapsigargin activation of UPR in CoV replication

The modulation of individual ER stress sensors genetically or pharmacologically revealed an intricate involvement of the UPR in CoV infection. The further investigation of this involvement using the ER stress inducer (and UPR activator) thapsigargin led to the discovery of its potent anti-viral effect on three different human CoV, including SARS-CoV-2. This strong anti-viral effect was observed on multiple levels including viral RNA synthesis, viral protein translation, and the production of infectious particles. This effect was still observed even when thapsigargin was added 8 hours after the start of the infection.

5.1.3.1 Role of BiP and IRE1 α in thapsigargin-mediated adaptive and anti-viral responses

The treatment of CoV-infected cells with thapsigargin reversed the CoV-induced down-regulation of multiple host factors involved in UPR signaling including BiP. This treatment also led to a substantial increase in the protein levels of IRE1 α .

BiP is a canonical marker of ER stress and UPR activation. An observation that can be seen in our data in Huh7 cells treated with thapsigargin for 16 and 24 hours with or without simultaneous CoV infection. The data in this study indicated that the maximum induction of BiP occurred 24 hours after thapsigargin treatment with or without infection. This coincided also with the anti-viral state imposed on the cellular models by thapsigargin. Hence, viewing the induction of BiP in the context of thapsigargin treatment as part of an anti-viral or an adaptive response to the prolonged stress-induced by thapsigargin cannot be excluded. Nevertheless, no upregulation or downregulation of BiP was observed in cells infected with SARS-CoV-2 only, i.e. in the absence of thapsigargin. Interestingly, no upregulation of BiP in cells treated with 1 μ M of thapsigargin for 1 hour has been observed, although most other ER stress markers tested in this study can be seen upregulated including PERK and eIF2 α phosphorylation. This last observation might point out a protective upregulation of BiP upon prolonged UPR activation.

Indeed multiple other studies indicated a protective role of BiP induction in the studied cellular model. For instance, it has been shown that inducing BiP using a small molecule inducer (called BiX) in neuronal cells protected them from death caused by ER stress (Kudo et al. 2008). Additionally, it has been shown that in yeast, the induction of Karp2 (BiP homolog) is crucial for clearing toxic proteins (Hsu et al. 2012). Hence, utilizing BiP inhibitors (or BiP KD cell line) to attempt to reverse thapsigargin-mediated induction of BiP can be a very interesting follow-up experiment with possible intriguing outcomes. For example, it can either increase the cytotoxicity of thapsigargin through diminishing this putative adaptive UPR response without affecting the virus replication, has no phenotype, or further contribute to the suppression of the tested CoV replication. The latter outcome would support the idea of a pro- rather than anti-viral role of BiP. A particularly interesting situation would be to observe

different outcomes of this experiment based on the virus used. This would indicate a virus-specific role of BiP, at least in the context of the anti-viral state imposed by thapsigargin.

Worth mentioning here that the role of BiP in CoV replication discussed in our publication Shaban et al. 2021 has been challenged as part of the matter arising section of Nature Communications from another group (Shaban et al. 2021). The group argued for a pro-viral role of BiP in SARS-CoV-2 replication using a BiP inhibitor and siRNA knockdown strategy (Shin et al. 2022). This prompted a reply from our side to their publication indicating that an exact role of BiP was not in the scope of the original publication and indeed in need of further elucidation (Shaban, Müller, et al. 2022). Both the challenge and the reply were published side by side in the same issue of the journal.

IRE1 α is known to mediate part of the adaptive arm of the UPR, promoting restoration of normal ER functioning and cell survival (Sircaik et al. 2021). Moreover, IRE1 α is heavily involved in maintaining the integrity of the lipid bilayer of the ER membrane (Ho et al. 2020). Indeed Volmer et al showed in a study that IRE1 α is able to sense lipid-bilayer changes (Volmer, van der Ploeg, and Ron 2013). Halbleib et al also showed that IRE1 α has capabilities to sense physiochemical properties of the ER membrane (Halbleib et al. 2017). According to that work, IRE1 α sensing of membrane lipid density depends on certain structural elements in the sensors luminal domain. These structural elements are responsive to the modulation of the membrane lipid density, which in turn affect the activation of IRE1 α through increasing its dimerization (Halbleib et al. 2017). Interestingly, PERK has also similar structural elements and can be activated by unusual membrane changes rendering it a possible player in this process (Volmer, van der Ploeg, and Ron 2013). Maintaining the integrity of the lipid bilayer of the ER membrane is a function that might be very much needed to counter the damage resulted from the viral assault on ER membrane through the establishment of DMVs and CMs. Hence, the upregulation of IRE1 α can add another layer of adaptive/anti-viral response invoked by thapsigargin treatment.

Nevertheless, a recent study indicated that the protection offered by IRE1 α against thapsigargin-induced cytotoxicity is cell-type dependent (Lindner et al. 2020). The study showed a pro-apoptotic role of IRE1 α under thapsigargin treatment in LNCaP prostate adenocarcinoma cells but not HCT116 colon carcinoma cells (Lindner et al. 2020). Indeed, the hyper-activation of this sensor led to an increase in the number of its RNase domain targets, that eventually led to apoptosis (R. Ghosh et al. 2014). Hence, a more profound investigation of the role of this sensor under thapsigargin treatment in context of CoV infection to determine its state of activation, downstream targets and interactors, is needed.

5.1.3.2 The proteomic changes in response to thapsigargin treatment of CoV-infected cells

The proteomic analysis carried out in this study indicated a pattern of upregulation of many other UPR factors when CoV-infected cells were treated with thapsigargin, including HERPUD1 and BiP.

The proteomic data also showed that amongst the highly upregulated pathways in CoV-infected cells, treated with thapsigargin, are those that are relevant to intracellular transportation, endocytosis and vesicle transportation. The involvement of these pathways in membrane remodeling is well known (Haucke and Kozlov 2018). The process through which the virus is inducing the formation of DMVs and CMs is heavily dependent on membrane rearrangements and remodeling (Wolff et al. 2020). Hence, it cannot be excluded that thapsigargin treatment is directly disrupting this process leading to a strong anti-viral effect. Nevertheless, the exact mechanism by which thapsigargin might exert this anti-viral effect is still unknown. One approach to elucidate this mechanism might be achieved by a systematic investigation of the most upregulated proteins involved in these processes.

The proteomic analysis also indicated a thapsigargin-dependent induction of multiple ERAD and ERQC factors. HERPUD1 functions as part of ERAD, which is a process that further contributes to an adaptive response of UPR to remove unwanted proteins. Indeed, a study in cardiac cells indicated a major protective role of this protein through contributing in the degradation of a Ca²⁺ channel inositol 1,4,5-trisphosphate receptor (IP3R) which is involved in cardiac hypertrophy pathology (Torrealba et al. 2017). While the knockout of this protein resulted in increased levels of IP3R and progression toward cardiac hypertrophy (Torrealba et al. 2017). Hence, the collective, adaptive action of UPR factors mentioned above, and others, might contribute to the overall restorative and anti-viral effect of thapsigargin.

Additionally, thapsigargin treatment of cells infected with MERS-CoV, and SARS-CoV-2 led to the upregulation of multiple proteins that are involved in ubiquitination. Ubiquitination is a post-translational modification that alter proteins functioning, for example through K63-linked polyubiquitination or target them for degradation through K48-linked polyubiquitination (Kliza and Husnjak 2020; Swatek and Komander 2016). One example of such protein from the data set is the E1 enzyme ubiquitin-like modifier-activating enzyme 6 (UBA6). The action of UBA6 and UBA1 (the other main E1 enzyme) results in controlling the proteome through targeting proteins to proteasomal degradation (Xianpeng Liu et al. 2017; Groettrup et al. 2008). In a recent study, researchers showed a major role of UBA6 in IFN- γ production in CD4⁺ and CD8⁺ T cells (J. Y. Lee et al. 2022). Their data indicated hyper-activation of IFN- γ production in both CD4⁺ and CD8⁺ T cells lacking UBA6 (J. Y. Lee et al. 2022). The proposed mechanism for this control is through modulating the stability of the NF- κ B inhibitor I κ B α (J. Y. Lee et al. 2022). Moreover, it has been shown that UBA6 activates FAT10, a molecule with function similar to ubiquitin (Groettrup et al. 2008). FAT10 targets its substrate to proteasomal degradation and is induced under pro-inflammatory conditions by IFN γ and TNF α (Groettrup et al. 2008). Together, these data suggest that induction of UBA6 might be part of the anti-viral state imposed on the cells after thapsigargin treatment. Possibly through targeting viral proteins to degradation and/or modulating host factors relevant to immune response. Nevertheless, a more thorough

investigation of this protein and its pathway is needed to elicit its role in thapsigargin-mediated anti-viral state.

5.1.3.3 The translational changes in response to thapsigargin treatment of CoV-infected cells

The pattern of upregulation of several UPR factors when CoV-infected cells were treated with thapsigargin seen in the proteomic data was in line with a partial restoration of translation seen using puromylation assay. Similar results has been indicated in a different study where the authors used metabolic labeling to investigate the effect of prolonged induction of UPR by thapsigargin on translation shut-off (Preston and Hendershot 2013). The study showed that this partial restoration is selective and geared toward repressing sets of specific proteins rather than a general decrease in the translation capacity (Preston and Hendershot 2013).

The general proposed mechanism for this partial restoration of translation is through a negative feedback loop that leads to the de-phosphorylation of eIF2 α by protein phosphatase 1 (PP1) under chronic UPR conditions (Ma and Hendershot 2003). Interestingly, the data in the present study indicated a decrease in eIF2 α phosphorylation in cells infected with CoV or treated with thapsigargin for more than 16 hours compared to cells treated with only 1 hour of this compound. Nevertheless, it did not show any decrease in the levels of eIF2 α phosphorylation in cells treated with thapsigargin for prolonged periods (including the CoV + thapsigargin combined treatment) when compared to CoV-only infected cells despite the obvious, partial, restoration of translation. This discrepancy highlights the possibility of the involvement of a mechanism that is eIF2 α -phosphorylation independent in thapsigargin-induced translational changes. Indeed data by (Preston and Hendershot 2013) indicated the involvement of 4E-BP1 hypo-phosphorylation in this rather partial restoration of translation by thapsigargin, confirming previous results showing that 4E-BP1 deletion results in full restoration of translation after UPR induction (Yamaguchi et al. 2008, Preston and Hendershot 2013). Together, these results point out a possible virus-specific mechanism to induce the translational shut off that is different from the one used by thapsigargin. It also points out that thapsigargin might switch the molecular mechanism used to induce translation shutdown depending on the length of the treatment. Additionally, the thapsigargin partial restoration of translation can be seen as part of the adaptive mechanism to the prolonged activation of UPR and might be anti-viral by excluding viral proteins from the partial restoration of translation.

A follow up experiment to elicit any bias toward translating or suppressing a particular subset of proteins in this partial restoration of translation can be performed using a click-chemistry-mediated, L-HPG/ biotin labeling approach. The double treatment condition (thapsigargin + CoV) and thapsigargin only condition for 24 hours or 1 hour can be compared. In such approach, cells under different treatment/infection conditions can be treated with the methionine analog and then conjugated to biotin

using click-chemistry. Subsequently, the labelled proteins can be pulled down and sent to mass-spectrometry for in-depth analysis of any differentially translated (or suppressed) proteins (Forester et al. 2018).

5.1.3.4 CoV might be a direct target of thapsigargin

The arguments above focused on the modulation of host pathways by thapsigargin that might be important for viral replication and hence the anti-viral effect. Nevertheless, one cannot exclude the possibility that thapsigargin directly interacts with viral proteins leading to blocking of the infectious cycle in a host-response independent manner. As delineated in the introduction, thapsigargin main target in the cell is the SERCA Ca^{2+} ion pump. Viral proteins that function as ion channels are well reported in many viruses and are especially common in RNA viruses (Nieva, Madan, and Carrasco 2012). The role of these viral ion channels can be critical for multiple stages of the virus life cycle and also in the modulation of the host response, including increased pathogenicity of the infection through different mechanisms that are still under investigation (Nieto-Torres et al. 2015). Hence, mutant viruses lacking the functions of these viral ion channels have been reported to be strongly attenuated (Nieto-Torres et al. 2015; Watanabe, Watanabe, and Kawaoka 2009; Netland et al. 2010; Nieva, Madan, and Carrasco 2012; Nieto-Torres et al. 2014).

Indeed, multiple viral auxiliary and structural proteins have been reported to function as ion channels (McClenaghan et al. 2020). For instance the E protein of SARS-CoV has been reported to form an ion channel in ERGIC/Golgi membranes with selective permeability to calcium ions (Nieto-Torres et al. 2015). Imbalance in Ca^{2+} concentrations triggers an innate immune response through activating inflammasomes and cytokines (Nieto-Torres et al. 2014). In that study, the researchers demonstrated that Ca^{2+} crossing through E protein had a major role in inducing inflammatory response through the overproduction of IL-1 β . Another example of such ion channel activity of a coronavirus protein is the ORF4a and auxiliary protein 3a of HCoV-229E and SARS-CoV-2, respectively (R. Zhang et al. 2014; Lu et al. 2006). In these studies, the authors demonstrated an important role of these auxiliary proteins functioning as ion channels. Lastly, the interaction between thapsigargin and other viral proteins (structural and non-auxiliary) can also occur through direct binding of the substance to residues in motifs similar to where it binds to the SERCA.

Together, these data indicates the importance of exploring the idea of thapsigargin interacting with these proteins as a possible anti-viral mechanism.

5.1.3.5 The role of the SERCA pump in thapsigargin-mediated anti-viral effect

The targeting of the SERCA Ca^{2+} pump by thapsigargin and the subsequent increase in the cytosolic concentrations of Ca^{2+} can also be thought of in itself as an anti-viral mechanism through the modulation of Ca^{2+} signaling (Saurav et al. 2021; Thastrup et al. 1990). Indeed a recent study have indicated that the modulation of cytosolic Ca^{2+} concentrations using calcium channel blockers (CCBs) may have a beneficial effect on reducing fatality rate in COVID-19 patients and resulted in reduced replication of SARS-CoV-2 in vitro (L.-K. Zhang et al. 2020). Worth pointing out here that although, thapsigargin and CBBs regulate cytosolic Ca^{2+} concentrations differently; the effect of blocking either of them is an increase in the cytosolic Ca^{2+} concentrations. Thapsigargin main action is to block pumping back leaked Ca^{2+} ions from the cytosol to the ER while CCBs action is to maintain the intracellular concentrations of the ion against the rush of non-cytoplasmic Ca^{2+} upon a stimuli (Thastrup et al. 1990; S. Wang et al. 2017). Hence, the anti-viral effect observed with CCBs or thapsigargin highlights the importance of calcium signaling for viral replication and as a target for future anti-viral drugs.

Lastly, the induction of ER stress by chemical compounds such as thapsigargin has been shown to proceed through multiple non-canonical cellular pathways (Bergmann et al. 2018). These pathways are thought to be mostly irrelevant to the classical UPR induced through overloading the ER with synthetic mal-or unfolded polypeptides (Bergmann et al. 2018). This observation suggests that the anti-viral effect seen with thapsigargin might be indeed achieved through other pathways that are independent of UPR-activated programs and only partially achieved by UPR modulation.

In the next section the role of thapsigargin in inducing and regulating autophagy flux, the general role of autophagy in CoV replication and its cross talk with UPR were discussed.

5.2 Role of autophagy in CoV replication and crosstalk with ER stress pathways

5.2.1 Role of autophagy in HCoV-229E

The role of autophagy in CoV replication, specially the formation of replicative DMVs, has been under extensive research for long time (Sargazi et al. 2021). Three major findings in this study regarding the role of autophagy in HCoV-229E replication can be summarized as follows: The infection caused the induction of selective autophagy (mediated by p62). The inhibition of autophagy by lysosomal acidification inhibitor (BafA1) resulted in a significant drop in the translation of the viral N protein and the production of infectious particles. Thapsigargin treatment of cells infected with the virus blocked both types of autophagy flux severely (selective and basal).

Selective autophagy relies on adaptor proteins that capture ubiquitinated targets and subsequently interact with LC3B-II to deliver the cargo to the maturing autophagosome (Cohen-Kaplan et al. 2016). Example of such an adaptor protein is p62 (Pankiv et al. 2007). Given the selectivity of this process, increasing number of studies started to focus on its role in the regulation of innate immunity. Indeed a recent study has shown that in *Drosophila*, the immune deficiency (IMD) pathway is a target for degradation by selective autophagy (Tsapras et al. 2022). IMD acts as an activator of NF- κ B pathway in insects and plays major role in the expression of most of anti-microbial peptides (Myllymäki, Valanne, and Rämetsä 2014) suggesting an important pro-pathogen role of selective autophagy.

Another piece of evidence supporting a possible pro-viral role of selective autophagy is a study that indicated the involvement of p62 in selectively degrading parts or whole of the ER (ER-phagy) (Ji et al. 2019). This degradation (or recycling) of the ER membrane might provide the virus with a source of material to generate the replicative DMVs.

PERK activation has been shown to induce autophagy (Avivar-Valderas et al. 2011). One finding of this study was that the GSK2606414 inhibition of PERK pathway resulted in a decoupling between HCoV-229E replication and autophagy flux inhibition. In other words, GSK2606414 inhibited the virus replication but did not affect autophagy flux. This decoupling might suggest that the activation of autophagy in CoV-infected cells is PERK independent.

Finally, although thapsigargin strongly activates PERK pathway, it resulted in the inhibition of both types of autophagy flux. It is well known that Ca^{+2} is required for the early steps of autophagosome biogenesis (Engedal et al. 2013). Hence, the inhibition of autophagy flux by thapsigargin can be understood because of Ca^{+2} gradient disruption rather than an ER stress/ UPR related mechanism (Engedal et al. 2013; Ganley, Wong, and Jiang 2011; Ganley et al. 2011-2).

5.2.2 Role of autophagy in MERS-CoV

Interestingly, inhibiting autophagy flux by BafA1 treatment did not result in any inhibition of MERS-CoV replication. The data in this study also indicated a significant downregulation of autophagy flux upon MERS-CoV infection. A recent study has identified SKP2 (S-phase kinase-associated protein 2) as an E3 ligase that promote the proteasomal degradation of the major autophagy regulator Beclin1 (Gassen et al. 2019). In this same study, it has been shown that the induction of autophagy by inhibiting SKP2 resulted in a significant reduction in the replication of MERS-CoV (Gassen et al. 2019). Taken together, it is reasonable to speculate that autophagy has an anti-viral role in MERS-CoV replication and hence it is downregulated upon infection with this CoV. Subsequently, countering this downregulation (i.e. inducing autophagy) can be detrimental to MERS-CoV replication as shown in Gassen et al. 2019. A key experiment in this context would be to investigate whether the induction of autophagy through other means (e.g. growth factors deprivation or inhibition of certain regulatory factors) would also result in a similar inhibition of MERS replication. Indeed, it has been shown that the inhibition of ERK/MAPK and PI3K/AKT/mTOR pathways (which are known to activate autophagy in their normal activated state) resulted in the inhibition of MERS-CoV replication (Kindrachuk et al. 2015).

5.2.3 Role of autophagy in SARS-CoV-2

In this study, BafA1 treatment of cells infected with SARS-CoV-2 led to a significant drop in the viral titer and viral N protein levels if the treatment was done 4 hours before the infection. On the other hand, the 8 hours post infection treatment did not result in any significant drop. This contradiction in SARS-CoV-2 replication between the two treatment conditions might be attributed to a possible impairment of the entry step of the virus when the cells are treated with BafA1 4 hours before infection. Indeed another compound, Chloroquine and its derivative hydroxychloroquine have also been shown to block SARS-CoV-2 replication in cellular models through the impairment of the TMPRSS2-independent entry step (Ou et al. 2021).

Chloroquine (and hydroxychloroquine) has been shown to block autophagy at the late step of autophagosome-lysosome fusion, resembling the mechanism of BafA1 inhibition of late autophagy (Mauthe et al. 2018; Edelstein, Venkatachalam, and Dong 2020). Nevertheless, a recent study has suggested that the autophagy as a process is dispensable for the replication of both SARS-CoV-2 and HCV and only certain autophagy factors are needed for both viruses replication (Twu et al. 2021). Indeed, the data in that study showed that both viruses exploit class III phosphatidylinositol 3-kinase (PI3K), a major factor needed for the formation of autophagosome, to generate the replicative DMVs (Twu et al. 2021). Hence, the blockage of late autophagy steps by Chloroquine or BafA1 might not be relevant to SARS-CoV-2 replication.

5.2.4 Is there a role for autophagy in CoV regulation? Integrating data from the study of the three viruses

Several studies have indicated that the replications of SARS-CoV and MHV were not affected by the deletion of key autophagy factors such as ATG 7 & 5, both of which are essential for the formation of the autophagosome (Schneider et al. 2012; Zijiang Zhao et al. 2007; Maity and Saha 2021). Moreover, the induction of autophagy resulted in no effect on the replication of MHV nor SARS-CoV (Schneider et al. 2012). These results point out a strain-specific exploitation or interaction of CoV with the autophagy factors. They might also indicate that the formation of the DMVs (and hence the formation of viral replication sites) does not necessary require an entire intact autophagy flux but rather certain autophagy components/factors would be sufficient depending on the CoV in question (Reggiori et al. 2010). Hence, it cannot be excluded that the inhibition of SARS-CoV-2 and HCoV-229E by BafA1 can be indeed understood (at least partially) as an effect of entry-step impairment rather than a direct effect of autophagy flux blocking. Consequently, the inhibition of both types of autophagy fluxes by thapsigargin can also be interpreted as a “by-product” of calcium gradient disruption. In this case, the disruption of autophagic flux does not directly or significantly contribute to the strong anti-viral effect of this compound.

Nevertheless, it has been shown that the deletion of Herp protein (also called HERPUD1) can upregulate autophagy flux and lead to a degradation of protein aggregates under proteasome inhibition and glucose starvation conditions (Quiroga et al. 2013). Hence, the induction of this protein seen in the mass spectrometry data with thapsigargin treatments (see results) might also indicate a pro-viral role of autophagy given the anti-viral state imposed by thapsigargin on the cells.

A possible limitation, complicating the interpretation of the data discussed in this section for MERS-CoV and SARS-CoV-2 (presented in figures 36 and 37 in the results section) was multiple technical difficulties. For instance, the highly cytotoxic MERS-CoV resulted in the death of the majority of cells in infected conditions (de Wilde et al. 2013). This created a major hurdle to obtain enough amount of proteins to investigate on a Western blot. This led, in some cases, to less effective detection of the bands by designated antibodies, and hence possibly underestimation of autophagy flux when calculating back the ratios. Moreover, the tendency of cells infected by MERS-CoV to form syncytia, a pathological multinucleate structure, adds another layer of complication in interpreting the data (Qian, Dominguez, and Holmes 2013b; Rajah et al. 2022)

Lastly, the handling of cellular lysates of experimental conditions infected by MERS-CoV and SARS-CoV-2 required lysing the cells in SDS buffer to inactivate the virus (details in the Methods section) before transporting them out of the BSL3 laboratory. The highly viscous lysates required a sonication step (three rounds on the bioruptur machine) that is not included (or needed) in case of HCoV-229E. Nevertheless, this sonication step did not yield any extra or unexpected bands upon investigating the lysates on Western blot.

Overall, the role of autophagy in viruses' replication is still highly debatable and can indeed be two-faced (pro- or anti-viral) depending on the virus family or even the strain, hence deeper investigation is needed for each of the viruses discussed in this study (Espert, Codogno, and Biard-Piechaczyk 2007; Zimmermann et al. 2021; Ahmad, Mostowy, and Sancho-Shimizu 2018).

5.3 The role of ATF3 in HCoV-229E infection

5.3.1 ATF3 knockdown in Huh7 cells in context of CoV replication

The stress-induced, activating transcription factor 3 (ATF3) has been shown to be implicated in multiple (patho)-physiological processes such as immunity, neuronal regeneration and various stress-related pathways including viral infection (Ku and Cheng 2020; Lindå, Sköld, and Ochsman 2011; Sood et al. 2017).

In this study, despite its strong induction by HCoV-229E infection, the CRISPR-CAS-9 –mediated knockdown of ATF3 in Huh7 cells did not affect the replication of the virus or any of the investigated host factors. In such a situation, it is tempting to explain this lack of phenotype because of a compensatory effect from another, closely related transcription regulator from the same family of factors. Most straightforward case would be functional redundancy by another AP-1 bHLH (basic helix-loop-helix) transcription factor that is expressed and inducible in Huh7 cells.

An alternative phenomenon is genetic compensation (or genetic adaptation) that has recently been reported as a (possibly) widespread event in response to a specific gene knockdown in several studies (El-Brolosy and Stainier 2017). Here, an incomplete genetic knockout that still allows the transcription of a truncated RNA, leads to compensatory transcriptional upregulation of a related gene (El-Brolosy et al. 2019; Kontarakis and Stainier 2020). This effect is lost, when the knockout is complete, i.e. does not result in any transcribed RNA (El-Brolosy et al. 2019; Sztal and Stainier 2020; Seroby et al. 2020; Kontarakis and Stainier 2020).

One prominent example of genetic compensation has been reported in mice lacking the ribosomal gene Rpl22 (O'Leary et al. 2013). The loss of Rpl22 did not result in any significant defects in translation as its function has been compensated by its paralogue, Rpl22l1 (O'Leary et al. 2013). Interestingly, the study has also shown that the paralogue protein is inhibited by Rpl22 under normal conditions (O'Leary et al. 2013).

Hence it is conceivable that classical CRISPR-Cas-9-mediated genome-editing which randomly introduces InDel mutations as in this study, results in an array of RNAs transcribed from the mutated ATF3 locus that activate some form of genetic compensation of this kind.

A possible work-around for this issue might be through employing a post-transcriptional, conditional and rapid loss of function approach such as auxin-inducible degron technology (Shetty, Reim, and Winston 2019). This technology depends on tagging a protein with a destabilizing domain referred to as degron (Yesbolatova et al. 2020). This tag will induce rapid degradation of the protein fused with it, conditionally as function of a ligand concentration (in this case, auxin) (Yesbolatova et al. 2020; Natsume et al. 2016). Such a technology might allow for a fast and dynamic assessment of protein functions without being hindered by the slow rate of depletion, or a possible, subsequent activation of difficult to assess compensatory responses associated with conventional loss of function methods. One key advantage of conditional degrons system is its reversibility and hence, the specificity of any phenotype can be confirmed upon re-expression of the targeted protein (Yesbolatova et al. 2020).

In addition to that, it is important to point out that the knockdown of ATF3 was only partial and traces of an induced ATF3 protein band can still be seen upon HCoV-229E infection on Western blot. This remaining amount of protein can be indeed enough to perform the supposed role of this factor or activate a possible feedback/compensatory mechanism.

Alternatively, the lack of phenotype of ATF3 KD on CoV replication can be seen as a cell-model specific peculiarity. Indeed, a study that has been conducted in bone marrow derived macrophages (BMDMs) has indicated a major involvement of ATF3 in modulating the levels of IFN β (basal or induced) in these cells (Labzin et al. 2015). The mechanism through which ATF3 carried out this function was through acting as a transcription repressor binding to a regulatory site in the *Ifnb1* gene promoter (Labzin et al. 2015). The study has also showed that the deletion of ATF3 in macrophages reduced viral infection of both lymphocytic choriomeningitis virus and vesicular stomatitis virus (Labzin et al. 2015). Hence, a pro-viral role of ATF3 induction in this cellular model against these two viruses can be established. Moreover, another study has indicated that the replication of Hepatitis C virus (HCV) is much more receptive to IFN γ treatment in Huh7, as opposite to Huh6 cells (Grünvogel et al. 2015). Pointing out again the peculiarity of different cellular models and the importance of choosing a cellular model that is suitable for a particular research question.

Integrating these studies together with data presented here from ATF3 KD, it cannot be excluded that the role of ATF3 in CoV replication is relevant (and phenotypic) only when investigated in an animal model or different cellular model. Additionally, the current study looked only at a handful of possibly ATF3-regulated host factors using Western blotting. Therefore, a very relevant (and phenotypic) role of ATF3 in regulating host gene response, through regulating chromatin accessibility or expression of gene networks, cannot be excluded. Hence, assessing the role of ATF3 in CoV replication and host response using other methods such as ChIPseq or BioID might be indeed an important next step.

5.3.2 Interactome studies using BioID method

5.3.2.1 Attempts to study the interactome of several ER factors using BioID method

The literature on ATF3-regulating networks and pathways is relatively limited (Jadhav and Zhang 2017). One aim of this study was to try to unravel partner proteins of ATF3 using the BioID method. Initial attempt to study the interactome of ATF3 (and other UPR factors, including PERK) has been made using the biotin ligase BirA. Nevertheless, this approach did not come to fruition due to multiple possible limitations that are related to the choice of biotin ligase itself or the bait protein.

For instance, it has been reported in multiple studies that BirA ligase is less efficient at temperatures lower than 37°C and in certain cellular compartments such as the ER (D. I. Kim et al. 2016; May et al. 2020). This rendered this biotin ligase inefficient for experiments that included HCoV-229E infection, as they were carried out at 33°C. Hence, the decision was to opt out for another, more efficient ligase, the miniTurbo biotin ligase (Branon et al. 2018).

The miniTurbo biotin ligase has proven to be much more efficient at 33°C for the miniTurbo-ATF3 construct, as seen in the biotinylation pattern in the results section. Nevertheless, the miniTurbo-PERK construct at 33°C constantly showed a reduced, inefficient biotinylation pattern when compared to the empty vector control or the miniTurbo-ATF3 construct. This led to speculate that the issue might be the bait protein itself (including the size of the protein and its three dimensional structure) or the generated bait + ligase construct rather than the ligase alone. For instance, the tagging of particular baits with the ligase might result in a mal-folded chimeric protein that is unable to function and behave in a way similar to the endogenous bait. The mal-folding hypothesis of this chimeric protein can also be used to explain the fact that the MYC (for BirA-PERK) or HA (for miniTurbo-PERK) tags were both undetectable on immunoblot. Moreover, the length of the linker sequence between the ligase and the bait protein plays an important role (D. I. Kim et al. 2016). In the case of both miniTurbo-PERK and BirA-PERK, the ligase was fused directly to the bait (i.e: a polylinker length of zero). Hence, future optimization of the length of this linker in the miniTurbo-PERK and BirA-PERK constructs might improve the efficiency of biotinylation.

A further expansion for optimizing these constructs might also involve comparing the biotinylation efficiency and localization of the chimeric protein when the same ligase is fused to the bait protein at its two different termini (N- or C- terminal tagging) (Mair et al. 2019; Xiaonan Liu et al. 2020). Moreover, the addition of a fluorophore to the biotin ligase constructs, as carried out in Mair et al. 2019, can be very important and a quick way to investigate the levels of the construct expression and its localization (Mair et al. 2019). Nevertheless, the authors of that study noted that this approach might also compromise biotinylation efficiency or the normal functioning of the bait protein. Finally, the

localization of PERK in the ER membrane might play an important factor in reducing the efficiency of biotinylation (Branon et al. 2018; May et al. 2020; D. I. Kim et al. 2016).

With the many hurdles discussed above that surrounded working with the miniTurbo-PERK construct, it was decided to leave it out from further experimentations. On the other hand, the miniTurbo-ATF3 construct showed promising biotinylation pattern. Hence, the biotinylated proteins (interactors) by this construct were sent to mass spectrometry for identification and analysis.

5.3.2.2 Studying the interactome of ATF3 using BioID method

A first striking observation of the mass spectrometry analysis was the large number of pulled down proteins (more than five thousands). This unexpected observation cannot be attributed to technical issues/failures in the pulldown or washing steps of the BioID protocol as the negative controls lacking the induction with doxycycline or exogenous biotin addition showed minimal number of pulled down proteins. Of note, multiple studies indicated a very rapid action of the miniTurbo ligase, sometimes within 10 minutes of exogenous biotin addition (Branon et al. 2018; Y. Zhang et al. 2019). In this present study, the intention behind adding biotin for 24 hours was to pulldown interacting proteins throughout the whole period of infection with HCoV-229E. Hence, it could not be excluded that this prolonged activation of the ligase resulted in a saturating effect. This effect would be caused from re-itering cycles of binding and release of interactors, causing very efficient biotinylation of one specific binding partner. Both, the miniTurbo ligase only and the miniTurbo-ATF3 are relatively small proteins, hence, they could be considered as mobile proteins, which stochastically can contact multiple intracellular factors. Hence, prolonged labelling times with biotin might result in significant protein intensities of “unphysiological substrates” in the pulldown experiments above background. Nevertheless, the miniTurbo-ATF3 behaviour is most likely similar (or approaching) to that of the endogenous ATF3 protein while the ligase only protein has uncharacterized (unspecific?) behavior. Hence, the comparison between ligase only (EV) vs ATF3 with or without infection yielded a relatively reasonable number of significant interactors of ATF3 (185 and 129 proteins respectively) with the indicated selection criteria.

To control for this issue, an experiment comparing pulled down proteins from conditions with exogenous biotin being added for varying lengths of time might be important. Moreover, the suggestion by Mair et al. 2019 for an additional control condition with the ligase only construct targeted to the compartment of interest (in this case the nucleus) might also help root out unspecific interactors. Nevertheless, one should not solely rely on such a control as it inherently assume that the presence (and hence interactors) of a certain protein is limited only to a certain compartment based on the known literature (which is not the case for many transcription factors including ATF2). Hence, such assumption might exclude the possibility of discovering authentic interactions or novel functions of protein of interest in other subcellular areas.

With this saturating effect, performing statistical analysis using stringent criteria did not yield any differential (or enriched) interactors of miniTurbo-ATF3 construct when compared to the empty vector control. Nevertheless, lowering the stringency of the effect size (i.e. the ratio of differential protein expression) and the statistical analysis (p values of $-\log_{10}(p) \geq 1.3$) and relying solely on the p values rather than the false discovery rate (FDR), yielded a plethora of interactors. These interactors mostly mapped to the nucleus hinting at a correct localization of the construct. In addition, several known interactors of ATF3 (e.g. p53, ATF2 and JUND) were uncovered after this analysis, serving as a good indicator of the reliability of the used statistical analysis (Yan and Boyd 2006; Hein et al. 2015; Huttlin et al. 2017).

CEBPD (CCAAT/enhancer-binding protein delta), which was one of the top interactors of ATF3 in the BioID screens, is a bZIP transcription factor with many important roles related to the regulation of genes involved in immune and inflammatory responses and also as an early ER stress effector and autophagy regulator in breast cancer cells (Ko, Chang, and Wang 2015; Ullmann et al. 2021; Sheshadri, Sharan, and Sterneck 2017). Additionally, this transcription factor has been reported to significantly enhance the phagocytic ability of macrophages during *A. fumigatus conidia* infection (L. Liu et al. 2022). Though the same transcription factor has been reported in an independent study to inhibit macrophage-mediated phagocytosis of dying neuron cells (Ko et al. 2012). A study conducted in macrophages relying on systems biology followed by experimental validations indicated that ATF3 is part of a regulatory network that involves NF- κ B and C/EBP δ (CEBPD) (Litvak et al. 2009). This network controls the expression of multiple inflammatory genes including CEBPD and discriminates between transient and prolonged Toll-like receptor 4-induced signals (Litvak et al. 2009). TLR4 ligands are prototypical activators of the NF- κ B pathway and of cytokine production leading to the activation of the innate immune system (Vaure and Liu 2014, 4). The role of ATF3 in the network uncovered by Litvak et al was to repress the transcription of CEBPD at later time point after the induction of TLR4. The additional layer of protein-protein interaction uncovered between these two proteins in this thesis makes an interesting observation that needs first to be validated and second to be corroborated at the functional level. For example, these results can also be used as a basis to further study the mRNA and protein levels of CEBPD in ATF3 KD Huh7 cells as well as the genome-wide chromatin recruitment of both transcription factors to enhancers or promoters to find out if they co-occupy coronavirus-regulated genomic regions under infection conditions.

Another interactor uncovered by this current study was a transcriptional repressor called THAP domain-containing protein 11 (THAP11). This factor has been reported to have strong similarities with the site-specific DNA-binding domain (DBD) of *Drosophila* P element transposase (Roussigne et al. 2003). THAP11 belongs to a family of Thanatos-associated proteins (THAP) that are involved in multiple cellular processes including chromatin modification, cell proliferation and transcriptional regulation (C.-Y. Zhu et al. 2009). THAP11 in particular has been shown to be involved in embryogenesis, ES cell

pluripotency and repressing the proliferation of cancer cells (C.-Y. Zhu et al. 2009). Parkin is an E3 ubiquitin ligase that promotes mitophagy (this is autophagy of damaged mitochondria) by ubiquitinating mitochondrial proteins (Potting et al. 2018). Interestingly, a genome-wide CRISPR screen identified a network of regulators including THAP11 as a major repressor of Parkin (Potting et al. 2018). Moreover, it has been recently shown that SARS-CoV-2 causes extensive damage and impairment of mitophagy (Shang et al. 2022). The same study also indicated a localization of dsRNA of the virus in the mitochondria and hence possibly active replication of the virus in there. Therefore, the protein-protein interaction between THAP11 and ATF3 might represent a novel layer of mitophagy and mitochondrial quality control (MQC) regulation in context of CoV replication if confirmed to be authentic.

Furthermore, ATF2, a member of the same family and a known interactor of ATF3, that is involved in multiple crucial signaling pathways including inflammation, oncogenesis and apoptosis (Yu et al. 2014; Jurida et al. 2015). ATF2 has been previously shown to localize to the mitochondrial membrane and play an important role in mitochondrial membrane potential maintenance (Lau and Ronai 2012). ATF2 and multiple solute carrier family (SLC) proteins including SLC25A5, which are known to localize to the mitochondrial membrane, has been uncovered as interactors of ATF3 in this study. Hence, the interaction between ATF3 and ATF2 or SLC25A5 might offer a recruitment mechanism and provide an explanation for the functional relevance of ATF3 in the mitochondrial membrane processes/homeostasis upon CoV infection. In particular, SLC25A5 is known to be a mediator of importing ADP to the mitochondrial matrix and exporting ATP to the cytoplasm (Gutiérrez-Aguilar and Baines 2013). Hence, if this interaction is confirmed to be authentic, it might suggest a role of ATF3 in controlling specific parts of the cellular energy metabolism upon CoV infection.

To further prove this hypothesis, it will be important to confirm the localization of ATF3 in or close to the mitochondrial membrane (or matrix) upon CoV infection. This can be done, for instance, by ectopically expressing an ATF3 construct tagged with green fluorescent protein (GFP), by tagging the endogenous ATF3 gene using genome-editing, or through monitoring the translocation of this protein using immunofluorescence staining combined with mitochondrial markers.

Furthermore, confirming individual interactors using orthogonal protein-protein interaction validation methods can increase the confidence in the BioID data. One such method is proximity ligation assay (PLA). The method relies on two primary antibodies (raised in different animal species) targeting the two proteins under investigation. Secondary antibodies with ssDNA can then be added and bind to the primary ones. If the two proteins under investigation are indeed in close proximity to each other, a rolling cycle DNA synthesis reaction would start (in the presence of oligonucleotides and other relevant enzymes) leading to the formation of a platform for fluorescent dyes to hybridize and then to be visualized by fluorescence microscopy (Mayr-Buro et al. 2019). This approach could, for example, be combined with (immune-) fluorescence staining of mitochondrial markers to prove a possible colocalization of specific ATF3 heterodimers to the mitochondria as discussed above.

Lastly, the strong induction of ATF3 by HCoV-229E infection can be interpreted as a pro-viral mechanism that is suppressing a (cell intrinsic) defense mechanism or the activation of an innate immune response by factors released from the infected cells (Jadhav and Zhang 2017; Sood et al. 2017; Labzin et al. 2015; De Nardo et al. 2014). A prominent example of such inhibitory effect of ATF3 on the innate immune system was described as part of the anti-inflammatory state imposed on macrophages by High density lipoprotein (HDL) (De Nardo et al. 2014). In that study, the authors proved that the suppression of pro-inflammatory cytokines by HDL was on the transcriptional level (De Nardo et al. 2014). To this end, the study utilized transcriptomic and ChIP-seq approaches to identify ATF3-dependent, HDL-regulated gene networks and several major pro-inflammatory genes targeted by ATF3 upon HDL treatment (De Nardo et al. 2014). Why certain host factors such as ATF3 are upregulated during the infection (despite the global translational shut-down), and how this is executed at the mechanistic level, is not known. It is also unclear, if CoV express a protein that can directly “activate” ATF3, i.e. by post-translational modification.

5.4 Limitations of the study and outlook

The results from the current study offer new and more in-depth insights into pathways involved in CoV replication and host response with a focus on ER and UPR roles in this process. Nevertheless, as with any experimental scientific study, this work has its own, intrinsic limitations that need to be acknowledged. Perhaps the most prominent limitation of this study is the usage of cell culture models to study the virus replication and host response. Although cellular models are widely used and have produced enormous amount of data and knowledge, they only represent (loose) approximation of the actual (patho)-physiological states associated with a viral infection (Mead and Karp 2019). For instance, the inhibitory effect of thapsigargin on CoV replication needs to be rigorously tested in pre-clinical and clinical settings including careful consideration for the dosage and treatment period. Hence, confirming the main findings in a more physiologically relevant model can be of utter most importance. Such models might include organoids or animal models (J. Kim, Koo, and Knoblich 2020; Lamers et al. 2021).

Moreover, the conclusions drawn from the bioinformatics analysis of the mass spectrometry data throughout this study are only preliminary and serve as hypothesis generating strategy. Deep and solid mechanistic insights need further experimentations and confirmation. In particular, the experimental design of the ATF3 BioID experiment can be improved upon to account for biotinylation efficiency of the miniTurbo biotin ligase. For instance, shorter biotinylation times can be considered at different stages of the virus infection.

Furthermore, the investigation of the effect of ATF3 KD on host response was limited to few factors. Hence a more thorough investigation of the possibly deregulated proteins is needed possibly using a mass spectrometry approach, RNA sequencing or ChIPsequencing.

Finally, the findings in this study answer some and open the doors for more questions related to the role of ER, UPR, ER stress, autophagy, ERAD and individual factors such as ATF3 and PERK in the replication of CoV and host response. Addressing these new questions including additional, more complex biological model systems with focused experiments (as delineated and suggested throughout the results and discussion sections) is the outlook of this study. Figure 63 summarizes the main findings of this study.

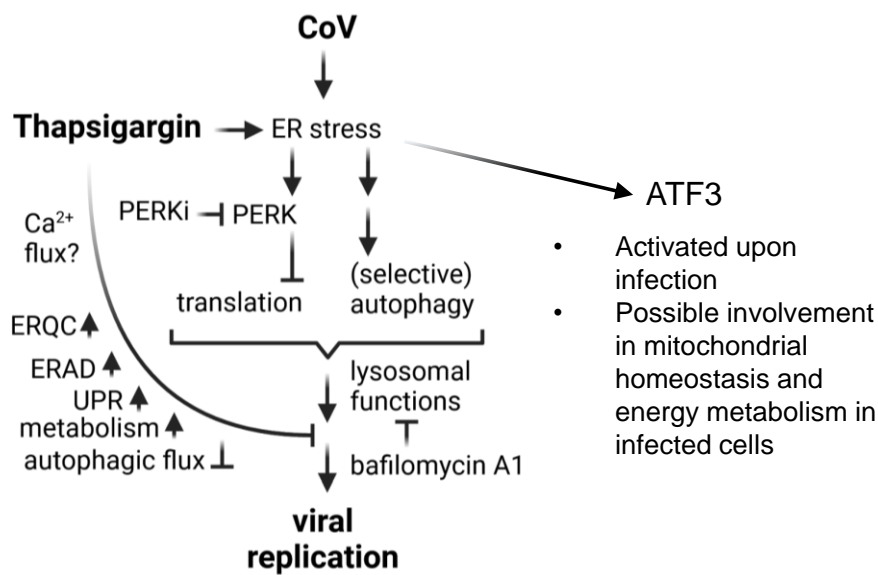


Figure 63: Summary of the newly uncovered findings in this study.

A schematic representation of the different pathways and factors that have been uncovered in this study to be possibly involved in the replication of CoV (including PERK pathways, autophagy and ATF3) and the antiviral effect of thapsigargin. PERKi: GSK2656157 or GSK2606414; ERQC: ER quality control; ERAD: ER-associated protein degradation. The figure was adapted from figure 2 Shaban et al, 2022 Elsevier (Shaban, Mayr-Buro, et al. 2022).

Literature

- Adams, Christopher J., Megan C. Kopp, Natacha Larburu, Piotr R. Nowak, and Maruf M. U. Ali. 2019. "Structure and Molecular Mechanism of ER Stress Signaling by the Unfolded Protein Response Signal Activator IRE1." *Frontiers in Molecular Biosciences* 6. <https://www.frontiersin.org/articles/10.3389/fmolb.2019.00011>.
- Ahmad, Liyana, Serge Mostowy, and Vanessa Sancho-Shimizu. 2018. "Autophagy-Virus Interplay: From Cell Biology to Human Disease." *Frontiers in Cell and Developmental Biology* 6. <https://www.frontiersin.org/article/10.3389/fcell.2018.00155>.
- Akimov, Vyacheslav, Inigo Barrio-Hernandez, Sten V. F. Hansen, Philip Hallenborg, Anna-Kathrine Pedersen, Dorte B. Bekker-Jensen, Michele Puglia, et al. 2018. "UbiSite Approach for Comprehensive Mapping of Lysine and N-Terminal Ubiquitination Sites." *Nature Structural & Molecular Biology* 25 (7): 631–40. <https://doi.org/10.1038/s41594-018-0084-y>.
- Alasiri, Glowii, Yannasittha Jiramongkol, Sasanan Trakansuebkul, Hui-Ling Ke, Zimam Mahmud, Kittu Intuyod, and Eric W. -F. Lam. 2020. "Reciprocal Regulation between GCN2 (EIF2AK4) and PERK (EIF2AK3) through the JNK-FOXO3 Axis to Modulate Cancer Drug Resistance and Clonal Survival." *Molecular and Cellular Endocrinology* 515 (September): 110932. <https://doi.org/10.1016/j.mce.2020.110932>.
- Amarante-Mendes, Gustavo P., Sandy Adjemian, Laura Migliari Branco, Larissa C. Zanetti, Ricardo Weinlich, and Karina R. Bortoluci. 2018. "Pattern Recognition Receptors and the Host Cell Death Molecular Machinery." *Frontiers in Immunology* 9. <https://www.frontiersin.org/articles/10.3389/fimmu.2018.02379>.
- Araki, Kazutaka, and Kazuhiro Nagata. 2011. "Protein Folding and Quality Control in the ER." *Cold Spring Harbor Perspectives in Biology* 3 (11): a007526. <https://doi.org/10.1101/cshperspect.a007526>.
- Aviner, Ranen. 2020. "The Science of Puromycin: From Studies of Ribosome Function to Applications in Biotechnology." *Computational and Structural Biotechnology Journal* 18: 1074–83. <https://doi.org/10.1016/j.csbj.2020.04.014>.
- Avivar-Valderas, Alvaro, Eduardo Salas, Ekaterina Bobrovnikova-Marjon, J. Alan Diehl, Chandandeep Nagi, Jayanta Debnath, and Julio A. Aguirre-Ghiso. 2011. "PERK Integrates Autophagy and Oxidative Stress Responses To Promote Survival during Extracellular Matrix Detachment." *Molecular and Cellular Biology* 31 (17): 3616–29. <https://doi.org/10.1128/MCB.05164-11>.
- Baer, Alan, and Kylene Kehn-Hall. 2014. "Viral Concentration Determination through Plaque Assays: Using Traditional and Novel Overlay Systems." *Journal of Visualized Experiments: JoVE*, no. 93 (November): e52065. <https://doi.org/10.3791/52065>.
- Bailey, Orville T., Alwin M. Pappenheimer, F. Sargent Cheever, and Joan B. Daniels. 1949. "A MURINE VIRUS (JHM) CAUSING DISSEMINATED ENCEPHALOMYELITIS WITH EXTENSIVE DESTRUCTION OF MYELIN." *The Journal of Experimental Medicine* 90 (3): 195–212.
- Bain, Jenny, Lorna Plater, Matt Elliott, Natalia Shpiro, C. James Hastie, Hilary McLauchlan, Iva Klevernic, J. Simon C. Arthur, Dario R. Alessi, and Philip Cohen. 2007. "The Selectivity of Protein Kinase Inhibitors: A Further Update." *The Biochemical Journal* 408 (3): 297–315. <https://doi.org/10.1042/BJ20070797>.
- Benedetti, Rossella, Maria Anele Romeo, Andrea Arena, Maria Saveria Gilardini Montani, Livia Di Renzo, Gabriella D'Orazi, and Mara Cirone. 2022. "ATF6 Prevents DNA Damage and Cell Death in Colon Cancer Cells Undergoing ER Stress." *Cell Death Discovery* 8 (1): 1–12. <https://doi.org/10.1038/s41420-022-01085-3>.
- Bergmann, Timothy J., Ilaria Fregno, Fiorenza Fumagalli, Andrea Rinaldi, Francesco Bertoni, Paul J. Boersema, Paola Picotti, and Maurizio Molinari. 2018. "Chemical Stresses Fail to Mimic the Unfolded Protein Response Resulting from Luminal Load with Unfolded Polypeptides." *The Journal of Biological Chemistry* 293 (15): 5600–5612. <https://doi.org/10.1074/jbc.RA117.001484>.

- Braakman, Ineke, and Daniel N. Hebert. 2013. "Protein Folding in the Endoplasmic Reticulum." *Cold Spring Harbor Perspectives in Biology* 5 (5): a013201. <https://doi.org/10.1101/cshperspect.a013201>.
- Bradford, Marion M. 1976. "A Rapid and Sensitive Method for the Quantitation of Microgram Quantities of Protein Utilizing the Principle of Protein-Dye Binding." *Analytical Biochemistry* 72 (1): 248–54. [https://doi.org/10.1016/0003-2697\(76\)90527-3](https://doi.org/10.1016/0003-2697(76)90527-3).
- Branon, Tess C., Justin A. Bosch, Ariana D. Sanchez, Namrata D. Udeshi, Tanya Svinkina, Steven A. Carr, Jessica L. Feldman, Norbert Perrimon, and Alice Y. Ting. 2018. "Efficient Proximity Labeling in Living Cells and Organisms with TurboID." *Nature Biotechnology* 36 (9): 880–87. <https://doi.org/10.1038/nbt.4201>.
- Brant, Ayslan Castro, Wei Tian, Vladimir Majerciak, Wei Yang, and Zhi-Ming Zheng. 2021. "SARS-CoV-2: From Its Discovery to Genome Structure, Transcription, and Replication." *Cell & Bioscience* 11 (1): 136. <https://doi.org/10.1186/s13578-021-00643-z>.
- Brunelle, Erica, Anh Minh Le, Crystal Huynh, Kelly Wingfield, Lenka Halámková, Juliana Agudelo, and Jan Halámek. 2017. "Coomassie Brilliant Blue G-250 Dye: An Application for Forensic Fingerprint Analysis." *Analytical Chemistry* 89 (7): 4314–19. <https://doi.org/10.1021/acs.analchem.7b00510>.
- Casais, Rosa, Volker Thiel, Stuart G. Siddell, David Cavanagh, and Paul Britton. 2001. "Reverse Genetics System for the Avian Coronavirus Infectious Bronchitis Virus." *Journal of Virology* 75 (24): 12359–69. <https://doi.org/10.1128/JVI.75.24.12359-12369.2001>.
- Chan, Shiu-Wan. 2014. "The Unfolded Protein Response in Virus Infections." *Frontiers in Microbiology* 5 (September): 518. <https://doi.org/10.3389/fmicb.2014.00518>.
- Chang, Tsun-Kai, David A. Lawrence, Min Lu, Jenille Tan, Jonathan M. Harnoss, Scot A. Marsters, Peter Liu, Wendy Sandoval, Scott E. Martin, and Avi Ashkenazi. 2018. "Coordination between Two Branches of the Unfolded Protein Response Determines Apoptotic Cell Fate." *Molecular Cell* 71 (4): 629–636.e5. <https://doi.org/10.1016/j.molcel.2018.06.038>.
- Chen, Ying, Qi Li, Qihang Li, Shuaishuai Xing, Yang Liu, Yijun Liu, Yao Chen, Wenyan Liu, Feng Feng, and Haopeng Sun. 2020. "P62/SQSTM1, a Central but Unexploited Target: Advances in Its Physiological/Pathogenic Functions and Small Molecular Modulators." *Journal of Medicinal Chemistry* 63 (18): 10135–57. <https://doi.org/10.1021/acs.jmedchem.9b02038>.
- Cheng, Vincent C. C., Susanna K. P. Lau, Patrick C. Y. Woo, and Kwok Yung Yuen. 2007. "Severe Acute Respiratory Syndrome Coronavirus as an Agent of Emerging and Reemerging Infection." *Clinical Microbiology Reviews* 20 (4): 660–94. <https://doi.org/10.1128/CMR.00023-07>.
- Choi, Younho, James W. Bowman, and Jae U. Jung. 2018. "Autophagy during Viral Infection — a Double-Edged Sword." *Nature Reviews Microbiology* 16 (6): 341–54. <https://doi.org/10.1038/s41579-018-0003-6>.
- Chu, Hin, Huiping Shuai, Yuxin Hou, Xi Zhang, Lei Wen, Xiner Huang, Bingjie Hu, et al. 2021. "Targeting Highly Pathogenic Coronavirus-Induced Apoptosis Reduces Viral Pathogenesis and Disease Severity." *Science Advances* 7 (25): eabf8577. <https://doi.org/10.1126/sciadv.abf8577>.
- Ciechomska, I. A., K. Gabrusiewicz, A. A. Szczepankiewicz, and B. Kaminska. 2013. "Endoplasmic Reticulum Stress Triggers Autophagy in Malignant Glioma Cells Undergoing Cyclosporine A-Induced Cell Death." *Oncogene* 32 (12): 1518–29. <https://doi.org/10.1038/onc.2012.174>.
- Clemens, M. J. 2001. "Initiation Factor EIF2 Alpha Phosphorylation in Stress Responses and Apoptosis." *Progress in Molecular and Subcellular Biology* 27: 57–89. https://doi.org/10.1007/978-3-662-09889-9_3.
- Cohen-Kaplan, Victoria, Ido Livneh, Noa Avni, Bertrand Fabre, Tamar Ziv, Yong Tae Kwon, and Aaron Ciechanover. 2016. "P62- and Ubiquitin-Dependent Stress-Induced Autophagy of the Mammalian 26S Proteasome." *Proceedings of the National Academy of Sciences* 113 (47): E7490–99. <https://doi.org/10.1073/pnas.1615455113>.
- "Consensus Document on the Epidemiology of Severe Acute Respiratory Syndrome (SARS)." n.d. Accessed November 3, 2022. [https://www.who.int/publications-detail-redirect/consensus-document-on-the-epidemiology-of-severe-acute-respiratory-syndrome-\(-sars\)](https://www.who.int/publications-detail-redirect/consensus-document-on-the-epidemiology-of-severe-acute-respiratory-syndrome-(-sars)).
- Cortese, Mirko, Ji-Young Lee, Berati Cerikan, Christopher J. Neufeldt, Viola M. J. Oorschot, Sebastian Köhrer, Julian Hennies, et al. 2020. "Integrative Imaging Reveals SARS-CoV-2-

- Induced Reshaping of Subcellular Morphologies.” *Cell Host & Microbe* 28 (6): 853-866.e5. <https://doi.org/10.1016/j.chom.2020.11.003>.
- Cottam, Eleanor M, Helena J Maier, Maria Manifava, Laura C Vaux, Priya Chandra-Schoenfelder, Wilhelm Gerner, Paul Britton, Nick T Ktistakis, and Tom Wileman. 2011. “Coronavirus Nsp6 Proteins Generate Autophagosomes from the Endoplasmic Reticulum via an Omegasome Intermediate.” *Autophagy* 7 (11): 1335–47. <https://doi.org/10.4161/auto.7.11.16642>.
- Cox, J. S., and P. Walter. 1996. “A Novel Mechanism for Regulating Activity of a Transcription Factor That Controls the Unfolded Protein Response.” *Cell* 87 (3): 391–404. [https://doi.org/10.1016/s0092-8674\(00\)81360-4](https://doi.org/10.1016/s0092-8674(00)81360-4).
- Crotzer, Victoria L, and Janice S Blum. 2010. “Autophagy and Adaptive Immunity.” *Immunology* 131 (1): 9–17. <https://doi.org/10.1111/j.1365-2567.2010.03321.x>.
- Cui, Wenjun, Jingzhi Li, David Ron, and Bingdong Sha. 2011. “The Structure of the PERK Kinase Domain Suggests the Mechanism for Its Activation.” *Acta Crystallographica Section D: Biological Crystallography* 67 (Pt 5): 423–28. <https://doi.org/10.1107/S0907444911006445>.
- Danzi, Matt C., Saloni T. Mehta, Kireeti Dulla, Giulia Zunino, Daniel J. Cooper, John L. Bixby, and Vance P. Lemmon. 2018. “The Effect of Jun Dimerization on Neurite Outgrowth and Motif Binding.” *Molecular and Cellular Neuroscience* 92 (October): 114–27. <https://doi.org/10.1016/j.mcn.2018.08.001>.
- Davies, S. P., H. Reddy, M. Caivano, and P. Cohen. 2000. “Specificity and Mechanism of Action of Some Commonly Used Protein Kinase Inhibitors.” *The Biochemical Journal* 351 (Pt 1): 95–105. <https://doi.org/10.1042/0264-6021:3510095>.
- De Nardo, Dominic, Larisa I. Labzin, Hajime Kono, Reiko Seki, Susanne V. Schmidt, Marc Beyer, Dakang Xu, et al. 2014. “High-Density Lipoprotein Mediates Anti-Inflammatory Reprogramming of Macrophages via the Transcriptional Regulator ATF3.” *Nature Immunology* 15 (2): 152–60. <https://doi.org/10.1038/ni.2784>.
- Dey, Madhusudan, Brian Rick Mann, Ashish Anshu, and M. Amin-ul Mannan. 2014. “Activation of Protein Kinase PKR Requires Dimerization-Induced Cis-Phosphorylation within the Activation Loop.” *The Journal of Biological Chemistry* 289 (9): 5747–57. <https://doi.org/10.1074/jbc.M113.527796>.
- Dikic, Ivan, and Zvulun Elazar. 2018. “Mechanism and Medical Implications of Mammalian Autophagy.” *Nature Reviews Molecular Cell Biology* 19 (6): 349–64. <https://doi.org/10.1038/s41580-018-0003-4>.
- Donnelly, Neysan, Adrienne M. Gorman, Sanjeev Gupta, and Afshin Samali. 2013. “The EIF2 α Kinases: Their Structures and Functions.” *Cellular and Molecular Life Sciences: CMLS* 70 (19): 3493–3511. <https://doi.org/10.1007/s00018-012-1252-6>.
- Drexler, Hans G., and Cord C. Uphoff. 2002. “Mycoplasma Contamination of Cell Cultures: Incidence, Sources, Effects, Detection, Elimination, Prevention.” *Cytotechnology* 39 (2): 75–90. <https://doi.org/10.1023/A:1022913015916>.
- Duve, C. de, B. C. Pressman, R. Gianetto, R. Wattiaux, and F. Appelmans. 1955. “Tissue Fractionation Studies. 6. Intracellular Distribution Patterns of Enzymes in Rat-Liver Tissue.” *Biochemical Journal* 60 (4): 604–17.
- Echavarría-Consuegra, Liliana, Georgia M. Cook, Idoia Busnadiego, Charlotte Lefèvre, Sarah Keep, Katherine Brown, Nicole Doyle, et al. 2021. “Manipulation of the Unfolded Protein Response: A Pharmacological Strategy against Coronavirus Infection.” *PLOS Pathogens* 17 (6): e1009644. <https://doi.org/10.1371/journal.ppat.1009644>.
- Edelstein, Charles L., Manjeri A. Venkatachalam, and Zheng Dong. 2020. “Autophagy Inhibition by Chloroquine and Hydroxychloroquine Could Adversely Affect Acute Kidney Injury and Other Organ Injury in Critically Ill Patients with COVID-19.” *Kidney International* 98 (1): 234–35. <https://doi.org/10.1016/j.kint.2020.05.001>.
- El-Brolosy, Mohamed A., Zacharias Kontarakis, Andrea Rossi, Carsten Kuenne, Stefan Günther, Nana Fukuda, Khrievono Kikhi, et al. 2019. “Genetic Compensation Triggered by Mutant mRNA Degradation.” *Nature* 568 (7751): 193–97. <https://doi.org/10.1038/s41586-019-1064-z>.
- El-Brolosy, Mohamed A., and Didier Y. R. Stainier. 2017. “Genetic Compensation: A Phenomenon in Search of Mechanisms.” *PLoS Genetics* 13 (7): e1006780. <https://doi.org/10.1371/journal.pgen.1006780>.

- Engedal, Nikolai, Maria L Torgersen, Ingrid J Guldvik, Stefan J Barfeld, Daniela Bakula, Frank Sætre, Linda K Hagen, et al. 2013. "Modulation of Intracellular Calcium Homeostasis Blocks Autophagosome Formation." *Autophagy* 9 (10): 1475–90. <https://doi.org/10.4161/auto.25900>.
- Espert, Lucile, Patrice Codogno, and Martine Biard-Piechaczyk. 2007. "Involvement of Autophagy in Viral Infections: Antiviral Function and Subversion by Viruses." *Journal of Molecular Medicine (Berlin, Germany)* 85 (8): 811. <https://doi.org/10.1007/s00109-007-0173-6>.
- Fan, Li, Xianlin Yang, Jian Du, MARK MARSHALL, Kerry Blanchard, and Xiang Ye. 2005. "A Novel Role of P38 α MAPK in Mitotic Progression Independent of Its Kinase Activity." *Cell Cycle* 4 (11): 1616–24. <https://doi.org/10.4161/cc.4.11.2125>.
- Fang, Xiaonan, Jinrong Gao, Hong Zheng, Baozong Li, Lingbao Kong, Yijuan Zhang, Wei Wang, Yingchun Zeng, and Linbai Ye. 2007. "The Membrane Protein of SARS-CoV Suppresses NF-KappaB Activation." *Journal of Medical Virology* 79 (10): 1431–39. <https://doi.org/10.1002/jmv.20953>.
- Feng, Yuchen, Ding He, Zhiyuan Yao, and Daniel J. Klionsky. 2014. "The Machinery of Macroautophagy." *Cell Research* 24 (1): 24–41. <https://doi.org/10.1038/cr.2013.168>.
- Filén, Sanna, Emmi Ylikoski, Subhash Tripathi, Anne West, Mari Björkman, Joel Nyström, Helena Ahlfors, et al. 2010. "Activating Transcription Factor 3 Is a Positive Regulator of Human IFNG Gene Expression." *Journal of Immunology (Baltimore, Md.: 1950)* 184 (9): 4990–99. <https://doi.org/10.4049/jimmunol.0903106>.
- Finkel, Yaara, Orel Mizrahi, Aharon Nachshon, Shira Weingarten-Gabbay, David Morgenstern, Yfat Yahalom-Ronen, Hadas Tamir, et al. 2021. "The Coding Capacity of SARS-CoV-2." *Nature* 589 (7840): 125–30. <https://doi.org/10.1038/s41586-020-2739-1>.
- Forester, Craig M., Qian Zhao, Nancy J. Phillips, Anatoly Urisman, Robert J. Chalkley, Juan A. Oses-Prieto, Li Zhang, Davide Ruggero, and Alma L. Burlingame. 2018. "Revealing Nascent Proteomics in Signaling Pathways and Cell Differentiation." *Proceedings of the National Academy of Sciences* 115 (10): 2353–58. <https://doi.org/10.1073/pnas.1707514115>.
- Fung, To S., and Ding X. Liu. 2014. "Coronavirus Infection, ER Stress, Apoptosis and Innate Immunity." *Frontiers in Microbiology* 5: 296. <https://doi.org/10.3389/fmicb.2014.00296>.
- Fung, To Sing, Ying Liao, and Ding Xiang Liu. 2016. "Regulation of Stress Responses and Translational Control by Coronavirus." *Viruses* 8 (7): 184. <https://doi.org/10.3390/v8070184>.
- Gadhav, Kundlik, Prateek Kumar, Ankur Kumar, Taniya Bhardwaj, Neha Garg, and Rajanish Giri. 2021. "Conformational Dynamics of 13 Amino Acids Long NSP11 of SARS-CoV-2 under Membrane Mimetics and Different Solvent Conditions." *Microbial Pathogenesis* 158 (September): 105041. <https://doi.org/10.1016/j.micpath.2021.105041>.
- Ganley, Ian G., Pui-Mun Wong, Noor Gammoh, and Xuejun Jiang. 2011. "Distinct Autophagosomal-Lysosomal Fusion Mechanism Revealed by Thapsigargin-Induced Autophagy Arrest." *Molecular Cell* 42 (6): 731–43. <https://doi.org/10.1016/j.molcel.2011.04.024>.
- Ganley, Ian G., Pui-Mun Wong, and Xuejun Jiang. 2011. "Thapsigargin Distinguishes Membrane Fusion in the Late Stages of Endocytosis and Autophagy." *Autophagy* 7 (11): 1397–99. <https://doi.org/10.4161/auto.7.11.17651>.
- Gardner, Brooke M., David Pincus, Katja Gotthardt, Ciara M. Gallagher, and Peter Walter. 2013. "Endoplasmic Reticulum Stress Sensing in the Unfolded Protein Response." *Cold Spring Harbor Perspectives in Biology* 5 (3): a013169. <https://doi.org/10.1101/cshperspect.a013169>.
- Gardner, Brooke M., and Peter Walter. 2011. "Unfolded Proteins Are Ire1-Activating Ligands That Directly Induce the Unfolded Protein Response." *Science (New York, N.Y.)* 333 (6051): 1891–94. <https://doi.org/10.1126/science.1209126>.
- Gassen, Nils C., Daniela Niemeyer, Doreen Muth, Victor M. Corman, Silvia Martinelli, Alwine Gassen, Kathrin Hafner, et al. 2019. "SKP2 Attenuates Autophagy through Beclin1-Ubiqutination and Its Inhibition Reduces MERS-Coronavirus Infection." *Nature Communications* 10 (December): 5770. <https://doi.org/10.1038/s41467-019-13659-4>.
- Ge, Liang, David Melville, Min Zhang, and Randy Schekman. 2013. "The ER–Golgi Intermediate Compartment Is a Key Membrane Source for the LC3 Lipidation Step of Autophagosome Biogenesis." *ELife* 2 (August): e00947. <https://doi.org/10.7554/eLife.00947>.
- Ghosh, Rajarshi, Likun Wang, Eric S. Wang, B. Gayani K. Perera, Aeid Igbaria, Shuhei Morita, Kris Prado, et al. 2014. "Allosteric Inhibition of the IRE1 α RNase Preserves Cell Viability and

- Function during Endoplasmic Reticulum Stress.” *Cell* 158 (3): 534–48.
<https://doi.org/10.1016/j.cell.2014.07.002>.
- Ghosh, Sourish, Teegan A. Dellibovi-Ragheb, Adeline Kerviel, Eowyn Pak, Qi Qiu, Matthew Fisher, Peter M. Takvorian, et al. 2020. “ β -Coronaviruses Use Lysosomes for Egress Instead of the Biosynthetic Secretory Pathway.” *Cell* 183 (6): 1520-1535.e14.
<https://doi.org/10.1016/j.cell.2020.10.039>.
- Giedroc, David P., and Peter V. Cornish. 2009. “Frameshifting RNA Pseudoknots: Structure and Mechanism.” *Virus Research* 139 (2): 193–208.
<https://doi.org/10.1016/j.virusres.2008.06.008>.
- Gorbalenya, Alexander E., Susan C. Baker, Ralph S. Baric, Raoul J. de Groot, Christian Drosten, Anastasia A. Gulyaeva, Bart L. Haagmans, et al. 2020. “The Species Severe Acute Respiratory Syndrome-Related Coronavirus: Classifying 2019-NCoV and Naming It SARS-CoV-2.” *Nature Microbiology* 5 (4): 536–44. <https://doi.org/10.1038/s41564-020-0695-z>.
- Gordon, David E., Gwendolyn M. Jang, Mehdi Bouhaddou, Jiewei Xu, Kirsten Obernier, Kris M. White, Matthew J. O’Meara, et al. 2020. “A SARS-CoV-2 Protein Interaction Map Reveals Targets for Drug Repurposing.” *Nature* 583 (7816): 459–68. <https://doi.org/10.1038/s41586-020-2286-9>.
- Gossen, M., S. Freundlieb, G. Bender, G. Müller, W. Hillen, and H. Bujard. 1995. “Transcriptional Activation by Tetracyclines in Mammalian Cells.” *Science (New York, N.Y.)* 268 (5218): 1766–69. <https://doi.org/10.1126/science.7792603>.
- Graham, Rachel L., Amy C. Sims, Ralph S. Baric, and Mark R. Denison. 2006. “The Nsp2 Proteins of Mouse Hepatitis Virus and SARS Coronavirus Are Dispensable for Viral Replication.” *Advances in Experimental Medicine and Biology* 581: 67–72. https://doi.org/10.1007/978-0-387-33012-9_10.
- Groettrup, Marcus, Christiane Pelzer, Gunter Schmidtke, and Kay Hofmann. 2008. “Activating the Ubiquitin Family: UBA6 Challenges the Field.” *Trends in Biochemical Sciences* 33 (5): 230–37. <https://doi.org/10.1016/j.tibs.2008.01.005>.
- Grootjans, Joep, Arthur Kaser, Randal J. Kaufman, and Richard S. Blumberg. 2016. “The Unfolded Protein Response in Immunity and Inflammation.” *Nature Reviews Immunology* 16 (8): 469–84. <https://doi.org/10.1038/nri.2016.62>.
- Grünvogel, Oliver, Katharina Esser-Nobis, Marc P. Windisch, Michael Frese, Martin Trippler, Ralf Bartenschlager, Volker Lohmann, and Marco Binder. 2015. “Type I and Type II Interferon Responses in Two Human Liver Cell Lines (Huh-7 and HuH6).” *Genomics Data* 7 (December): 166–70. <https://doi.org/10.1016/j.gdata.2015.12.017>.
- Gutiérrez-Aguilar, Manuel, and Christopher P. Baines. 2013. “Physiological and Pathological Roles of Mitochondrial SLC25 Carriers.” *The Biochemical Journal* 454 (3): 371–86.
<https://doi.org/10.1042/BJ20121753>.
- Haan, Cornelis A. M. de, Lili Kuo, Paul S. Masters, Harry Vennema, and Peter J. M. Rottier. 1998. “Coronavirus Particle Assembly: Primary Structure Requirements of the Membrane Protein.” *Journal of Virology* 72 (8): 6838–50. <https://doi.org/10.1128/JVI.72.8.6838-6850.1998>.
- Halbleib, Kristina, Kristina Pesek, Roberto Covino, Harald F. Hofbauer, Dorith Wunnicke, Inga Hänelt, Gerhard Hummer, and Robert Ernst. 2017. “Activation of the Unfolded Protein Response by Lipid Bilayer Stress.” *Molecular Cell* 67 (4): 673-684.e8.
<https://doi.org/10.1016/j.molcel.2017.06.012>.
- Hamre, D., and J. J. Procknow. 1966. “A New Virus Isolated from the Human Respiratory Tract.” *Proceedings of the Society for Experimental Biology and Medicine. Society for Experimental Biology and Medicine (New York, N.Y.)* 121 (1): 190–93. <https://doi.org/10.3181/00379727-121-30734>.
- Han, Dan, Alana G. Lerner, Lieselotte Vande Walle, John-Paul Upton, Weihong Xu, Andrew Hagen, Bradley J. Backes, Scott A. Oakes, and Feroz R. Papa. 2009. “IRE1 α Kinase Activation Modes Control Alternate Endoribonuclease Outputs to Determine Divergent Cell Fates.” *Cell* 138 (3): 562–75. <https://doi.org/10.1016/j.cell.2009.07.017>.
- Haucke, Volker, and Michael M. Kozlov. 2018. “Membrane Remodeling in Clathrin-Mediated Endocytosis.” *Journal of Cell Science* 131 (17): jcs216812.
<https://doi.org/10.1242/jcs.216812>.

- Hein, Marco Y., Nina C. Hubner, Ina Poser, Jürgen Cox, Nagarjuna Nagaraj, Yusuke Toyoda, Igor A. Gak, et al. 2015. “A Human Interactome in Three Quantitative Dimensions Organized by Stoichiometries and Abundances.” *Cell* 163 (3): 712–23. <https://doi.org/10.1016/j.cell.2015.09.053>.
- Hemert, Martijn J. van, Sjoerd H. E. van den Worm, Kèvin Knoops, A. Mieke Mommaas, Alexander E. Gorbalenya, and Eric J. Snijder. 2008. “SARS-Coronavirus Replication/Transcription Complexes Are Membrane-Protected and Need a Host Factor for Activity In Vitro.” *PLoS Pathogens* 4 (5): e1000054. <https://doi.org/10.1371/journal.ppat.1000054>.
- Hillary, Robert F., and Una FitzGerald. 2018. “A Lifetime of Stress: ATF6 in Development and Homeostasis.” *Journal of Biomedical Science* 25 (1): 48. <https://doi.org/10.1186/s12929-018-0453-1>.
- Ho, Nurulain, Wei Sheng Yap, Jiaming Xu, Haoxi Wu, Jhee Hong Koh, Wilson Wen Bin Goh, Bhawana George, Shu Chen Chong, Stefan Taubert, and Guillaume Thibault. 2020. “Stress Sensor Ire1 Deploys a Divergent Transcriptional Program in Response to Lipid Bilayer Stress.” *Journal of Cell Biology* 219 (7): e201909165. <https://doi.org/10.1083/jcb.201909165>.
- Hoffmann, Markus, Hannah Kleine-Weber, Simon Schroeder, Nadine Krüger, Tanja Herrler, Sandra Erichsen, Tobias S. Schiergens, et al. 2020. “SARS-CoV-2 Cell Entry Depends on ACE2 and TMPRSS2 and Is Blocked by a Clinically Proven Protease Inhibitor.” *Cell* 181 (2): 271–280.e8. <https://doi.org/10.1016/j.cell.2020.02.052>.
- Hollien, Julie, and Jonathan S. Weissman. 2006. “Decay of Endoplasmic Reticulum-Localized MRNAs During the Unfolded Protein Response.” *Science* 313 (5783): 104–7. <https://doi.org/10.1126/science.1129631>.
- Hsu, Chia-Ling, Rupali Prasad, Christie Blackman, and Davis T. W. Ng. 2012. “Endoplasmic Reticulum Stress Regulation of the Kar2p/BiP Chaperone Alleviates Proteotoxicity via Dual Degradation Pathways.” *Molecular Biology of the Cell* 23 (4): 630–41. <https://doi.org/10.1091/mbc.e11-04-0297>.
- Huang, Chaolin, Yeming Wang, Xingwang Li, Lili Ren, Jianping Zhao, Yi Hu, Li Zhang, et al. 2020. “Clinical Features of Patients Infected with 2019 Novel Coronavirus in Wuhan, China.” *The Lancet* 0 (0). [https://doi.org/10.1016/S0140-6736\(20\)30183-5](https://doi.org/10.1016/S0140-6736(20)30183-5).
- Huttlin, Edward L., Raphael J. Bruckner, Joao A. Paulo, Joe R. Cannon, Lily Ting, Kurt Baltier, Greg Colby, et al. 2017. “Architecture of the Human Interactome Defines Protein Communities and Disease Networks.” *Nature* 545 (7655): 505–9. <https://doi.org/10.1038/nature22366>.
- Isaacs, John T., William Nathaniel Brennen, Søren Brøgger Christensen, and Samuel R. Denmeade. 2021. “Mipsagargin: The Beginning—Not the End—of Thapsigargin Prodrug-Based Cancer Therapeutics.” *Molecules* 26 (24): 7469. <https://doi.org/10.3390/molecules26247469>.
- Jacob Machado, Denis, Rachel Scott, Sayal Guirales, and Daniel A. Janies. 2021. “Fundamental Evolution of All Orthocoronavirinae Including Three Deadly Lineages Descendent from Chiroptera-Hosted Coronaviruses: SARS-CoV, MERS-CoV and SARS-CoV-2.” *Cladistics* 37 (5): 461–88. <https://doi.org/10.1111/cla.12454>.
- Jadhav, Kavita, and Yanqiao Zhang. 2017. “Activating Transcription Factor 3 in Immune Response and Metabolic Regulation.” *Liver Research* 1 (2): 96–102. <https://doi.org/10.1016/j.livres.2017.08.001>.
- Ji, Chang Hoon, Hee Yeon Kim, Ah Jung Heo, Su Hyun Lee, Min Ju Lee, Su Bin Kim, Ganipiseti Srinivasrao, et al. 2019. “The N-Degron Pathway Mediates ER-Phagy.” *Molecular Cell* 75 (5): 1058–1072.e9. <https://doi.org/10.1016/j.molcel.2019.06.028>.
- Johansen, Terje, and Trond Lamark. 2011. “Selective Autophagy Mediated by Autophagic Adapter Proteins.” *Autophagy* 7 (3): 279–96. <https://doi.org/10.4161/auto.7.3.14487>.
- Jurida, Liane, Johanna Soelch, Marek Bartkuhn, Katja Handschick, Helmut Müller, Doris Newel, Axel Weber, et al. 2015. “The Activation of IL-1-Induced Enhancers Depends on TAK1 Kinase Activity and NF-KB P65.” *Cell Reports* 10 (5): 726–39. <https://doi.org/10.1016/j.celrep.2015.01.001>.
- Kabeya, Y., N. Mizushima, T. Ueno, A. Yamamoto, T. Kirisako, T. Noda, E. Kominami, Y. Ohsumi, and T. Yoshimori. 2000. “LC3, a Mammalian Homologue of Yeast Apg8p, Is Localized in Autophagosomal Membranes after Processing.” *The EMBO Journal* 19 (21): 5720–28. <https://doi.org/10.1093/emboj/19.21.5720>.

- Kaiser, Stephen E., Kai Mao, Asad M. Taherbhoy, Shanshan Yu, Jennifer L. Olszewski, David M. Duda, Igor Kurinov, et al. 2012. “Noncanonical E2 Recruitment by the Autophagy E1 Revealed by Atg7–Atg3 and Atg7–Atg10 Structures.” *Nature Structural & Molecular Biology* 19 (12): 1242–49. <https://doi.org/10.1038/nsmb.2415>.
- Kamitani, Wataru, Krishna Narayanan, Cheng Huang, Kumari Lokugamage, Tetsuro Ikegami, Naoto Ito, Hideyuki Kubo, and Shinji Makino. 2006. “Severe Acute Respiratory Syndrome Coronavirus Nsp1 Protein Suppresses Host Gene Expression by Promoting Host mRNA Degradation.” *Proceedings of the National Academy of Sciences of the United States of America* 103 (34): 12885–90. <https://doi.org/10.1073/pnas.0603144103>.
- Kankuan, Wilairat, Chaitip Wanichanon, Rossella Titone, Attakorn Engsusophon, Chanudporn Sumpownon, Worawit Suphamungmee, Federica Morani, et al. 2017. “Starvation Promotes Autophagy-Associated Maturation of the Ovary in the Giant Freshwater Prawn, *Macrobrachium rosenbergii*.” *Frontiers in Physiology* 8. <https://www.frontiersin.org/articles/10.3389/fphys.2017.00300>.
- Kaushik, Susmita, and Ana Maria Cuervo. 2018. “The Coming of Age of Chaperone-Mediated Autophagy.” *Nature Reviews. Molecular Cell Biology* 19 (6): 365–81. <https://doi.org/10.1038/s41580-018-0001-6>.
- Kawase, Miyuki, Kazuya Shirato, Shutoku Matsuyama, and Fumihiko Taguchi. 2009. “Protease-Mediated Entry via the Endosome of Human Coronavirus 229E.” *Journal of Virology* 83 (2): 712–21. <https://doi.org/10.1128/JVI.01933-08>.
- Kelly, Jamie A., Alexandra N. Olson, Krishna Neupane, Sneha Munshi, Josue San Emeterio, Lois Pollack, Michael T. Woodside, and Jonathan D. Dinman. 2020. “Structural and Functional Conservation of the Programmed –1 Ribosomal Frameshift Signal of SARS-CoV-2.” *BioRxiv*, June, 2020.03.13.991083. <https://doi.org/10.1101/2020.03.13.991083>.
- Kershaw, Christopher J., Martin D. Jennings, Francesco Cortopassi, Margherita Guaita, Hawra Al-Ghafli, and Graham D. Pavitt. 2021. “GTP Binding to Translation Factor EIF2B Stimulates Its Guanine Nucleotide Exchange Activity.” *IScience* 24 (12): 103454. <https://doi.org/10.1016/j.isci.2021.103454>.
- Khandia, Rekha, Maryam Dadar, Ashok Munjal, Kuldeep Dhama, Kumaragurubaran Karthik, Ruchi Tiwari, Mohd. Iqbal Yattoo, et al. 2019. “A Comprehensive Review of Autophagy and Its Various Roles in Infectious, Non-Infectious, and Lifestyle Diseases: Current Knowledge and Prospects for Disease Prevention, Novel Drug Design, and Therapy.” *Cells* 8 (7): 674. <https://doi.org/10.3390/cells8070674>.
- Kim, Dae In, Samuel C. Jensen, Kyle A. Noble, Birendra Kc, Kenneth H. Roux, Khatereh Motamedchaboki, and Kyle J. Roux. 2016. “An Improved Smaller Biotin Ligase for BioID Proximity Labeling.” *Molecular Biology of the Cell* 27 (8): 1188–96. <https://doi.org/10.1091/mbc.E15-12-0844>.
- Kim, Dongwan, Joo-Yeon Lee, Jeong-Sun Yang, Jun Won Kim, V. Narry Kim, and Hyesik Chang. 2020. “The Architecture of SARS-CoV-2 Transcriptome.” *Cell* 181 (4): 914–921.e10. <https://doi.org/10.1016/j.cell.2020.04.011>.
- Kim, Jihoon, Bon-Kyoung Koo, and Juergen A. Knoblich. 2020. “Human Organoids: Model Systems for Human Biology and Medicine.” *Nature Reviews Molecular Cell Biology* 21 (10): 571–84. <https://doi.org/10.1038/s41580-020-0259-3>.
- Kimura, Shunsuke, Takeshi Noda, and Tamotsu Yoshimori. 2007. “Dissection of the Autophagosomal Maturation Process by a Novel Reporter Protein, Tandem Fluorescent-Tagged LC3.” *Autophagy* 3 (5): 452–60. <https://doi.org/10.4161/auto.4451>.
- Kindrachuk, Jason, Britini Ork, Brit J. Hart, Steven Mazur, Michael R. Holbrook, Matthew B. Frieman, Dawn Traynor, et al. 2015. “Antiviral Potential of ERK/MAPK and PI3K/AKT/MTOR Signaling Modulation for Middle East Respiratory Syndrome Coronavirus Infection as Identified by Temporal Kinome Analysis.” *Antimicrobial Agents and Chemotherapy* 59 (2): 1088–99. <https://doi.org/10.1128/AAC.03659-14>.
- Klein, Steffen, Mirko Cortese, Sophie L. Winter, Moritz Wachsmuth-Melm, Christopher J. Neufeldt, Berati Cerikan, Megan L. Stanifer, Steeve Boulant, Ralf Bartenschlager, and Petr Chlanda. 2020. “SARS-CoV-2 Structure and Replication Characterized by in Situ Cryo-Electron Tomography.” *Nature Communications* 11 (1): 5885. <https://doi.org/10.1038/s41467-020-19619-7>.

- Klionsky, Daniel J., Eeva-Liisa Eskelinen, and Vojo Deretic. 2014. "Autophagosomes, Phagosomes, Autolysosomes, Phagolysosomes, Autophagolysosomes... Wait, I'm Confused." *Autophagy* 10 (4): 549–51. <https://doi.org/10.4161/auto.28448>.
- Kliza, Katarzyna, and Koraljka Husnjak. 2020. "Resolving the Complexity of Ubiquitin Networks." *Frontiers in Molecular Biosciences* 7. <https://www.frontiersin.org/articles/10.3389/fmolb.2020.00021>.
- Knoops, Kèvin, Marjolein Kikkert, Sjoerd H. E. van den Worm, Jessika C Zevenhoven-Dobbe, Yvonne van der Meer, Abraham J Koster, A. Mieke Mommaas, and Eric J Snijder. 2008. "SARS-Coronavirus Replication Is Supported by a Reticulovesicular Network of Modified Endoplasmic Reticulum." *PLoS Biology* 6 (9): e226. <https://doi.org/10.1371/journal.pbio.0060226>.
- Ko, Chiung-Yuan, Ling-Hua Chang, Yi-Chao Lee, Esta Sterneck, Chun-Pei Cheng, Shun-Hua Chen, A-Mei Huang, Joseph T. Tseng, and Ju-Ming Wang. 2012. "CCAAT/Enhancer Binding Protein Delta (CEBPD) Elevating PTX3 Expression Inhibits Macrophage-Mediated Phagocytosis of Dying Neuron Cells." *Neurobiology of Aging* 33 (2): 422.e11-422.e25. <https://doi.org/10.1016/j.neurobiolaging.2010.09.017>.
- Ko, Chiung-Yuan, Wen-Chang Chang, and Ju-Ming Wang. 2015. "Biological Roles of CCAAT/Enhancer-Binding Protein Delta during Inflammation." *Journal of Biomedical Science* 22 (1): 6. <https://doi.org/10.1186/s12929-014-0110-2>.
- Kokic, Goran, Hauke S. Hillen, Dimitry Tegunov, Christian Dienemann, Florian Seitz, Jana Schmitzova, Lucas Farnung, Aaron Siewert, Claudia Höbartner, and Patrick Cramer. 2021. "Mechanism of SARS-CoV-2 Polymerase Stalling by Remdesivir." *Nature Communications* 12 (1): 279. <https://doi.org/10.1038/s41467-020-20542-0>.
- Kontarakis, Zacharias, and Didier Y. R. Stainier. 2020. "Genetics in Light of Transcriptional Adaptation." *Trends in Genetics: TIG* 36 (12): 926–35. <https://doi.org/10.1016/j.tig.2020.08.008>.
- Kopp, Megan C., Natacha Larburu, Vinoth Durairaj, Christopher J. Adams, and Maruf M. U. Ali. 2019. "UPR Proteins IRE1 and PERK Switch BiP from Chaperone to ER Stress Sensor." *Nature Structural & Molecular Biology* 26 (11): 1053–62. <https://doi.org/10.1038/s41594-019-0324-9>.
- Kopp, Megan C, Piotr R Nowak, Natacha Larburu, Christopher J Adams, and Maruf MU Ali. 2018. "In Vitro FRET Analysis of IRE1 and BiP Association and Dissociation upon Endoplasmic Reticulum Stress." Edited by Franz-Ulrich Hartl. *ELife* 7 (January): e30257. <https://doi.org/10.7554/eLife.30257>.
- Krähling, Verena, David A. Stein, Martin Spiegel, Friedemann Weber, and Elke Mühlberger. 2009. "Severe Acute Respiratory Syndrome Coronavirus Triggers Apoptosis via Protein Kinase R but Is Resistant to Its Antiviral Activity." *Journal of Virology* 83 (5): 2298–2309. <https://doi.org/10.1128/JVI.01245-08>.
- Krishnamoorthy, Jothi, Kamindla Rajesh, Farzaneh Mirzajani, Polixenia Kesoglidou, Andreas Papadakis, and Antonis E. Koromilas. 2014. "Evidence for EIF2 α Phosphorylation-Independent Effects of GSK2656157, a Novel Catalytic Inhibitor of PERK with Clinical Implications." *Cell Cycle* 13 (5): 801–6. <https://doi.org/10.4161/cc.27726>.
- Ku, Hui-Chen, and Ching-Feng Cheng. 2020. "Master Regulator Activating Transcription Factor 3 (ATF3) in Metabolic Homeostasis and Cancer." *Frontiers in Endocrinology* 11. <https://www.frontiersin.org/articles/10.3389/fendo.2020.00556>.
- Kudo, T, S Kanemoto, H Hara, N Morimoto, T Morihara, R Kimura, T Tabira, K Imaizumi, and M Takeda. 2008. "A Molecular Chaperone Inducer Protects Neurons from ER Stress." *Cell Death & Differentiation* 15 (2): 364–75. <https://doi.org/10.1038/sj.cdd.4402276>.
- Kung, Jennifer E., and Natalia Jura. 2016. "Structural Basis for the Non-Catalytic Functions of Protein Kinases." *Structure* 24 (1): 7–24. <https://doi.org/10.1016/j.str.2015.10.020>.
- LaBarre, D. D., and R. J. Lowy. 2001. "Improvements in Methods for Calculating Virus Titer Estimates from TCID50 and Plaque Assays." *Journal of Virological Methods* 96 (2): 107–26. [https://doi.org/10.1016/s0166-0934\(01\)00316-0](https://doi.org/10.1016/s0166-0934(01)00316-0).
- Labzin, Larisa I., Susanne V. Schmidt, Seth L. Masters, Marc Beyer, Wolfgang Krebs, Kathrin Klee, Rainer Stahl, et al. 2015. "ATF3 Is a Key Regulator of Macrophage IFN Responses." *The Journal of Immunology*, September. <https://doi.org/10.4049/jimmunol.1500204>.

- Laemmli, U. K. 1970. "Cleavage of Structural Proteins during the Assembly of the Head of Bacteriophage T4." *Nature* 227 (5259): 680–85. <https://doi.org/10.1038/227680a0>.
- Lamers, Mart M., and Bart L. Haagmans. 2022. "SARS-CoV-2 Pathogenesis." *Nature Reviews Microbiology* 20 (5): 270–84. <https://doi.org/10.1038/s41579-022-00713-0>.
- Lamers, Mart M, Jelte van der Vaart, Kèvin Knoops, Samra Riesebosch, Tim I Breugem, Anna Z Mykytyn, Joep Beumer, et al. 2021. "An Organoid-Derived Bronchioalveolar Model for SARS-CoV-2 Infection of Human Alveolar Type II-like Cells." *The EMBO Journal* 40 (5): e105912. <https://doi.org/10.15252/embj.2020105912>.
- Larhammar, Martin, Sarah Huntwork-Rodriguez, Zhiyu Jiang, Hilda Solanoy, Arundhati Sengupta Ghosh, Bei Wang, Joshua S Kaminker, et al. 2017. "Dual Leucine Zipper Kinase-Dependent PERK Activation Contributes to Neuronal Degeneration Following Insult." Edited by Andrew Dillin. *ELife* 6 (April): e20725. <https://doi.org/10.7554/eLife.20725>.
- Lau, Eric, and Ze'ev A. Ronai. 2012. "ATF2 – at the Crossroad of Nuclear and Cytosolic Functions." *Journal of Cell Science* 125 (12): 2815–24. <https://doi.org/10.1242/jcs.095000>.
- Lee, Amy S. 2005. "The ER Chaperone and Signaling Regulator GRP78/BiP as a Monitor of Endoplasmic Reticulum Stress." *Methods (San Diego, Calif.)* 35 (4): 373–81. <https://doi.org/10.1016/j.ymeth.2004.10.010>.
- Lee, Ann-Hwee, Neal N. Iwakoshi, and Laurie H. Glimcher. 2003. "XBP-1 Regulates a Subset of Endoplasmic Reticulum Resident Chaperone Genes in the Unfolded Protein Response." *Molecular and Cellular Biology* 23 (21): 7448–59. <https://doi.org/10.1128/MCB.23.21.7448-7459.2003>.
- Lee, Ji Yeon, Eun-Koung An, Juyoung Hwang, Jun-O. Jin, and Peter C. W. Lee. 2022. "Ubiquitin Activating Enzyme UBA6 Regulates Th1 and Tc1 Cell Differentiation." *Cells* 11 (1): 105. <https://doi.org/10.3390/cells11010105>.
- Lee, Ju-Hyun, Dun-Sheng Yang, Chris N. Goulbourne, Eunju Im, Philip Stavrides, Anna Pensalfini, Han Chan, et al. 2022. "Faulty Autolysosome Acidification in Alzheimer's Disease Mouse Models Induces Autophagic Build-up of A β in Neurons, Yielding Senile Plaques." *Nature Neuroscience* 25 (6): 688–701. <https://doi.org/10.1038/s41593-022-01084-8>.
- Lei, Chengfeng, Jian Yang, Jia Hu, and Xiulian Sun. 2021. "On the Calculation of TCID₅₀ for Quantitation of Virus Infectivity." *Virologica Sinica* 36 (1): 141–44. <https://doi.org/10.1007/s12250-020-00230-5>.
- Lei, Jian, Yuri Kusov, and Rolf Hilgenfeld. 2018. "Nsp3 of Coronaviruses: Structures and Functions of a Large Multi-Domain Protein." *Antiviral Research* 149 (January): 58–74. <https://doi.org/10.1016/j.antiviral.2017.11.001>.
- Lennemann, Nicholas J., and Carolyn B. Coyne. 2015. "Catch Me If You Can: The Link between Autophagy and Viruses." *PLOS Pathogens* 11 (3): e1004685. <https://doi.org/10.1371/journal.ppat.1004685>.
- Levine, Beth, and Vojo Deretic. 2007. "Unveiling the Roles of Autophagy in Innate and Adaptive Immunity." *Nature Reviews Immunology* 7 (10): 767–77. <https://doi.org/10.1038/nri2161>.
- Li, Chuang, Qianqian Fan, Hongyang Quan, Meng Nie, Yunping Luo, and Lin Wang. 2018. "The Three Branches of the Unfolded Protein Response Exhibit Differential Significance in Breast Cancer Growth and Stemness." *Experimental Cell Research* 367 (2): 170–85. <https://doi.org/10.1016/j.yexcr.2018.03.033>.
- Li, Yang, Shijia Huang, Jingsi Wang, Jianli Dai, Jie Cai, Shuai Yan, Zhiliang Huang, et al. 2022. "Phosphorylation at Ser724 of the ER Stress Sensor IRE1 α Governs Its Activation State and Limits ER Stress-Induced Hepatosteatosis." *Journal of Biological Chemistry* 298 (6): 101997. <https://doi.org/10.1016/j.jbc.2022.101997>.
- Li, Zhijie, Aidan CA Tomlinson, Alan HM Wong, Dongxia Zhou, Marc Desforages, Pierre J Talbot, Samir Benlekbir, John L Rubinstein, and James M Rini. n.d. "The Human Coronavirus HCoV-229E S-Protein Structure and Receptor Binding." *ELife* 8. Accessed January 31, 2020. <https://doi.org/10.7554/eLife.51230>.
- Liang, Guosheng, Curt D. Wolfgang, Benjamin P. C. Chen, Tsu-Hua Chen, and Tsonwin Hai. 1996. "ATF3 Gene: GENOMIC ORGANIZATION, PROMOTER, AND REGULATION (*)." *Journal of Biological Chemistry* 271 (3): 1695–1701. <https://doi.org/10.1074/jbc.271.3.1695>.
- Liang, Yanwen, Mong-Lien Wang, Chian-Shiu Chien, Aliaksandr A. Yarmishyn, Yi-Ping Yang, Wei-Yi Lai, Yung-Hung Luo, et al. 2020. "Highlight of Immune Pathogenic Response and

- Hematopathologic Effect in SARS-CoV, MERS-CoV, and SARS-Cov-2 Infection.” *Frontiers in Immunology* 11. <https://www.frontiersin.org/articles/10.3389/fimmu.2020.01022>.
- Lindå, Hans, Mattias K. Sköld, and Thomas Ochsmann. 2011. “Activating Transcription Factor 3, a Useful Marker for Regenerative Response after Nerve Root Injury.” *Frontiers in Neurology* 2 (May): 30. <https://doi.org/10.3389/fneur.2011.00030>.
- Lindner, Paula, Søren Brøgger Christensen, Poul Nissen, Jesper Vuust Møller, and Nikolai Engedal. 2020. “Cell Death Induced by the ER Stressor Thapsigargin Involves Death Receptor 5, a Non-Autophagic Function of MAP1LC3B, and Distinct Contributions from Unfolded Protein Response Components.” *Cell Communication and Signaling : CCS* 18 (January): 12. <https://doi.org/10.1186/s12964-019-0499-z>.
- Litvak, Vladimir, Stephen A. Ramsey, Alistair G. Rust, Daniel E. Zak, Kathleen A. Kennedy, Aaron E. Lampano, Matti Nykter, Ilya Shmulevich, and Alan Aderem. 2009. “Role of the Transcription Factor C/EBP δ in a Regulatory Circuit That Discriminates between Transient and Persistent Toll-like Receptor 4-Induced Signals.” *Nature Immunology* 10 (4): 437–43. <https://doi.org/10.1038/ni.1721>.
- Liu, Ding X., Jia Q. Liang, and To S. Fung. 2021. “Human Coronavirus-229E, -OC43, -NL63, and -HKU1 (Coronaviridae).” *Encyclopedia of Virology*, 428–40. <https://doi.org/10.1016/B978-0-12-809633-8.21501-X>.
- Liu, Lulu, Jinjin Zhong, Bilin Chen, Weiping Wang, Haiyan Xi, and Xin Su. 2022. “CCAAT/Enhancer Binding Protein (C/EBP) Delta Promotes the Expression of PTX3 and Macrophage Phagocytosis during *A. Fumigatus* Infection.” *Journal of Leukocyte Biology* 111 (6): 1225–34. <https://doi.org/10.1002/JLB.4MA1121-451RR>.
- Liu, Xianpeng, Limin Sun, Demirkan B. Gursel, Chonghui Cheng, Sui Huang, Alfred W. Rademaker, Seema A. Khan, Jun Yin, and Hiroaki Kiyokawa. 2017. “The Non-Canonical Ubiquitin Activating Enzyme UBA6 Suppresses Epithelial-Mesenchymal Transition of Mammary Epithelial Cells.” *Oncotarget* 8 (50): 87480–93. <https://doi.org/10.18632/oncotarget.20900>.
- Liu, Xiaonan, Kari Salokas, Rigbe G. Weldatsadik, Lisa Gawriyski, and Markku Varjosalo. 2020. “Combined Proximity Labeling and Affinity Purification–mass Spectrometry Workflow for Mapping and Visualizing Protein Interaction Networks.” *Nature Protocols* 15 (10): 3182–3211. <https://doi.org/10.1038/s41596-020-0365-x>.
- Liu, Yuanzhi, Mingshu Wang, Anchun Cheng, Qiao Yang, Ying Wu, Renyong Jia, Mafeng Liu, et al. 2020. “The Role of Host EIF2 α in Viral Infection.” *Virology Journal* 17 (1): 112. <https://doi.org/10.1186/s12985-020-01362-6>.
- Loos, Ben, André du Toit, and Jan-Hendrik S Hofmeyr. 2014. “Defining and Measuring Autophagosome Flux—Concept and Reality.” *Autophagy* 10 (11): 2087–96. <https://doi.org/10.4161/15548627.2014.973338>.
- Lu, Wei, Bo-Jian Zheng, Ke Xu, Wolfgang Schwarz, Lanying Du, Charlotte K. L. Wong, Jiadong Chen, Shuming Duan, Vincent Deubel, and Bing Sun. 2006. “Severe Acute Respiratory Syndrome-Associated Coronavirus 3a Protein Forms an Ion Channel and Modulates Virus Release.” *Proceedings of the National Academy of Sciences* 103 (33): 12540–45. <https://doi.org/10.1073/pnas.0605402103>.
- Lui, Grace Chung-Yan, Terry Cheuk-Fung Yip, Vincent Wai-Sun Wong, Viola Chi-Ying Chow, Tracy Hang-Yee Ho, Timothy Chun-Man Li, Yee-Kit Tse, Henry Lik-Yuen Chan, David Shu-Cheong Hui, and Grace Lai-Hung Wong. 2020. “Significantly Lower Case-Fatality Ratio of Coronavirus Disease 2019 (COVID-19) than Severe Acute Respiratory Syndrome (SARS) in Hong Kong—A Territory-Wide Cohort Study.” *Clinical Infectious Diseases: An Official Publication of the Infectious Diseases Society of America*, October, ciaa1187. <https://doi.org/10.1093/cid/ciaa1187>.
- Ma, Yanjun, and Linda M. Hendershot. 2003. “Delineation of a Negative Feedback Regulatory Loop That Controls Protein Translation during Endoplasmic Reticulum Stress*.” *Journal of Biological Chemistry* 278 (37): 34864–73. <https://doi.org/10.1074/jbc.M301107200>.
- Madden, Emma, Susan E. Logue, Sandra J. Healy, Serge Manie, and Afshin Samali. 2019. “The Role of the Unfolded Protein Response in Cancer Progression: From Oncogenesis to Chemoresistance.” *Biology of the Cell* 111 (1): 1–17. <https://doi.org/10.1111/boc.201800050>.

- Madhugiri, Ramakanth, Markus Fricke, Manja Marz, and John Ziebuhr. 2014. “RNA Structure Analysis of Alphacoronavirus Terminal Genome Regions.” *Virus Research*, Nidoviruses I, 194 (December): 76–89. <https://doi.org/10.1016/j.virusres.2014.10.001>.
- Mair, Andrea, Shou-Ling Xu, Tess C Branon, Alice Y Ting, and Dominique C Bergmann. 2019. “Proximity Labeling of Protein Complexes and Cell-Type-Specific Organellar Proteomes in Arabidopsis Enabled by TurboID.” Edited by Frank LH Menke and Christian S Hardtke. *ELife* 8 (September): e47864. <https://doi.org/10.7554/eLife.47864>.
- Maity, Subhajit, and Abhik Saha. 2021. “Therapeutic Potential of Exploiting Autophagy Cascade Against Coronavirus Infection.” *Frontiers in Microbiology* 12. <https://www.frontiersin.org/article/10.3389/fmicb.2021.675419>.
- Malek, Mouhannad, Anna M. Wawrzyniak, Peter Koch, Christian Luchtenborg, Manuel Hessenberger, Timo Sachsenheimer, Wonyul Jang, Britta Brügger, and Volker Haucke. 2021. “Inositol Triphosphate-Triggered Calcium Release Blocks Lipid Exchange at Endoplasmic Reticulum-Golgi Contact Sites.” *Nature Communications* 12 (1): 2673. <https://doi.org/10.1038/s41467-021-22882-x>.
- Malone, Brandon, Nadya Urakova, Eric J. Snijder, and Elizabeth A. Campbell. 2022. “Structures and Functions of Coronavirus Replication–Transcription Complexes and Their Relevance for SARS-CoV-2 Drug Design.” *Nature Reviews Molecular Cell Biology* 23 (1): 21–39. <https://doi.org/10.1038/s41580-021-00432-z>.
- Marciano, Ran, Gabriel Leprivier, and Barak Rotblat. 2018. “Puromycin Labeling Does Not Allow Protein Synthesis to Be Measured in Energy-Starved Cells.” *Cell Death & Disease* 9 (2): 39. <https://doi.org/10.1038/s41419-017-0056-x>.
- Masre, Siti Fathiah, Nurul Farhana Jufri, Farah Wahida Ibrahim, and Sayyidi Hamzi Abdul Raub. 2021. “Classical and Alternative Receptors for SARS-CoV-2 Therapeutic Strategy.” *Reviews in Medical Virology* 31 (5): e2207. <https://doi.org/10.1002/rmv.2207>.
- Maurel, M., E. Chevet, J. Tavernier, and S. Gerlo. 2014. “Getting RIDD of RNA: IRE1 in Cell Fate Regulation.” *Trends in Biochemical Sciences* 39 (5): 245–54. <https://doi.org/10.1016/j.tibs.2014.02.008>.
- Mauthe, Mario, Idil Orhon, Cecilia Rocchi, Xingdong Zhou, Morten Luhr, Kerst-Jan Hijlkema, Robert P. Coppes, Nikolai Engedal, Muriel Mari, and Fulvio Reggiori. 2018. “Chloroquine Inhibits Autophagic Flux by Decreasing Autophagosome-Lysosome Fusion.” *Autophagy* 14 (8): 1435–55. <https://doi.org/10.1080/15548627.2018.1474314>.
- Mauvezin, Caroline, Péter Nagy, Gábor Juhász, and Thomas P. Neufeld. 2015. “Autophagosome–Lysosome Fusion Is Independent of V-ATPase-Mediated Acidification.” *Nature Communications* 6 (1): 7007. <https://doi.org/10.1038/ncomms8007>.
- May, Danielle G., Kelsey L. Scott, Alexandre R. Campos, and Kyle J. Roux. 2020. “Comparative Application of BioID and TurboID for Protein-Proximity Biotinylation.” *Cells* 9 (5): 1070. <https://doi.org/10.3390/cells9051070>.
- Mayr-Buro, Christin, Eva Schlereth, Knut Beuerlein, Ulas Tenekeci, Johanna Meier-Soelch, M. Lienhard Schmitz, and Michael Kracht. 2019. “Single-Cell Analysis of Multiple Steps of Dynamic NF- κ B Regulation in Interleukin-1 α -Triggered Tumor Cells Using Proximity Ligation Assays.” *Cancers* 11 (8). <https://doi.org/10.3390/cancers11081199>.
- McBride, Ruth, Marjorie Van Zyl, and Burtram C. Fielding. 2014. “The Coronavirus Nucleocapsid Is a Multifunctional Protein.” *Viruses* 6 (8): 2991–3018. <https://doi.org/10.3390/v6082991>.
- McClenaghan, Conor, Alex Hanson, Sun-Joo Lee, and Colin G. Nichols. 2020. “Coronavirus Proteins as Ion Channels: Current and Potential Research.” *Frontiers in Immunology* 11. <https://www.frontiersin.org/article/10.3389/fimmu.2020.573339>.
- Mead, Benjamin E., and Jeffrey M. Karp. 2019. “All Models Are Wrong, but Some Organoids May Be Useful.” *Genome Biology* 20 (1): 66. <https://doi.org/10.1186/s13059-019-1677-4>.
- Mekahli, Djalila, Geert Bultynck, Jan B. Parys, Humbert De Smedt, and Ludwig Missiaen. 2011. “Endoplasmic-Reticulum Calcium Depletion and Disease.” *Cold Spring Harbor Perspectives in Biology* 3 (6): a004317. <https://doi.org/10.1101/cshperspect.a004317>.
- Menachery, Vineet D., Boyd L. Yount, Kari Debink, Sudhakar Agnihotram, Lisa E. Gralinski, Jessica A. Plante, Rachel L. Graham, et al. 2015. “A SARS-like Cluster of Circulating Bat Coronaviruses Shows Potential for Human Emergence.” *Nature Medicine* 21 (12): 1508–13. <https://doi.org/10.1038/nm.3985>.

- Mendez, Aaron S, Jennifer Alfaro, Marisol A Morales-Soto, Arvin C Dar, Emma McCullagh, Katja Gotthardt, Han Li, et al. 2015. "Endoplasmic Reticulum Stress-Independent Activation of Unfolded Protein Response Kinases by a Small Molecule ATP-Mimic." Edited by John Kuriyan. *ELife* 4 (May): e05434. <https://doi.org/10.7554/eLife.05434>.
- Miao, Zhichao, Antonin Tidu, Gilbert Eriani, and Franck Martin. n.d. "Secondary Structure of the SARS-CoV-2 5'-UTR." *RNA Biology* 18 (4): 447–56. <https://doi.org/10.1080/15476286.2020.1814556>.
- Mijaljica, Dalibor, Mark Prescott, and Rodney J. Devenish. 2012. "The Intriguing Life of Autophagosomes." *International Journal of Molecular Sciences* 13 (3): 3618–35. <https://doi.org/10.3390/ijms13033618>.
- Mishra, Tarun, M. Sreepadmanabh, Pavitra Ramdas, Amit Kumar Sahu, Atul Kumar, and Ajit Chande. 2021. "SARS CoV-2 Nucleoprotein Enhances the Infectivity of Lentiviral Spike Particles." *Frontiers in Cellular and Infection Microbiology* 11. <https://www.frontiersin.org/article/10.3389/fcimb.2021.663688>.
- Moustaqil, Mehdi, Emma Ollivier, Hsin-Ping Chiu, Sarah Van Tol, Paulina Rudolffi-Soto, Christian Stevens, Akshay Bhumkar, et al. 2021. "SARS-CoV-2 Proteases PLpro and 3CLpro Cleave IRF3 and Critical Modulators of Inflammatory Pathways (NLRP12 and TAB1): Implications for Disease Presentation across Species." *Emerging Microbes & Infections* 10 (1): 178–95. <https://doi.org/10.1080/22221751.2020.1870414>.
- Mu, Jingfang, Yaohui Fang, Qi Yang, Ting Shu, An Wang, Muhan Huang, Liang Jin, Fei Deng, Yang Qiu, and Xi Zhou. 2020. "SARS-CoV-2 N Protein Antagonizes Type I Interferon Signaling by Suppressing Phosphorylation and Nuclear Translocation of STAT1 and STAT2." *Cell Discovery* 6 (September): 65. <https://doi.org/10.1038/s41421-020-00208-3>.
- Münz, Christian. 2017. "The Autophagic Machinery in Viral Exocytosis." *Frontiers in Microbiology* 8 (February): 269. <https://doi.org/10.3389/fmicb.2017.00269>.
- Myllymäki, Henna, Susanna Valanne, and Mika Rämet. 2014. "The Drosophila Imd Signaling Pathway." *The Journal of Immunology* 192 (8): 3455–62. <https://doi.org/10.4049/jimmunol.1303309>.
- Nakabayashi, H., K. Taketa, K. Miyano, T. Yamane, and J. Sato. 1982. "Growth of Human Hepatoma Cells Lines with Differentiated Functions in Chemically Defined Medium." *Cancer Research* 42 (9): 3858–63.
- Nakatogawa, Hitoshi. 2020. "Mechanisms Governing Autophagosome Biogenesis." *Nature Reviews Molecular Cell Biology* 21 (8): 439–58. <https://doi.org/10.1038/s41580-020-0241-0>.
- Nardacci, R., F. Ciccosanti, C. Marsella, G. Ippolito, M. Piacentini, and G. M. Fimia. 2017. "Role of Autophagy in HIV Infection and Pathogenesis." *Journal of Internal Medicine* 281 (5): 422–32. <https://doi.org/10.1111/joim.12596>.
- Nascimbeni, Anna Chiara, Patrice Codogno, and Etienne Morel. 2017. "Local Detection of PtdIns3P at Autophagosome Biogenesis Membrane Platforms." *Autophagy* 13 (9): 1602–12. <https://doi.org/10.1080/15548627.2017.1341465>.
- Natsume, Toyoaki, Tomomi Kiyomitsu, Yumiko Saga, and Masato T. Kanemaki. 2016. "Rapid Protein Depletion in Human Cells by Auxin-Inducible Degron Tagging with Short Homology Donors." *Cell Reports* 15 (1): 210–18. <https://doi.org/10.1016/j.celrep.2016.03.001>.
- Nazio, Francesca, Flavie Strappazon, Manuela Antonioli, Pamela Bielli, Valentina Cianfanelli, Matteo Bordi, Christine Gretzmeier, et al. 2013. "MTOR Inhibits Autophagy by Controlling ULK1 Ubiquitylation, Self-Association and Function through AMBRA1 and TRAF6." *Nature Cell Biology* 15 (4): 406–16. <https://doi.org/10.1038/ncb2708>.
- Netherton, Christopher L, and Tom Wileman. 2011. "Virus Factories, Double Membrane Vesicles and Viroplasm Generated in Animal Cells." *Current Opinion in Virology* 1 (5): 381–87. <https://doi.org/10.1016/j.coviro.2011.09.008>.
- Netland, Jason, Marta L. DeDiego, Jincun Zhao, Craig Fett, Enrique Álvarez, José L. Nieto-Torres, Luis Enjuanes, and Stanley Perlman. 2010. "Immunization with an Attenuated Severe Acute Respiratory Syndrome Coronavirus Deleted in E Protein Protects against Lethal Respiratory Disease." *Virology* 399 (1): 120–28. <https://doi.org/10.1016/j.virol.2010.01.004>.
- Newman, Joseph A., Alice Douangamath, Setayesh Yadzani, Yuliana Yosaatmadja, Antony Aimon, José Brandão-Neto, Louise Dunnett, et al. 2021. "Structure, Mechanism and Crystallographic

- Fragment Screening of the SARS-CoV-2 NSP13 Helicase.” *Nature Communications* 12 (1): 4848. <https://doi.org/10.1038/s41467-021-25166-6>.
- Nguyen, Long C., David M. Renner, Diane Silva, Dongbo Yang, Nicholas Parenti, Kaeri M. Medina, Vlad Nicolaescu, et al. 2022. “SARS-CoV-2 Diverges from Other Betacoronaviruses in Only Partially Activating the IRE1 α /XBP1 ER Stress Pathway in Human Lung-Derived Cells.” *BioRxiv*, June, 2021.12.30.474519. <https://doi.org/10.1101/2021.12.30.474519>.
- Nieto-Torres, Jose L., Marta L. DeDiego, Carmina Verdiá-Báguena, Jose M. Jimenez-Guardeño, Jose A. Regla-Nava, Raul Fernandez-Delgado, Carlos Castaño-Rodriguez, et al. 2014. “Severe Acute Respiratory Syndrome Coronavirus Envelope Protein Ion Channel Activity Promotes Virus Fitness and Pathogenesis.” *PLOS Pathogens* 10 (5): e1004077. <https://doi.org/10.1371/journal.ppat.1004077>.
- Nieto-Torres, Jose L., Carmina Verdiá-Báguena, Jose M. Jimenez-Guardeño, Jose A. Regla-Nava, Carlos Castaño-Rodriguez, Raul Fernandez-Delgado, Jaume Torres, Vicente M. Aguilera, and Luis Enjuanes. 2015. “Severe Acute Respiratory Syndrome Coronavirus E Protein Transports Calcium Ions and Activates the NLRP3 Inflammasome.” *Virology* 485 (November): 330–39. <https://doi.org/10.1016/j.virol.2015.08.010>.
- Nieva, José Luis, Vanesa Madan, and Luis Carrasco. 2012. “Viroporins: Structure and Biological Functions.” *Nature Reviews. Microbiology* 10 (8): 563–74. <https://doi.org/10.1038/nrmicro2820>.
- Novoa, Isabel, Huiqing Zeng, Heather P. Harding, and David Ron. 2001. “Feedback Inhibition of the Unfolded Protein Response by GADD34-Mediated Dephosphorylation of EIF2 α .” *The Journal of Cell Biology* 153 (5): 1011–22.
- Ogando, Natacha S., Jessika C. Zevenhoven-Dobbe, Yvonne van der Meer, Peter J. Bredenbeek, Clara C. Posthuma, and Eric J. Snijder. n.d. “The Enzymatic Activity of the Nsp14 Exoribonuclease Is Critical for Replication of MERS-CoV and SARS-CoV-2.” *Journal of Virology* 94 (23): e01246-20. <https://doi.org/10.1128/JVI.01246-20>.
- Ogata, Maiko, Shin-ichiro Hino, Atsushi Saito, Keisuke Morikawa, Shinichi Kondo, Soshi Kanemoto, Tomohiko Murakami, et al. 2006. “Autophagy Is Activated for Cell Survival after Endoplasmic Reticulum Stress.” *Molecular and Cellular Biology* 26 (24): 9220–31. <https://doi.org/10.1128/MCB.01453-06>.
- Oikonomou, Christina, and Linda M. Hendershot. 2020. “Disposing of Misfolded ER Proteins: A Troubled Substrate’s Way out of the ER.” *Molecular and Cellular Endocrinology* 500 (January): 110630. <https://doi.org/10.1016/j.mce.2019.110630>.
- O’Leary, Monique N., Katherine H. Schreiber, Yong Zhang, Anne-Cécile E. Duc, Shuyun Rao, J. Scott Hale, Emmeline C. Academia, et al. 2013. “The Ribosomal Protein Rpl22 Controls Ribosome Composition by Directly Repressing Expression of Its Own Paralog, Rpl2211.” *PLOS Genetics* 9 (8): e1003708. <https://doi.org/10.1371/journal.pgen.1003708>.
- Orvedahl, Anthony, Sarah MacPherson, Rhea Sumpter, Zsolt Tallóczy, Zhongju Zou, and Beth Levine. 2010. “Autophagy Protects against Sindbis Virus Infection of the Central Nervous System.” *Cell Host & Microbe* 7 (2): 115–27. <https://doi.org/10.1016/j.chom.2010.01.007>.
- Oslowski, Christine M., and Fumihiko Urano. 2011. “Measuring ER Stress and the Unfolded Protein Response Using Mammalian Tissue Culture System.” *Methods in Enzymology* 490: 71–92. <https://doi.org/10.1016/B978-0-12-385114-7.00004-0>.
- Ou, Tianling, Huihui Mou, Lizhou Zhang, Amrita Ojha, Hyeryun Choe, and Michael Farzan. 2021. “Hydroxychloroquine-Mediated Inhibition of SARS-CoV-2 Entry Is Attenuated by TMPRSS2.” *PLoS Pathogens* 17 (1): e1009212. <https://doi.org/10.1371/journal.ppat.1009212>.
- Pankiv, Serhiy, Terje Høyvarde Clausen, Trond Lamark, Andreas Brech, Jack-Ansgar Bruun, Heidi Outzen, Aud Øvervatn, Geir Bjørkøy, and Terje Johansen. 2007. “P62/SQSTM1 Binds Directly to Atg8/LC3 to Facilitate Degradation of Ubiquitinated Protein Aggregates by Autophagy*.” *Journal of Biological Chemistry* 282 (33): 24131–45. <https://doi.org/10.1074/jbc.M702824200>.
- Paredes, Felipe, Valentina Parra, Natalia Torrealba, Mario Navarro-Marquez, Damian Gatica, Roberto Bravo-Sagua, Rodrigo Troncoso, et al. 2016. “HERPUD1 Protects against Oxidative Stress-Induced Apoptosis through Downregulation of the Inositol 1,4,5-Trisphosphate Receptor.” *Free Radical Biology and Medicine* 90 (January): 206–18. <https://doi.org/10.1016/j.freeradbiomed.2015.11.024>.

- Park, Gina J., Adam Osinski, Genaro Hernandez, Jennifer L. Eitson, Abir Majumdar, Marco Tonelli, Katie Henzler-Wildman, et al. 2022. "The Mechanism of RNA Capping by SARS-CoV-2." *Research Square*, February, rs.3.rs-1336910. <https://doi.org/10.21203/rs.3.rs-1336910/v1>.
- Parzych, Katherine R., and Daniel J. Klionsky. 2014. "An Overview of Autophagy: Morphology, Mechanism, and Regulation." *Antioxidants & Redox Signaling* 20 (3): 460–73. <https://doi.org/10.1089/ars.2013.5371>.
- Poppe, Michael, Sascha Wittig, Liane Jurida, Marek Bartkuhn, Jochen Wilhelm, Helmut Müller, Knut Beuerlein, et al. 2017. "The NF- κ B-Dependent and -Independent Transcriptome and Chromatin Landscapes of Human Coronavirus 229E-Infected Cells." *PLOS Pathogens* 13 (3): e1006286. <https://doi.org/10.1371/journal.ppat.1006286>.
- Potting, Christoph, Christophe Crochemore, Francesca Moretti, Florian Nigsch, Isabel Schmidt, Carole Manneville, Walter Carbone, et al. 2018. "Genome-Wide CRISPR Screen for PARKIN Regulators Reveals Transcriptional Repression as a Determinant of Mitophagy." *Proceedings of the National Academy of Sciences* 115 (2): E180–89. <https://doi.org/10.1073/pnas.1711023115>.
- Preston, Amanda M., and Linda M. Hendershot. 2013. "Examination of a Second Node of Translational Control in the Unfolded Protein Response." *Journal of Cell Science* 126 (18): 4253–61. <https://doi.org/10.1242/jcs.130336>.
- Putyrski, Mateusz, Olesya Vakhrusheva, Florian Bonn, Suchithra Guntur, Andrew Vorobyov, Christian Brandts, Ivan Dikic, and Andreas Ernst. 2020. "Disrupting the LC3 Interaction Region (LIR) Binding of Selective Autophagy Receptors Sensitizes AML Cell Lines to Cytarabine." *Frontiers in Cell and Developmental Biology* 8 (March): 208. <https://doi.org/10.3389/fcell.2020.00208>.
- Qian, Zhaohui, Samuel R. Dominguez, and Kathryn V. Holmes. 2013a. "Role of the Spike Glycoprotein of Human Middle East Respiratory Syndrome Coronavirus (MERS-CoV) in Virus Entry and Syncytia Formation." *PLoS ONE* 8 (10): e76469. <https://doi.org/10.1371/journal.pone.0076469>.
- . 2013b. "Role of the Spike Glycoprotein of Human Middle East Respiratory Syndrome Coronavirus (MERS-CoV) in Virus Entry and Syncytia Formation." *PLoS ONE* 8 (10): e76469. <https://doi.org/10.1371/journal.pone.0076469>.
- Quiroga, Clara, Damian Gatica, Felipe Paredes, Roberto Bravo, Rodrigo Troncoso, Zully Pedrozo, Andrea E. Rodriguez, et al. 2013. "Herp Depletion Protects from Protein Aggregation by Up-Regulating Autophagy." *Biochimica et Biophysica Acta (BBA) - Molecular Cell Research* 1833 (12): 3295–3305. <https://doi.org/10.1016/j.bbamcr.2013.09.006>.
- Rabanal-Ruiz, Yoana, Elsje G. Otten, and Viktor I. Korolchuk. 2017. "MTORC1 as the Main Gateway to Autophagy." *Essays in Biochemistry* 61 (6): 565–84. <https://doi.org/10.1042/EBC20170027>.
- Rajah, Maaran Michael, Annie Bernier, Julian Buchrieser, and Olivier Schwartz. 2022. "The Mechanism and Consequences of SARS-CoV-2 Spike-Mediated Fusion and Syncytia Formation." *Journal of Molecular Biology* 434 (6): 167280. <https://doi.org/10.1016/j.jmb.2021.167280>.
- Ramakrishnan, Muthannan Andavar. 2016. "Determination of 50% Endpoint Titer Using a Simple Formula." *World Journal of Virology* 5 (2): 85–86. <https://doi.org/10.5501/wjv.v5.i2.85>.
- Ran, F. Ann, Patrick D. Hsu, Jason Wright, Vineeta Agarwala, David A. Scott, and Feng Zhang. 2013. "Genome Engineering Using the CRISPR-Cas9 System." *Nature Protocols* 8 (11): 2281–2308. <https://doi.org/10.1038/nprot.2013.143>.
- REED, L.J., and H. MUENCH. 1938. "A SIMPLE METHOD OF ESTIMATING FIFTY PER CENT ENDPOINTS12." *American Journal of Epidemiology* 27 (3): 493–97. <https://doi.org/10.1093/oxfordjournals.aje.a118408>.
- Reggiori, Fulvio, Iryna Monastyrska, Monique H. Verheije, Tito Cali, Mustafa Ulasli, Siro Bianchi, Riccardo Bernasconi, Cornelis A. M. de Haan, and Maurizio Molinari. 2010. "Coronaviruses Hijack the LC3-I-Positive EDEMosomes, ER-Derived Vesicles Exporting Short-Lived ERAD Regulators, for Replication." *Cell Host & Microbe* 7 (6): 500–508. <https://doi.org/10.1016/j.chom.2010.05.013>.
- Roingard, Philippe, Sébastien Eymieux, Julien Burlaud-Gaillard, Christophe Hourieux, Romuald Patient, and Emmanuelle Blanchard. 2022. "The Double-Membrane Vesicle (DMV): A Virus-

- Induced Organelle Dedicated to the Replication of SARS-CoV-2 and Other Positive-Sense Single-Stranded RNA Viruses.” *Cellular and Molecular Life Sciences* 79 (8): 425. <https://doi.org/10.1007/s00018-022-04469-x>.
- Romero-Brey, Inés, and Ralf Bartenschlager. 2016. “Endoplasmic Reticulum: The Favorite Intracellular Niche for Viral Replication and Assembly.” *Viruses* 8 (6): 160. <https://doi.org/10.3390/v8060160>.
- Roussigne, Myriam, Sophia Kossida, Anne-Claire Lavigne, Thomas Clouaire, Vincent Ecochard, Alexandra Glories, François Amalric, and Jean-Philippe Girard. 2003. “The THAP Domain: A Novel Protein Motif with Similarity to the DNA-Binding Domain of P Element Transposase.” *Trends in Biochemical Sciences* 28 (2): 66–69. [https://doi.org/10.1016/S0968-0004\(02\)00013-0](https://doi.org/10.1016/S0968-0004(02)00013-0).
- Roux, Kyle J., Dae In Kim, Manfred Raida, and Brian Burke. 2012. “A Promiscuous Biotin Ligase Fusion Protein Identifies Proximal and Interacting Proteins in Mammalian Cells.” *The Journal of Cell Biology* 196 (6): 801–10. <https://doi.org/10.1083/jcb.201112098>.
- Runwal, Gautam, Eleanna Stamatakou, Farah H. Siddiqi, Claudia Puri, Ye Zhu, and David C. Rubinsztein. 2019. “LC3-Positive Structures Are Prominent in Autophagy-Deficient Cells.” *Scientific Reports* 9 (1): 10147. <https://doi.org/10.1038/s41598-019-46657-z>.
- Russo, Lilian Cristina, Rebeka Tomasin, Isaac Araújo Matos, Antonio Carlos Manucci, Sven T. Sowa, Katie Dale, Keith W. Caldecott, et al. 2021. “The SARS-CoV-2 Nsp3 Macrodomain Reverses PARP9/DTX3L-Dependent ADP-Ribosylation Induced by Interferon Signaling.” *The Journal of Biological Chemistry* 297 (3): 101041. <https://doi.org/10.1016/j.jbc.2021.101041>.
- Sagnier, Sophie, Coralie F. Daussy, Sophie Borel, Véronique Robert-Hebmann, Mathias Faure, Fabien P. Blanchet, Bruno Beaumelle, Martine Biard-Piechaczyk, and Lucile Espert. 2014. “Autophagy Restricts HIV-1 Infection by Selectively Degrading Tat in CD4+ T Lymphocytes.” *Journal of Virology* 89 (1): 615–25. <https://doi.org/10.1128/JVI.02174-14>.
- Samtleben, Samira, Juliane Jaepel, Caroline Fecher, Thomas Andreska, Markus Rehberg, and Robert Blum. 2013. “Direct Imaging of ER Calcium with Targeted-Esterase Induced Dye Loading (TED).” *Journal of Visualized Experiments : JoVE*, no. 75 (May): 50317. <https://doi.org/10.3791/50317>.
- Sanjana, Neville E., Ophir Shalem, and Feng Zhang. 2014. “Improved Vectors and Genome-Wide Libraries for CRISPR Screening.” *Nature Methods* 11 (8): 783–84. <https://doi.org/10.1038/nmeth.3047>.
- Santulli, Gaetano, Ryutaro Nakashima, Qi Yuan, and Andrew R. Marks. 2017. “Intracellular Calcium Release Channels: An Update.” *The Journal of Physiology* 595 (10): 3041–51. <https://doi.org/10.1113/JP272781>.
- Sanvictores, Terrence, and Donald D. Davis. 2022. “Histology, Rough Endoplasmic Reticulum.” In *StatPearls*. Treasure Island (FL): StatPearls Publishing. <http://www.ncbi.nlm.nih.gov/books/NBK563126/>.
- Sargazi, Saman, Roghayeh Sheervalilou, Mohsen Rokni, Milad Shirvaliloo, Omolbanin Shahraki, and Nima Rezaei. 2021. “The Role of Autophagy in Controlling SARS-CoV-2 Infection: An Overview on Virophagy-mediated Molecular Drug Targets.” *Cell Biology International*, April, 10.1002/cbin.11609. <https://doi.org/10.1002/cbin.11609>.
- Satarker, Sairaj, and Madhavan Nampoothiri. 2020. “Structural Proteins in Severe Acute Respiratory Syndrome Coronavirus-2.” *Archives of Medical Research* 51 (6): 482–91. <https://doi.org/10.1016/j.arcmed.2020.05.012>.
- Satoo, Kenji, Nobuo Noda, Hiroyuki Kumeta, Yuko Fujioka, Noboru Mizushima, Yoshinori Ohsumi, and Fuyuhiko Inagaki. 2009. “The Structure of Atg4B–LC3 Complex Reveals the Mechanism of LC3 Processing and Delipidation during Autophagy.” *The EMBO Journal* 28 (9): 1341–50. <https://doi.org/10.1038/emboj.2009.80>.
- Saurav, Suman, Jyoti Tanwar, Kriti Ahuja, and Rajender K. Motiani. 2021. “Dysregulation of Host Cell Calcium Signaling during Viral Infections: Emerging Paradigm with High Clinical Relevance.” *Molecular Aspects of Medicine* 81 (October): 101004. <https://doi.org/10.1016/j.mam.2021.101004>.
- Schaletzky, Julia, and Tom A. Rapoport. 2006. “Ribosome Binding to and Dissociation from Translocation Sites of the Endoplasmic Reticulum Membrane.” *Molecular Biology of the Cell* 17 (9): 3860–69. <https://doi.org/10.1091/mbc.E06-05-0439>.

- Schmitz, M. Lienhard, M. Samer Shaban, B. Vincent Albert, Anke Gökçen, and Michael Kracht. 2018. “The Crosstalk of Endoplasmic Reticulum (ER) Stress Pathways with NF-KB: Complex Mechanisms Relevant for Cancer, Inflammation and Infection.” *Biomedicines* 6 (2): 58. <https://doi.org/10.3390/biomedicines6020058>.
- Schneider, Martha, Kerstin Ackermann, Melissa Stuart, Claudia Wex, Ulrike Protzer, Hermann M. Schätzl, and Sabine Gilch. 2012. “Severe Acute Respiratory Syndrome Coronavirus Replication Is Severely Impaired by MG132 Due to Proteasome-Independent Inhibition of M-Calpain.” *Journal of Virology* 86 (18): 10112–22. <https://doi.org/10.1128/JVI.01001-12>.
- Schoeman, Dewald, and Burtram C. Fielding. 2019. “Coronavirus Envelope Protein: Current Knowledge.” *Virology Journal* 16 (May): 69. <https://doi.org/10.1186/s12985-019-1182-0>.
- Schuck, Sebastian. 2020. “Microautophagy – Distinct Molecular Mechanisms Handle Cargoes of Many Sizes.” *Journal of Cell Science* 133 (17): jcs246322. <https://doi.org/10.1242/jcs.246322>.
- Schwarz, Dianne S., and Michael D. Blower. 2016. “The Endoplasmic Reticulum: Structure, Function and Response to Cellular Signaling.” *Cellular and Molecular Life Sciences* 73: 79–94. <https://doi.org/10.1007/s00018-015-2052-6>.
- Sears, Rhiannon M., Danielle G. May, and Kyle J. Roux. 2019. “BioID as a Tool for Protein-Proximity Labeling in Living Cells.” *Methods in Molecular Biology (Clifton, N.J.)* 2012: 299–313. https://doi.org/10.1007/978-1-4939-9546-2_15.
- Seroby, Vahan, Zacharias Kontarakis, Mohamed A El-Brolosy, Jordan M Welker, Oleg Tolstenkov, Amr M Saadeldein, Nicholas Retzer, Alexander Gottschalk, Ann M Wehman, and Didier YR Stainier. 2020. “Transcriptional Adaptation in *Caenorhabditis Elegans*.” Edited by Oliver Hobert, Jessica K Tyler, Michael Petrascheck, and Scott Kennedy. *ELife* 9 (January): e50014. <https://doi.org/10.7554/eLife.50014>.
- Shaban, Mohammed Samer, Christin Mayr-Buro, Johanna Meier-Soelch, Benadict Vincent Albert, M. Lienhard Schmitz, John Ziebuhr, and Michael Kracht. 2022. “Thapsigargin: Key to New Host-Directed Coronavirus Antivirals?” *Trends in Pharmacological Sciences*, April, S0165614722000840. <https://doi.org/10.1016/j.tips.2022.04.004>.
- Shaban, Mohammed Samer, Christin Müller, Christin Mayr-Buro, Hendrik Weiser, Johanna Meier-Soelch, Benadict Vincent Albert, Axel Weber, et al. 2021. “Multi-Level Inhibition of Coronavirus Replication by Chemical ER Stress.” *Nature Communications* 12 (1): 5536. <https://doi.org/10.1038/s41467-021-25551-1>.
- Shaban, Mohammed Samer, Christin Müller, Christin Mayr-Buro, Hendrik Weiser, M. Lienhard Schmitz, John Ziebuhr, and Michael Kracht. 2022. “Reply to: The Stress-Inducible ER Chaperone GRP78/BiP Is Upregulated during SARS-CoV-2 Infection and Acts as a pro-Viral Protein.” *Nature Communications* 13 (1): 6550. <https://doi.org/10.1038/s41467-022-34066-2>.
- Shalem, Ophir, Neville E. Sanjana, Ella Hartenian, Xi Shi, David A. Scott, Tarjei Mikkelsen, Dirk Heckl, et al. 2014. “Genome-Scale CRISPR-Cas9 Knockout Screening in Human Cells.” *Science (New York, N.Y.)* 343 (6166): 84–87. <https://doi.org/10.1126/science.1247005>.
- Shang, Chao, Zirui Liu, Yilong Zhu, Jing Lu, Chenchen Ge, Cuiling Zhang, Nan Li, et al. 2022. “SARS-CoV-2 Causes Mitochondrial Dysfunction and Mitophagy Impairment.” *Frontiers in Microbiology* 12. <https://www.frontiersin.org/articles/10.3389/fmicb.2021.780768>.
- Shapiro, David J., Mara Livezey, Liqun Yu, Xiaobin Zheng, and Neal Andruska. 2016. “Anticipatory UPR Activation: A Protective Pathway and Target in Cancer.” *Trends in Endocrinology and Metabolism: TEM* 27 (10): 731–41. <https://doi.org/10.1016/j.tem.2016.06.002>.
- Shen, Jingshi, and Ron Prywes. 2004. “Dependence of Site-2 Protease Cleavage of ATF6 on Prior Site-1 Protease Digestion Is Determined by the Size of the Luminal Domain of ATF6.” *The Journal of Biological Chemistry* 279 (41): 43046–51. <https://doi.org/10.1074/jbc.M408466200>.
- Sheshadri, Namratha, Shikha Sharan, and Esta Sterneck. 2017. “Abstract 4501: CEBPD Is an Early Endoplasmic Reticulum Stress Response Gene Implicated in Breast Cancer Cell Survival.” *Cancer Research* 77 (13_Supplement): 4501. <https://doi.org/10.1158/1538-7445.AM2017-4501>.
- Shetty, Ameet, Natalia I. Reim, and Fred Winston. 2019. “Auxin-Inducible Degron System for Depletion of Proteins in *S. Cerevisiae*.” *Current Protocols in Molecular Biology* 128 (1): e104. <https://doi.org/10.1002/cpmb.104>.

- Shi, Junchao, Zi Li, Rongyi Xu, Jing Zhang, Qianyu Zhou, Rui Gao, Huijun Lu, et al. 2022. “The PERK/PKR-EIF2 α Pathway Negatively Regulates Porcine Hemagglutinating Encephalomyelitis Virus Replication by Attenuating Global Protein Translation and Facilitating Stress Granule Formation.” *Journal of Virology* 96 (1): e0169521. <https://doi.org/10.1128/JVI.01695-21>.
- Shin, Woo-Jin, Dat P. Ha, Keigo Machida, and Amy S. Lee. 2022. “The Stress-Inducible ER Chaperone GRP78/BiP Is Upregulated during SARS-CoV-2 Infection and Acts as a pro-Viral Protein.” *Nature Communications* 13 (1): 6551. <https://doi.org/10.1038/s41467-022-34065-3>.
- Sicari, Daria, Aristotelis Chatziioannou, Theodoros Koutsandreas, Roberto Sitia, and Eric Chevet. 2020. “Role of the Early Secretory Pathway in SARS-CoV-2 Infection.” *Journal of Cell Biology* 219 (9): e202006005. <https://doi.org/10.1083/jcb.202006005>.
- Sielaff, Malte, Jörg Kuharev, Toszka Bohn, Jennifer Hahlbrock, Tobias Bopp, Stefan Tenzer, and Ute Distler. 2017. “Evaluation of FASP, SP3, and IST Protocols for Proteomic Sample Preparation in the Low Microgram Range.” *Journal of Proteome Research* 16 (11): 4060–72. <https://doi.org/10.1021/acs.jproteome.7b00433>.
- Sims, Amy C., Hugh D. Mitchell, Lisa E. Gralinski, Jennifer E. Kyle, Kristin E. Burnum-Johnson, Mariam Lam, M. Leslie Fulcher, et al. n.d. “Unfolded Protein Response Inhibition Reduces Middle East Respiratory Syndrome Coronavirus-Induced Acute Lung Injury.” *MBio* 12 (4): e01572-21. <https://doi.org/10.1128/mBio.01572-21>.
- Sircaik, Shabnam, Elvira Román, Priyanka Bapat, Keunsook K. Lee, David R. Andes, Neil A. R. Gow, Clarissa J. Nobile, Jesús Pla, and Sneha Lata Panwar. 2021. “The Protein Kinase Ire1 Impacts Pathogenicity of *Candida Albicans* by Regulating Homeostatic Adaptation to Endoplasmic Reticulum Stress.” *Cellular Microbiology* 23 (5): e13307. <https://doi.org/10.1111/cmi.13307>.
- Slanina, Heiko, Ramakanth Madhugiri, Ganesh Bylapudi, Karin Schultheiß, Nadja Karl, Anastasia Gulyaeva, Alexander E. Gorbalenya, Uwe Linne, and John Ziebuhr. 2021. “Coronavirus Replication–Transcription Complex: Vital and Selective NMPylation of a Conserved Site in Nsp9 by the NiRAN-RdRp Subunit.” *Proceedings of the National Academy of Sciences* 118 (6): e2022310118. <https://doi.org/10.1073/pnas.2022310118>.
- Smither, Sophie J., Calli Lear-Rooney, Julia Biggins, Jamie Pettitt, Mark S. Lever, and Gene G. Olinger. 2013. “Comparison of the Plaque Assay and 50% Tissue Culture Infectious Dose Assay as Methods for Measuring Filovirus Infectivity.” *Journal of Virological Methods* 193 (2): 565–71. <https://doi.org/10.1016/j.jviromet.2013.05.015>.
- Song, Qiaoyun, Bo Meng, Haidong Xu, and Zixu Mao. 2020. “The Emerging Roles of Vacuolar-Type ATPase-Dependent Lysosomal Acidification in Neurodegenerative Diseases.” *Translational Neurodegeneration* 9 (1): 17. <https://doi.org/10.1186/s40035-020-00196-0>.
- Sood, Vikas, Kiran Bala Sharma, Vishal Gupta, Dhurjhoti Saha, Parashar Dhapola, Manish Sharma, Utsav Sen, et al. 2017. “ATF3 Negatively Regulates Cellular Antiviral Signaling and Autophagy in the Absence of Type I Interferons.” *Scientific Reports* 7 (1): 8789. <https://doi.org/10.1038/s41598-017-08584-9>.
- Strong, Lisa M, Chunmei Chang, Julia F Riley, C Alexander Boecker, Thomas G Flower, Cosmo Z Buffalo, Xuefeng Ren, Andrea KH Stavoe, Erika LF Holzbaur, and James H Hurley. 2021. “Structural Basis for Membrane Recruitment of ATG16L1 by WIPI2 in Autophagy.” Edited by Wade Harper and Volker Dötsch. *ELife* 10 (September): e70372. <https://doi.org/10.7554/eLife.70372>.
- Sun, Di, Xingjian Wen, Mingshu Wang, Sai Mao, Anchun Cheng, Xiaoyao Yang, Renyong Jia, et al. 2019. “Apoptosis and Autophagy in Picornavirus Infection.” *Frontiers in Microbiology* 10 (September): 2032. <https://doi.org/10.3389/fmicb.2019.02032>.
- Sungsuwan, Suttipun, Anan Jongkaewwattana, and Peera Jaru-Ampornpan. 2020. “Nucleocapsid Proteins from Other Swine Enteric Coronaviruses Differentially Modulate PEDV Replication.” *Virology* 540 (January): 45–56. <https://doi.org/10.1016/j.virol.2019.11.007>.
- Swatek, Kirby N., and David Komander. 2016. “Ubiquitin Modifications.” *Cell Research* 26 (4): 399–422. <https://doi.org/10.1038/cr.2016.39>.
- Szklarczyk, Damian, Annika L. Gable, David Lyon, Alexander Junge, Stefan Wyder, Jaime Huerta-Cepas, Milan Simonovic, et al. 2019. “STRING V11: Protein-Protein Association Networks

- with Increased Coverage, Supporting Functional Discovery in Genome-Wide Experimental Datasets.” *Nucleic Acids Research* 47 (D1): D607–13. <https://doi.org/10.1093/nar/gky1131>.
- Sztal, Tamar E., and Didier Y. R. Stainier. 2020. “Transcriptional Adaptation: A Mechanism Underlying Genetic Robustness.” *Development* 147 (15): dev186452. <https://doi.org/10.1242/dev.186452>.
- Tao, Sha, and Ingo Drexler. 2020. “Targeting Autophagy in Innate Immune Cells: Angel or Demon During Infection and Vaccination?” *Frontiers in Immunology* 11. <https://www.frontiersin.org/articles/10.3389/fimmu.2020.00460>.
- Tchesnokov, Egor P., Joy Y. Feng, Danielle P. Porter, and Matthias Götte. 2019. “Mechanism of Inhibition of Ebola Virus RNA-Dependent RNA Polymerase by Remdesivir.” *Viruses* 11 (4): 326. <https://doi.org/10.3390/v11040326>.
- Teske, Brian F., Thomas D. Baird, and Ronald C. Wek. 2011. “Chapter Nineteen - Methods for Analyzing EIF2 Kinases and Translational Control in the Unfolded Protein Response.” In *Methods in Enzymology*, edited by P. Michael Conn, 490:333–56. The Unfolded Protein Response and Cellular Stress, Part B. Academic Press. <https://doi.org/10.1016/B978-0-12-385114-7.00019-2>.
- Thastrup, O, P J Cullen, B K Drøbak, M R Hanley, and A P Dawson. 1990. “Thapsigargin, a Tumor Promoter, Discharges Intracellular Ca²⁺ Stores by Specific Inhibition of the Endoplasmic Reticulum Ca²⁺(+)-ATPase.” *Proceedings of the National Academy of Sciences of the United States of America* 87 (7): 2466–70.
- Thiel, Volker, Konstantin A. Ivanov, Ákos Putics, Tobias Hertzog, Barbara Schelle, Sonja Bayer, Benedikt Weißbrich, et al. 2003. “Mechanisms and Enzymes Involved in SARS Coronavirus Genome Expression.” *The Journal of General Virology* 84 (Pt 9): 2305–15. <https://doi.org/10.1099/vir.0.19424-0>.
- Thompson, Matthew, Dakang Xu, and Bryan R.G. Williams. 2009. “ATF3 Transcription Factor and Its Emerging Roles in Immunity and Cancer.” *Journal of Molecular Medicine (Berlin, Germany)* 87 (11): 1053–60. <https://doi.org/10.1007/s00109-009-0520-x>.
- Tong, XiaoYong, Alicia Evangelista, and Richard A. Cohen. 2010. “Targeting the Redox Regulation of SERCA in Vascular Physiology and Disease.” *Current Opinion in Pharmacology* 10 (2): 133–38. <https://doi.org/10.1016/j.coph.2009.11.008>.
- Torrealba, Natalia, Mario Navarro-Marquez, Valeria Garrido, Zully Pedrozo, Diego Romero, Yuka Eura, Elisa Villalobos, et al. 2017. “Herpud1 Negatively Regulates Pathological Cardiac Hypertrophy by Inducing IP3 Receptor Degradation.” *Scientific Reports* 7 (1): 13402. <https://doi.org/10.1038/s41598-017-13797-z>.
- Torres, Mauricio, Gonzalo Encina, Claudi Soto, and Claudio Hetz. 2011. “Abnormal Calcium Homeostasis and Protein Folding Stress at the ER.” *Communicative & Integrative Biology* 4 (3): 258–61. <https://doi.org/10.4161/cib.4.3.15019>.
- Travers, K. J., C. K. Patil, L. Wodicka, D. J. Lockhart, J. S. Weissman, and P. Walter. 2000. “Functional and Genomic Analyses Reveal an Essential Coordination between the Unfolded Protein Response and ER-Associated Degradation.” *Cell* 101 (3): 249–58. [https://doi.org/10.1016/s0092-8674\(00\)80835-1](https://doi.org/10.1016/s0092-8674(00)80835-1).
- Tsapras, Panagiotis, Stavroula Petridi, Selina Chan, Marta Geborys, Anne-Claire Jacomin, Antonia P. Sagona, Pascal Meier, and Ioannis P. Nezis. 2022. “Selective Autophagy Controls Innate Immune Response through a TAK1/TAB2/SH3PX1 Axis.” *Cell Reports* 38 (4): 110286. <https://doi.org/10.1016/j.celrep.2021.110286>.
- Tsukada, M., and Y. Ohsumi. 1993. “Isolation and Characterization of Autophagy-Defective Mutants of *Saccharomyces Cerevisiae*.” *FEBS Letters* 333 (1–2): 169–74. [https://doi.org/10.1016/0014-5793\(93\)80398-e](https://doi.org/10.1016/0014-5793(93)80398-e).
- Tvarogová, Jana, Ramakanth Madhugiri, Ganesh Bylapudi, Lyndsey J. Ferguson, Nadja Karl, and John Ziebuhr. n.d. “Identification and Characterization of a Human Coronavirus 229E Nonstructural Protein 8-Associated RNA 3'-Terminal Adenylyltransferase Activity.” *Journal of Virology* 93 (12): e00291-19. <https://doi.org/10.1128/JVI.00291-19>.
- Twu, Woan-Ing, Ji-Young Lee, Heeyoung Kim, Vibhu Prasad, Berati Cerikan, Uta Haselmann, Keisuke Tabata, and Ralf Bartenschlager. 2021. “Contribution of Autophagy Machinery Factors to HCV and SARS-CoV-2 Replication Organelle Formation.” *Cell Reports* 37 (8): 110049. <https://doi.org/10.1016/j.celrep.2021.110049>.

- Ullmann, Tatjana, Sonja Luckhardt, Markus Wolf, Michael J. Parnham, and Eduard Resch. 2021. "High-Throughput Screening for CEBPD-Modulating Compounds in THP-1-Derived Reporter Macrophages Identifies Anti-Inflammatory HDAC and BET Inhibitors." *International Journal of Molecular Sciences* 22 (6): 3022. <https://doi.org/10.3390/ijms22063022>.
- Vasudevan, Deepika, Sarah D. Neuman, Amy Yang, Lea Lough, Brian Brown, Arash Bashirullah, Timothy Cardozo, and Hyung Don Ryoo. 2020. "Translational Induction of ATF4 during Integrated Stress Response Requires Noncanonical Initiation Factors EIF2D and DENR." *Nature Communications* 11 (1): 4677. <https://doi.org/10.1038/s41467-020-18453-1>.
- Vaure, Céline, and Yuanqing Liu. 2014. "A Comparative Review of Toll-Like Receptor 4 Expression and Functionality in Different Animal Species." *Frontiers in Immunology* 5. <https://www.frontiersin.org/articles/10.3389/fimmu.2014.00316>.
- Velthuis, Aartjan J.W. te, Sjoerd H. E. van den Worm, and Eric J. Snijder. 2012. "The SARS-Coronavirus Nsp7+nsp8 Complex Is a Unique Multimeric RNA Polymerase Capable of Both de Novo Initiation and Primer Extension." *Nucleic Acids Research* 40 (4): 1737–47. <https://doi.org/10.1093/nar/gkr893>.
- Vembar, Shruthi S., and Jeffrey L. Brodsky. 2008. "One Step at a Time: Endoplasmic Reticulum-Associated Degradation." *Nature Reviews Molecular Cell Biology* 9 (12): 944–57. <https://doi.org/10.1038/nrm2546>.
- Verfaillie, T, N Rubio, A D Garg, G Bultynck, R Rizzuto, J-P Decuypere, J Piette, et al. 2012. "PERK Is Required at the ER-Mitochondrial Contact Sites to Convey Apoptosis after ROS-Based ER Stress." *Cell Death and Differentiation* 19 (11): 1880–91. <https://doi.org/10.1038/cdd.2012.74>.
- Vijgen, Leen, Els Keyaerts, Kalina Zlateva, and Marc Van Ranst. 2004. "Identification of Six New Polymorphisms in the Human Coronavirus 229E Receptor Gene (Aminopeptidase N/CD13)." *International Journal of Infectious Diseases: IJID: Official Publication of the International Society for Infectious Diseases* 8 (4): 217–22. <https://doi.org/10.1016/j.ijid.2004.03.004>.
- V'kovski, Philip, Annika Kratzel, Silvio Steiner, Hanspeter Stalder, and Volker Thiel. 2021. "Coronavirus Biology and Replication: Implications for SARS-CoV-2." *Nature Reviews Microbiology* 19 (3): 155–70. <https://doi.org/10.1038/s41579-020-00468-6>.
- Volmer, Romain, Kattria van der Ploeg, and David Ron. 2013. "Membrane Lipid Saturation Activates Endoplasmic Reticulum Unfolded Protein Response Transducers through Their Transmembrane Domains." *Proceedings of the National Academy of Sciences of the United States of America* 110 (12): 4628–33. <https://doi.org/10.1073/pnas.1217611110>.
- Walter, P., and A. E. Johnson. 1994. "Signal Sequence Recognition and Protein Targeting to the Endoplasmic Reticulum Membrane." *Annual Review of Cell Biology* 10: 87–119. <https://doi.org/10.1146/annurev.cb.10.110194.000511>.
- Wang, Chiung-Min, Victoria C. Brennan, Ninoska M. Gutierrez, Xirui Wang, Lizhong Wang, and Wei-Hsiung Yang. 2013. "SUMOylation of ATF3 Alters Its Transcriptional Activity on Regulation of TP53 Gene." *Journal of Cellular Biochemistry* 114 (3): 589–98. <https://doi.org/10.1002/jcb.24396>.
- Wang, Miao, and Randal J. Kaufman. 2014. "The Impact of the Endoplasmic Reticulum Protein-Folding Environment on Cancer Development." *Nature Reviews Cancer* 14 (9): 581–97. <https://doi.org/10.1038/nrc3800>.
- . 2016. "Protein Misfolding in the Endoplasmic Reticulum as a Conduit to Human Disease." *Nature* 529 (7586): 326–35. <https://doi.org/10.1038/nature17041>.
- Wang, Peng, Jingzhi Li, Jiahui Tao, and Bingdong Sha. 2018. "The Luminal Domain of the ER Stress Sensor Protein PERK Binds Misfolded Proteins and Thereby Triggers PERK Oligomerization." *Journal of Biological Chemistry* 293 (11): 4110–21. <https://doi.org/10.1074/jbc.RA117.001294>.
- Wang, Shaobo, Yang Liu, Jiao Guo, Peilin Wang, Leike Zhang, Gengfu Xiao, and Wei Wang. 2017. "Screening of FDA-Approved Drugs for Inhibitors of Japanese Encephalitis Virus Infection." *Journal of Virology* 91 (21): e01055-17. <https://doi.org/10.1128/JVI.01055-17>.
- Wang, Yongyao, Linsen Li, Chen Hou, Ying Lai, Jiangang Long, Jiankang Liu, Qing Zhong, and Jiajie Diao. 2016. "SNARE-Mediated Membrane Fusion in Autophagy." *Seminars in Cell &*

- Developmental Biology* 60 (December): 97–104.
<https://doi.org/10.1016/j.semcd.2016.07.009>.
- Warren, Wesley C., Anna J. Jasinska, Raquel García-Pérez, Hannes Svardal, Chad Tomlinson, Mariano Rocchi, Nicoletta Archidiacono, et al. 2015. “The Genome of the Vervet (*Chlorocebus Aethiops Sabaeus*).” *Genome Research* 25 (12): 1921–33.
<https://doi.org/10.1101/gr.192922.115>.
- Watanabe, Shinji, Tokiko Watanabe, and Yoshihiro Kawaoka. 2009. “Influenza A Virus Lacking M2 Protein as a Live Attenuated Vaccine.” *Journal of Virology* 83 (11): 5947–50.
<https://doi.org/10.1128/JVI.00450-09>.
- Weiss, Susan R. 2020. “Forty Years with Coronaviruses.” *The Journal of Experimental Medicine* 217 (5): e20200537. <https://doi.org/10.1084/jem.20200537>.
- Weiss, Susan R., and Sonia Navas-Martin. 2005. “Coronavirus Pathogenesis and the Emerging Pathogen Severe Acute Respiratory Syndrome Coronavirus.” *Microbiology and Molecular Biology Reviews* 69 (4): 635–64. <https://doi.org/10.1128/MMBR.69.4.635-664.2005>.
- Wilamowski, Mateusz, Darren A. Sherrell, George Minasov, Youngchang Kim, Ludmilla Shuvalova, Alex Lavens, Ryan Chard, et al. 2021. “2'-O Methylation of RNA Cap in SARS-CoV-2 Captured by Serial Crystallography.” *Proceedings of the National Academy of Sciences* 118 (21): e2100170118. <https://doi.org/10.1073/pnas.2100170118>.
- Wilde, Adriaan H. de, V. Stalin Raj, Diede Oudshoorn, Theo M. Bestebroer, Stefan van Nieuwkoop, Ronald W. A. L. Limpens, Clara C. Posthuma, et al. 2013. “MERS-Coronavirus Replication Induces Severe in Vitro Cytopathology and Is Strongly Inhibited by Cyclosporin A or Interferon- α Treatment.” *The Journal of General Virology* 94 (Pt 8): 1749–60.
<https://doi.org/10.1099/vir.0.052910-0>.
- Wolff, Georg, Charlotte E. Melia, Eric J. Snijder, and Montserrat Bárcena. 2020. “Double-Membrane Vesicles as Platforms for Viral Replication.” *Trends in Microbiology*, June, S0966842X20301359. <https://doi.org/10.1016/j.tim.2020.05.009>.
- Wolfgang, C. D., B. P. Chen, J. L. Martindale, N. J. Holbrook, and T. Hai. 1997. “Gadd153/Chop10, a Potential Target Gene of the Transcriptional Repressor ATF3.” *Molecular and Cellular Biology* 17 (11): 6700–6707. <https://doi.org/10.1128/MCB.17.11.6700>.
- Wong, Louise H., James R. Edgar, Andrea Martello, Brian J. Ferguson, and Emily R. Eden. 2021. “Exploiting Connections for Viral Replication.” *Frontiers in Cell and Developmental Biology* 9. <https://www.frontiersin.org/articles/10.3389/fcell.2021.640456>.
- Wu, Haoxi, Benjamin S. H. Ng, and Guillaume Thibault. 2014. “Endoplasmic Reticulum Stress Response in Yeast and Humans.” *Bioscience Reports* 34 (4): e00118.
<https://doi.org/10.1042/BSR20140058>.
- Wu, Hung-Yi, and David A. Brian. 2010. “Subgenomic Messenger RNA Amplification in Coronaviruses.” *Proceedings of the National Academy of Sciences* 107 (27): 12257–62.
<https://doi.org/10.1073/pnas.1000378107>.
- Xie, Zhiping, and Daniel J. Klionsky. 2007. “Autophagosome Formation: Core Machinery and Adaptations.” *Nature Cell Biology* 9 (10): 1102–9. <https://doi.org/10.1038/ncb1007-1102>.
- Xu, Chengchao, and Davis T. W. Ng. 2015. “Glycosylation-Directed Quality Control of Protein Folding.” *Nature Reviews Molecular Cell Biology* 16 (12): 742–52.
<https://doi.org/10.1038/nrm4073>.
- Xu, Yi, and N. Tony Eissa. 2010. “Autophagy in Innate and Adaptive Immunity.” *Proceedings of the American Thoracic Society* 7 (1): 22–28. <https://doi.org/10.1513/pats.200909-103JS>.
- Xue, Mei, Fang Fu, Yanlong Ma, Xin Zhang, Liang Li, Li Feng, and Pinghuang Liu. 2018. “The PERK Arm of the Unfolded Protein Response Negatively Regulates Transmissible Gastroenteritis Virus Replication by Suppressing Protein Translation and Promoting Type I IFN Production.” *Journal of Virology*, May, JVI.00431-18. <https://doi.org/10.1128/JVI.00431-18>.
- Yadav, Rohitash, Jitendra Kumar Chaudhary, Neeraj Jain, Pankaj Kumar Chaudhary, Supriya Khanra, Puneet Dhamija, Ambika Sharma, Ashish Kumar, and Shailendra Handu. 2021. “Role of Structural and Non-Structural Proteins and Therapeutic Targets of SARS-CoV-2 for COVID-19.” *Cells* 10 (4): 821. <https://doi.org/10.3390/cells10040821>.
- Yamaguchi, Suguru, Hisamitsu Ishihara, Takahiro Yamada, Akira Tamura, Masahiro Usui, Ryu Tominaga, Yuichiro Munakata, et al. 2008. “ATF4-Mediated Induction of 4E-BP1

- Contributes to Pancreatic Beta Cell Survival under Endoplasmic Reticulum Stress.” *Cell Metabolism* 7 (3): 269–76. <https://doi.org/10.1016/j.cmet.2008.01.008>.
- Yan, Chunhong, and Douglas D. Boyd. 2006. “ATF3 Regulates the Stability of P53: A Link to Cancer.” *Cell Cycle (Georgetown, Tex.)* 5 (9): 926–29. <https://doi.org/10.4161/cc.5.9.2714>.
- Yan, Chunhong, Dan Lu, Tsonwin Hai, and Douglas D Boyd. 2005. “Activating Transcription Factor 3, a Stress Sensor, Activates P53 by Blocking Its Ubiquitination.” *The EMBO Journal* 24 (13): 2425–35. <https://doi.org/10.1038/sj.emboj.7600712>.
- Yang, Yiyang, Wei Yan, A Brantley Hall, and Xiaofang Jiang. 2021. “Characterizing Transcriptional Regulatory Sequences in Coronaviruses and Their Role in Recombination.” *Molecular Biology and Evolution* 38 (4): 1241–48. <https://doi.org/10.1093/molbev/msaa281>.
- Yesbolatova, Aisha, Yuichiro Saito, Naomi Kitamoto, Hatsune Makino-Itou, Rieko Ajima, Risako Nakano, Hirofumi Nakaoka, et al. 2020. “The Auxin-Inducible Degron 2 Technology Provides Sharp Degradation Control in Yeast, Mammalian Cells, and Mice.” *Nature Communications* 11 (1): 5701. <https://doi.org/10.1038/s41467-020-19532-z>.
- Yim, Willa Wen-You, and Noboru Mizushima. 2020. “Lysosome Biology in Autophagy.” *Cell Discovery* 6 (1): 6. <https://doi.org/10.1038/s41421-020-0141-7>.
- Yorimitsu, Tomohiro, Usha Nair, Zhifen Yang, and Daniel J. Klionsky. 2006. “Endoplasmic Reticulum Stress Triggers Autophagy.” *The Journal of Biological Chemistry* 281 (40): 30299–304. <https://doi.org/10.1074/jbc.M607007200>.
- Yoshida, H., K. Haze, H. Yanagi, T. Yura, and K. Mori. 1998. “Identification of the Cis-Acting Endoplasmic Reticulum Stress Response Element Responsible for Transcriptional Induction of Mammalian Glucose-Regulated Proteins. Involvement of Basic Leucine Zipper Transcription Factors.” *The Journal of Biological Chemistry* 273 (50): 33741–49. <https://doi.org/10.1074/jbc.273.50.33741>.
- Yoshii, Saori R., and Noboru Mizushima. 2017. “Monitoring and Measuring Autophagy.” *International Journal of Molecular Sciences* 18 (9). <https://doi.org/10.3390/ijms18091865>.
- Yu, Tao, Yong Jun Li, Ai Hong Bian, Hui Bin Zuo, Ti Wen Zhu, Sheng Xiang Ji, Fanming Kong, et al. 2014. “The Regulatory Role of Activating Transcription Factor 2 in Inflammation.” *Mediators of Inflammation* 2014 (June): e950472. <https://doi.org/10.1155/2014/950472>.
- Zhang, Dejiu, Lei Zhu, Yin Wang, Peifeng Li, and Yanyan Gao. 2022. “Translational Control of COVID-19 and Its Therapeutic Implication.” *Frontiers in Immunology* 13. <https://www.frontiersin.org/article/10.3389/fimmu.2022.857490>.
- Zhang, Lei-Ke, Yuan Sun, Haolong Zeng, Qingxing Wang, Xiaming Jiang, Wei-Juan Shang, Yan Wu, et al. 2020. “Calcium Channel Blocker Amlodipine Besylate Therapy Is Associated with Reduced Case Fatality Rate of COVID-19 Patients with Hypertension.” *Cell Discovery* 6 (1): 96. <https://doi.org/10.1038/s41421-020-00235-0>.
- Zhang, Mei-Ling, Ming-Li Li, Adeola Oluwakemi Ayoola, Robert W. Murphy, Dong-Dong Wu, and Yong Shao. 2019. “Conserved Sequences Identify the Closest Living Relatives of Primates.” *Zoological Research* 40 (6): 532–40. <https://doi.org/10.24272/j.issn.2095-8137.2019.057>.
- Zhang, Ronghua, Kai Wang, Wei Lv, Wenjing Yu, Shiqi Xie, Ke Xu, Wolfgang Schwarz, Sidong Xiong, and Bing Sun. 2014. “The ORF4a Protein of Human Coronavirus 229E Functions as a Viroporin That Regulates Viral Production.” *Biochimica et Biophysica Acta (BBA) - Biomembranes, Viral Membrane Proteins - Channels for Cellular Networking*, 1838 (4): 1088–95. <https://doi.org/10.1016/j.bbamem.2013.07.025>.
- Zhang, Yongliang, Gaoyuan Song, Neeraj K. Lal, Ugrappa Nagalakshmi, Yuanyuan Li, Wenjie Zheng, Pin-jui Huang, et al. 2019. “TurboID-Based Proximity Labeling Reveals That UBR7 Is a Regulator of N NLR Immune Receptor-Mediated Immunity.” *Nature Communications* 10 (1): 1–17. <https://doi.org/10.1038/s41467-019-11202-z>.
- Zhao, Zhenyu, Kefeng Lu, Binli Mao, Shi Liu, Mirko Trilling, Ailong Huang, Mengji Lu, and Yong Lin. 2021. “The Interplay between Emerging Human Coronavirus Infections and Autophagy.” *Emerging Microbes & Infections* 10 (1): 196–205. <https://doi.org/10.1080/22221751.2021.1872353>.
- Zhao, Zijiang, Larissa B. Thackray, Brian C. Miller, Teresa M. Lynn, Michelle M. Becker, Eric Ward, Noboru N. Mizushima, Mark R. Denison, and Herbert W. Virgin. 2007. “Coronavirus Replication Does Not Require the Autophagy Gene ATG5.” *Autophagy* 3 (6): 581–85. <https://doi.org/10.4161/auto.4782>.

- Zheng, Wei, Weiwei Xie, Danyang Yin, Rui Luo, Min Liu, and Fengjin Guo. 2019. "ATG5 and ATG7 Induced Autophagy Interplays with UPR via PERK Signaling." *Cell Communication and Signaling* 17 (1): 42. <https://doi.org/10.1186/s12964-019-0353-3>.
- Zhou, Yingyao, Bin Zhou, Lars Pache, Max Chang, Alireza Hadj Khodabakhshi, Olga Tanaseichuk, Christopher Benner, and Sumit K. Chanda. 2019. "Metascape Provides a Biologist-Oriented Resource for the Analysis of Systems-Level Datasets." *Nature Communications* 10 (1): 1523. <https://doi.org/10.1038/s41467-019-09234-6>.
- Zhu, C.-Y., C.-Y. Li, Y. Li, Y.-Q. Zhan, Y.-H. Li, C.-W. Xu, W.-X. Xu, H. B. Sun, and X.-M. Yang. 2009. "Cell Growth Suppression by Thanatos-Associated Protein 11 (THAP11) Is Mediated by Transcriptional Downregulation of c-Myc." *Cell Death & Differentiation* 16 (3): 395–405. <https://doi.org/10.1038/cdd.2008.160>.
- Zhu, Zhixing, Xihua Lian, Xiaoshan Su, Weijing Wu, Giuseppe A. Marraro, and Yiming Zeng. 2020. "From SARS and MERS to COVID-19: A Brief Summary and Comparison of Severe Acute Respiratory Infections Caused by Three Highly Pathogenic Human Coronaviruses." *Respiratory Research* 21 (1): 224. <https://doi.org/10.1186/s12931-020-01479-w>.
- Ziebuhr, John, and Stuart G. Siddell. 1999. "Processing of the Human Coronavirus 229E Replicase Polyproteins by the Virus-Encoded 3C-Like Proteinase: Identification of Proteolytic Products and Cleavage Sites Common to Pp1a and Pp1ab." *Journal of Virology* 73 (1): 177–85.
- Ziebuhr, John, Eric J. Snijder, and Alexander E. YR 2000 Gorbalenya. n.d. "Virus-Encoded Proteinases and Proteolytic Processing in the Nidovirales." *Journal of General Virology* 81 (4): 853–79. <https://doi.org/10.1099/0022-1317-81-4-853>.
- Zimmermann, Christine, Nadine Krämer, Steffi Krauter, Dennis Strand, Elisabeth Sehn, Uwe Wolfrum, Anja Freiwald, Falk Butter, and Bodo Plachter. 2021. "Autophagy Interferes with Human Cytomegalovirus Genome Replication, Morphogenesis, and Progeny Release." *Autophagy* 17 (3): 779–95. <https://doi.org/10.1080/15548627.2020.1732686>.

List of abbreviations:

°C	Degree celsius
μ	micro
ARDS	Acute respiratory distress syndrome
as	Antisense
ATP	Adenosine triphosphate
BCoV	Bovine coronavirus
bp	Base pairs
BSA	Bovine serum albumin
Cas9	CRISPR associated protein 9
CFR	Case fatality rate
ChIP	chromatin immunoprecipitation
CIAP	Calf Intestinal Alkaline Phosphatase
CM	Convolutated membrane
CMA	Chaperone-mediated autophagy
CoV	Coronaviruses
CRISPR	Clustered regularly interspaced short palindromic repeats
Da	Dalton
ddH ₂ O	Double distilled water
DMEM	Dulbecco's modified Eagle's Medium
DMSO	Dimethyl sulfoxide
DMV	Double-membrane vesicle
DNA	Deoxyribonucleic acid
dNTP	Deoxynucleotide triphosphates
<i>E. coli</i>	<i>Escherichia coli</i>
e.g.	Example
EDTA	Ethylenediaminetetraacetic acid
ER	Endoplasmic reticulum
ERAD	ER-associated degradation
ERGIC	ER/Golgi intermediate compartment
ERQC	ER-quality control
ERSE	ER stress response element
FBS	Fetal bovine serum
FCS	Foetal calf serum
Fig.	Figure
GFP	Green fluorescent protein
HBSS	Hank's Balanced Salt Solution
i.e.	That means
kDa	kilodalton
M	Molar
mA	Milliampere
MERS	Middle East respiratory syndrome
MHV	Murine hepatitis virus
mM	Millimolar
ng	Nanogram
NSP, nsp	Nonstructural protein

PBS	Phosphate buffered saline
PEDV	Porcine epidemic diarrhea virus
PVDF	Polyvinylidene fluoride
qPCR	Quantitative polymerase chain reaction
RBD	Receptor binding domain
RNA	Ribonucleic acid
RO	Replicative organelle
RPM	Rounds per minute
RTC	Replication-transcription complex
SARS	Severe acute respiratory syndrome
se	Sense
seq	sequencing
sgmRNA	Sub-genomic messenger RNA
sgRNA	Single guide RNA
ssgRNA	Single-stranded viral genomic RNA
TAE	Tris-Acetate EDTA
TBS	Tris buffered saline
TCID ₅₀	Tissue culture infectious dose 50%
TEMED	N,N,N',N'-Tetramethylethylenediamine
TGEV	Transmissible gastroenteritis virus
U	Unit (The enzyme unit)
UPR	Unfolded protein response
UTR	Untranslated region
V	Volts
μl	Microliter
μm	Micrometer
μM	Micromolar

List of figures:

Figure 1: Taxonomy of Coronaviridae with the seven coronaviruses that infect human beings.....	14
Figure 2: Genomic structure of the seven coronaviruses that infect human beings.	16
Figure 3: CoV structural and accessory proteins are produced from sub-genomic messenger RNAs..	17
Figure 4: CoV replication cycle.	21
Figure 5: The three branches of UPR.	26
Figure 6: Autolysosome formation.....	31
Figure 7: An illustrative example taken from this study of the TCID ₅₀ calculations using the Reed–Muench method.	63
Figure 8: An illustrative example taken from this study of the MOI calculations using plaque assay...	64
Figure 9: An illustrative example taken from this study of quantifying protein bands using ImageLab software.	69
Figure 10: Example of a workflow of raw data processing in Perseus.	83
Figure 11: The putative roles of the canonical UPR pathways in the host response to CoV replication.	85
Figure 12: Differential effects of the PERK inhibitor GSK2606414 and the IRE1 α inhibitor KIRA6 on the ER stress response and replication of HCoV-229E.....	86
Figure 13: Differential regulation of host proteins de-novo synthesis in the presence or absence of HCoV-229E infection by PERK inhibitor GSK2606414 and the IRE1 α inhibitor KIRA6.	89
Figure 14: CoV and thapsigargin activation of ER stress and UPR pathways.....	91
Figure 15: Thapsigargin profoundly inhibits the replication of HCoV-229E in Huh7 cells.	94
Figure 16: The anti-viral effect of thapsigargin observed by immuno-florescence analysis.....	96
Figure 17: Prolonged treatment of infected cells with thapsigargin partially reverses the HCoV-229E-induced translational shutdown.	98
Figure 18: Thapsigargin anti-viral effect is reproducible in MRC-5 cells.	100
Figure 19: Thapsigargin inhibits HCoV-229E replication in Huh7 cells with an EC ₅₀ in the lower nanomolar range while exerting cytotoxicity with a CC ₅₀ in the micromolar range.	102
Figure 20: Thapsigargin inhibition of HCoV-229E is readily visible at lower concentrations and up to 14 hours post-infection.	104
Figure 21: Thapsigargin inhibition of HCoV-229E is durable over prolonged incubation periods and after medium exchange.	106
Figure 22: Thapsigargin inhibits the replication of MERS-CoV and SARS-CoV-2 in cellular models.	108
Figure 23: PERK inhibition does not affect the anti-viral state induced by thapsigargin.	110
Figure 24: Proteome-wide investigation of thapsigargin’s anti-viral effects.	112
Figure 25: Overview of all deregulated proteins in response to thapsigargin treatment in the presence or absence of CoV infection.	113
Figure 26: Thapsigargin-induced regulations of proteins dominate over CoV-induced regulations. .	115
Figure 27: Thapsigargin regulation of several ERAD/ERQC factors.	117
Figure 28: heatmaps of the top 100 differentially enriched pathways in MERS-CoV infected Huh7 and SARS-CoV-2 infected VERO-E6 cells for 12 or 24 hours.	120
Figure 29: Top 5 (for both viruses at both time points) and top 10 (for thapsigargin treatments at both time points) pathways of up- or downregulated DEPs extracted from the top 100 deregulated pathways.	122
Figure 30: Thapsigargin treatments of cellular models invoked a unique metabolic response that coincided with an anti-viral effect.	123
Figure 31: HCoV-229E infection induces specific (p62 based) autophagy flux, while thapsigargin inhibits it.....	126
Figure 32: Bafilomycin A1 inhibition of HCoV-229E is time of treatment dependent.	128

Figure 33: Representative images of one out of two biological replicas of fluorescently labeled Huh7 cells with nsp8 (green) and p62 (red) antibodies along with phase-contrast (Ph) light microscopy images. Green signal indicates the HCoV-229E replication sites while red signal shows p62-positive puncta under indicated conditions.	129
Figure 34: Bafilmycine A1 inhibition of CoV replication is pathogen- and time of treatment-dependent.	130
Figure 35: Regulation of autophagy flux and HCoV-229E replication in the context of PERK inhibition.	132
Figure 36: Regulation of autophagy flux and MERS-CoV replication in the context of PERK inhibition.	134
Figure 37: Regulation of autophagy flux and SARS-CoV-2 replication in the context of GSK treatments.	136
Figure 38: The schematic representation described in figure 11 is used here to illustrate the targets of the CRISPR-CAS-9-mediated genetic approach used in this study.	138
Figure 39: Establishing a stable PERK knockdown cell line.	140
Figure 40: Establishing a stable IRE1 α knockdown cell line.	142
Figure 41: Differential effects of CRISPR-CAS-9 engineered cell lines lacking PERK or IRE1 α on the ER stress response and HCoV-229E replication.	144
Figure 42: Differential effects of CRISPR-CAS-9 engineered PERK KD cell line on de novo protein synthesis.	146
Figure 43: Differential effects of CRISPR-CAS-9 engineered IRE1 α knockdown cell line on de novo protein synthesis.	147
Figure 44: Upregulation of de novo synthesis of the viral N protein in CRISPR-CAS-9 engineered PERK cell lines.	150
Figure 45: Attempts to establish stable ATF3 knockdown cell lines.	152
Figure 46: Analysis of the effects of CRISPR-CAS-9 engineered ATF3 knockdown cell line on the ER stress response and the replication of HCoV-229E.	152
Figure 47: Revealing the interactomes of major ER stress factors using proximity-based biotinylation labelling strategies.	154
Figure 48: Expression of Myc-BirA-Empty-Vector and Myc-BirA- PERK, -BiP, -IRE1 α , -ATF3 constructs.	156
Figure 49: Biotinylation efficiency of Myc-BirA-EV (ligase only) and Myc-BirA-PERK, -BiP, -IRE1 α , -ATF3 fusion proteins.	158
Figure 50: Biotinylation efficiency of miniTurbo-ATF3 construct is superior to that of BirA-ATF3 construct at 33°C and 37°C.	160
Figure 51: Biotinlaytion efficiency of miniTurbo-PERK construct is superior to that of MYC-BirA-PERK construct at 37 °C.	162
Figure 52: Biotinylation levels of miniTurbo constructs at 33 °C are doxycycline concentration dependent.	165
Figure 53: Pulldown of biotinylated proteins by miniTurbo-PERK or miniTurbo ligase only in the presence or absence of HCoV-229E infection.	166
Figure 54: Pulldown of biotinylated proteins by miniTurbo-ATF3 or miniTurbo ligase only in the presence or absence of HCoV-229E infection.	167
Figure 55: Volcano plot representations of all mass spectrometry data to identify proteins enriched with the miniTurbo-ATF3 fusion protein.	170
Figure 56: miniTurbo-ATF3 interacts with a variety of transcriptional regulators and factors, including those involved in immune response and inflammation.	172
Figure 57: Compared to EV D+B the interactors of ATF3 D+B+ fusion protein predominantly localize to the nucleus and are partially engaged in known physical or functional protein: protein interaction (PPI) networks.	174
Figure 58: Compared to EV V+D+B+, DEPs from the ATF3 V+D+B+ condition overwhelmingly localize to the nucleus.	176

Figure 59: In the ATF3 D+B+ vs ATF3 V+D+B+ comparison, DEPs enriched in the latter condition showed a strong localization to the mitochondria.	177
Figure 60: Top 100 DEPs of the ATF3 V+D+B+ unique list showed strong localization to the mitochondria.....	178
Figure 61: Top 40 enriched pathways mapping to DEPs from ATF3 D+B+ (compared to EV D+B+) (left) and ATF3 V+D+B+ (compared to EV V+D+B+) (right) revealed by Metascape analysis.	179
Figure 62: Top 40 enriched pathways mapping to DEPs unique to the ATF3 V+D+B+ (see figure 56 B) and ATF3 V+D+B+ (compared to ATF3 D+B+) revealed by Metascape analysis.	180
Figure 63: Summary of the newly uncovered findings in this study.....	203

List of tables:

Table 1: Factors for conversion between cell culture vessels.	48
Table 2: List of abbreviations used in this section	168
Table 3: List of conditions used in the interactome experiments	168

List of figures involved external contributions:

Figure	Contributions
Figure 10	The workflow was designed and carried out together with Dr. Axel Weber (Prof. Kracht working group). Raw data were mapped to the human and viral proteomes by Dr. Uwe Linne and Dr. Axel Weber using the MaxQuant framework.
Figure 15	The experiment was performed together with the technician Hendrik Weiser (Prof. Kracht working group). Hendrik Weiser helped perform the biological replicas.
Figure 16	The experiment was performed together with Dr. Christin Mayer-Buro (Prof. Kracht working group). Dr. Mayer-Buro helped perform the biological replicas and analyzing the data.
Figure 17	(A): The experiment was performed together with the technician Hendrik Weiser. Hendrik Weiser helped perform the biological replicas. (B): The experiment was performed together with Dr. Christin Mayer-Buro. Dr. Mayer-Buro helped perform the biological replicas.
Figure 18	The experiment was performed together with the technician Hendrik Weiser and Dr. Christin Mayer-Buro. They both helped perform the biological replicas.
Figure 19	The experiment was performed together with the technician Hendrik Weiser and Dr. Christin Mayer-Buro. They both helped perform the biological replicas. Hendrik Weiser performed the experiment shown in panel B.
Figure 21	The experiments shown in panels A & B were performed together with the technician Hendrik Weiser and Dr. Christin Mayer-Buro. They both helped perform the biological replicas. Dr. Mayer-Buro performed the qPCR absolute quantification shown in panel B.
Figure 22	The infection experiments were performed together with Hendrik Weiser and Dr. Christin Mueller (Prof. Ziebuhr working group). Dr. Mueller performed all SARS-CoV-2 and MERS-CoV infections, plaque assays and cell viability assays in the BSL3 laboratory of the Institute of Medical Virology, Justus Liebig University Giessen. Cell pellets from infected cells were then transferred to the Rudolf Buchheim Institute of Pharmacology and Western blot experiments were performed together with Hendrik Weiser.
Figure 23	The experiments were performed together with Hendrik Weiser and Dr. Christin Mueller. Dr. Mueller performed all MERS-CoV infections and plaque assays in the BSL3 laboratory of the Institute of Medical Virology, Justus Liebig

	University Giessen. Hendrik Weiser performed all the biological replicas shown in panels A, B & C.
Figures 25, 26, 27, 28, 29 & 30	The Proteome-wide experiment was carried out with extensive contributions from multiple people. Dr. Christin Mueller performed all MERS-CoV and SARS-CoV-2 infections. Hendrik Weiser pre-prepared the samples. LC-MS/MS mass spectrometry measurements were done in the mass spectrometry facility of the Department of Chemistry, Philipps University, Marburg (headed by Dr. Uwe Linne). Raw data were mapped to the human and viral proteomes by Dr. Uwe Linne and Dr. Axel Weber (Prof. Kracht working group) using the MaxQuant framework. The bioinformatics strategy and the entire subsequent analyses (figures 25, 26, 27, 28, 29 & 30) were devised, carried out and visualized by Prof. Michael Kracht. M.Samer Shaban extensively discussed, checked and re-analyzed the entire data set.
Figure 32	The experiments shown in panels B, C & D were performed together with the technician Hendrik Weiser. Hendrik Weiser helped perform the biological replicas.
Figure 33	The experiment was performed together with Dr. Christin Mayer-Buro. Dr. Mayer-Buro helped perform the biological replicas and analyzing the data.
Figure 34	The experiments were performed together with Hendrik Weiser and Dr. Christin Mueller. Dr. Mueller performed all MERS-CoV and SARS-CoV-2 infections and plaque assays. Hendrik Weiser helped perform the biological replicas of the HCoV-229E experiment.
Figure 36	The experiment was performed together with Dr. Christin Mueller. Dr. Mueller performed all MERS-CoV infections and plaque assays.
Figure 37	The experiment was performed together with Dr. Christin Mueller. Dr. Mueller performed all SARS-CoV-2 infections and plaque assays.

Declaration:

I declare the following:

I have completed this dissertation single-handedly without the unauthorized help of a second party and only with the assistance acknowledged therein. I have appropriately acknowledged and referenced all text passages that are derived literally from or are based on the content of published or unpublished work of others, and all information that relates to verbal communications. I have abided by the principles of good scientific conduct laid down in the charter of the Justus Liebig University of Giessen in carrying out the investigations described in the dissertation.

Mohammed Samer Shikh Shaban

Acknowledgement:

At the time of writing these words, five years have already passed since this work started. During these five years, many people have nurtured, supported, and contributed to this scientific journey. Without their support, this ship would've never been able to reach its destination.

First and most, I would like to express my deepest gratitude to Professor Michael Kracht for accepting me into his working group at the Rudolf-Buchheim-Institut für Pharmakologie, for supervising this work, and for the many hours of fruitful discussions, brainstorming, and suggestions, all of which have shaped this work, and finally, for his firm support throughout this journey including in helping navigating bureaucratic requirements.

I would also like to extend my deepest appreciation to Hendrik Weiser. From the first day of my work, Hendrik Weiser supported my integration into the working group. With his extensive technical knowledge, practical suggestions, patience, and strong support throughout this journey especially during the publication process of our thapsigargin paper, this work came to see the light of the day.

I also wish to thank Dr. Christin Mayer-Buro for her support. Her helpful advice and invaluable contribution during the publication process of our thapsigargin paper are enormously appreciated.

I'd also like to extend my gratitude to Dr. Johanna Meier-Soelch, Dr. Axel Weber, and Dr. Ulas Tenekeci for offering their extensive scientific knowledge and invaluable insight into several hurdles that have been encountered during this work.

I gratefully acknowledge the effort of Benadict Vincent Albert in introducing me to the technical work of the lentivirus system and for the multiple occasions on which we had insightful scientific exchanges.

Thanks should also go to Sebastian Werner for the very insightful scientific discussions we regularly had, especially on issues related to bioinformatics.

I would also like to thank Heike Schubert and Jasmine Gaspar Dörr for taking the burden of solving bureaucratic issues that been encountered on multiple occasions.

Thanks also to all current and previous members of the "Rudolf-Buchheim-Institut für Pharmakologie" for their support and positive interactions on a day-to-day basis.

From the institute of Medical Virology, Justus Liebig University Giessen, I would like to thank Dr. Christin Mueller for performing the BSL3 experiments and her invaluable contribution during the publication process of our thapsigargin paper.

From the mass spectrometry facility of the Department of Chemistry, Philipps University, Marburg, I would like to thank Dr. Uwe Linne and his team for performing the mass spectrometry measurements.

Finally and on a personal note, I cannot begin to express my appreciation and deepest gratitude to my parents. Their unrelenting love and support, patience, and wisdom, keep me going. I owe them a great debt of gratitude. For my dear sister; no words can express the debt of gratitude for your unwavering support, consistent friendship, and reliable advice throughout my entire life.

Personal data sheet:

Publications:

Schmitz, M. Lienhard, **M. Samer Shaban**, B. Vincent Albert, Anke Gökçen, and Michael Kracht. 2018. “The Crosstalk of Endoplasmic Reticulum (ER) Stress Pathways with NF- κ B: Complex Mechanisms Relevant for Cancer, Inflammation and Infection.” *Biomedicines* 6 (2): 58.
<https://doi.org/10.3390/biomedicines6020058>.

Shaban, Mohammed Samer, Christin Mayr-Buro, Johanna Meier-Soelch, Benadict Vincent Albert, M. Lienhard Schmitz, John Ziebuhr, and Michael Kracht. 2022. “Thapsigargin: Key to New Host-Directed Coronavirus Antivirals?” *Trends in Pharmacological Sciences*, April, S0165614722000840.
<https://doi.org/10.1016/j.tips.2022.04.004>.

Shaban, Mohammed Samer, Christin Müller, Christin Mayr-Buro, Hendrik Weiser, Johanna Meier-Soelch, Benadict Vincent Albert, Axel Weber, et al. 2021. “Multi-Level Inhibition of Coronavirus Replication by Chemical ER Stress.” *Nature Communications* 12 (1): 5536.
<https://doi.org/10.1038/s41467-021-25551-1>.

Shaban, Mohammed Samer, Christin Müller, Christin Mayr-Buro, Hendrik Weiser, M. Lienhard Schmitz, John Ziebuhr, and Michael Kracht. 2022. “Reply to: The Stress-Inducible ER Chaperone GRP78/BiP Is Upregulated during SARS-CoV-2 Infection and Acts as a pro-Viral Protein.” *Nature Communications* 13 (1): 6550.
<https://doi.org/10.1038/s41467-022-34066-2>.

Phongsavanh X, Al-Qatabi N, **Shaban MS**, Khoder-Agha F, El Asri M, Comisso M, Guérois R, Mirande M. How HIV-1 Integrase Associates with Human Mitochondrial Lysyl-tRNA Synthetase. *Viruses*. 2020 Oct 21;12(10):1202.

[doi: 10.3390/v12101202](https://doi.org/10.3390/v12101202). PMID: 33096929; PMCID: PMC7589778.

Conferences Contributions:

Benadict Vincent Albert, **Samer Shaban**, Hendrik Weiser, Michael Kracht
Phosphorylation-dependent regulation of the RNA metabolism in the host response to coronavirus infection”- International Symposium (SFB1021/KFO309 2018-Marburg) - **Team Poster Presentation**

M.Samer Shikh Shaban, Benadict Vincent Albert, Hendrik Weiser, Johanna Meier-Sölch, Michael Kracht, “The crosstalk of endoplasmic reticulum (ER) stress pathways with NF- κ B in coronavirus infected cells”, 12th Annual GGL Conference 2019-**Oral Presentation**

Shaban M.S., Albert B.V., Weiser H., Kracht M. "Characterizing the crosstalk of endoplasmic reticulum (ER) stress pathways with NF- κ B, JNK, P38 in Coronavirus infected cells", 1st Digital GGL Conference on Life Sciences 29th - 30th September 2020-**Oral Presentation.**

Shaban MS, Muller C , Christin Mayr-Buro, Weiser H, Albert BV , Weber A, Linne U , Karl N , Lienhard Schmitz M, Ziebuhr J , Kracht M. „Chemical ER stress inhibits Replication of three human coronaviruses in cultured cells”, 14th GGL Annual Conference on 29-30 September 2021- **Oral Presentation.**

Shaban MS as a chairperson for PD Dr. Michael Mühlebach (Paul Ehrlich Institute, Langen) presentation titled “Platform-based Vaccines – Short-cut to Protection”. Part of the 14th GGL Annual Conference on 29-30 September 2021.

Mohammed Samer Shaban, Christin Müller , Christin Mayr-Buro, Hendrik Weiser, Benadict Vincent Albert, Nadja Karl, M. Lienhard Schmitz, John Ziebuhr, and Michael Kracht “Autophagy- and ER stress-related processes contribute to the replication of human coronaviruses”. The 8th German Pharm-Tox Summit-2022. **Oral Presentation.**

Shaban, M. S., C. Mueller, C. Mayr-Buro, H. Weiser, B. V. Albert, N. Karl, M. L. Schmitz, J. Ziebuhr, and M. Kracht. "Autophagy-and ER stress-related processes contribute to the replication of human coronaviruses." In *NAUNYN-SCHMIEDEBERGS ARCHIVES OF PHARMACOLOGY*, vol. 395, no. SUPPL 1, pp. S10-S10. ONE NEW YORK PLAZA, SUITE 4600, NEW YORK, NY, UNITED STATES: SPRINGER, 2022.

Shaban, M. S., Mueller, C., Mayr-Buro, C., Weiser, H., Albert, B. V., Weber, A., ... & Kracht, M. (2021, March). Chemical ER stress inhibits replication of three human coronaviruses in cultured cells. In *NAUNYN-SCHMIEDEBERGS ARCHIVES OF PHARMACOLOGY* (Vol. 394, No. SUPPL 1, pp. S9-S9). ONE NEW YORK PLAZA, SUITE 4600, NEW YORK, NY, UNITED STATES: SPRINGER.

Functional analysis of human genes regulated by HCoV-229E using genome-editing by CRISPR-Cas9
Albert, B. V.; **Shaban, M. S.**; Werner, S.; Meier-Soelch, J.; Mayr-Buro, C.; Weiser, H.; Hain, T.; Schmitz, L.; Kracht, M..*Naunyn-Schmiedebergs Archives of Pharmacology* ; 394(SUPPL 1):S29-S29, 2021.Artigo em Inglês | Web of Science | ID: covidwho-1390056

Seminars:

Internal Seminar (Kracht Group)	12/11/2017
Internal Seminar (Kracht Group)	3/19/2018
Internal Seminar (Kracht Group)	8/10/2018
Internal Seminar (Kracht Group)	2/18/2019
Internal Seminar (Kracht Group)	6/28/2019
Internal Seminar (Kracht Group)	9/2/2019
Internal Seminar (Kracht Group)	5/11/2020
Internal Seminar (Kracht Group)	10/2/2020
Internal Seminar (Kracht Group)	2/1/2021
Internal Seminar (Kracht Group)	5/17/2021
Internal Seminar (Kracht Group)	10/25/2021
Internal Seminar (Kracht Group)	2/21/2022
Internal Seminar (Kracht Group)	9/19/2022
SFB1021 ProgressReport	10/19/2018
SFB1021 ProgressReport	12/6/2019
SFB1021 ProgressReport	9/3/2021
Current Topics in Applied Immunology (GGL)	6/30/2019
Current Topics in Applied Immunology (GGL)	2/3/2020

Practical courses supervision:

“Master-Modul Molekulare Medizin” WS 2022/23

„Pharmakologie-Praktikum“ (F17) October 2022

Awards:

Rudolf-Buchheim-Price 2022 (DGPT)

